

Extreme Nonlinear Dynamics in the Filamentation Regime

Von der Fakultät für Mathematik und Physik
der Gottfried Wilhelm Leibniz Universität Hannover
zur Erlangung des Grades

Doktor der Naturwissenschaften

- Dr. rer. nat. -

genehmigte Dissertation von

Dipl.-Phys. Martin Kretschmar

geboren am 27.08.1985 in Meißen

2016

Referent: Prof. Dr. Milutin Kovačev

Erster Korreferent: Prof. Dr. Uwe Morgner

Zweiter Korreferent: Prof. Dr. Danielle Faccio

Tag der Promotion: 15.08.2016

Hiermit erkläre ich an Eides statt, dass ich vorliegende Dissertation selbst verfasst habe, keine Textabschnitte von Dritten oder eigenen Prüfungsarbeiten ohne Kennzeichnung übernommen und alle benutzten Hilfsmittel und Quellen in der Arbeit angegeben habe, sowie die Regeln der geltenden Promotionsordnung kenne und eingehalten habe und mit einer Prüfung nach den Bestimmungen der Promotionsordnung einverstanden bin.

Darüber hinaus erkläre ich, dass ich Dritten weder unmittelbar noch mittelbar geldwerte Leistungen für Vermittlungstätigkeiten oder für die inhaltliche Ausarbeitung der Dissertation erbracht habe, d.h. die wissenschaftliche Arbeit ist weder in Teilen noch in Gänze von Dritten gegen Entgelt oder sonstige Gegenleistung erworben oder vermittelt worden.

Ich erkläre, dass die Dissertation noch nicht als Prüfungsarbeit für eine andere Prüfung eingereicht wurde, die gleiche oder eine in wesentlichen Teilen ähnliche Arbeit bei einer anderen Fakultät oder bei einer anderen Hochschule als Dissertation eingereicht wurde, und das keine andere Abhandlung als Dissertation eingereicht wurde.

Außerdem bin ich damit einverstanden, dass die Dissertation einer Überprüfung der Einhaltung allgemein geltender wissenschaftlicher Standards unterzogen wird, dies beinhaltet insbesondere die Verwendung elektronischer Datenverarbeitungsprogramme.

Hannover, 15. Juni 2016

Martin Kretschmar

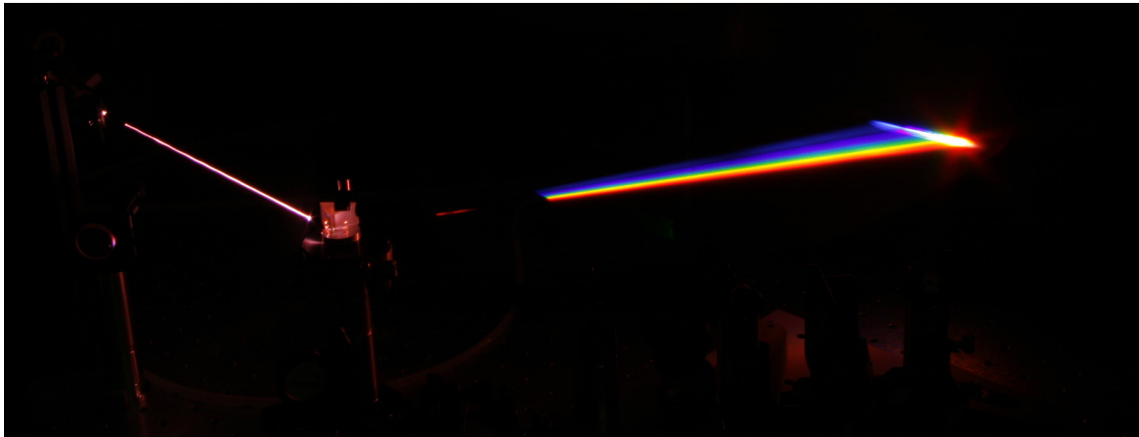
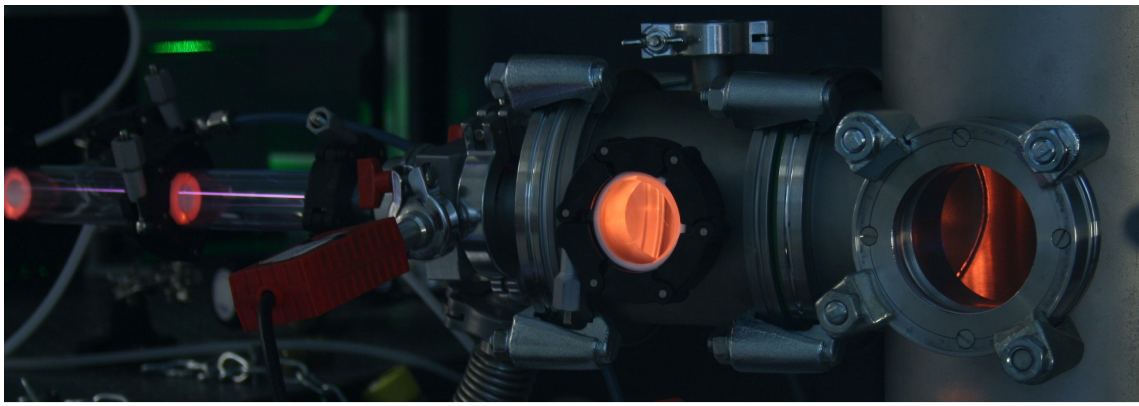


Figure 1: (top) A filament being truncated by a pressure gradient. (bottom) Angular dispersed spectral emission from a filament.

Kurzfassung

Martin Kretschmar

Extreme nichtlineare Dynamiken im Filamentationsregime

Intensive, ultrakurze Laserpulse mit einer Pulsdauer von wenigen optischen Zyklen haben ein breites Anwendungsgebiet in der Femtosekunden-Spektroskopie sowie der Erzeugung hoher harmonischer Strahlung (engl. *high-order harmonic generation*, HHG). Die Realisierung dieser Pulse stellt eine experimentelle Hürde dar, da deren Synthetisierung eine große spektrale Bandbreite erfordert. Üblicherweise werden hierzu verstärkte Laserpulse anhand nichtlinearer Prozesse wie der Selbstphasenmodulation in Gasen spektral verbreitert und mithilfe spezieller Phasenverzögerungsoptiken zeitlich komprimiert. Die resultierenden hochintensiven Femtosekundenpulse ermöglichen die Erzeugung der bisher kürzesten synthetisierten Pulse im Attosekundenbereich über den Frequenzkonversionsprozess der HHG.

In dieser Arbeit wird die Verwendung der Filamentation zur direkten Erzeugung von ultrakurzen, komprimierten Pulsen untersucht. Hierbei werden die komplexen, extrem nichtlinearen Pulsdynamiken entlang des Filaments experimentell studiert. Zur Realisierung dieser Beobachtung wird das Filament durch einen starken Druckgradienten abgeschnitten. Der emittierte Laserpuls wird anschließend unter Vakuumbedingungen analysiert. Signaturen eines zeitlichen Aufbrechens des fundamentalen Pulses sowie dessen Selbstkomprimierung entlang des Filaments werden in dieser Arbeit aufgezeigt. Ein Vergleich der Ergebnisse mit numerischen Resultaten ermöglicht die Identifizierung von charakteristischen Propagationsregimen entlang des Filaments und erlaubt eine Bewertung des zugrunde liegenden numerischen Modells.

Die hohe Spitzenintensität im Filament ermöglicht die direkte Erzeugung hoher harmonischer Strahlung, welche als ein Indikator für bisher unbeobachtbare Eigenschaften der Pulse verwendet werden kann. Insbesondere wird der Effekt der Selbstaufteilung des Laserpulses in den Zusammenhang mit einer spektralen Aufspaltung im Spektrum der XUV-Strahlung erforscht. Die korrekte Evaluation des Aufteilungsprozesses wird anhand eines Vergleiches zu Simulationen des HHG-Prozesses erzielt. Der Einblick in den Erzeugungsprozess der HHG wird zudem über die Betrachtung der Phasen Anpassung vertieft.

Des Weiteren wird die HHG verwendet um einen Rückschluss auf die Spitzenintensität im Filament zu erhalten. Dies wird über die Bestimmung der höchsten emittierten Frequenz (engl. *Cut-Off*) bewerkstelligt und zur Analyse einer propagationsinduzierten Intensitätslimitierung (engl. *intensity clamping*) verwendet. Zudem wird der Einfluss der Fokussierung auf die Intensität im Filament untersucht und mit einem analytischen Modell verglichen.

Schlagnworte: Filamentation, Selbstkomprimierung, Selbstaufteilung, Erzeugung hoher harmonischer Strahlung, intensity clamping

Abstract

Martin Kretschmar

Extreme Nonlinear Dynamics in the Filamentation Regime

Intense, ultrashort laser pulses approaching the few-cycle regime are applied in ultrafast spectroscopy and attosecond physics and require a broadband fundamental spectrum. Commonly, amplified pulses are spectrally broadened using nonlinear effects, such as self-phase modulation (SPM) in gases. The emerging pulses have a large bandwidth, but their pulse duration is still in the vicinity of the initial pulse's length. By applying a fine-adjusted amount of negative and positive group-delay-dispersion (GDD), the temporal compression close to the pulse's Fourier-limit is achieved. The produced high-intensity femtosecond pulses can then be used to generate even shorter pulses on the attosecond timescale through a frequency conversion process called high-order-harmonic generation (HHG).

In the present thesis, the application of filamentation for the direct generation of ultra-short compressed pulses is investigated. The studies examine the complex nonlinear pulse dynamics along a femtosecond-filament by the use of a pressure-gradient truncation stage and an in-situ SHG-FROG pulse detection scheme. Phenomena of pulse splitting and self-compression are identified at different positions in the filament. A comparison with numerical simulations of the pulse propagation dynamics allows for the determination of characteristic stages in the filamentary life cycle. The correspondence between the theoretical and experimental findings is further used to evaluate the applied numerical modeling.

The nonlinear dynamics along the filament lead to ultra-short pulse structures such that the intensity inside the filament is sufficiently high to generate high-order harmonic radiation directly from the filament itself. This XUV-radiation is used to deduce on characteristics of the evolving fundamental pulse that are inaccessible by a conventional pulse-detection setup. In particular, the effect of self-steepening, which leads to drastic envelope dynamics on a single femtosecond time scale, is identified and thoroughly characterized by high-harmonic spectroscopy with the aid of simulations. To further understand the detected XUV-spectral features, the phase matching of the high-harmonic conversion process is evaluated for the special case of filamentation.

Additionally, the peak-intensity along the filament is investigated by the evaluation of the Cut-Off in the high-order harmonic spectrum. This allows to draw conclusions on the effect of intensity clamping. The influence of the external focusing length on the intensity inside the filament is examined and compared to an adapted analytical model.

Key words: filamentation, self-compression, self-steepening, high-harmonic spectroscopy, intensity clamping

Contents

1	Introduction	1
1.1	Motivation and Aims	2
1.2	Organisation of the Thesis	4
2	The Basic Theory	5
2.1	Vacuum Propagation	5
2.2	Interaction of Light with Matter	6
2.2.1	The Optical Kerr-Effect	6
2.2.2	Field Ionization	9
2.2.3	Laser-Plasma Interaction	13
3	Filamentation	15
3.1	The Spatial Balance of Nonlinear Effects	16
3.2	Focusing Competition and Wavefront Curvatures	17
3.2.1	Calculation of the Wavefront Sag	18
3.2.2	Experiments - Evaluating The Dominating Nonlinearity	21
3.3	Spatio-Temporal Dynamics Inside a Filament	24
3.3.1	Obtaining the Wave-Equation	25
3.3.2	Tracking Pulse Dynamics - Experimental Methods and Setup	27
3.3.3	Experimental Diagnostics of the Fundamental Beam Dynamics	33
3.3.4	Spatio-Temporal Dynamics - Simulations and Discussion	36
3.3.5	The Spectral Content of the Reconstructed Pulses - Experimental Shortcomings	46
3.3.6	The Influence of the Truncating Stage	48

3.3.7	Determination of the Correct Ionization Model	51
3.3.8	Conclusion	53
4	Application of an Extreme Nonlinear Probe - Filamentation and High-Order Harmonic Generation	55
4.1	Theoretical Description and Modeling of High-Order Harmonic Generation	56
4.1.1	The Three-Step Model	56
4.1.2	The Lewenstein Model	58
4.1.3	Phase Matching - The Macroscopic Response	60
4.1.4	Transient Phase Matching	62
4.1.5	Spectral Properties of HHG	65
4.2	The Experimental Setup	66
4.3	Direct High-Order-Harmonic Generation Connected to Pulse Dynamics . .	68
4.3.1	Experimental Results	68
4.3.2	Discussion - The Frequency Red-Shift	69
4.3.3	Phase Matching of High-Order Harmonic Generation along a Femtosecond Filament	79
4.3.4	Influence of Pre-Chirped Pulses	84
4.3.5	Conclusion	87
4.4	Reevaluation of the Clamping Intensity	89
4.4.1	An Improved Analytical Determination of the Clamping Intensity .	89
4.4.2	Determination of the Clamping Intensity through HHG	93
4.4.3	Conclusion	101
5	Conclusion and Outlook	103
 Appendix		
 Appendix		
		107
A	Determination of Ionization Rates	109
A.1	Keldysh-Rates	109

A.2 Multi-Photon Ionization-Rates	110
A.3 PPT-Theory	110
A.4 ADK-Theory	111
B Calculation of the wavefront sag	113
Acknowledgments	145
Publications	147

CONTENTS

Abbreviations and symbols

Abbreviations

ADK	Ammosov-Delone-Krainov
ATI	above threshold ionization
CCD	charge-coupled device
CEO	carrier-envelope offset
CEP	carrier-envelope phase
CPA	chirped pulse amplification
DCM	double-chirped mirror
FROG	frequency-resolved optical gating
FWHM	full width at half maximum
GDD	group-delay dispersion
GVD	group-velocity dispersion
HHG	high-order harmonic generation
LIBS	laser-induced breakdown spectroscopy
MPI	multiphoton ionization
MCP	multi-channel plate
OTBI	over-the-barrier ionization
PM	phase matching
PPT	Peremolov-Popov-Ternetev
SAEA	single active electron approximation
SFA	strong-field approximation
SHG	second-harmonic generation
SIGC	semi-infinite gas cell
SPM	self-phase modulation
TG	transient grating
TPM	transient phase matching
VUV	vacuum ultraviolet
XUV	extreme ultraviolet
YI	Yudin-Ivanov

Table 1: Abbreviations.

Mathematical symbols

\vec{A}	vector potential
α	slope of atomic phase ϕ_{at} versus intensity
c	speed of light in vacuum
c.c.	complex conjugate
\vec{D}	electric displacement
D	dispersion operator
ε_0	permittivity of vacuum
e	electron charge
E	electric field
E	Electric field
f	focal length
\mathcal{FT}	Fourier transform
ϕ_{atom}	atomic phase
ϕ_{geo}	geometric phase
$\Delta\phi_{\text{neu}}$	phase mismatch from dispersion of neutral atoms
$\Delta\phi_{\text{el}}$	phase mismatch from dispersion of free electrons
$\Delta\phi_{\text{total}}$	phase mismatch from dispersion of free electrons
γ	Keldysh parameter
Γ	Gamma function
\vec{H}	magnetic field strength
i	imaginary number
I	intensity
I_c	clamping intensity
I_p	ionization potential
\vec{J}	current density
J_0	Bessel function
K	number of photons
\vec{k}	wave vector
$\Delta\vec{k}$	phase-mismatch wave vector
L_{abs}	absorption length
L_{coh}	coherence length
L_{med}	length of the medium
λ	laser wavelength
\mathbf{M}	dipole-transition matrix element
m_e	electron mass
n_0	refractive index
n_2	nonlinear refractive index
Δn_{NL}	nonlinear refractive index change
p	pressure
\vec{p}	canonical momentum
P	Polarization

P_0	peak power
P_{cr}	critical power for self focusing
r	coordinate perpendicular to the propagation direction
r_{el}	classical electron radius
R	radius of curvature
ρ_e	density of free electrons
ρ_{nt}	density of neutrals
ρ_{crit}	critical density
q	harmonic order
Re	real part
S	wavefront sag
S_g	geometrical wavefront sag
S_k	Kerr wavefront sag
S_p	Plasma wavefront sag
S_{MPI}	MPI plasma wavefront sag
S_{ADK}	ADK plasma wavefront sag
S_{sc}	quasi-classical action
σ_K	multiphoton ionization cross section
t	time coordinate
T	space-time focusing operator
τ	pulse duration
τ_{exc}	traveling time
τ_{d}	delay
U_p	ponderomotive potential
W	ionization rate
w_0	beam waist
ω	angular frequency
$\Delta\omega$	induced frequency
ω_p	plasma frequency
χ	susceptibility
z	coordinate in propagation direction
z_r	Rayleigh length
ζ_a	asymmetry factor

Table 2: Mathematical symbols.

CONTENTS

Chapter 1

Introduction

Pulsed lasers enable to study ultrafast processes ranging down to the attosecond timescale (10^{-18} s) [1–3, and references therein]. Ultrashort pulses have been applied in pump-probe schemes to gain insight into fundamental physical concepts on timescales of the respective laser pulse duration [4–6, and references therein]. The monitoring of chemical reactions by femtosecond pump-probe methods for example has been awarded with the noble-price in chemistry at hand of Ahmed Zewail "for his studies of the transition states of chemical reactions using femtosecond spectroscopy" in 1999 [7]. The required pulse duration for the observation of these fragmentation dynamics ranges from 600 fs down to 100 fs [8]. To generate pulses with a duration short enough to examine not only fragmentation dynamics, but also the rotational and vibrational motion in molecules and halogens [9, 10] or Rabi-flopping in semiconductors [11], the pulse duration needs to approach a few optical cycles (corresponding to ≈ 5 -10 fs) at 800 nm. This requires a spectral bandwidth exceeding 100 nm [12, 13]. The broadband spectrum connected to the short pulses itself can be applied for spectroscopic applications and has been utilized as an analytic tool in e.g. tomographic imaging [14, 15].

Utilizing nonlinear effects such as self-phase modulation (SPM) can efficiently generate the necessary frequency components and increase the spectral bandwidth of the fundamental pulse [16]. SPM has been first observed in liquids [16] and quickly adapted to solids [17, 18], where the effect has been reliably exploited to deliver few-cycle pulses from fibers and oscillators with energies in the nJ up to the μ J level [19–25].

The nowadays available chirped-pulse amplification technique drastically scaled the pulse's peak power to the millijoule level [26]. The achievable peak intensities exceed the damage-threshold of solids which requires the application of gases to effectively exploit SPM. External spectral broadening setups have been designed to efficiently utilize SPM, such as hollow-core fibers (HCF) [27–29]. The shortest pulse length can be achieved, when all generated frequencies show no phase delay. Therefore, pulse-compression setups are usually applied to compensate the chirp of the spectrally broadened pulses by the use of specially designed chirped mirrors [30–34].

To achieve even shorter pulses, the carrier frequency of the pulse needs to be shifted to higher frequencies. As the fundamental pulse duration approaches the few-cycle regime and the intensity of the focused ultrashort pulses is able to compete with the inner-atomic field strength, the generation of harmonic radiation outside of the perturbative regime is accessible. This enables to push the pulse duration below the femtosecond barrier, as the carrier frequency is shifted to the extreme-ultraviolet (XUV) spectral regime through high-order harmonic generation (HHG) [1]. This conversion process has been first observed in 1987 by McPherson et. al., shortly followed by the semi-classically theoretical description by Corkum and the fully quantum-mechanically treatment introduced by Lewenstein et. al. [35, 36]. Different geometries have been used as a source for HHG such as the gas-jet [37], capillary wave-guides [38], finite and semi-infinite gas-cells [39–42]. The emitted harmonic radiation shows good temporal and spatial coherence properties, making a synthesis of an isolated attosecond pulse by the process of HHG possible [43–47]. The record of the shortest pulse generated to date is 67 as [48]. The coherence properties enable the use of the harmonic spectrum itself as a tool to monitor dynamics in the generating medium and of the driving laser pulse [2, 49–51]. Since the observable time-scale shifts below the femtosecond barrier, the observation of electron dynamics within atomic systems is possible in pump-probe schemes [52–55].

1.1 Motivation and Aims

As introduced, the generation and application of mJ-level ultrashort pulses relies on concatenated spectral broadening, a subsequent pulse-compression and an additional stage for HHG or a spectroscopic setup. In this thesis, the possible combination of all these steps into a single highly nonlinear process called filamentation is investigated. The generation of a filament relies on the balance of nonlinear effects during the propagation of the laser pulse. The Kerr-effect, which is responsible for the generation of new frequencies through SPM, can also lead to a self-focusing of the intense beam [56]. During interaction with a nonlinear medium e.g. noble gases, this action will dominate the nonlinear propagation and result in an increasing intensity until a plasma is created. The generated free electrons induce a defocusing effect on the beam [57]. If the two nonlinear processes counterweight, a *filament* is formed. Therein, the laser pulse is self-guided over distances well exceeding the *Rayleigh* range [58, and references therein]. Consequently, nonlinear effects such as SPM and self-steepening can modulate the spectrum along an extended propagation distance resulting in a broadband spectral emission. The achievable bandwidth has been shown to enable the generation of sub-10 fs pulses [59, 60]. The self-confinement additionally results in a controversially discussed phenomenon of intensity clamping, which limits the achievable peak intensity inside the filament due to the dynamical interplay of the nonlinear effects [61–65].

The perception of the filamentary process and its modeling started with a simple self-channeling approach [57, 61, 62, 66] and the moving-focus-model [67] where the plasma-

dynamics occurring along the temporal pulse shape are omitted. Approaches like the dynamic spatial replenishment model implemented the time-dependent evolution of the nonlinear contributions along the envelope of the pulse, leading to a more precise description of filamentation [68]. Modern-days modeling of the propagation tries to conclude from the Maxwell's equations by applying a bridge between envelope- and Maxwell's formalism to gain a unidirectional optical pulse propagation equation (UPPE) [58, 69, 70].

Many works have predicted self-shortening dynamics into the few-cycle regime [71–73], but their evolution remains undisclosed by the previous experimental observations [74–76]. However, the modeling using the nonlinear generalized Schrödinger type equation is an extremely challenging task and the findings need to be verified experimentally [77]. The undisturbed observation of dynamics along a femtosecond filament is limited by the high-intensity self-guiding of the fundamental laser pulse, limiting the insight into the propagating filament to the observation of fluorescence lines along the filament or pulse characteristics after the filament [58, 62, 75, 76, 78, 79]. The content of this thesis aims at a direct measurement of the spatio-temporal pulse dynamics which enables a straightforward comparison to numerical simulations.

A method developed in references [60, 80, 81] is applied, in which the filament is truncated during its propagation by a steep pressure gradient. The removal of the guiding medium rapidly stops the nonlinear propagation and the pulse continues to propagate under vacuum conditions to be analyzed. The findings are used to elaborate on predictions of self-compression from the theoretical modeling. The goal hereby is the determination of regimes along the filament where the different nonlinear contributions connected to the Kerr- or the plasma-initiated effects are predominant.

It has been shown previously that high-order harmonic radiation can originate directly from a femtosecond filament, omitting an external setup for its generation [80–82]. Here, the high-intensity characteristics of the self-guiding channel are exploited to use directly emitted high-order harmonic radiation from the filament as a spectroscopic tool to more precisely monitor the complex propagation dynamics of the fundamental pulse. HHG is sensitive to the fundamental pulse's intensity and is therefore used to investigate intensity clamping along the filament. Additionally, an estimation of self-steepening dynamics can be performed since HHG exhibits a direct dependency on the slope of the driving pulse's envelope.

Filaments are not solely limited to the use of self-compression for the purpose of ultrashort pulse-generation but have various other applications which benefit from a better understanding of the pulse dynamics inside the filament. The ultrashort pulses along the filament can excite rotational or vibrational states in molecules which can be probed by impulse stimulated Raman-scattering [13, and references therein]. This means that filaments have already been used to monitor processes connected to femtosecond chemistry due to their self-shortening characteristics and the applications would profit from the precise evaluation of the pulse dynamics. The ability to manipulate the point at which the fundamental pulses self-compress can favor the detection efficiency in these sensing schemes. The pulse

dynamics and their control not only influences the chemical state of the medium but also benefits frequency conversion processes such as four-wave mixing, cross-phase modulation, low- and high-order harmonic generation along the filament [80, 81, 83–85].

Further applications rely on high-intensities and the correlated density of free electrons and rather aim at the application of the most intense instead of the shortest pulse. For example, filaments have been employed for remote sensing, utilizing the stand-off high intensities along the self-guided channel for laser-induced-breakdown-spectroscopy (LIBS) [86–88]. These fields benefit from the knowledge of the intensity-evolution along the filament, which is investigated in this thesis. The connected insight into the evolution of free electrons can also be useful for the application of filamentation in the wireless transfer of electrical discharges or THz-generation [89–91].

1.2 Organisation of the Thesis

The thesis is organized into 5 chapters. Chapter 2 introduces basic concepts of laser-matter interaction which are predominant in filamentation, recalling the influence of the Kerr-effect, the modeling of ionization and the respective impact on the propagation dynamics. In section 3, the concepts of filamentation are introduced step-wise. First the interaction of purely spatial effects is investigated through the experimental evaluation of spectral properties. The complexity of the modeling and the experiments increases as the spatio-temporal coupling is added subsequently to the theoretical modeling and the experimental observations shift towards the determination of the fundamental pulse shape along the femtosecond filament. The experimental setup is explained and the theoretical model is discussed at hand of the experimental findings. Along chapter 4 the theory of high-order harmonic generation is explained. Also, the modified experimental setup for the purpose of XUV-detection is described. The experimental findings focus on three topics, discussing the interplay between self-steepening and HHG, the phase matching along a filament and the evaluation of the clamping intensity. The results of the thesis will be summarized in chapter 5, where future possible projects will be presented.

Chapter 2

The Basic Theory

The forthcoming chapter describes the basic concepts of the interaction of intense ultra-short laser pulses with matter. The findings will be essential for the modeling of filamentation as well as high-order harmonic generation, as both theoretical models will be introduced at a later point along the thesis. This section covering the fundamental theory will start with a short explanation of linear vacuum propagation and shift its focus on basic nonlinear effects present in gaseous matter.

2.1 Vacuum Propagation

The basics for the evaluation of laser-matter interactions has been set by the formulation of the Maxwell equations [92], connecting the evolving electric field \vec{E} with a co-propagating magnetic field \vec{B} :

$$\vec{\nabla} \cdot \vec{D} = \rho \quad (2.1a)$$

$$\vec{\nabla} \cdot \vec{B} = 0 \quad (2.1b)$$

$$\vec{\nabla} \times \vec{E} = -\frac{\partial \vec{B}}{\partial t} \quad (2.1c)$$

$$\vec{\nabla} \times \vec{H} = \vec{J} + \frac{\partial \vec{D}}{\partial t}. \quad (2.1d)$$

Here, ρ denotes the free charge density, $\vec{H} = \mu_0 \vec{B}$ the magnetic field strength, \vec{D} the electric displacement and \vec{J} the current density. A simple solution of the Maxwell equations with no free charges can be obtained by separating the spatial (x, y, z) and temporal (t) coordinates of the solution $E(x, y, z, t) = \frac{1}{2} E(t, z) u(x, y, z) + c.c.$ to obtain the Helmholtz-equation $(\vec{\nabla}^2 + k^2)u(x, y, z) = 0$. The constant k is defined as $k = \omega n_0 / c$, where ω labels the angular frequency, n_0 the refractive index and c the speed of light. A Gaussian solution

$u(x, y, z)$ (assuming z as the propagation direction) is expressed as:

$$u(x, y, z) = u_0(x, y, z)e^{ikz} \quad (2.2a)$$

$$= u_0 \frac{w_0}{w(z)} e^{i\phi_G(z)} e^{-\frac{x^2+y^2}{w^2(z)}} e^{i\frac{k(x^2+y^2)}{2R(z)}} e^{ikz}. \quad (2.2b)$$

Many important characteristics are already represented in the above formula. The beam radius evolves as $w(z) = w_0 \sqrt{1 + (\frac{z}{z_r})^2}$ with w_0 denoting the beam waist. The curvature of the wave fronts changes according to $R(z) = z(1 + (\frac{z}{z_r})^2)$, whereas $z_r = n_0 \pi w_0^2 / \lambda$ is the Rayleigh-length. An additional phase term $\phi_G(z) = -\arctan(z/z_r)$ denotes the Gouy-phase which will be described in detail at a later point in this thesis (c.f. Sec. 4.3.3). A free propagating Gaussian beam naturally diffracts because it is accumulating a phase in dependence of the transverse beam dimension $r = \sqrt{x^2 + y^2}$ according to:

$$\phi_{\text{diff}} = -\frac{kr^2}{2R(z)}. \quad (2.3)$$

The connected divergence of the Gaussian beam along z can also be expressed by an angle θ between the propagation axis and the beam's edge at $w(z)$ by:

$$\theta \underset{z \gg z_r}{\propto} \frac{\lambda}{\pi w_0} = \frac{w_0}{z_r}. \quad (2.4)$$

The (linear) basis for the understanding of a electromagnetic wave propagating in vacuum has been laid out. The scaling of the divergence of the beam $\propto \lambda/w_0$ will play an important role for the nonlinear interaction of the beam with its surrounding matter, which will be introduced in the following.

2.2 Interaction of Light with Matter

The previous description of a propagating electromagnetic wave and the diffracting effect do not require a medium to be present for interaction. This changes with the introduction of the nonlinear propagation effects.

2.2.1 The Optical Kerr-Effect

The nonlinear response of a medium to the electromagnetic field is embedded in the electric displacement term $\vec{D} = \epsilon_0 \vec{E} + \vec{P}$. The interaction of an electromagnetic wave with matter is described by the polarization $\vec{P} = \chi \vec{E}$, where χ is the susceptibility of the medium [93].

The susceptibility is connected to dispersion as well as absorption through its real and imaginary parts and can be expanded into a Taylor series [93, 94]:

$$\chi = \underbrace{\chi_1}_{\chi_L} + \underbrace{\chi_2 \vec{E} + \chi_3 \vec{E}^2 + \chi_4 \vec{E}^3 + \chi_5 \vec{E}^4 + \dots}_{\chi_{NL}}, \quad (2.5)$$

where the linear part of the susceptibility is denoted by $\chi_1 = \chi_L$. A frequency-dependent $\chi_L(\omega)$ results in dispersion, as $n(\omega) = \sqrt{1 + \chi_L(\omega)}$. The nonlinear susceptibility χ_{NL} is connected to coefficients χ_i with $i > 1$. Consequently, the polarization \vec{P} is decomposed into a corresponding linear and a nonlinear term $\vec{P} = \vec{P}_L + \vec{P}_{NL}$. To evaluate which nonlinear terms effectively influence the propagating electromagnetic wave, the dominating contribution of \vec{P}_{NL} has to be determined. A centro-symmetric medium (e.g. an atomic gas) neglects even contributions, making the third-order process the first influential non-linearity [95]. This results in a modification of the refractive index Δn_{Kerr} of the medium by [56]:

$$\Delta n_{\text{Kerr}} = n_2 I, \quad (2.6)$$

where $n_2 = \frac{3\chi_3}{4n_0^2 \epsilon_0 c}$ is the nonlinear refractive index. As a result, $n = n_0 + \Delta n_{\text{Kerr}}$ is directly proportional to the intensity distribution $I(r, z, t)$ of the electromagnetic wave. The spatial dependence of the intensity leads to a modification of n , which is, under the assumption of a spatial Gaussian intensity profile, similar to the shape of a focusing lens. A spatial phase $\phi_{\text{Kerr}}(r) = (n_0 + \Delta n_{\text{Kerr}}) \omega \Delta z / c$ is imprinted on the beam [56]. Following Eq. (2.6) for $I(r, z, t)$ in dependence of r , the phase evolution along the beam profile reads as [96]:

$$\begin{aligned} \phi_{\text{Kerr}}(r) &= (n_0 + n_2 I_0 e^{-r^2/w_0^2}) \omega \Delta z / c \\ &\approx \left(n_0 + n_2 I_0 \left(1 - 2 \frac{r^2}{w_0^2} \right) \right) \omega \Delta z / c. \end{aligned} \quad (2.7)$$

Consequently, the natural diffraction ϕ_{diff} (c.f. Eq. (2.3)) of the beam can be compensated by $\phi_{\text{Kerr}}(r)$, when the critical power of self-focusing:

$$P_{cr} = \frac{3.77 \pi c^2}{2 n_0 n_2 \omega_0^2} \quad (2.8)$$

is exceeded [97, 98].

Assuming a pulsed emission of the laser, the spatial self-focusing effect has a temporal counterpart, since the temporal dependence of the intensity introduces a time dependent phase term along the Gaussian pulse envelope, which is expressed by $\phi_{\text{tempKerr}} = (n_0 + \Delta n_{\text{Kerr}}) \omega_0 z / c - \omega_0 t$. The temporal variation of the phase results in the generation of new frequencies that are connected to the slope of the fundamental pulse by [17, 18]:

$$\Delta \omega = - \frac{\partial \phi_{\text{tempKerr}}}{\partial t} \propto \omega_0 - n_2 \frac{\partial I(t)}{\partial t}. \quad (2.9)$$

Hence, a symmetric temporal pulse-profile results in uniform generation of new frequencies around ω_0 . Figure 2.1 highlights the influence of the Kerr effect on the frequency

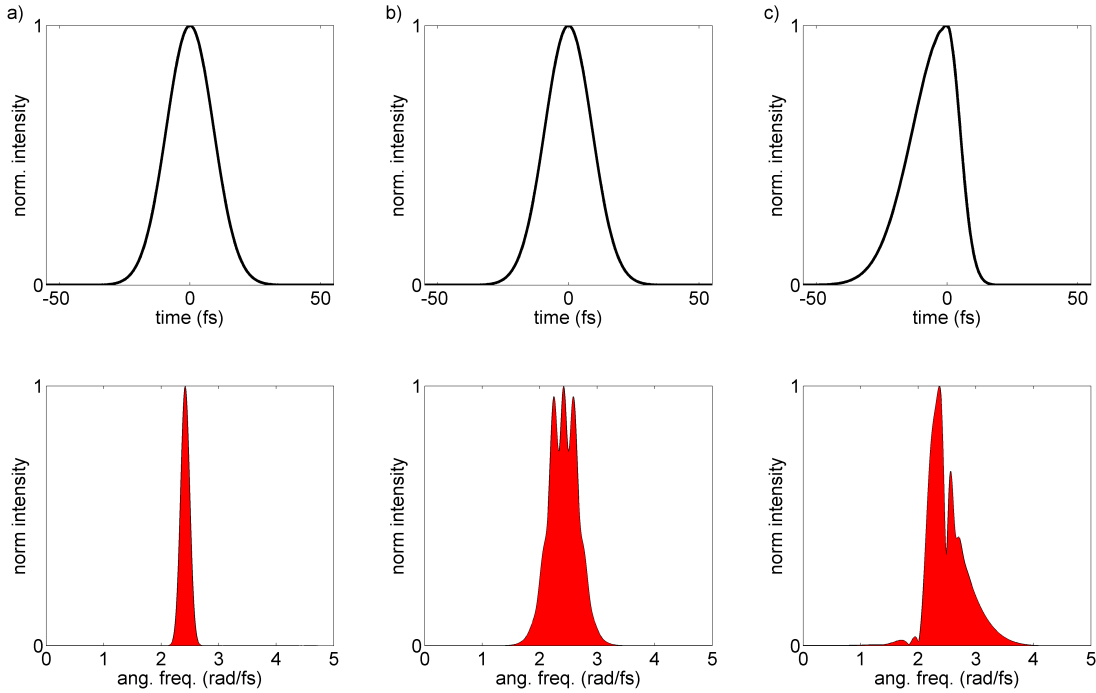


Figure 2.1: Calculation of the effect of self-phase modulation on the fundamental spectrum for pulses with a different steepness. For this case a 30 fs pulse with an intensity of $100 \text{ TW}/\text{cm}^2$ is used to model the generation of new frequency components along the temporal pulse shape. Case (a) shows the initial pulse and its spectrum, (b) shows the SPM-effect for a Gaussian pulse, whereas case (c) displays the results for a 30 fs pulse steepened by a factor of 0.45.

modulation of the initial pulse. Panel (a) displays a Fourier-limited 30 fs pulse with a peak intensity of $I_0=100 \text{ TW}/\text{cm}^2$, centered at 800 nm with its corresponding spectrum below. Part (b) shows the exemplary symmetric generation of new frequencies around the initial spectrum due to the Kerr-effect.

Since the electric field components along the temporal pulse shape experience different intensity-dependent refractive indexes, the envelope can be modulated during propagation. The peak of the pulse experiences a larger refractive index compared to its pedestals, effectively slowing down the most intense content along the envelope. The trailing segment is able to overtake the peak during propagation, leading to an increasing slope on the falling edge of the pulse. In the same manner, the leading segment moves faster as the peak and stretches the corresponding edge of the pulse. As a consequence, the pulse experiences self-steepening.

The effect of self-steepening on the frequency-distribution (comp. Eq. (2.9)) can be seen in Fig. 2.1 (c). Here, the initially symmetric pulse shape is modified to discard 45% of the envelope from the falling edge and add this to the leading part of the pulse. The generation of red-shifted frequencies in the leading edge is weakened, as the pulse is turning on more smoothly compared to the symmetric case. On the other hand, the blue spectral region

originating from the steep falling edge of the pulse is strongly enhanced. For the case of strongly steepened pulse shapes, the spectral content connected to the falling edge is ranging up to very high frequencies due to the direct dependence on the envelopes negative gradient. The respective intensity of the spectrum is rather low, since the conversion originates from a localized area covered by the steep falling edge of the pulse.

2.2.2 Field Ionization

Ionization of a medium plays a key role throughout the whole thesis, as the process of filamentation as well as high-order harmonic generation are strongly dependent on the connected free electron density ρ_e along the medium. The amount of electrons is directly linked to the number of singly charged ions for moderate intensities. Even if the laser pulse is strong enough to ionize 25% of the particles in the medium, the rate for the generation of doubly charged ions will be orders of magnitude lower. Moderate intensities favor the mechanism of multiphoton ionization [99], whereas increasing intensities lead to dominant contributions of tunneling rates. In order to estimate the key contribution, the Keldysh-parameter γ [100] is used:

$$\gamma = \sqrt{I_p/2U_p}, \quad (2.10)$$

giving the relation between the ionization potential I_p to the ponderomotive potential energy U_p :

$$U_p = \frac{e^2 \vec{E}^2}{4 m_e \omega^2}, \quad (2.11)$$

where e denotes the elementary charge and m_e the electron mass.

For cases of a weak fundamental field it can be found, that U_p is much smaller than I_p and the Keldysh-parameter is larger than 1. This resembles the range of laser intensities, where the multiphoton process is dominating as compared to $\gamma \ll 1$, where the tunneling ionization is predominant. Depending on the peak intensity and the wavelength of the fundamental pulse, the ionization dynamics along the pulse shape will be dominated by one of these two processes. The determination of the actual ionization rates leaves a wide choice of theories with an applicability strongly depending on the γ parameter. The **m**ultiphoton **i**onization (MPI) rate is proportional to I^K with K being the number of photons necessary to ionize and very well estimates the dynamics for low intensities with $\gamma \gg 1$ [99, 101]. The MPI method enables a quick analytical estimation of the generated free electrons. The **A**mmosov-**D**elone-**K**rainov (ADK)-formalism [102] focuses on the description of ionization-rates through the tunneling-effect and is valid for $\gamma \ll 1$.

Figure 2.2 shows calculated γ -values in dependence of the fundamental pulse's intensity and wavelength. The position at which $\gamma = 1$ shows a strong dependency on both parameters due to the connection to $U_p \propto I/\omega^2$. The Keldysh parameter can also be interpreted as the ratio between the tunneling time of the electron and half the duration of a laser cycle. The deformation of the Coulomb potential, sketched in the top-right corner of Fig. 2.2, has to endure long enough for the electron to tunnel through the barrier. If the field-modulation has a sufficiently high-frequency, the barrier will be increased on a timescale smaller than the tunneling time. Therefore, the potential effectively shapes like it is sketched in the left bottom corner of the figure and the MPI-rates apply. An increasing intensity leads to a stronger suppression of the potential and therefore to a reduction of the tunneling time, which favors the applicability of the ADK-rates. The black dotted lines delimit the areas in which the MPI- or ADK-models are applicable.

Problems arise as the intensity along the fundamental pulse crosses the border between the tunneling and the multiphoton regime, calling for models that accurately describe the ionization dynamics for both cases. The theory initially developed by Keldysh is able to fulfill this requirement, albeit being limited to monochromatic fields and pulse envelopes [100]. Additionally, the long range Coulomb interaction between the electron and the atomic core is only estimated by a quasi-classical analysis [100]. The later issue is addressed in the **P**eremolov-**P**opov-**T**ernetev (PPT)-model, as the long range Coulomb interaction between the electron and the atomic core are accounted for and effects of the atomic structure itself are implemented [103]. The most accurate analytic description of the ionization rates has been developed by **Y**udin and **I**vanov (YI), as the PPT-theory is expanded to describe field-dependent ionization dynamics [104]. A detailed description of the ionization rate equations and their evaluation can be found in Appendix A.

The numerical reference for the introduced analytical models is given by the solution of the time-dependent-Schrödinger equation (TDSE), usually applying the single-active-electron approximation (SAE) [105, 106]. Comparisons between the presented formalisms and the TDSE-results find a good agreement for the PPT- as well as the Yudin-Ivanov-theory [107, 108]. From the experimental point of view, time-of-flight spectroscopy is used

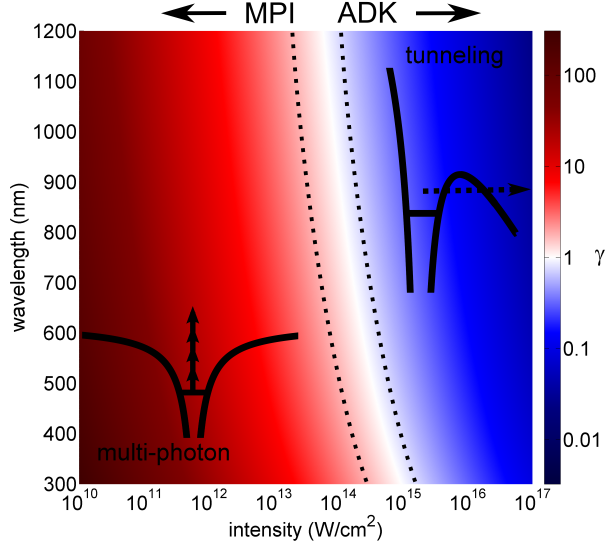


Figure 2.2: Color-encoded values of the Keldysh-parameter γ in dependence of the laser intensity and wavelength. The Coulomb potential of an atom interacting with the external laser field is drawn in black for the case of multi-photon ionization and tunneling ionization.

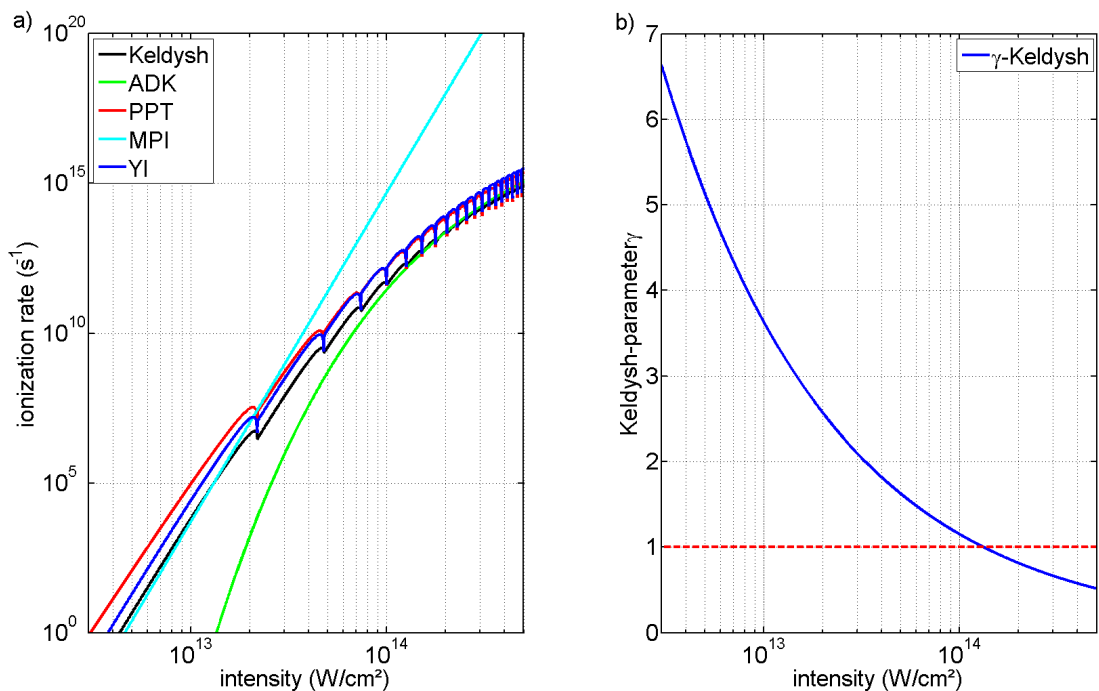


Figure 2.3: (a) Ionization rates in dependence of the driving intensity. (b) Corresponding evolution of the Keldysh-parameter. The gas chosen for the calculations is argon which interacts with a 780 nm driving wavelength.

to either detect ion species or electron distributions in dependence of the fundamental pulse's intensity and fully support the TDSE calculations and consequently the analytical models, which show a good agreement with the numerical findings [109].

The dependence of ionization rates on the driving laser intensity is depicted in Fig. 2.3 (a) for the case of argon ($I_p = 15.76 \text{ eV}$) interacting with a 800 nm field. The various ionization models are depicted in different colors and the assignment can be extracted from the inlet in Fig. 2.3. The corresponding evolution of the Keldysh-parameter γ is shown in Fig. 2.3 (b). The various models result in differing ionization rates depending on the intensity, where in these cases the Yudin-Ivanov-rates (shown in blue) serve as the reference. This model is chosen to be the reference, since it shows the best agreement to TDSE-simulations as well as experimental comparative studies [109]. It can be seen, that the PPT-theory (red) shows an excellent agreement and the Keldysh-theory (black) also reasonably delivers comparable results. The strong restrictions of the MPI-(cyan) as well as the ADK-formalism (green) can easily be noticed. Comparing the deviations of these two simple methods with the evolving γ parameter, it can be seen, that the ADK-rates sufficiently converge for $\gamma < 0.9$ and that the MPI-rates can faithfully be used for values of $\gamma > 1.75$. These values also define the borders in Fig. 2.2.

When the ionization rates are used to model the interaction of the generated free electrons on a fundamental pulse, the choice of the applied model has a crude influence on the

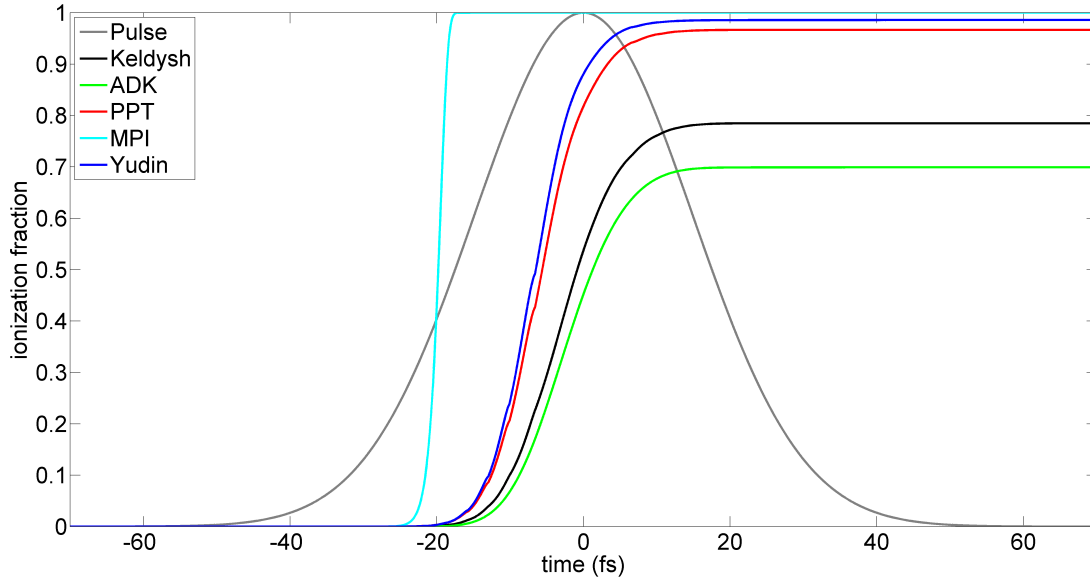


Figure 2.4: Evolution of the degree of ionization along a 35 fs pulse at 780 nm with a peak intensity of 250 TW/cm². The results from the different ionization models are compared and their assignment is denoted in the key.

outcome of the simulations and their interpretation, as the generated plasma can modify the spatial as well as spectral properties of the propagating beam.

Fig. 2.4 shows the ionization fraction, which is the density of neutrals ρ_{nt} divided by the density of free electrons ρ_e , for the introduced models. A fundamental pulse with a pulse duration of 35 fs, centered at 780 nm with a peak intensity of 2.5×10^{14} W/cm² has been applied (shown in gray). A comparison with the evolution of γ in dependence of the intensity (c.f. Fig. 2.3 (b)) reveals, that the pulse is chosen to cross the intensity at which $\gamma = 1$ and therefore switches between multiphoton- and tunneling ionization along its temporal envelope. The MPI-rates overestimate the ionization, since the multiphoton regime is well exceeded by the peak intensity of the pulse, leading to a quick depletion of the medium along the pulse. The rates predicted by the PPT- and YI-rates result in a coherent picture of the ionization dynamics along the pulse envelope. The ADK-model slightly underestimates the evolution since it is adapted to the tunneling regime, being only present for intensity regions above 70 percent of the peak intensity. The findings from Figs. 2.4 and 2.3 show that the analytical outcome is strongly dependent on the method of choice.

Two explicit cases need to be mentioned, where the presented models need to be adjusted for further use. The first problem arises as the target gains complexity, which is the case for molecular targets. Here, the orientation dependency of the ionization as well as the complex nature of the internal orbital structure call for an optimization of the analytical expressions for the ionization rates [110–113]. Second, the use of extreme intensities can lead to a complete suppression of the atomic potential-barrier, which also changes the analytical

formalism [114, 115]. Fortunately, this regime is trustfully described by a modified ADK-theory and minor adjustments of the initial formalism are sufficient to account for the vanishing Coulomb barrier [116, 117].

In conclusion, care has to be taken when choosing a model for the calculation of ionization dynamics along an intense ultrashort pulse. In practice, the model should turn out to be a compromise between the desired accuracy and the available computational resources. A simplified theory, as the MPI- or ADK-rates, should only be used for their respective validated intensities connected to the Keldysh-parameter. The PPT- and YI-models are estimated to be the most accurate but also require the most computational effort for their evaluation.

2.2.3 Laser-Plasma Interaction

The free electrons generated due to the interaction of the medium with a high-intensity laser pulse have multiple effects on the propagating beam. The refractive index of the medium changes according to [118–120]:

$$\Delta n \approx -\rho_e(r, t)/2\rho_{\text{crit}}. \quad (2.12)$$

Here, $\rho_{\text{crit}} = \varepsilon_0 m_e \omega_0^2 / e^2$ describes the critical plasma density, which is the point where the plasma becomes nontransparent for the laser frequency ω_0 . The induced refractive index change is negative and therefore induces a Δn similar to a defocusing lens. As shown in the previous section (c.f. Fig. 2.4), the electron density ρ_e accumulates along the temporal pulse shape which allows to conclude that $\rho_e(r, t)$ most significantly changes on the rising edge of the pulse, with a constantly positive contribution of $\frac{\partial \rho_e(r, t)}{\partial t}$. The changing density of free electrons results in the generation of new frequencies, similar to the effect of self-phase modulation in Eq. (2.9). The evolving ρ_e introduces a nonlinear phase term described by [119–121]:

$$\phi_{\text{plasma}} \approx -\frac{\omega_0 \rho_e(r, t) \Delta z}{2c\rho_{\text{crit}}}. \quad (2.13)$$

The temporal derivative of this phase results in a frequency shift according to:

$$\Delta \omega_t \approx \frac{\omega_0 \Delta z}{2c\rho_{\text{crit}}} \frac{\partial \rho_e(r, t)}{\partial t}. \quad (2.14)$$

The steadily rising nature of the free electron density leads to an asymmetric contribution of the induced frequencies, favoring blue spectral components.

The generated plasma itself carries a characteristic oscillation period connected to the restoring forces being present between the free electrons and their respective ionic cores. Therefore, it is ρ_e , which determines the plasma frequency [119–121]:

$$\omega_{\text{plasma}} = \sqrt{\frac{e^2 \rho_e(r, t)}{m_e \varepsilon_0}}. \quad (2.15)$$

This defines the frequency at which the plasma becomes critical, meaning that it becomes over-dense, non-transparent for all frequencies $\omega < \omega_{\text{plasma}}$ [121]. The introduced basics of nonlinear interaction of a laser pulse with its surrounding medium serves as the groundwork for the process of filamentation in the upcoming chapter, and later for the generation of high frequencies by the process of high-harmonic generation.

Chapter 3

Filamentation

The previous chapter described how the fundamental laser beam can be focused as well as defocused due to its sole interaction with the surrounding medium. The counteracting properties of the Kerr-effect and the plasma can be used to counterbalance each other over a long interaction length, which leads to a high-intensity interaction region, well exceeding the usual Rayleigh length of the initial focusing optics. Consequently, the laser pulse forms a channel using the Kerr- and plasma-induced nonlinearities of the surrounding medium, which is called *filamentation*. After more than 20 years of research on filamentation in gaseous matter, additional approaches besides the Kerr-plasma-balance are discussed as the underlying mechanism of self-guiding. A piece-wise self focusing of the temporal pulse shape to different positions along the propagation axis is the basis of the moving focus model [67, 122]. For an interaction with dense and strongly dispersive materials, filamentation is explained by a transformation of the propagating pulse into a Bessel beam, explaining a commonly observed conical emission of the spectrum by the formation of X-waves [123–128]. Also, the possible saturation of the Kerr-effect due to contributions of higher nonlinearities to P_{NL} is being discussed (c.f. Eq. 2.5) [129–132].

The self-guiding plasma channels have various applications, many of them being connected to frequency conversion, such as THz generation [89–91], four-wave mixing as well as low- and high-harmonic generation [80–84]. Other applications focus on the remote detection of material properties using Laser-induced-breakdown-spectroscopy (LIBS) [86–88] as well as lasing-similar action in excited states along the filament’s core [133, 134]. The extended high intensity region allows for an efficient modification of the fundamental spectrum due to self-phase modulation as well as self-steepening, making filaments a promising approach for the generation of intense, ultrashort laser pulses [60, 135–138]. This presents to be an alternative to the commonly used spectral broadening techniques, like the use of a hollow-core fiber [27–29]. The application of two successive filamentation stages in separate gas-cells enabled the compression of 43 fs pulses with an energy of 0.85 mJ down to 5.7 fs with a conservation of the carrier-envelope-phase (CEO) during filamentation [59]. Later it was shown, that a single filamentation stage is able to deliver pulses with sub-1.5-cycle

duration applying 0.9 mJ pulses of 40 fs duration to form a filament in argon. These setups rely on a post-compression stage to shorten the pulses extracted from the filament [60].

Theoretical works predict a pulse-self compression due to spatio-temporal effects inside the filament, which would circumvent the use of specialized optics inducing a negative group-velocity-dispersion in external pulse compression setups.

3.1 The Spatial Balance of Nonlinear Effects

This chapter aims at the theoretical and experimental investigation of filamentation in a stepwise manner, where the introduced spatial balance between Kerr- and plasma-initiated nonlinear effects is put into focus first. The spatial approach is followed by more complex models to describe the spatio-temporal filamentary propagation dynamics in Sec. 3.3. The introduced ionization models of section 2.2.2 play a key role in the theoretical approach to filamentation. By putting the contributions from the self- and defocusing from Eq. (2.7) and (2.12) plus the influence of the natural diffraction from Eq. 2.3 into one formula, the spatial balance in dependence of the initial intensity reads as [57, 61]:

$$n_2 I = \frac{(1.22\lambda_0)^2}{8\pi n_0 w_0^2} + \frac{\rho_e(I)}{2\rho_{\text{crit}}}. \quad (3.1)$$

The intensity connected to an equilibrium of both sides of the equation is called the *clamping intensity* I_c . An external focusing setup adds a supplementary term to the left hand side of Eq. (3.1), effectively increasing the achievable intensity inside the filament's core. The value of the clamping intensity is subject of an ongoing debate [63, 65, 80, 139, 140] and will be treated in detail throughout this thesis (c.f. Sec. 4.4). The easiest evaluation of its value can be performed by neglecting the diffracting contribution in Eq. (3.1) and by using the most simple assumption of MPI to model the free electron density $\rho_e(I) = \sigma_K I^K (\rho_{\text{nt}} - \rho_e)\tau$, with the laser pulses duration τ , σ_K denoting the multiphoton ionization cross section and ρ_{nt} labeling the neutral medium density. The intensity connected to an equal left- and right-hand-side in Eq. (3.1) scales as:

$$I \approx \left(\frac{2\rho_{\text{crit}} n_2}{\tau \sigma_K \rho_{\text{nt}}} \right)^{\frac{1}{K-1}}, \quad (3.2)$$

and yields a clamping intensity value of $\approx 3.9 \times 10^{13} \frac{\text{W}}{\text{cm}^2}$ for argon at atmospheric pressures interacting with a 30 fs pulse centered at 800 nm. The applied values for the variables are given in table 3.1 of Sec. 3.2. A comparison of this upper limit of the intensity with the findings from Fig. 2.3 suggests, that the use of the MPI model is sufficient for the determination of the free electron density ρ_e .

In order to check for a deviation of the clamping intensity induced by the choice of the ionization model, the balance from Eq. (3.1) has been computed for the various underlying theories, which handle the ionization rate in dependence of the laser intensity (c.f. Sec. 2.2.2). The resulting absolute value of the nonlinear refractive index change between

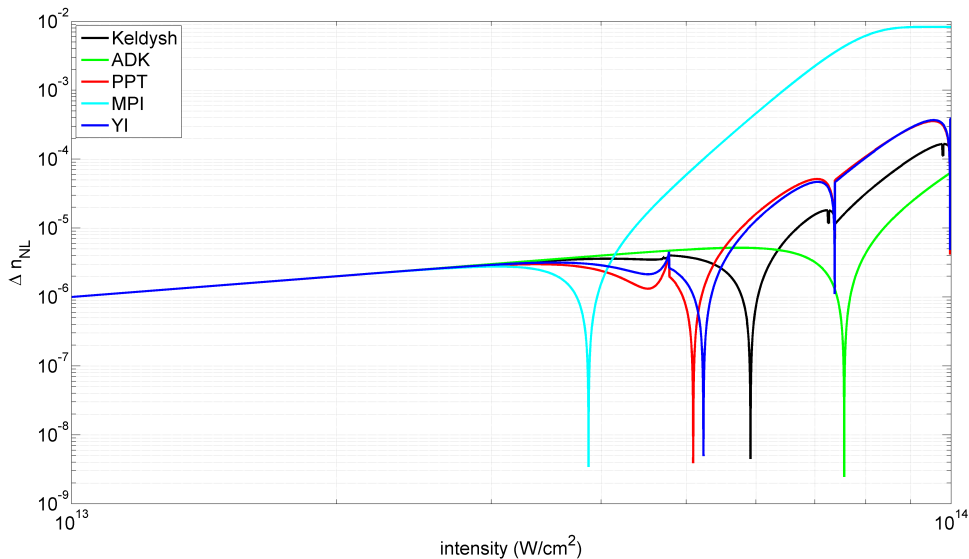


Figure 3.1: Determination of the clamping intensity I_c through the evolution of the nonlinear refractive index change Δn_{NL} in dependence of the intensity. The points, where the absolute value approaches zero determines I_c .

the Kerr-induced term and the ionization term $\Delta n_{NL} = |n_2 I - \frac{\rho_e(I)}{2\rho_{crit}}|$ is plotted in Fig. 3.1. The minimum of each curve determines the clamping intensity connected to each model for a 30 fs pulse interacting with one bar of argon. In agreement with the previous calculations, the MPI rates yield the smallest clamping intensity, since the focusing Kerr-term is balanced out in the most drastic way by the overestimated ionization rates. The ADK-model yields the highest clamping value as it is underestimating the ionization fraction for the lower intensities. The discrepancy ranging from the value obtained for the MPI-rates of $3.895 \times 10^{13} \text{ W/cm}^2$ and the one belonging to the ADK-rates of $7.62 \times 10^{13} \text{ W/cm}^2$ is approximately a factor of 2, which can already have a crucial influence on the conversion efficiency of nonlinear processes along the filament. Putting the attention only on the advanced models (Keldysh-, PPT- and YI-approximation), the discrepancy is reduced to a range between $5.12 - 5.95 \times 10^{13} \text{ W/cm}^2$, differing by a much smaller factor of 1.16.

3.2 Focusing Competition and Wavefront Curvatures

Since the nonlinear effects effectively influence the beam's focusing characteristics, it comes natural to try to distinguish between the plasma- and Kerr-induced focusing and their respective contribution along filamentary propagation.

The determination of the influence of a generated plasma on the refractive index and consequently the induced instantaneous frequency (c.f. Eq. (2.14)) is not only limited to the application in filaments. Recent works, specializing on pulse dynamics in hollow-core photonic crystal fibers, distinguished the influence of SPM, plasma-SPM and modulation

instabilities on soliton dynamics along a hollow-core photonic crystal fiber [141].

Tightly focused, high-power pulses are reported to generate an asymmetric spectrum with an emphasis on the blue spectral region, but suffer from the strong distortions to the spatial beam profile induced by the high plasma densities present [142]. The Kerr-contribution also leaves clear fingerprints in the generated spectrum as filaments are usually accompanied by self-phase modulated spectra, which are influenced by self-steepening [143].

As a first estimate about the dominating part to the focusing dynamics in filamentation in Eq. (3.1), a look at the induced wavefront curvature of the Kerr- and plasma-effect to the nonlinear competition is performed. A comparison of its relative strengths can be used to determine if the filamentary propagation is dominated by the Kerr nonlinearity or by the defocusing contribution originating from free electrons. Temporal effects along the fundamental pulse shape as well as cross-coupling between the different focusing and defocusing contributions are neglected in this part. The sole purpose of this initial observations of the wavefront curvature is to find a tool which can effortlessly determine the spatial effect dominating the filamentary propagation. The presented calculations refer to a model proposed by Lim et al. [144]. Here, the wavefront curvature is represented by a value named the *wavefront sag*, which will be explained and calculated in the following.

3.2.1 Calculation of the Wavefront Sag

The wavefront sag is a value connected to the wavefront curvature by comparing the distance between an ideally plane wavefront and a curved one at the beam width $w(z)$. It is a measure for stable filamentary propagation with three contributing components, the influence of the geometrical phase S_g , a term connected to the Kerr self-focusing S_k and one for the plasma induced defocusing S_p .

Figure 3.2 shows the definition of the wavefront sag for a focused Gaussian beam with a focusing length of f propagating along the direction z . The focusing lens imprints a spatial phase on the beam, the curved wavefront. The corresponding radius of curvature increases with ongoing propagation until the wavefront turns into a plane wave at the position of the focus.

The contribution is calculated by the geometric arguments (c.f. Appendix B) to be [144]:

$$S_g = \frac{w_0^2}{2z_r^2}(z - f). \quad (3.3)$$

Approaching the measure for the radius of curvature $R(z)$ in this manner seems like a unnecessary complication of the fundamental formula $R(z) = z(1 + (\frac{z_r}{z})^2)$, but will prove to be beneficial as the nonlinear terms need to be estimated. The wavefront sag denotes an optical path difference between the center of the beam and its radial wings, as opposed to the value obtained by $R(z)$. When handling the nonlinear terms, the problem reduces to a comparison of the refractive index modulation Δn at the center of the radial beam profile with the unaffected case of an unmodulated region in the outer part of the beam profile.

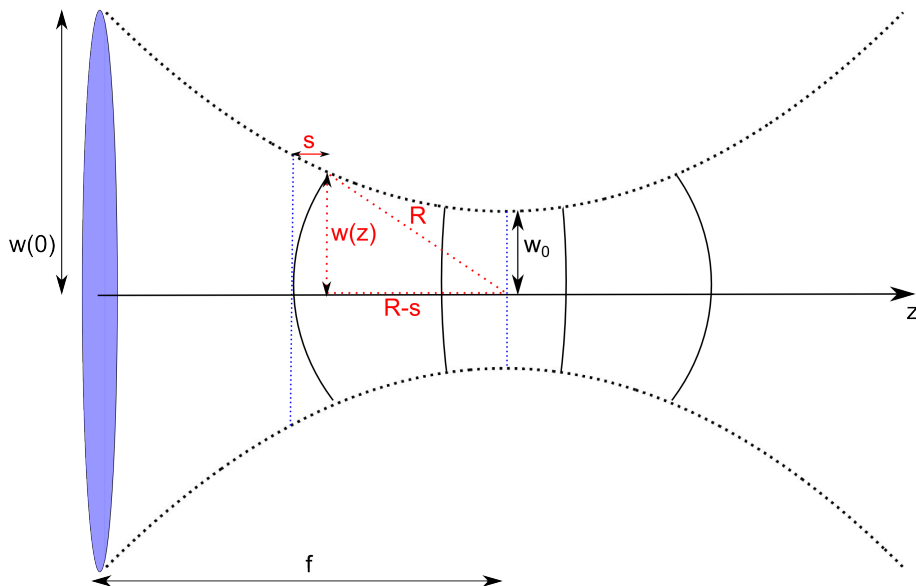


Figure 3.2: Sketch describing the basic idea behind the calculation of the wavefront sag for the case of a focused Gaussian beam. The wavefront sag S follows the wavefront curvature $R(z)$ which is imprinted by the focusing optic and shows a decreasing behavior as it reaches the focus at position f . Here, w_0 is the minimum beam waist, $w(z)$ is the waist in dependence of the propagation distance z .

The wavefront sag S_{NL} resulting from the nonlinear contributions of the Kerr effect and plasma defocusing is derived from the respective modulation of the refractive index Δn by calculating the overall optical path length difference between the center and the edge of the beam, using an integral with a similar form as the B-integral [145]:

$$S_{\text{NL}} = - \int_0^z \Delta n(z') dz'. \quad (3.4)$$

Taking $\Delta n_{\text{Kerr}} = n_2 I$ into account, the wavefront sag for the Kerr contribution calculates as (c.f. Appendix B):

$$S_k = \frac{2P_0 n_2}{\pi w_0^2} \left(\arctan \left(\frac{z-f}{z_r} \right) + \arctan \left(\frac{f}{z_r} \right) \right), \quad (3.5)$$

where P_0 denotes the peak power of the laser pulse. An additional contribution arises from the plasma and is derived from $\Delta n_{\text{EL}} = -\rho_e / (2\rho_{\text{crit}})$. In the presented framework, the density of the free electrons is calculated by the MPI-approximation and the ADK-approximation, whereas both serve as upper and lower boundaries for the plasma-induced wavefront sag. The more complex rates (PPT, Keldysh and YI) are avoided at this point, since the evaluation of the ionization rates has to be performed for an integration along z and is time consuming for the complex models. The findings from the multiphoton ionization rates lead to a direct analytical expression [144]:

$$S_p = \frac{\sigma_k \rho_{\text{nt}} z_r \tau}{2\rho_{\text{crit}}} \frac{(2K-2)!}{(2^{K-1}(K-1)!)^2} \left(\frac{2P_0}{\pi w_0^2} \right)^K (f_k((z-f)/z_r) + f_k(f/z_r)), \quad (3.6)$$

n_2	$1.25 \times 10^{-23} \frac{m^2}{W}$
ρ_{crit}	$1.74 \times 10^{27} m^{-3}$
ρ_{nt}	$2.89 \times 10^{25} m^{-3}$
σ_K	$5.06 \times 10^{-184} \frac{1}{s} (\frac{m^2}{W})^K$
K	11

Table 3.1: Values used for the calculation of the wavefront sag for 1 bar of argon interacting with a pulse centered at 800 nm [144].

where the factor f_k is expressed as:

$$f_k(x) = \arctan(x) - \sum_{n=0}^{K-1} \frac{(2^n n!)^2}{(2n)!} \frac{x}{2n(1+x^2)^n}. \quad (3.7)$$

The same can be applied for the ADK-rates, introduced in section 2.2.2, where the free electron density is calculated by a more complex relation, which is introduced in Appendix B of the thesis.

Figure 3.3 displays the different contributions to the wavefront curvature as a function of z . Note that absolute values are shown for all contributions in order to compare the influence of the terms with different signs. The Kerr contribution S_k , the Gaussian contribution S_g and the plasma wavefront sag S_p are shown for the case of a focusing length of 2 m and an initial power of 25 GW. The plasma contribution is shown for the case of the MPI- as well as the ADK-rates. The chosen gas type for the calculations is argon at a pressure of 1 bar. The detailed parameters used for the calculations, which closely follow the specifications from reference [144], can be found in Tab. 3.1. The Gaussian evolution S_g is explained by the monotonically increasing wavefront curvature $R(z)$ connected to the Gaussian beams properties along the focal distance, which results in a linear decrease of S_g . The Kerr term S_k is strongly dependent on the intensity and therefore on the beam diameter (c.f. Eq (2.7)) along the focal distribution. As the beam is focused and $w(z)$ is decreasing, the Kerr contribution grows quadratically, showing a drastic influence as the beam approaches the focal point. The plasma sag shows an even stronger connection to the intensity, since the electron density in the given ionization model scales with I^K . Consequently, the defocusing effect of the plasma sets in as the most rapid term of the three counteracting effects. As expected, the MPI-rates lead to a more influential defocusing due to the overestimation of the ionization rates as compared to the underestimated values of the ADK-rates. In accordance to Figs. 2.3 and 2.4, the outcome of the two models is sufficient to delimit the area of S_p . The interaction process of a laser beam with its surrounding

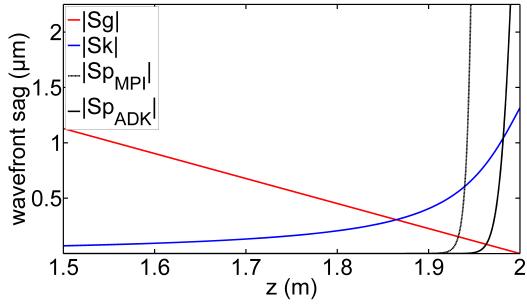


Figure 3.3: The contribution of the different wavefront sags for $f=2$ m and an input power of 25 GW. The term connected to the Kerr effect S_k crosses the fundamental Gaussian distribution S_g before the plasma curvature S_p can affect the propagation significantly.

medium is considered to be Kerr-dominated, when the connected contribution S_k crosses the influence of the initial focusing before the plasma part. This means, the Kerr term can effectively influence and dominate the propagation dynamics, leading to the effect of filamentation in a more precise sense. In this case, the focusing terms S_k and S_g are already sufficiently strong to counteract the occurrence of the appearing plasma terms, leading to a stable self-guided filament [58, 144]. Contrarily, if the plasma-connected wavefront sag contributes first, the propagation will be dominated by the rapid defocusing term and a trapping of the beam into an intense channel is circumvented as the Kerr-nonlinearity needs to sufficiently grow quickly after the plasma defocusing influences the beam ¹.

3.2.2 Experiments - Evaluating The Dominating Nonlinearity

In this part, the possibility to track the dominating nonlinear contributor from the spectral characteristics of the pulse is investigated. The aim of the experiments is the determination of focusing regimes at which either the Kerr- or the plasma-response is dominating the filamentary pulse propagation. The main indicator for this is the spectrum emitted by the beam after propagation through the high-intensity interaction region, as the nonlinear effect which dominates the spatial propagation characteristics is also assumed to have a key influence on the spectral properties (c.f. Sec. 2). The experimental arrangement is sketched in Fig. 3.4 (a), where the fundamental pulse with an energy of 1.35 mJ, a pulse duration of 40-45 fs, centered at 780 nm, has been focused by exchangeable curved mirrors with differing focal lengths into a tube filled with argon at atmospheric pressure. The applied focal length were 500 mm, 625 mm, 750 mm, 1000 mm, 1250 mm and 1500 mm respectively, covering the commonly applied external focusing lengths in laboratory filamentation experiments. The input windows of the gas filled tube were chosen to have a length of 200 μm in order to avoid nonlinear effects occurring in the crystalline structure of the window materials. The spectrum originating from the filament has been detected via a reflection of a diffusing screen for averaging, using a spectrometer in the visible wavelength range (Avantes-AvaSpec (250-1000 nm)).

The evolution of the fundamental spectrum in dependence of the initial focusing condition is shown in Fig. 3.4 (b). The nonlinear interaction with the surrounding medium clearly influences the spectral properties of the propagating beam and shows a strong dependence on the choice of the external focusing setup. A minimum in the spectral width $\Delta\lambda$ becomes observable for $f=750$ mm.

Changing the focusing length to shorter as well as longer values than 750 mm leads to an increase in the spectral bandwidth of the emitted radiation. A line-out of fundamental spectra at three exemplary positions is shown in panel (c) in Fig 3.4, exhibiting a strong spectral broadening for both, the short and long focal distances. The displayed single spec-

¹Note that the used definitions of a plasma-dominated and Kerr-dominated regime in the context of the wavefront sag are not connected to the debate covering the influence of higher-order Kerr-effects (HOKE) [129–131, 146].

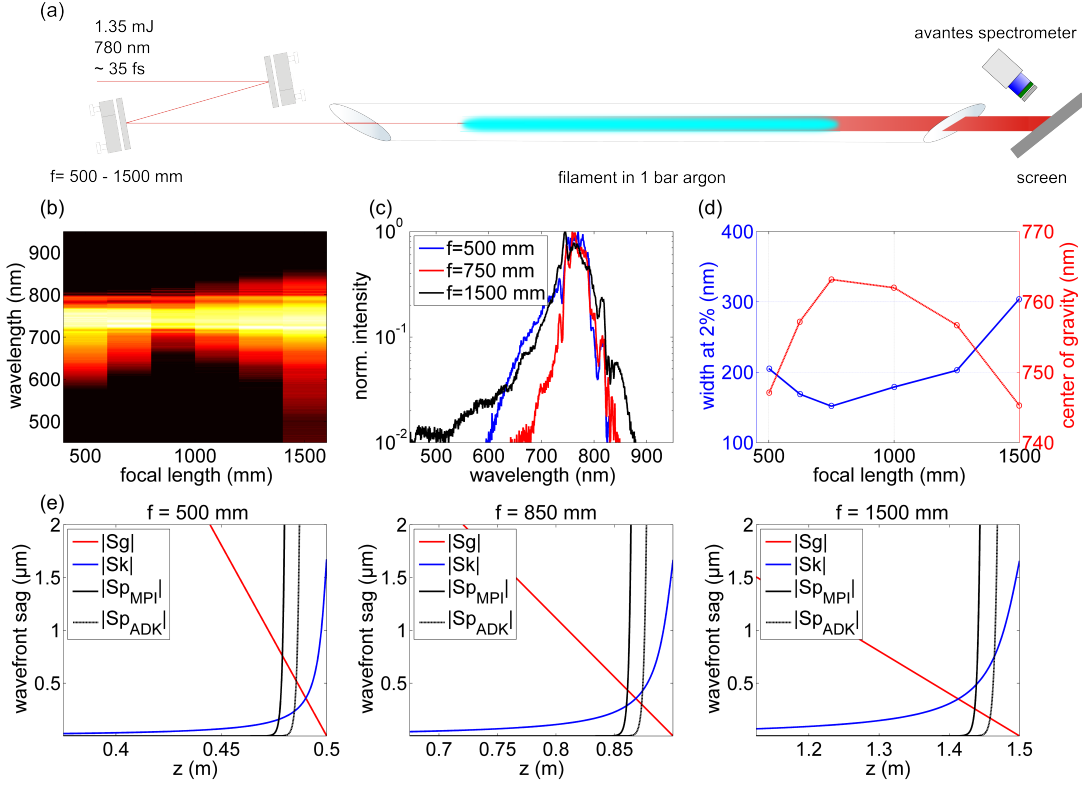


Figure 3.4: Determination of the dominating nonlinear effect to filamentation at different focusing geometries. Sub-figure (a) sketches the experimental setup, where the fundamental beam (1.35 mJ, 35-40 fs, 780 nm) is focused by different curved mirrors ($f=500, 625, 750, 1000, 1250, 1500$ mm) into an argon-filled gas cell. The emerging spectrum is detected after the interaction chamber and displayed in panel (b), where the color-code represents the normalized spectral intensity. Three examples of the spectral evolution are presented in (c). The spectral width at a 2% level as well as the central wavelength of the recorded spectra is shown in (d). The evolution of the wavefront sag is shown for three focusing setups in (e). It can be seen that the propagation dynamics change between a Kerr-dominated and plasma-dominated propagation regime.

tra show characteristic differences in their shape, giving indications on the dominating nonlinear effect. The spectrum connected to the longest focal length of 1500 mm distinguishes itself from the other cases by its weak spectral tail ranging down to 550 nm as well as the occurrence of red-shifted spectral components. Applying a short focal length, as in this case 500 mm, leads to a modulation of the spectrum in which the generated spectral components only appear at frequencies higher than the initial carrier.

The spectral width and the center-of-gravity (CoG) of the spectrum with respect to the external focusing length are displayed in panel (d). The main indication for the experimental verification of the dominating nonlinear effect during propagation is not the spectral width by itself, which is of similar order for $f=500$ mm and $f=1250$ mm, but the weight of the emitted spectrum. The experiments show that the broadband spectrum for a focusing length of $f=500$ mm is far more centered to the blue spectral region as compared

to its broadened counterpart of $f=1250$ mm, indicating that different mechanisms are the originators of the emitted spectrum. The modeling of the wavefront sag is adapted from the experimental values, showing its evolution for three initial focusing setups of 500 mm, 850 mm and 1500 mm in Fig. 3.4 (e). All wavefront sags shows a strong dependency upon the changing external focusing length. The results for the longest and shortest focal length reveal that the connected experimental setup corresponds to conditions of a plasma dominated ($f=500$ mm) and a Kerr dominated ($f=1500$ mm) case.

For the case of $f=500$ mm, the plasma contribution (independent of the choice of the ionization model) distorts the propagation before the Kerr-term has a significant influence. The opposite is true for the case of $f=1500$ mm, as the influence of the Kerr-effect on the radial phase of the beam initiates much earlier. The findings from the wavefront sag model are connected to the observed spectral properties, where the plasma induced frequency modulation, which only occurs during the rising edge of the laser pulse, leaves the red part of the spectrum completely unmodulated and only generates frequencies higher than the initial carrier.

For the case of $f=1500$ mm, red spectral components are also influenced by the Kerr-induced SPM and appear in the measured spectra. The observed spectral blue tail in panel (c) ($f=1500$ mm) is a typical feature of filamentation and is connected to self-steepening of the laser pulse during its propagation and the resulting asymmetric SPM (c.f. Fig. 2.1). The theoretical findings for an external focusing setup with $f=850$ mm shows the position at which filamentation transfers from being plasma-dominated to a Kerr-dominated case. As a result, the dominating effects during propagation of an intense laser beam in transparent, gaseous media can be experimentally determined by looking at the spectral width and the weight of the frequency-modulated spectra. Also, a simple comparison of the emitted spectrum with the input one enables the evaluation of the red-shifted frequency components and therefore the effect of the Kerr-related SPM.

One question to be addressed is the reduced spectral broadening for conditions of $f=750$ mm. The analytical calculations predict a simultaneous strengthening of the plasma- and the Kerr-response for the point at which the experimentally measured spectral width minimizes. The self-focusing influence of the Kerr effect is immediately overtaken by the plasma defocusing mechanism, circumventing a self-channeling of the beam and therefore efficient SPM of the fundamental spectrum. However, the external focusing is still too weak, compared with the case of $f=500$ mm, to induce a sufficiently strong refractive index modulation ($\propto \partial\rho_e/\partial t$) connected to the generation of free electrons. As a result, an effective generation of the blue spectral components along the fundamental pulse's rising edge is suppressed.

Conclusion

The simplified underlying model shows a reasonable agreement with the experimental findings. It is applicable for a rough determination of the dominating propagation regime. The

spatial influence of the delicate balance between the Kerr- and plasma nonlinearity are sufficiently covered by the analytical model such that the commanding contribution can be extracted experimentally by analyzing the spectral weight of the emerging radiation. Applications desiring pulse self-shortening or an extended high-intensity propagation should rely on the Kerr-dominated regime. Experiments such as THz-generation or close-range LIDAR applications [89], which call for high electron densities benefit from a plasma-dominated regime. The presented experiments together with the simplified theoretical modeling take only the spatial properties of the key filamentary dynamics into account and give a narrow insight into the extremely nonlinear temporal dynamics of filamentation. The following section expands the view on femtosecond filaments by the temporal coordinate, introducing spatio-temporal effects, which lead to multiple characteristic features of filamentation.

3.3 Spatio-Temporal Dynamics Inside a Filament

In order to obtain a deeper theoretical insight into the propagation dynamics along the filament, the spatial effects need to be connected to the temporal dynamics of the fundamental pulse [68]. The coupling between the spatial- and temporal-nonlinear effects in filamentation is referred to as the *Dynamic-Spatial-Replenishment model*, which considers the pulse-propagation along the filament as a highly dynamical process through a coupled nonlinear wave-equation [68]. This section breaks down the governing wave-equation to its most necessary parts and is based on a model which has been developed and improved by works of Bergé, Skupin and Brée among others [72, 75, 147].

The observations of the spatial dynamics in the last chapter reveal that ionization plays an important role during filamentation. The free electrons lead to significant contributions of the free charge density ρ and the current density \vec{J} , which participate in a highly nonlinear manner to the pulse dynamics [92, 121, 148]. As introduced in Eq. (2.5), the polarization \vec{P} of the medium also needs to be modeled in a nonlinear approach for the high intensities along the focal distribution. In this framework, the wave vector \vec{k} consists of a dominating part $k_z > 0$ along the laser propagation direction z . The transverse components $k_\perp = \sqrt{k_x^2 + k_y^2}$ satisfy the paraxial approximation $k_\perp/|\vec{k}| \ll 1$ [121, 149]. Femtosecond filaments require the modeling of broadband and ultrashort pulses, which strongly influences the validity of simplifications for the modeling of the pulse propagation, since the commonly adapted slowly varying envelope approximation (SVEA) fails for these conditions [150]. Consequently, the Nonlinear Schrödinger Equation (NLSE), which appropriately describes the propagation of narrow-band pulses, is expanded to a Nonlinear Envelope Equation (NEE) due to the larger bandwidth of the pulses [70, 75, 151, 152].

3.3.1 Obtaining the Wave-Equation

The source terms fulfill the Maxwell-equations (2.1), which yields a set of equations describing the propagation of an electromagnetic wave in a medium through the wave-equation [77, 148, 153]:

$$\vec{\nabla}(\vec{\nabla}\vec{E}) - \vec{\nabla}^2\vec{E} = -\mu_0 \left(\frac{\partial\vec{J}}{\partial t} + \frac{\partial^2\vec{D}}{\partial t^2} \right), \quad (3.8)$$

where the dielectric displacement $\vec{D} = \epsilon_0\vec{E} + \vec{P}$ carries the contribution of the polarization $\vec{P} = \vec{P}_L + \vec{P}_{NL}$. The governing Eq. (3.8) has all the necessary terms for the implementation of the linear and nonlinear response of the bound electrons via \vec{P} , and also takes the free electron charges into consideration through the current density \vec{J} [153]. To investigate Eq. (3.8), various approximations need to be applied [153]. The aforementioned paraxial assumption $\vec{\nabla}_\perp^2\vec{E} \approx 0$ allows a decoupling of the spatial coordinates of the electric field \vec{E} . The linear terms are treated in the Fourier space, where $\mathcal{FT}\left[\frac{\partial^n}{\partial t^n}f(t)\right] = i^n\omega^n f(\omega)$, with \mathcal{FT} denoting the Fourier-transformation. The Fourier-transformation of a time-dependent function $\mathcal{FT}[F(t)]$ yields the frequency domain analogue denoted as \tilde{F} throughout the theoretical description. Introducing the wave vector in the frequency domain as $k^2(\omega) = \frac{\omega^2}{c^2}(1 + \chi_1(\omega))$ delivers the second order wave equation [153]:

$$\frac{\partial^2}{\partial z^2}\tilde{\vec{E}} + \vec{\nabla}_\perp^2\tilde{\vec{E}} + k^2(\omega)\tilde{\vec{E}} = -\mu_0\omega^2 \left(\frac{i\tilde{\vec{J}}}{\omega} + \tilde{\vec{P}}_{NL} \right). \quad (3.9)$$

In order to break down the second-order equation to a first order problem, usually the SVEA is applied [145, 151]. As mentioned above, this has to be avoided for the description of femtosecond filaments. In order to solve this issue, the second order equation is regarded in the Fourier space, performing the transformation with respect to the propagation variable z [77]. The resulting electric field can be decomposed into a forward- and a backward-propagating term, both being linearly dependent on the wave vector \vec{k} [69, 77, 153, 154]. The assumption of a negligible backward propagating field, which is assumed to be valid for the case of filamentation, and an inverse transformation into the z space yields the linear equation in dependence of z , the Forward-Maxwell-Equation (FME) [152, 153]:

$$\frac{\partial}{\partial z}\tilde{\vec{E}} = \frac{i}{2k(\omega)}\vec{\nabla}_\perp^2\tilde{\vec{E}} + ik(\omega)\tilde{\vec{E}} - \frac{i\mu_0\omega^2}{2k(\omega)} \left(\frac{i\tilde{\vec{J}}}{\omega} + \tilde{\vec{P}}_{NL} \right). \quad (3.10)$$

To obtain a final representation of the reduced equation, the nonlinear term \vec{P}_{NL} and the generation of free electrons contributing to \vec{J} need to be implemented. The generation of higher optical harmonic frequencies is neglected in the modeling of \vec{P}_{NL} , reducing the contributions to self-induced refractive index changes. Introducing an envelope according to $\vec{\mathcal{E}} = \sqrt{\mu_0/(n_0\epsilon_0)}(\vec{E}\exp(k_0z - i\omega_0t) + \text{c.c.})$ derives the Nonlinear-Envelope-Equation (NEE) from (3.10). The assumptions lead to the following final equation [153]:

$$\begin{aligned}
 \partial_z \vec{\mathcal{E}} = & \underbrace{\frac{i}{2k_0} T^{-1} \vec{\nabla}_\perp^2 \vec{\mathcal{E}}}_I + \underbrace{i D \vec{\mathcal{E}}}_{II} + \underbrace{i \frac{\omega_0}{c} n_2 T |\vec{\mathcal{E}}|^2 \vec{\mathcal{E}}}_{III} \\
 & \underbrace{-i \frac{k_0}{2\rho_{crit}} T^{-1} \rho_e \vec{\mathcal{E}} - \frac{\sigma_{coll}}{2} \rho_e \vec{\mathcal{E}} - \frac{I_p W(I) (\rho_{nt} - \rho_e)}{2I} \vec{\mathcal{E}}}_{IV}.
 \end{aligned} \tag{3.11}$$

All terms can be traced back to a corresponding part in Eq. (3.10), this time only being written in the temporal representation. Equation (3.11) can be divided into four parts to explain the physical meaning of the single contributions. Part I of Eq. (3.11) describes the diffraction of the beam, whereas part II corresponds to the dispersion and is equivalent to the second term on the right-hand side of Eq. (3.10). The dispersion is implemented by the operator D , which is represented in the Fourier domain according to $\tilde{D}(\omega) = k(\omega) - k_0 - (\omega - \omega_0) \frac{\partial k}{\partial \omega} |_{\omega=\omega_0}$, with $k(\omega) = n(\omega)\omega/c$. The frequency-dependent refractive index $n(\omega)$ is determined according to Dalgarno and Kingston [155]. Contribution III is connected to the initial term \vec{P}_{NL} and models the influence of the Kerr-effect. The operator $T = 1 + (i/\omega_0)\partial t$ allows to implement the space-time focusing and the self-steepening effect. The inverse operator T^{-1} is evaluated in the Fourier domain [152]. The remaining part IV is connected to the current density \vec{J} , where the first imaginary term includes the defocusing effect of the free electron density ρ_e . The second contribution in IV adds the generation of free electrons due to collisional ionization processes, where $\sigma_{coll} = 1 \times 10^{-19} \text{ cm}^2$ is the cross section for collisional ionization. The third term accounts for the generation of free electrons due to field ionization. The value of the electron density ρ_e is determined by an additional equation (c.f. Sec. 2.2.2). Therefore, the wave equation is coupled to the plasma density of the medium via [153]:

$$\partial_t \rho_e = W(I) (\rho_{nt} - \rho_e) + \frac{\sigma_{coll}}{I_p} \rho_e I. \tag{3.12}$$

The ionization rate $W(I)$ is modeled according to PPT-theory, which is assumed to adequately describe the ionization processes, even when the pulse intensity constantly changes between the MPI and the tunneling regime (c.f. Sec. 2.2.2) [103]. Other implementations according to the MPI-rates or the ADK-rates are also possible for the sake of comparison (c.f. Sec. 3.3.7).

The FORTRAN90 code applied in this thesis was kindly provided by Carste Brée (WIAS²) and is based on a code developed in the group of Luc Bergé. The simulation employs a numerical integration scheme for Eqs. (3.11) and (3.12). Hereby, the envelope equation (3.11) is integrated using a split-step pseudospectral method [153].

²Weierstraß-Institut, Dr. Carsten Brée, Mohrenstraße 39, 10117 Berlin

Essential Theoretical Works

The introduced model has been applied in numerous publications on numerical studies of pulse dynamics along a filament. The pulse-splitting and -shortening dynamics along a femtosecond filament have been investigated and predict a self-shortening of the fundamental pulse shape along a filament as the pulse undergoes the dynamic balance between plasma-defocusing and Kerr self-focusing [147, 156]. Simulations using the model without self-steepening and SPM contributions show, that the underlying plasma dynamics themselves are a strong contributor to the modification of the duration and shape of the propagating pulse [72, 157]. Fig. 3.5 taken from [157] shows the investigation of these reduced effects (see [157] for detailed parameters). The calculated spatio-temporal evolution along the propagation axis z shown on top of Fig. 3.5 reveals a strong influence of the plasma-defocusing as the focal point with high intensities is approached. The pulse-shape at 1.55 m shows a characteristic double-hump structure with a shortened leading pulse feature and a weak trailing pulse, proving a strong influence of the spatial nonlinearities on the temporal pulse shape.

The phenomena of pulse-splitting as well as self-shortening have been observed by all groups handling the task of filamentation numerically [71, 73, 158–160]. The findings even predict the generation of intense sub-cycle pulses, short enough to generate isolated attosecond pulses [71, 73, 139]. The theory tries to decouple the different nonlinearities and their effects on the pulse dynamics along the filament [157, 161], only experimental methods to sufficiently track the fundamental pulses dynamics are needed to investigate the predictions of self-shortening and validate the numerical findings. In the following, the dynamic defocusing of a fraction of the pules shape (comp. Fig. 2.4) and their subsequent refocusing due to the Kerr-effect is dubbed *refocusing cycle*.

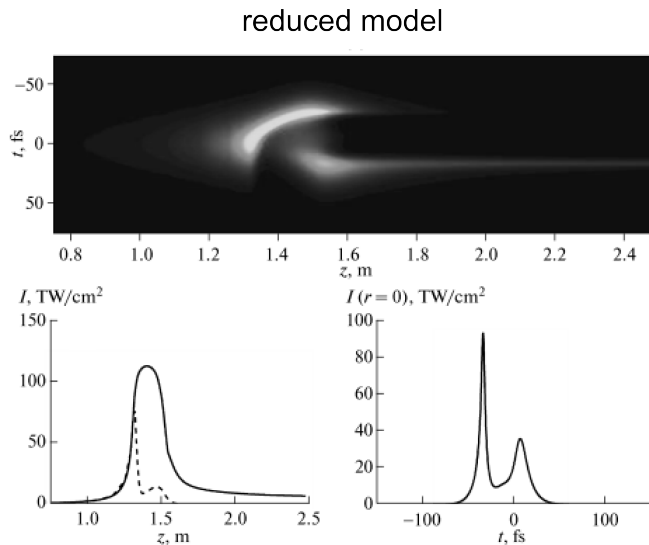


Figure 3.5: On-axis temporal intensity profile along the filament and the corresponding on-axis intensity evolution for a reduced numerical model. The pulse shape at a position of 1.55 m is shown in the bottom right panel. (Figure taken from [157])

3.3.2 Tracking Pulse Dynamics - Experimental Methods and Setup

The simulation of filamentary pulse dynamics relies on various approximations such that the choice of the ionization model strongly influences the outcome of the theoretical re-

sults. The complex evolution of the fundamental is strongly influenced by the spatial- and temporal nonlinearities, and an experimental distinction of these effects calls for a direct investigation of the filaments dynamics as they occur. A direct experimental view at the filamentary pulse dynamics should also help to reveal the mechanism behind the self-shortening dynamics along the filament. Doing this, the applicability of the PPT-ionization-model can be validated as well.

Previous Experimental Methods

The possibility of temporal self-compression along a filament is a very promising approach to circumvent the common techniques of ultrashort pulse compression which employ a combination of a spectral broadening and a pulse compression setup [1, 29, 162]. Numerous works measured self-compression effects of differing strength's through the reconstruction of the emerging pulses from the filament. Table 3.2 summarizes a great amount of these findings by comparing the achieved pulse duration after the filamentary interaction and the achieved compression ratio with respect to the input pulse duration³. All measurements were able to reduce the pulse duration by at least 50% and the maximum pulse-shortening ratio to date is reported to be 5.76 [74]. The theoretical analysis of these experiments in [75] could not fully reconstruct the appearance of the measured ultrashort pulse features along the filament, but was able to find a partial agreement in the spectral intensity and phase distribution, concluding that the propagation after the filament played a crucial role in the self-compression mechanism. In order to decouple the detection of the self-compressed pulse-shape in the filament and the subsequent propagation, a direct experimental view on the pulse dynamics is needed.

The earliest approaches to gain an experimental perception of a femtosecond filament strongly rely on the validity of the theoretical modeling. The insight into the pulse dynamics is obtained by comparing the dependency of the resulting fundamental beams spectrum and shape after the filamentary interaction [76, 79, 136]. Many experimental setups rely on propagating the spectrally broadened pulse out of the filaments cell, with a subsequent propagation section leading to the pulse detection setup and lack the direct view into the filament [60, 74, 75, 147, 163, 164]. There are a few experimental techniques, which enable the direct detection of the fundamental pulse in the filament. A transient-grating (TG) frequency-resolved optical gating (FROG) setup and the STARFISH-method are able to probe the pulses directly in the filament [167, 169, 170]. However, the published results only show the evolution of the pulse shape at a fixed position along the filament for changing surrounding condition such as the pressure that fails to directly observe the propagating pulse along the pulse's propagation direction [167]. The STARFISH method is able to shift the position from which the pulse is extracted, but still suffers from the subsequent accumulated dispersion and the need for a well-defined reference pulse, which is usually obtained from a hollow-core fiber [169, 170]. Another method relies on the

³The examples are limited to experiments handling laser-gas interactions.

Paper	τ_{Input}	τ_{SC}	Ratio
Breé et al. [147]	45 fs	22 fs	2.05
Skupin et al. [75]	45	7.8 fs	5.76
Stibenz et al. [74]			
Hauri et al. [165]	42 fs	9.6 fs	4.375
Uryupina et al. [166]	55 fs	12 fs	4.58
Odhner et al. [167]	50 fs	17 fs	2.94
Bethge et al. [76]	120 fs	35 fs	3.3
Odhner et al [168]	40 fs	9 fs	4.44
Schulz et al [163]	30 fs	8.2 fs	3.65

Table 3.2: Findings from previous efforts to measure the self-compression in a femtosecond filament.

analysis of impulse-shifted Raman-scattering (ISRS) and is able to indirectly track the pulse-duration along the filament, as the detection of the scattering-process is selective to the pulse duration τ [168]. This method allows to estimate approximate boundaries for the actual value of τ inside the filament and it could be concluded that pulses with a duration of less than 9 fs appear along the filament. However, a sensitive detection of actual pulse envelopes or even double-pulse structures (c.f. Fig. 3.5) is not possible. Consequently, none of the above mentioned methods directly measured the complex pulse evolution along the femtosecond filament’s propagation axis and could not distinguish between the spatial and temporal propagation effects along the filament.

The Experimental Setup

The approach used in this thesis, relies on the truncation of the filamentary propagation by removing the surrounding medium rapidly in a differential pumping stage, effectively truncating the nonlinear propagation dynamics at a certain position along the filament. The findings from this setup allow to track the evolution of the pulse’s properties along the filament and can then be used to directly prove the theoretical modeling. The corresponding experimental setup is presented in Fig. 3.6 and described in detail in the following.

The Laser Source The high-intensity laser pulses are generated in a chirped-pulse amplification laser system (KMLabs-Dragon). An oscillator (Venteon-customized Setup) delivers pulses centered at 780 nm with a bandwidth of ≈ 100 nm and a Fourier-limited pulse duration of $\tau_{\text{osc}} \approx 15$ fs. The weak pulses, having a pulse energy of $E=2.75$ nJ at $f_{\text{rep}}=91$ MHz, are stretched in their duration by a grating setup to 250 ps and subsequently picked by a Pockels-cell to a repetition rate of 1 kHz. A multiple-pass amplification stage, guiding the beam via 14 to 15 passes through a Ti:Sa crystal, boosts the pulse energy up to 3.5 to 4 mJ. The amplified stretched pulses are re-compressed by a pair of gratings,

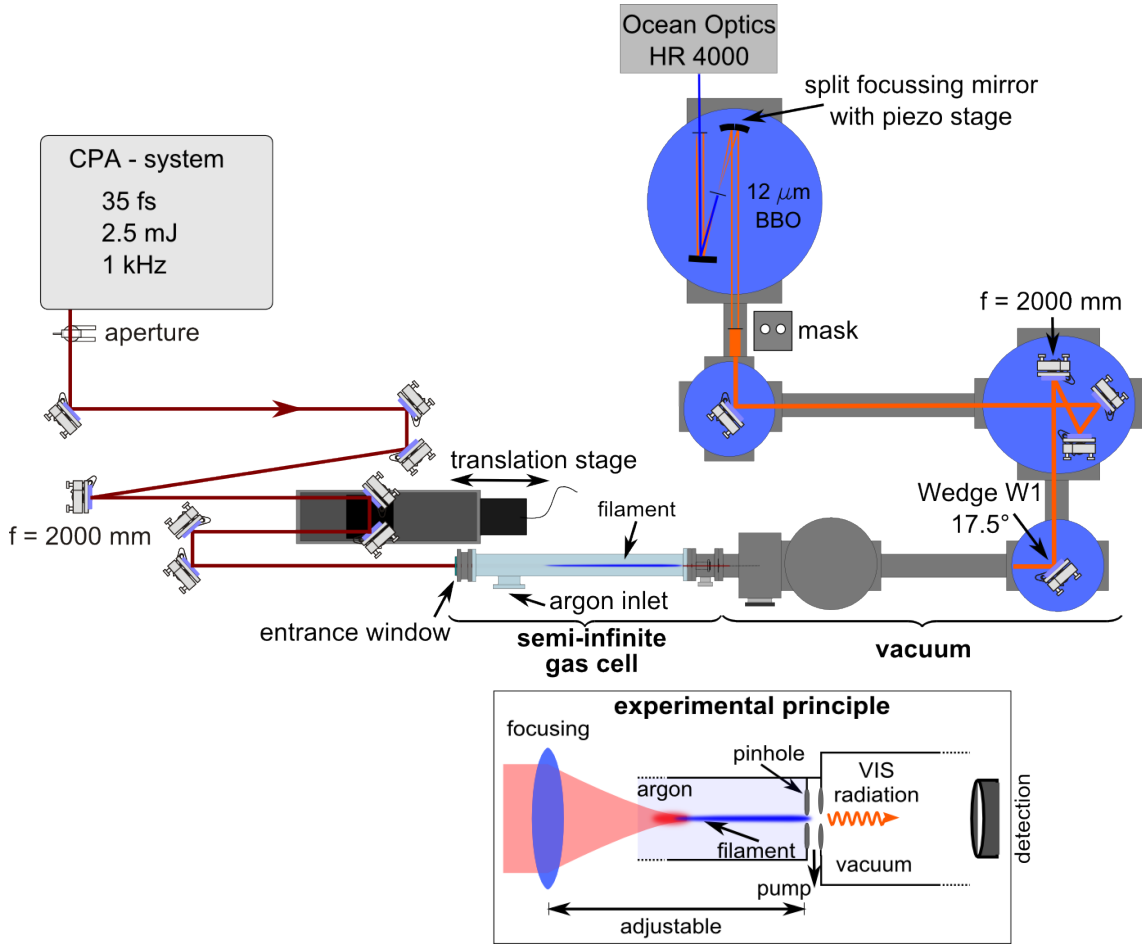


Figure 3.6: Sketch of the experimental setup for the detection of the fundamental pulses dynamics. The filament can be scanned along a truncating differential pumping stage, allowing for a subsequent all-vacuum detection of the fundamental spectrum and pulse shape in dependence of the filament length.

yielding a minimal pulse duration of $\tau_{\text{amp}} \approx 40 - 45$ fs with a power of 2.5 mJ at a central wavelength of 780 nm.

The Filamentation and Truncation Setup At high input powers, multiple filamentation will appear as the initial power of the fundamental pulse exceeds the critical power of self-focusing P_{cr} by a large factor [171, 172]. Distortions along the initial spatial beam profile will lead to the formation of several co-propagating filaments instead of one channel, which needs to be avoided by taking certain measures in the setup. In the experimental procedure described in in Fig. 3.6, this is done by cleaning the spatial pedestals of the radial beam profile by a variable aperture. Additionally, the beam is attenuated down to an energy of 0.9 mJ. The spacing of the gratings in the compressor setup is used to influence the pulse duration of the amplified pulse. The filamentation setup starts with a curved mirror ($R=-4000$ mm), which guides the beam via a variable path length into a gas

tube filled with 1 bar of argon. The path length is controlled by a motorized translation stage (Newport-UTS100PP) with a 150 mm traveling range and a minimum step width of 0.1 mm. The positions denoted in the upcoming experimental results refer to the absolute distance between the focusing mirror and the differential pumping stage, measured to be 205 ± 5 cm for the central positioning of the translation stage. The findings from the previous Sec. 3.2.2 covering the *wavefront sag* predict that the conditions of the experiment are connected to a Kerr-dominated propagation regime due to the long focal length used in this experiments ($f=2000$ mm). As the focused beam propagates along the gas-filled tube, a filament is formed. The filamentary propagation is abruptly put to an end by a differential pumping stage, which is confined by two metal plates. Therein, the filament drills small pinholes into the metal plates to ensure that the diameter of the opening is sufficiently small in order to minimize the gas ballast for the subsequent evacuating stage. The metal plates have an approximate spacing of 1 cm, which enables a connection of a rough vacuum pump (Edwards-XDS35i) perpendicular to the beam propagation direction at this position between the two mounted plates. The pinhole diameter is measured to be 400-500 μm for the first pinhole and ≈ 150 μm for the second one. The pressure in the differential pumping stage is dependent on the applied pressure in the filamentary cell and on the drilled pinhole diameter, and is usually in the vicinity of 5-10 mbar. The ensuing setup is also evacuated to pressures between 1-5 mbar with a rough pump (Pfeiffer-Penta) and can be further evacuated to pressures below 1×10^{-4} mbar, using turbomolecular pumps (Pfeiffer-TMH521P). Moving the motorized translation stage changes the path length between the focusing optic and the gas cell. This effectively translates the ignited filament through the point of truncation, which allows to scan the filament along its propagation direction.

The Pulse Detection Setup The fundamental pulse emerging from the second pinhole is subsequently guided by silver-coated mirrors and/or surface reflections of wedged Fused-Silica substrates to be detected by either a spectrometer (Avantes-AvaSpec) or by a **second-harmonic-generation frequency-resolved-optical-gating (SHG-FROG)** pulse detection setup, which is also sketched in Fig. 3.6. For the diagnostics of fundamental spectrum, the beam is either measured through a reflection from a highly diffusive material or directly coupled into the spectrometer through an optical fiber after surpassing several neutral density filters (CVI-Melles Griot) for attenuation purposes.

For the FROG-setup, the pulse originating from the truncation stage is re-collimated using a silver mirror with $f=2$ m. A mask with two holes of 1 mm diameter each and a separation of 2 mm is put into the beam to pick two exact copies of the pulse. This is crosschecked by the measurement of the fundamental spectrum of each copy. The replicas are shifted temporally with respect to each other by the use of a piezoelectric translation stage (piezosystem jena-PX100). The beams are focused in a non-collinear geometry into a 12 μm thick Beta-Bariumborat-crystal (BBO) to generate the second-harmonic signal. Although beam smearing effects can occur in the non-collinear detection scheme [173, 174], it is chosen because the fundamental spectra can well extend into the spectral region of the

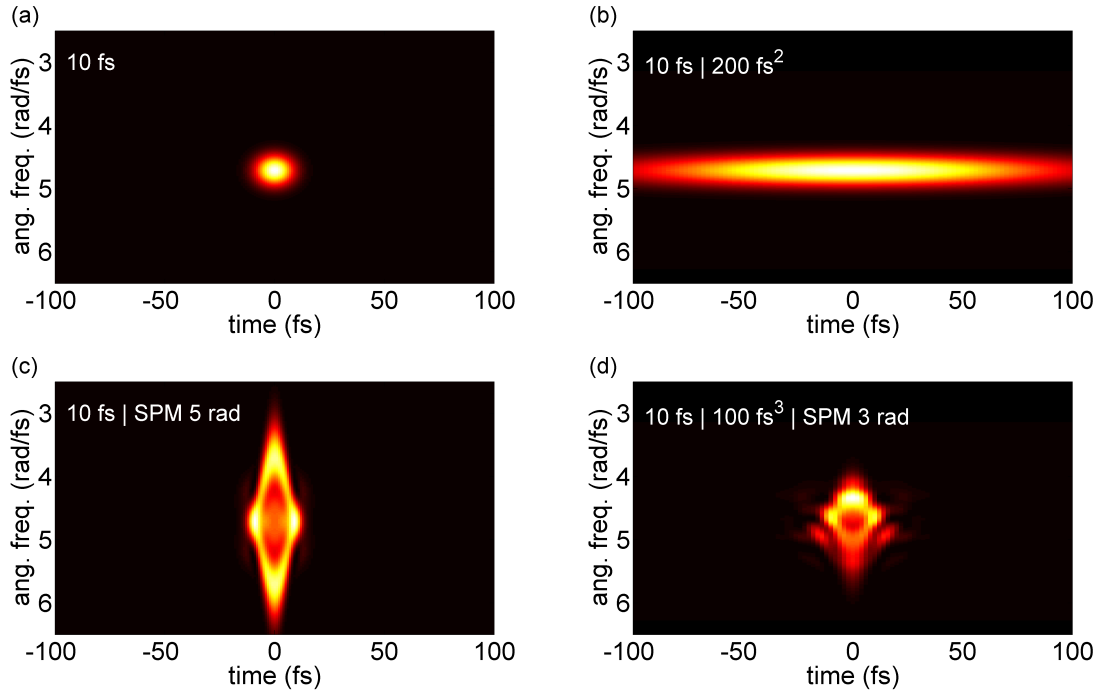


Figure 3.7: Calculated FROG traces for a 10 fs pulse centered at 800 nm with different imprinted phases. The influence of a linear or a SPM-induced chirp is observed.

signal to be analyzed, making a collinear geometry less favorable. The second-harmonic signal is coupled out of the vacuum setup through a 3 mm thick fused-silica window. An aluminum-coated mirror images the source in the SHG-FROG setup onto a fiber-entrance which couples the beam into a spectrometer (OceanOptics-HR4000). This records the second-harmonic signal in dependence of the temporal delay Δt of the two pulse replicas, generating the SHG-FROG traces, which carry information about the amplitude and phase of the pulse [175].

In order to get an intuitive understanding of the connection between the fundamental pulse's phase and the generated SHG-FROG signal, calculated traces are presented in Fig. 3.7. As a reference pulse, a 10 fs pulse with a central wavelength of 800 nm is chosen. The first FROG-trace in the upper column corresponds to trace generated by this pulse under the assumption of a flat phase. A linear chirp is added in Fig 3.7 (b), imprinting a dispersion of 200 fs^2 , which results in a stretching of the trace along t . The signal evolution corresponding to a linear chirp is identical for positively and negatively chirped pulses, leaving an ambiguity in the reconstruction procedure. The influence of symmetric (no self-steepening) SPM is shown for the case of 5 rad in Fig 3.7 (c). A splitting with respect to the temporal axis is induced and resembles the amount of imprinted SPM. As soon as different phase-effects couple with each other, more complicated structures appear, as shown in the panel situated in Fig. 3.7 (d). Here, the influence of SPM can still be tracked due to the occurring gap in the center of the trace, as a cubic phase of -100 fs^3

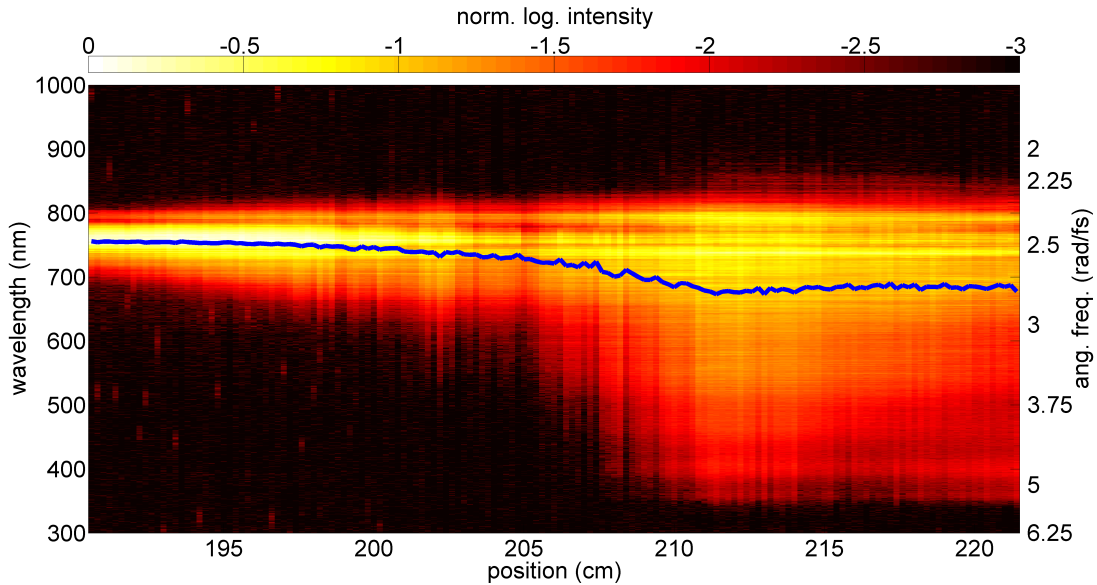


Figure 3.8: Evolution of the fundamental spectrum emerging from the femtosecond filament as a function of the propagation distance along the filament. The blue line displays the center-of-gravity (CoG) of each recorded spectrum [176].

adds an asymmetry with respect to the wavelength axis. Overall, the SHG-FROG setup is capable to directly pinpoint to certain phase contributions in the pulse shape and the high sensitivity to SPM modulated spectra makes it an ideal tool to track the pulses originating from a femtosecond filament.

3.3.3 Experimental Diagnostics of the Fundamental Beam Dynamics

The analysis of the experimental results is split into the evolution of the fundamental spectrum and the evolution of the fundamental pulse shape.

Figure 3.8 shows the on-axis spectrum emerging from the filament in dependence of the propagation distance. The insertion of the double pinhole setup ensures the exclusive detection of spectral components originating from the core of the filament. Therefore, the spatial dynamics occurring along the radial coordinate can only be evaluated by indirect conclusions from the on-axis properties. The center-of-gravity (CoG) of the detected spectra is shown as a blue overlaying line. The spectrum broadens symmetrically at the beginning of the filament (190 cm-205 cm), coinciding with a negligible change of the spectrally weighted frequency. During the subsequent propagation, the spectral width increases rapidly with a strong emphasis on the blue spectral region, which is accompanied by a strong shift in the CoG towards higher frequency components. The spectral observations indicate a dynamic propagation regime between 200 and 210 cm, switching from a moderate spectral broadening (<205 cm) towards a super-continuum stage (>205 cm). The generated high frequency components connected to the super-continuum regime barely

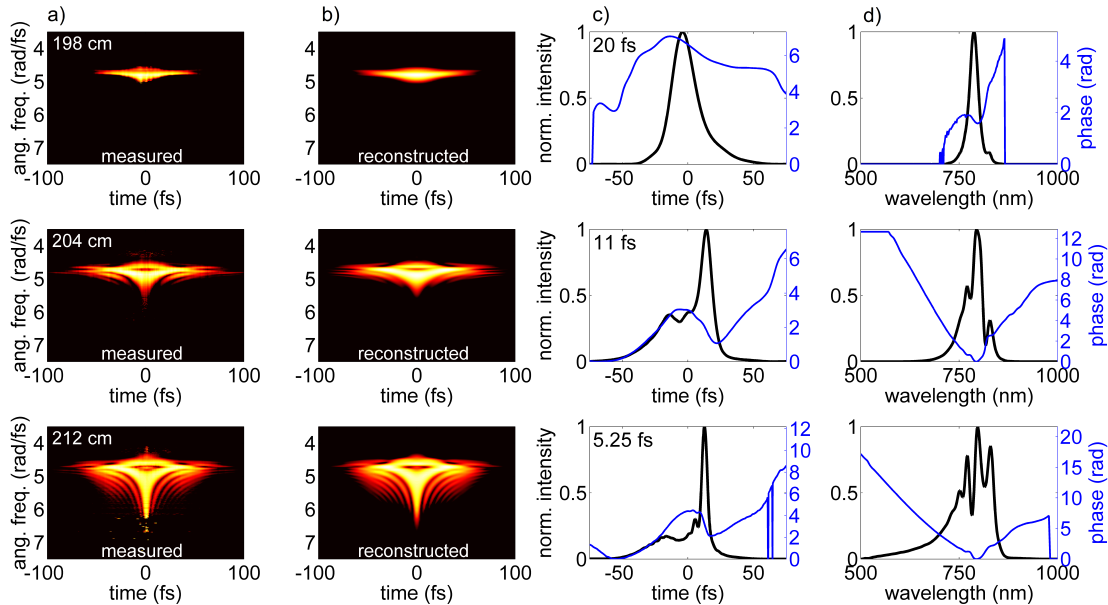


Figure 3.9: SHG-FROG traces recorded at positions of 198 cm, 204 cm and 212 cm. Next to the recorded traces, the reconstructed pulse shape with the corresponding FWHM pulse duration and the reconstructed spectrum are shown. The evolution of the intensity signal is displayed in black, whereas the phase evolution is shown in blue.

overcome the 10% level of the spectral peak intensity and show a characteristic spectral tail. A comparison to the experimental findings from Fig. 3.4 concludes that the propagation of the pulse is Kerr-dominated due to the appearance of the spectral wings in the blue part of the spectrum.

The direct insight into the filamentary pulse dynamics is obtained by the analysis of the recorded SHG-FROG traces. The three rows in Fig. 3.9 show exemplary SHG-FROG traces recorded at different positions along the propagation direction of the filament together with their associated reconstruction. The recorded (column (a)) and reconstructed (b) FROG-traces are displayed on a logarithmic scale with the purpose to increase the visibility of minor spectral details in the figures. The comparison between the related traces shows an excellent agreement and stresses the quality of the recorded SHG-FROG traces. The reconstruction has a FROG-error between 0.35-0.65% for all measurements and is performed on a grid-size of 1024 points with a marginal correction being applied. The symmetry of the measured data-sets proves the stability of the emitted pulse shapes as the acquisition of each FROG trace takes 1-6 minutes, depending on the integration time of the spectrometer (10-100 ms) and the step-size chosen in the delay stage (0.33fs). Next to the traces, the associated pulse shape and spectrum is depicted ((c) and (d)-black line). The respective spectral and temporal phase evolution is portrayed as a blue line. The positions chosen for these examples are the very beginning of the pulse measurements at approximately 198 cm, the point of the shortest measured pulse duration $\tau = 5.25$ fs at 212 cm and a point located in between those two positions chosen at 204 cm.

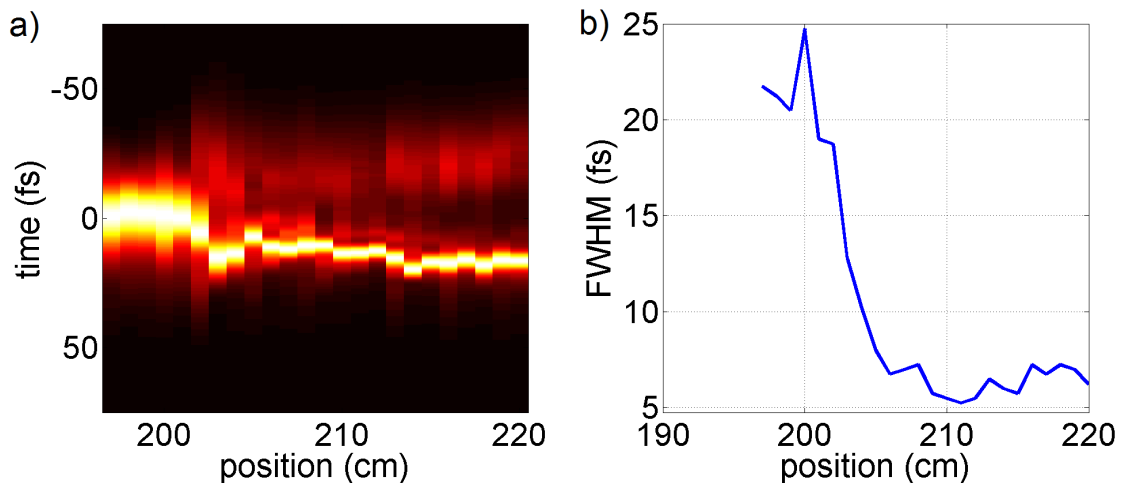


Figure 3.10: Reconstructed temporal pulse-shapes as a function of the propagation direction, detected with the SHG-FROG setup. The pulse’s FWHM duration is shown below the evolving pulse shapes. A clear splitting into two sub-pulses is observed, coinciding with a pronounced pulse-shortening [176].

The initial pulse duration before the gas-cell is 47.2 fs, measured with an evacuated gas-cell, being a factor of 2.35 bigger than the duration at the first point of 198 cm, corresponding to $\tau \approx 20.5$ fs. The second point at position 204 cm shows the build-up of a pulse structure in the trailing section of the temporal pulse shape. The SHG-FROG trace itself starts to show the appearance of a gap-like structure in the center, indicating that SPM-like effects are influencing the phase of the pulse (c.f. Fig. 3.7). The temporal phase is strongly modulated, showing a rapid down-chirp along the tail of the pulse-structure and the pulse is shortened to $\tau = 11$ fs. Note, that the SHG-FROG reconstruction yields an ambiguity in the determination of a leading and a trailing section of the pulse, since the traces are symmetric with respect to the time axis. The appearing peak at position 212 cm is interpreted as a trailing feature because it carries blue spectral components which are connected to the falling edge of the pulse in the SPM process. At the last position of 212 cm, the SHG-FROG trace shows an even more prominent influence of SPM, as the gap grows bigger with ongoing propagation. The pulse shape consists of two prominent peaks, which are temporally separated, with the trailing peak being shortened by a significant factor of 9 compared to the input beams duration, down to a duration of 5.25 fs [176].

The detailed evolution of the reconstructed fundamental pulses temporal shape is shown in Fig. 3.10 (a). The corresponding FWHM pulse duration is shown in panel (b). The positions of truncation are chosen to cover the range over which a plasma channel is visible to the eye inside the argon-filled gas-cell. The pulse-splitting event observed in the single SHG-FROG traces at 204 cm can be confined to positions between 201-204 cm. The FWHM pulse duration strongly decreases along this stage from 25 fs at 200 cm down to ≈ 7.75 fs at 205 cm. After the pulse-splitting, the two sub-pulses co-propagate with an increasing temporal separation. The FWHM pulse duration drops further with ongoing

propagation to a minimum of 5.25 fs.

Connecting the findings from the spectral evolution in Fig. 3.8 and the temporal evolution in Fig. 3.10, gives further insight into the interplay of temporal and spectral dynamics. The position where the pulse structure in the trailing part of the pulse appears turns out to be crucial in the time and frequency domain. The spectral evolution (c.f. Fig. 3.8) is dominated by a symmetrical broadening up until the point of 204 cm. After the pulse splitting occurred, the extreme spectral broadening with the typical filament like asymmetric spectral behavior is observed [142]. The strongest change in the blue spectral region is connected to the subsequent propagation of the occurring short pulse feature. The position of the broadest fundamental spectrum around 212 cm in Fig. 3.8 also corresponds to the shortest pulse duration of 5.25 fs. The experiments show a strong connection between the pulse splitting and the spectral evolution and shall now be connected to the results from the theoretical modeling for an in depth discussion.

3.3.4 Spatio-Temporal Dynamics - Simulations and Discussion

Here, the predictions of the modeling of filamentary propagation introduced in Sec 3.3 are tested by a comparison between the experimental findings and the results obtained by the simulated pulse propagation. The input parameters for the simulations are matched to the experimental conditions, using a pulse with a duration of 47.2 fs, a positive chirp of 415 fs^2 (according to the experimental SHG-FROG measurements) and an input energy of 0.9 mJ being focused by a 2000 mm lens into 1 bar of argon. In the experiments, the initial beam is spatially cleaned by an variable aperture (c.f. Fig. 3.6). This is taken into account by evaluating the Fraunhofer-diffracted far-field profile on the focusing mirror before the filament [176]. The ionization is modeled according to the PPT-theory. The choice of the model will be validated later in this thesis (c.f. Fig. 3.23).

The results from the simulations are shown in Fig. 3.11 and span over a propagation distance much larger than the experimentally measured one in order to expand the insight into the occurring pulse dynamics. First of all, the experimental findings are shown again in Fig. 3.11 (a) and (b) to stress the good agreement between the experimental and theoretical results, shown in the panels (c) and (d). Here, the sub-figures (a) and (c) display the evolution of the temporal intensity profiles, whereas (b) and (d) display the spectral evolution in dependence of the filaments length. For the simulations, on-axis ($r=0$) results in the near-field are shown, covering a propagation range of the filament from 175 cm up to 240 cm. The changing pulse-shapes and the fundamental spectrum show a good agreement with each other, as the position of the splitting and the subsequent separation of two sub-pulses can faithfully be predicted by the theoretical model without the necessity for any fine-tuning of the input parameters. The simulated spectral evolution in Fig 3.11 (d) recreate the experimentally measured asymmetric spectral broadening with an emphasis on the blue spectral components. The theoretical results additionally extend towards lower wavelengths and range up to $\approx 7 \text{ rad/fs}$, compared to the measured spectrum which

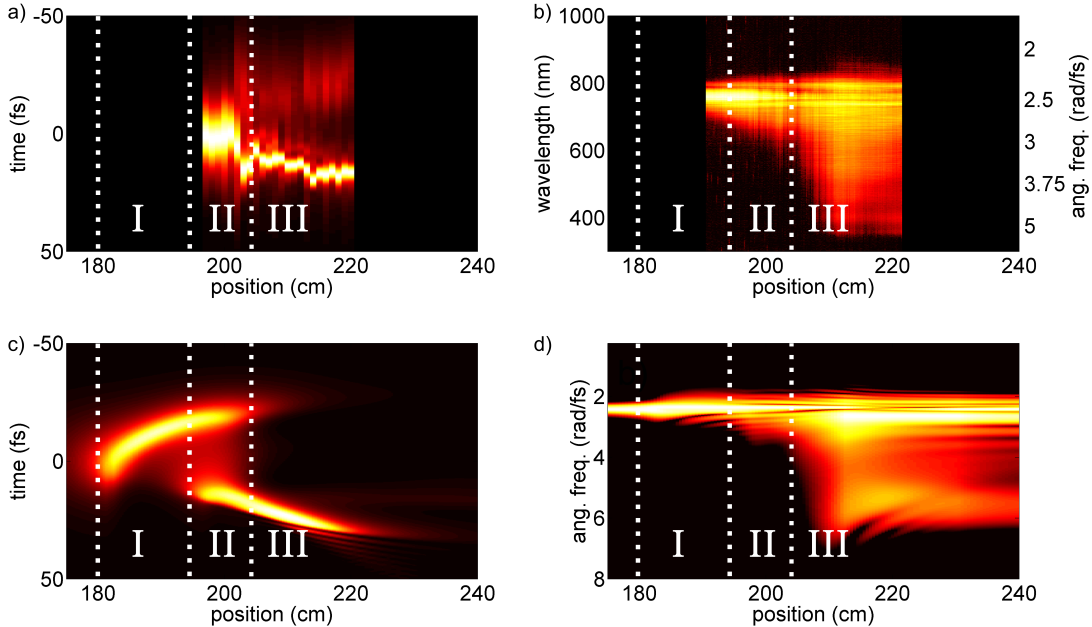


Figure 3.11: Comparison of the measured pulse-characteristics with the results from the numerical model. In (a) and (b) the experimental results from Sec. 3.3.2 are shown again. Panel (c) displays the simulated on-axis evolution of the pulse envelope as a function of the propagation length. The corresponding spectrum is shown in (d). The labels I-III refer to stages dominated by defocusing (I), refocusing (II) and propagation dynamics (III).

extends to ≈ 5 rad/fs. The properties of the simulated spectra reproduce the moderate spectral broadening at the initial stage of the filament followed by a rapid extension of the spectral width at later positions. Even smaller, more detailed features in the spectral evolution, as the vanishing blue spectral components after the point of the maximum spectral width around 212 cm agree with the experimental findings. Fig. 3.12 displays the simulated spatio-temporal field distribution of the fundamental pulse for multiple positions along the filament. Here, the temporal pulse-structure is evaluated in dependence of the radial coordinate for 12 distinct propagation distances, which are labeled in their respective plots. The positions are chosen to cover the spatio-temporal dynamics along the filament. As the pulse propagates along the filament, a strong modification of the time-dependent radial beam profile can be seen. Each group of four spatio-temporal representations, being aligned in separate rows, represents one characteristic stage of filamentary propagation, being I the defocusing-, II the refocusing- and III the propagation stage. The three regions I-III are also displayed in Fig. 3.11 to emphasize the stage along the filamentary life cycle for further discussion.

Fig. 3.13 concentrates on values, which are deduced properties of the experimentally and theoretically obtained pulses evolution, being (a) the Full-Width-Half-Maximum (FWHM) pulse-duration, (b) the slope connected to the falling edge of the fundamental pulse and (c) the peak intensity of the on-axis temporal pulse shape along the filament. All three plots

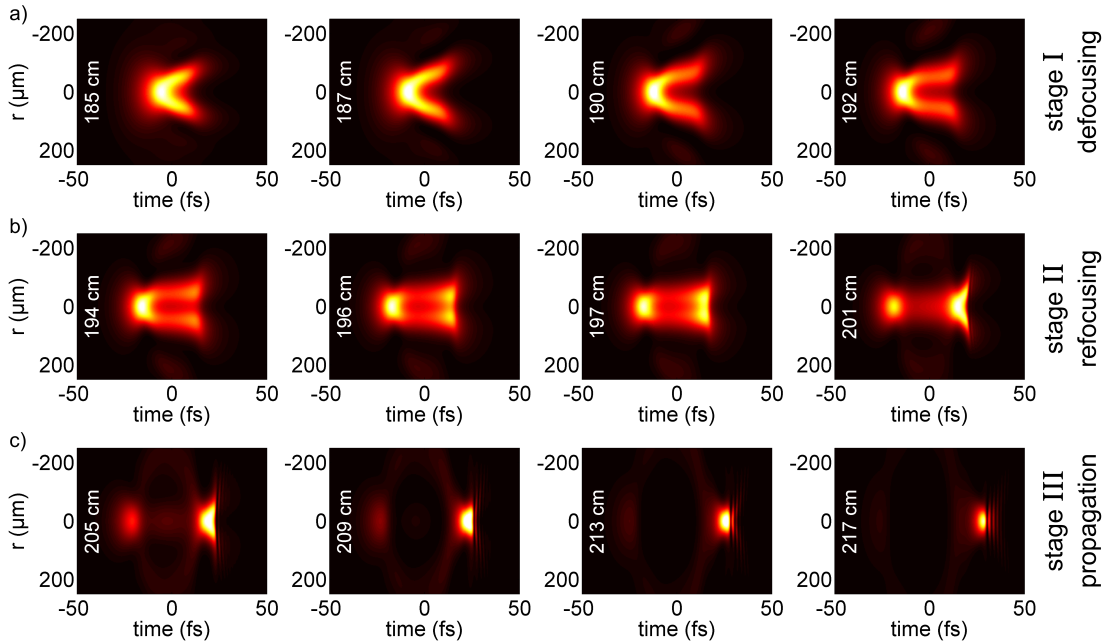


Figure 3.12: Simulated spatio-temporal profiles which characterize three stages I-III along the life cycle of the filament. I is the defocusing stage, II covers the refocusing event and III the pulse propagation after refocusing.

are again demonstrating the introduced stages for the sake of comparability. The FWHM initially decreases in the theoretical findings with a subsequent broadening stage followed by a drastically dropping pulse duration. The rapid switch to low values in the pulses duration is connected to the pulse-splitting event, showing a very drastic influence as the pulse duration in the simulations drops within less than a centimeter of propagation from ≈ 42 fs to 8 fs. The minimal duration of the simulated filamenting pulse shape corresponds to 4.5 fs. The evolution along stage II and III can be directly compared to the experimental findings and shows a good agreement.

Secondly, the steepness of the falling edge of the pulse in panel (b) is evaluated by the determination of the strongest negative gradient along the respective pulse shapes from the experimental and simulated data. The analysis of the falling slope is a direct indicator for the self-steepening dynamics along the femtosecond filament.

The increasing falling slope in the numerical findings is connected to an increasing amount of self-steepening along the pulse propagation which cannot be well reproduced by the experimental measurements. This shortcoming will be picked up at a later point along this thesis (c.f. Sec. 3.3.5). An improved determination of the falling slope through high-order harmonic spectroscopy will be presented in Sec. 4.3.2. The last panel (c) additionally shows the evolving intensity along the filaments propagation direction and is inaccessible by the measured pulse evolution. The simulations show, that the intensity along the filament rises as the pulse is approaching its focal point followed by an intermediate minimum and an extended plateau afterwards. The physics along each of the three stages of a femtosecond

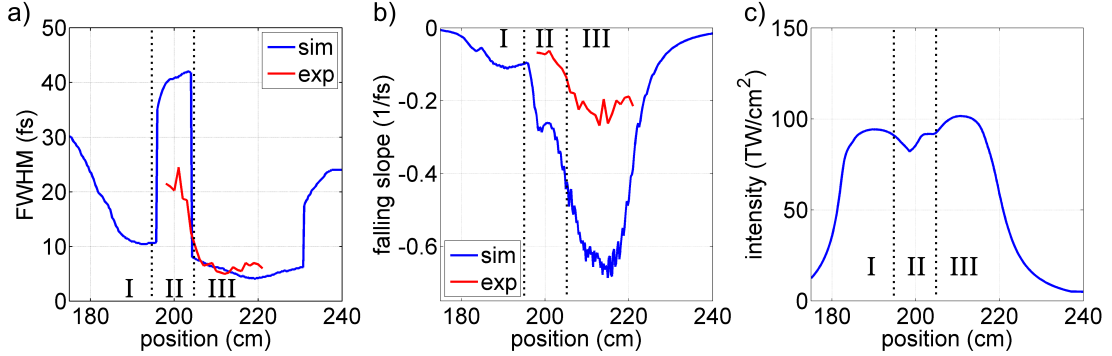


Figure 3.13: Derived properties from the evolution of the pulse shape. The (a) full-width-half-maximum, (b) falling slope of the pulse, being a measure for the steepness and (c) the peak intensity are shown for the propagating on-axis ($r=0$) pulses.

filament will be explained by using the content from Figs. 3.11 to 3.13 in the following.

Connection between Simulations and Experiments along the three Propagation Stages

The agreement between the theoretical results and the experiments allows for the use of the simulated spatio-temporal pulse shapes as a guideline through the filaments life cycle. Additionally, the simulated spectrum will be analyzed with respect to its divergence angle θ to connect the occurring temporal dynamics to spectral features. This is performed by a two-dimensional Fourier-transformation of the simulated spatio-temporal profiles, where the electric field along each radial position is first transformed into the frequency-domain and secondly the radial components are Fourier-transformed to yield the radial wave vector K_{\perp} . This vector is connected to the divergence angle via $\theta = K_{\perp}/k_0$ with $k_0 = \omega_0 n/c$ [177].

Stage I - Defocusing A closer look at the changing temporal pulse-shape along the first stage between positions 175 cm and 194 cm shows, that the trailing edge of the envelope is disappearing with ongoing propagation (c.f Fig. 3.11 (c)). The spatial influence connected to this effect can be seen in the four pictures describing the spatio-temporal evolution in Fig. 3.12 (a) for positions 185 cm, 187 cm, 190 cm and 192 cm. The trailing section of the initial pulse is pushed off-axis as the defocusing effect of the free electrons influences the propagating beam (c.f. Sec. 2.2.3). The diverging features in the back of the pulse form a characteristic C-shape in the spatio-temporal representation shown in Fig. 3.12 (a). Due to this interaction, the on-axis pulse-shape loses its trailing components and the FWHM-pulse duration decreases steadily as the beam approaches its (nonlinear) focus position (c.f. Figs. 3.13 (a) and 3.11 (c)). The falling slope of the pulses envelope starts to steepen, as the time-dependent buildup of the plasma-initiated defocusing lens influences the propagating beam.

Fig. 3.14 displays the plasma-induced refractive index change along a 100 TW/cm^2 pulse of 20 fs to stress the rapid onset of the plasma-connected defocusing lens along the pulse shape (c.f. Eq. (2.13)). Due to the highly nonlinear nature of the ionization process the free electron density and the refractive index change occurs within a few optical cycles and explains the initial steepening as well as shortening of the beam along the defocusing stage I (c.f. Figs. 3.13 (a) and (b)). The self-shortening due to the plasma build-up has not directly been tracked in the presented experiments, as the measurements start at a position of 198 cm. The fact, that the pulse measured at position 200 cm has a duration of ≈ 25 fs (c.f. Fig. 3.9 (top)) supports the assumption of a self-shortening mechanism connected to the plasma-defocusing effect alone along stage I. Therefore, not even a refocusing cycle is necessary to shorten the propagating pulse. This qualitatively agrees with the numerical findings of the reduced propagation model in Fig. 3.5 and plasma-induced self-shortening observed during relativistic laser-matter interaction [157, 178, 179]. The frequency components, accompanying the on-axis pulse-shortening originate from the instantaneous frequency connected to the changing electron density along the pulse shape and from self-phase modulation (c.f. Eq. (2.14) and (2.9)). Similarly to the temporal pulse structure, the spectrum undergoes a spatial evolution.

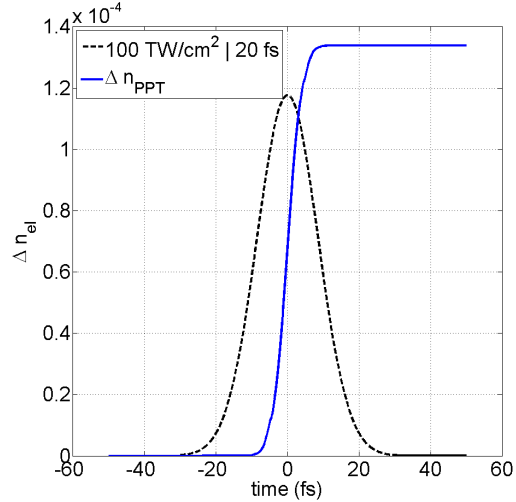


Figure 3.14: Change of the plasma-induced refractive index along a 20 fs pulse with a peak intensity of 100 TW/cm^2 . The refractive index jump is defined to a small window along the temporal pulse shape.

The connection between the divergence angle θ and the angular frequency ω is shown in Fig. 3.15 for a position of 185 cm together with the initial spectral distribution at 175 cm for the sake of comparison. The white dotted line represents the highest frequency measured in the experiments (c.f. Fig. 3.11 (b)). It can be seen that the range of spectral signal is moderately broadened from 2.2-2.6 rad/fs at 175 cm to 2.1-2.7 rad/fs at 185 cm. Hereby, the higher frequencies show a stronger divergence, as these are generated along the changing free-electron density, which has a defocusing effect. As the medium is ionized along the defocusing stage, the leading edge of the pulse constantly loses energy, which is apparent in the intermediate decrease in the simulated intensity evolution in Fig. 3.12 (a).

The defocusing stage I is defined by the spatio-temporal profiles up to the point, at which the off-axis components in Fig. 3.11 (e) stop showing the characteristic C-shape and start to approach the optical axis to initiate the next stage of filamentation, the refocusing stage.

Stage II - Refocusing Fig. 3.12 (b) describes the second important stage II of filamentation, where the off-axis components reappear at the optical axis. This is depicted for distinct propagation distances of 194 cm, 196 cm, 197 cm and 201 cm. This stage of the filamentary life cycle is partly observed by the measurement of the temporal pulse shape (c.f. Fig 3.10). The spatial refocusing of the temporally trailing part has direct consequences for the FWHM-pulse duration in Fig. 3.13 (a). The increasing intensity in the trailing part of the pulse results in an intermediate increase of the FWHM in the simulations because the two structures in the leading and trailing part of the pulse are of similar field-strength for positions between 197 and 204 cm (c.f. Fig. 3.11 (c)). The scenario is depicted in Fig. 3.16 where the simulated as well as measured pulse shape is displayed for a position of 204 cm. A double-hump structure occurs in the simulations with an M-shaped appearance, which has been singled out by the reduced numerical model in Fig. 3.5. The double-peak could be identified in the experiments albeit it shows a significantly differing ratio of the peaks compared to the simulations. This explains why the FWHM pulse-duration in Fig. 3.13 (a)

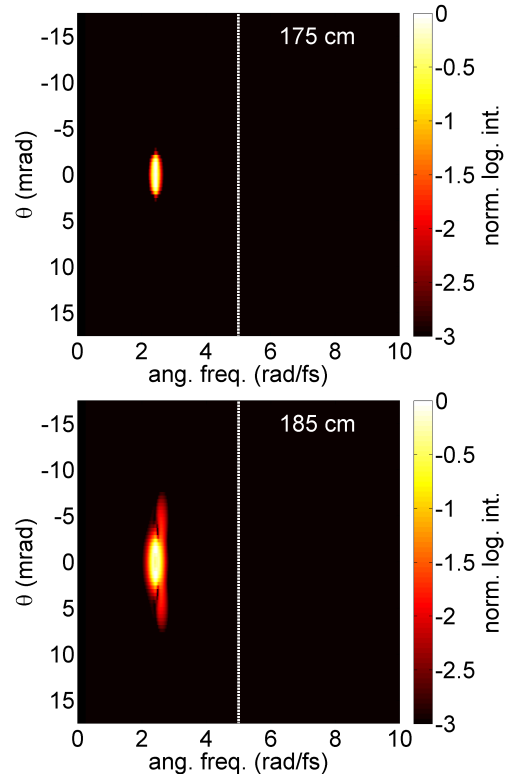


Figure 3.15: Divergence θ of the spectral components at positions 175 cm and 185 cm. The defocusing of blue-shifted spectrum can be seen at 185 cm. The white dotted line depicts the highest experimentally measured frequency.

maximizes to ≈ 25 fs for the experimental results as compared to ≈ 42 fs for the simulations.

The end of the refocusing cycle manifests itself in the strong drop-off in the FWHM pulse duration to ≈ 8 fs in the simulations at 203.2 cm and ≈ 7.75 fs in the experiments (c.f. Fig. 3.13) at a position of 205 cm. This rapid decrease is connected to the trailing part of the pulse starting to dominate the pulse's structure. Therefore, the influence of the refocusing cycle on the self-shortening dynamics could be distinguished from the upcoming propagation dynamics by the strongly varying pulse duration between 200 cm and 205 cm in the experiments.

Not only the width, but also the slopes and peak intensity of the pulse are influenced by the refocusing dynamics (c.f. Fig. 3.13 (b) and (c)). The steepness of the falling edge is influenced by the pulse-dynamics as the increasing strength of the trailing pulse structure leads to the steeper falling slope. This is inherently connected to decreasing pulse duration since shorter pulse shapes exhibit stronger gradients along their envelope. The simulated on-axis intensity evolution along the filament shows a local minimum along the refocusing stage II. The leading part of the pulse is weakened due to plasma generation and its divergence properties, since the initial nonlinear focus of the setup is surpassed. Simultaneously, the trailing part is refocused and leads to a subsequent increase of the on-axis intensity, explaining the minimum at position 197 cm in Fig. 3.13 (c). The influence of the refocused trailing pulse feature on the spectrum can be seen for positions of 197 cm and 200 cm in Fig. 3.17. The increasing intensity in combination with the appearance of a short pulse feature enable the generation of new on-axis frequencies through the shortened trailing pulse feature and SPM during propagation. The spectrum spans up to ≈ 3 rad/fs (630 nm) for the case of 197 cm and to ≈ 3.5 rad/fs (540 nm) for the case of 200 cm, being emitted with small divergence angles as the refocused part of the pulse is re-approaching the optical axis. Coinciding with the increasingly structured spatio-temporal shapes, the spatio-spectral properties gain complexity.

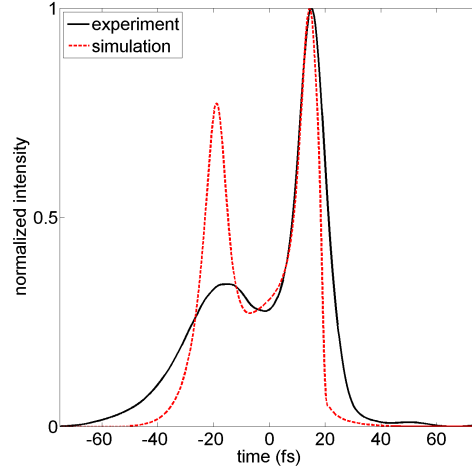


Figure 3.16: Comparison of the simulated and measured pulse-shape at a position of 204 cm. The refocusing event results in a double-peak structure, which is clearly visible in the simulations. The measurements show this behavior to a lesser extent.

A possibility to maximize the influence of the refocusing cycle on the filamentary pulse dynamics is the choice of a medium with a small ionization potential. A strong external focusing setup is also favoring the influence of the defocusing-refocusing cycle on the self-shortening dynamics. This is the case in the works of Bethge et. al. [76], as Krypton at atmospheric pressures is used to interact with 120 fs, 1 mJ pulses focused by a 75 cm lens, where the dynamics for long initial pulses has been analyzed. All the parameters favor a strong influence of the plasma-defocusing since the pulse duration is sufficiently long and intense enough to effectively generate large amounts of free electrons along the pulse shape. Still, the propagating pulse could be shortened by a factor of 3.3, proving the essential role of the refocusing cycle in the self-compression dynamics along a femtosecond filament [72, 76, 157].

The re-appearance of the off-axis components on the optical axis is the phenomenon that triggers the dynamics, that leave the most obvious fingerprints in the fundamental spectrum, dubbed as the propagation stage III of the filaments dynamical evolution in the panel covering the temporal dynamics in Fig. 3.11 (c).

Stage III - Propagation

The spatio-temporal profiles which correspond to the propagation stage are displayed for exemplary positions of 205 cm, 209 cm, 213 cm and 217 cm in Fig. 3.12 (c). This appears as the most stable and spatially least dynamic regime as the simulated radial pulse-profiles are less influenced by plasma-contributions during their propagation due to their decreased pulse duration (c.f. Fig. 3.13 (a)). This section along a filament is characterized by the propagation of an ultrashort pulse at high intensities, strongly favoring the influence of the Kerr-effect [58, 180]. Spatially, this results in further self-focusing which leads to a high-intensity plateau along the propagation axis (c.f. Fig. 3.13 (c)). The temporal influence of the Kerr-effect gives rise to a steady impact of SPM, effectively modulating the fundamental spectrum due to the elongated high-intensity interaction region (c.f. Fig. 3.13 (c)). Additionally, the pulse self-steepens, as the Kerr-effect leads to a Gaussian evolution of the refractive index along the pulse's envelope

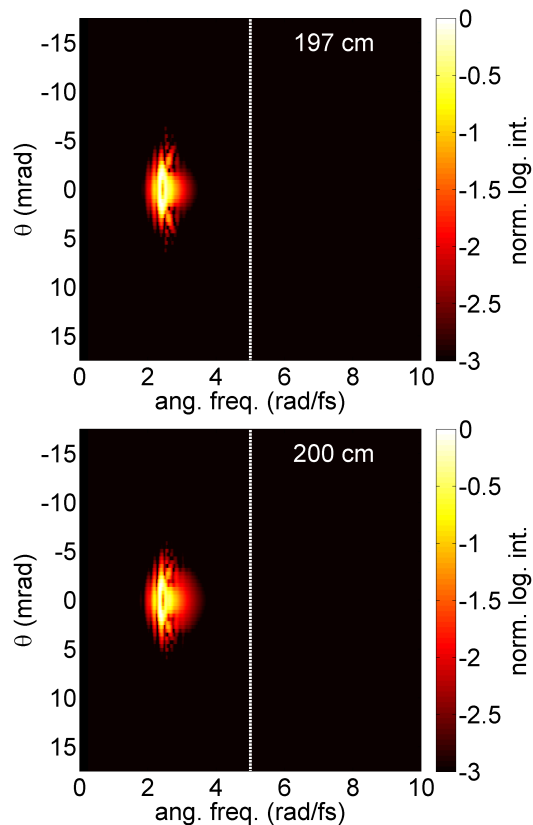


Figure 3.17: Angular resolved emission for positions 197 cm and 200 cm. The initially defocused spectral features approach the optical axis and new frequencies are generated through SPM.

(c.f. Fig. 3.13 (b)). The responsible terms for self-steepening in Eq. 3.11 (III) are described by $in_2\omega/cT|E|^2E$ with $T = 1 + (i/\omega_0)\partial t$. Consequently, not only the SPM term leads to the generation of new spectral frequencies but also the self-steepening term. The combination of SPM and self-steepening is the nonlinear interaction which effectively contributes to the generation of the typical filament-like spectrum, consisting of a weak blue spectral tail ranging up to the ultraviolet region. The appearance of such spectra has been observed in numerous experiments [58, 60, 74, 79, 118, 135, 136, 181, 182]. The changing FWHM pulse duration along the filament reveals, that the shortest obtainable pulse along the interaction region is not generated by the sole refocusing cycle itself, but emerges as the propagating pulses trailing edge catches up with the high intensity peak [143, 182].

After the spectrum is influenced by the strong asymmetric SPM, induced by the mentioned self-steepening term, the spectral width for the on-axis spectral components starts to decrease again for $z > 211$ cm (theory) and $z > 212$ cm (experiment) in Fig. 3.11 (c) and (d) respectively. The divergence properties of the high frequency components can be seen in Fig. 3.18 where positions 214 cm and 220 cm are displayed. The highest frequencies > 5 rad/fs ($\lambda < 375$ nm) show a strongly diverging behavior and form a fish-tail like structure. The shape resembles observations made in filaments generated in solids and liquids, called X-waves [128, 183]. In this context, the strongly changing divergence along the spectrum is connected to a dominant group-velocity dispersion (GVD) and used to explain phenomena such as conical emission [126, 128, 177]. In the presented case an additional possible source for the diverging high-frequency components besides the material dispersion comes into play. Here, the divergence might be connected to the refractive index change induced by the free electrons, inducing a defocusing effect and a frequency dependent refractive index modulation connected to $-\frac{\rho_e}{2\rho_{\text{crit}}}$. The frequency dependency hereby stems from $\rho_{\text{crit}} = \epsilon_0 m_e \omega_0^2 / e^2$. The high-frequency components are generated along the falling edge of the steepened pulse. The highest photon-energies can be obtained as the trailing pulse front breaks and the gradient along the falling edge is maximized. Therefore, the highest frequencies are located in the tail of the pulse, where the influence of the generated and accumulated free electron density is most pronounced and can influence the propagation. The spectrum connected to the fish-tail has not been observed in the experiments, as the experimentally measured spectrum is limited to $\lambda > 380$ nm. Concentrating on this spectral region in Fig. 3.18 reveals that the frequency components ranging up to 5 rad/fs weaken with ongoing propagation, which is in good agreement with the findings from Fig. 3.11 (b) and (d).

This evolution of the blue frequencies has to be taken into account when the spectral content after a filamentation cell is evaluated with the purpose of gaining detailed insight into the pulse characteristics, such as the pulse's steepness [143]. The complete cycle and especially the self-steepening remain undisclosed by a sole observation of the final pulse-shape or spectral properties after an untruncated filamentation cell, as the resulting spectrum is strongly influenced by the propagation dynamics, even after the filamentary life cycle. As the pulse propagates further along the filament, dispersion as well as diffraction influence the pulse during the ongoing propagation and result in the disappearance of nonlinear propagation dynamics.

Previous works report a significant self-compression of pulses emerging from a filament without an external compression setup [74, 75]. The possibility to observe the self-shortening has two reasons. First, the beam was characterized shortly after the filamentation cell. As the pulse-detection setup uses focusing optics, a certain position along the propagation axis z is being imaged by the optical component into the measurement device. Therefore it is possible to detect parts of the off-axis propagating spectral components.

Second, the subsequent propagation through air and output windows can have beneficial effects on certain parts of the spectrum, as the spectral phase of the pulses emerging from the filament is strongly modulated and certain parts of the spectrum can be compressed through ensuing propagation [184].

The propagation stage finalizes the life cycle of a filament. The dynamics of pulse splitting are shown for the first time in a complete comparative picture and the foundation of the simulations is strongly supported by the good agreement to the experimental findings. It could be illustrated that the self-compression of the fundamental pulse-shape is strongly connected to the refocusing and the propagation stages II and III along the filament, whereas both enable an efficient shortening of the fundamental pulse.

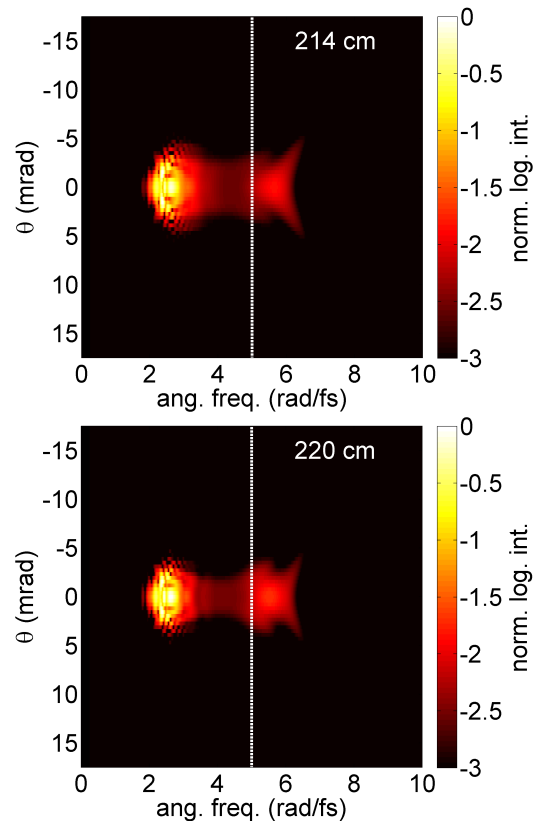


Figure 3.18: Spectral emission at positions 214 cm and 220 cm along the propagation stage III. The modulated spectrum shows strongly frequency-dependent divergence properties. The highest frequencies form a fish-tail like structure and a weak signal between 3 rad/fs and 5 rad/fs. The initial carrier at 2.4 rad/fs is the most dominant spectral component but strongly modulated.

3.3.5 The Spectral Content of the Reconstructed Pulses - Experimental Shortcomings

Despite the good resemblance between experiments and simulations (c.f. Fig. 3.11), certain characteristic features of the pulse dynamics exist, which are very challenging to measure with the conventional pulse detection setup used in the experiments. Figure. 3.13 (b) displays the comparison of the steepest slope of the fundamental pulse's falling edge in dependence of the propagation distance. The experimentally retrieved pulse shapes are lacking these extreme slopes, showing values which differ by a factor of three at their respective steepest positions. The disagreement between the theoretical findings and the experimental results is non-negligible but can be explained by the experimental setup, which is used for the pulse detection and its spectral sensitivity. To better understand the discrepancies between simulations and experiments, calculated X-FROG traces are used for further evaluation.

The traces are generated by multiplying a finite temporal gate to the on-axis electric field in order to obtain the instantaneous frequency along the width of the governing function which is chosen to be a Gaussian distribution of 3 fs width. By delaying the gate-function, an analysis of the instantaneous frequency along the on-axis temporal pulse shape is possible. The frequency map along the pulse's temporal shape is obtained for the measured pulse shapes as well as the calculated ones and is shown in Fig. 3.19. The traces are coupling the temporal and spectral data and the analysis is expanded from absolute characteristics of the pulse, such as the peak intensity, its spectrum or its pulse duration towards properties including the phase evolution, like the instantaneous frequency along the temporal shape of the pulse. For a comparison of the experimental shortcomings, three exemplary positions are selected at 197 cm, 206 cm and 212 cm. The first presented case at 197 cm, connects stage I and II (c.f. Fig 3.11 (e) and (g)) so that the leading pulse is strongly influenced by the foregoing defocusing and the trailing structure is building up because of the refocusing effect. Therefore, an asymmetric pulse shape can be observed in the simulated results in Fig. 3.19. A similar structure is observed in the experiments, albeit less clearly. Here, the first experimental shortcoming can be seen, as the absolute determination of the temporal position of the pulses structures is ambiguous for SHG-FROG traces.

The second exemplary position of 206 cm shows only a partial agreement. For the numerical findings, the generation of new, blue spectral components starts to set in as the position corresponds to the beginning of propagation stage III. The position and appearance of the dominating blue spectral content in the experiments agrees and only the very weak tail with relative intensities $<10\%$ could not be reconstructed. These wavelength however do not significantly disturb the reconstruction of the temporal pulse-shapes due to their weak contribution.

The third position of 212 cm is clearly situated in stage III. The previous section concluded that the ongoing propagation along this stage results in a dominating self-steepening. This

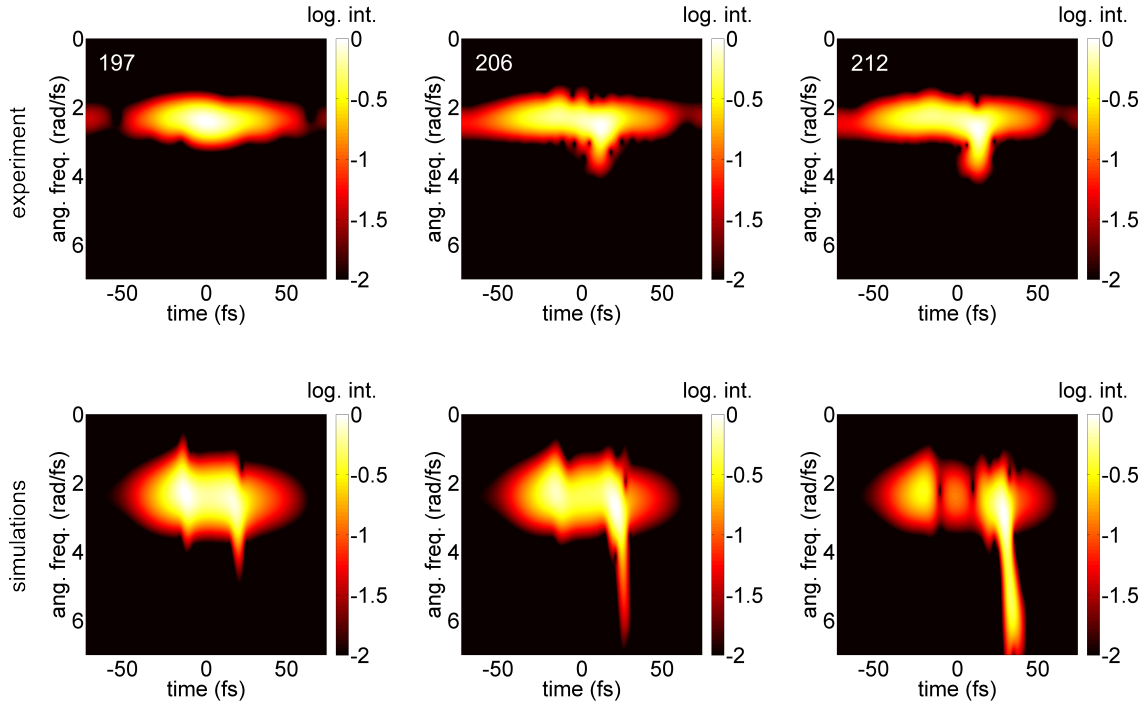


Figure 3.19: Calculated X-FROG traces, portraying the spectral distribution along the on-axis temporal shapes. The traces are calculated for the pulse shapes originating from the experimental measurements and the simulations.

is evident by the extreme blue tail in the theoretical findings, where a spectrum ranging from approximately 925 nm (2.1 rad/fs) down to 280 nm (6.75 rad/fs) is conglomerated in a temporal window of less than 10 fs in the trailing part of the pulse. It can be seen in Fig. 3.19, that the experimentally retrieved pulses are lacking the information in the blue spectral region, which is situated in the trailing part of the pulse, as the retrieved spectrum only ranges from approximately 925 nm (2.1 rad/fs) to 500 nm (3.75 rad/fs). This shortcoming can be explained by the beam propagation along the experimental setup. The beam guiding by reflective mirrors as well as the bandwidth limitations of the phase matching in the SHG-FROG device can strongly influence the spectral components which contribute to the pulse reconstruction. The blue spectral part emerging from the filament is also the most vulnerable to losses induced by poor reflection properties, since its relative signal-strength in the spectrum is significantly smaller compared to the input wavelength. Recalling Fig. 3.13, the discrepancies in the determination of the steep falling edge are directly connected to the observed spectral shortcomings in the X-FROG traces, as the falling edge is directly connected to the generation of the highest frequencies. From this it can be concluded that the SHG-FROG is capable to reconstruct most of the pulse features but is lacking the insight into the self-steepening dynamics.

3.3.6 The Influence of the Truncating Stage

The investigation of shortcomings is essential for further improvement of the experimental characterization of femtosecond filaments. Discrepancies could not only be induced by the poor beam guiding into the pulse detection setup. Other reasons have to be investigated to again confirm the experimental outcome and their correspondence to the numerical findings. An obvious choice would be the implemented pair of pinholes, which truncate the beam along the filamentation stage. Therefore, the influence of the small-diameter pinholes in the experimental setup (P1 \approx 400 μm , P2 \approx 150 μm) is analyzed theoretically [185]. The first plate is always exposed to the plasma generated by the filament and starts to increase in its diameter drastically due to the heated plasma, which induces thermal melting of the metal plate. This explains why its diameter is large opposed to the typical diameter of the filaments core (\approx 100-200 μm) [64, 186]. The second metal plate is not exposed to the plasma itself, since the differential pumping stage clears the environment of the ambient gas. Therefore, the drilling process is confined to a pure laser-matter interaction at the metal plate's surface, resulting in a much smaller pinhole diameter of \approx 150 μm .

The subsequent propagation to the detector is taken into account and has a significant effect on the measured pulse profiles. To analyze the far-field temporal pulse shapes in a systematic manner, the Fraunhofer diffraction integral is evaluated to yield the far-field on-axis intensity distribution of the filament pulses (assuming cylindrical symmetry) [185]:

$$\begin{aligned} \vec{E}_{\text{far-field}}(r, \omega, z) &= 2\pi \int_0^{d/2} \vec{E}_{\text{pinhole}}(r', \omega) J_0\left(\frac{\omega r' r}{cz}\right) r' dr' \\ r = 0 : \vec{E}_{\text{far-field}}(\omega, z) &= 2\pi \int_0^{d/2} \vec{E}_{\text{pinhole}}(r', \omega) r' dr'. \end{aligned} \quad (3.13)$$

Here, the radial electric field distribution at the pinhole \vec{E}_{pinhole} and in the far-field $\vec{E}_{\text{far-field}}$ are connected through the integration over the Bessel-function J_0 with their corresponding observation point r and the position in the aperture r' . Note, that both field distributions are not solely depending on the radial coordinate r , but also on the frequency ω . Since only the on-axis distribution in the far-field is of interest, r is set to zero. A Fourier-transformation back into the temporal domain yields the temporal pulse shape at the position of the detector [185]. Panel (a) displays the already introduced simulated pulse evolution, as it occurs inside the filament according to Fig. 3.11. Panel (b) shows the propagated pulse evolution after the fundamental pulse passed a pinhole with a diameter of 100 μm and propagates 1 m to the detection setup. Sub-figures (c)-(f) show the result for increasingly larger diameters of 150 μm , 250 μm , 500 μm and 1000 μm respectively. The findings appear to be counter intuitive, as a smaller opening is supposed to distort the subsequent vacuum-propagation more drastically through diffraction. The opposite is the case, as the smallest pinhole diameter results in the closest resemblance to the near field results in panel (a). The pulse-splitting and the clear separation into a weak leading and a short, intense trailing part are reproduced for pinhole diameters smaller than 200 μm . Additionally, the position of the defocusing and refocusing stage is only slightly shifted by \approx 1 cm towards smaller propagation distances.

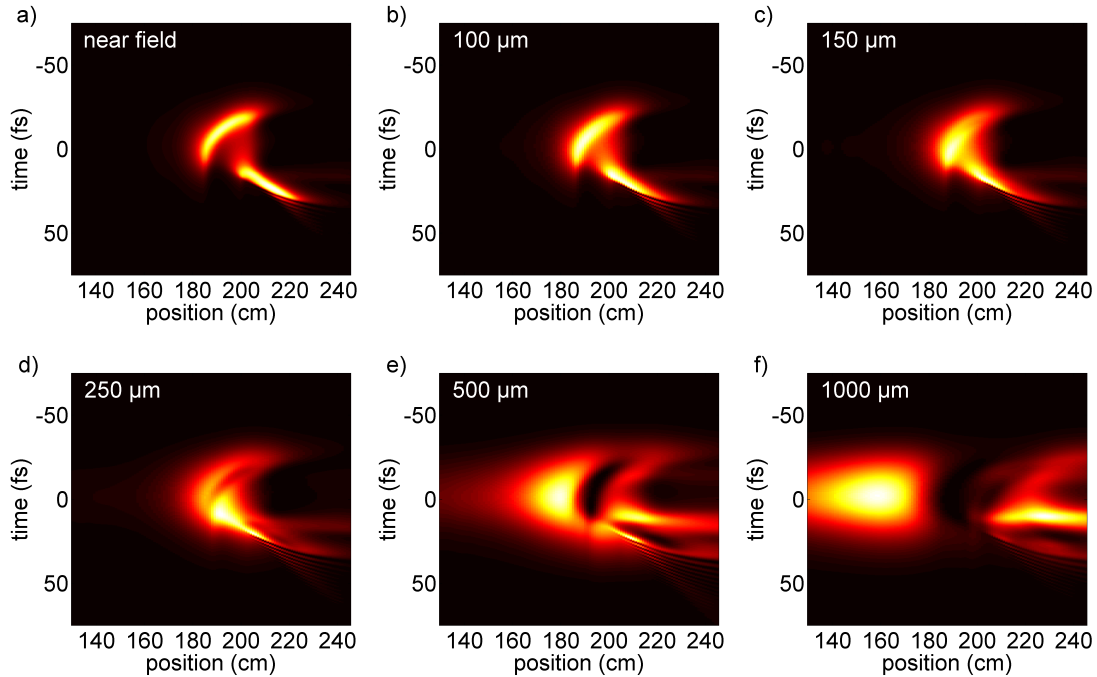


Figure 3.20: Influence of the pinhole setup upon the measurable pulse dynamics. Panel (a) shows the already introduced pulse dynamics inside the filament. The sub-figures (b)-(f) show the pulse evolution, which will be measured after passing a pinhole with a diameter of $d=150, 250, 500, 1000 \mu\text{m}$ plus 1 m of vacuum propagation. The detectable pulse dynamics rapidly change with an increasing pinhole diameter.

For larger pinhole diameters, the observable pulse-dynamics change rapidly. The pulse-splitting appears at a much earlier position along the filament, mimicking pulse dynamics that have no resemblance to the actual near-field case. The observations along the near-field propagation stage for pinhole diameters $> 250 \mu\text{m}$ also show no clear signatures of strong self-steepening or self-compression. The FWHM pulse-duration at the position of the shortest measured pulse at 212 cm corresponds to 10.8 fs for the case of a $500 \mu\text{m}$ opening and to 11.3 fs for the $1000 \mu\text{m}$ one. Consequently it is the strong truncation of the propagating beam that enables a correct representation of the on-axis near-field dynamics. The positive influence of strong truncation can be explained by the refocusing dynamics of the fundamental pulse in the filament. The spectrum along the complex pulse shape has varying beam diameters, diffraction lengths and divergences (c.f. Fig. 3.17 and 3.18) [185]. In order to estimate the influence of the truncating pinhole on the spectrum, the radial distribution of the frequency components is shown in Fig. 3.21. The spectrum connected to the initial pulse-shape ($\omega < 3 \text{ rad/fs}$) undergoes the complete de- and refocusing cycle along stage I and II. Therefore it shows different divergence properties than for example the blue spectral components ($\omega > 4 \text{ rad/fs}$) connected to the propagation stage III.

The chosen representation allows to directly pinpoint to the spectral content which is most affected by the truncating pinholes. A small-diameter opening results in a uniform distribution of the spectrum and limits the effects of the subsequent propagation along the vacuum stage. Increasing the pinhole diameter enables a contribution of off-axis components to the vacuum propagation and therefore can strongly change the appearance of the spatio-temporal dynamics in the far-field (c.f. Fig. 3.20) The spatial filtering needed to obtain a reasonable representation of the near-field pulse shapes is estimated to be $<200\ \mu\text{m}$ in Fig. 3.20. Figure 3.22 evaluates the influence of the present experimental setup on the temporal shape of the pulse at (a) 204 cm and (b) 220 cm. The experimentally retrieved pulse-shape is compared to the simulated near-field one and the one which has been propagated through a $150\ \mu\text{m}$ pinhole. For the position of 204 cm, the pinhole setup mainly decreases the strength of the leading pulse feature, leaving a better resemblance with the actual measurements. This explains why the experimental findings in Fig. 3.16 were unable to directly prove the existence of the M-shaped double peak structure along the refocusing cycle. The agreement between the experimental measurement and the far-field simulations including a $150\ \mu\text{m}$ pinhole are convincing and further prove the good applicability of the numerical model.

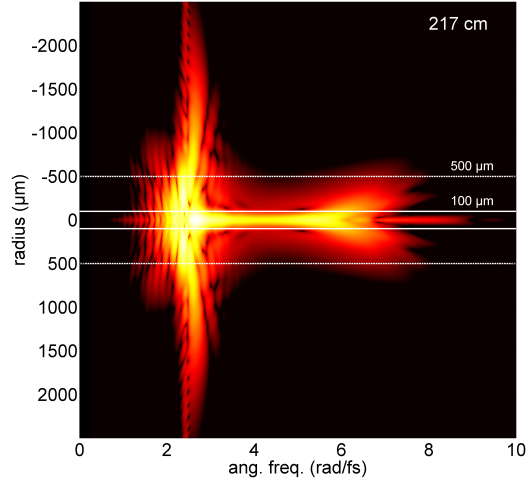


Figure 3.21: Influence of the pinhole setup on the subsequent propagation. The radial properties of the spectrum is strongly structured. A small-diameter filtering by a $100\ \mu\text{m}$ pinhole (white line) cuts out a uniform profile, limiting the distortions during subsequent propagation. A bigger pinhole diameter of $500\ \mu\text{m}$ allows for a mixing due to the strongly differing divergence properties of the frequencies.

A similar influence can be observed at 220 cm, where the front part of the pulse-shape is enhanced by the vacuum propagation, resulting in a good agreement with the experiments. It can be concluded that the main pulse structures remain intact during the subsequent vacuum propagation if the pinhole diameter is sufficiently small, with a slight disturbance being introduced to the leading feature of the pulse shape.

Truncation setups, which have been used previously relied on a single pinhole setup to extract the pulses under investigation [60]. The correct determination of the pulse-shape is impossible to fulfill with a single pinhole setup, as the diameter of the first opening grows drastically [185]. The findings also show, that the use of pressure windows and similar techniques to truncate the propagating filament are not sufficient enough to observe the actual dynamics in the filament and explain why many groups were unable to find real evidence of self-compression during filamentary propagation and instead relied on post-compression setups [76, 131, 158, 187]. One additional possibility to overcome the errors induced by subsequent vacuum propagation is to fully image the source point of the pulse under investigation into the pulse detection setup. Doing this, care has to be taken to avoid propagation effects induced by a lens or astigmatism induced by the implementation of reflective optics. If the imaging is applied properly, the near-field pulse structure from the filament could be used in an ensuing application stage.

3.3.7 Determination of the Correct Ionization Model

In the upcoming section the influence of the chosen ionization model, which have been introduced in Sec. 2.2.2, on the numerical findings will be evaluated. So far, only the PPT-

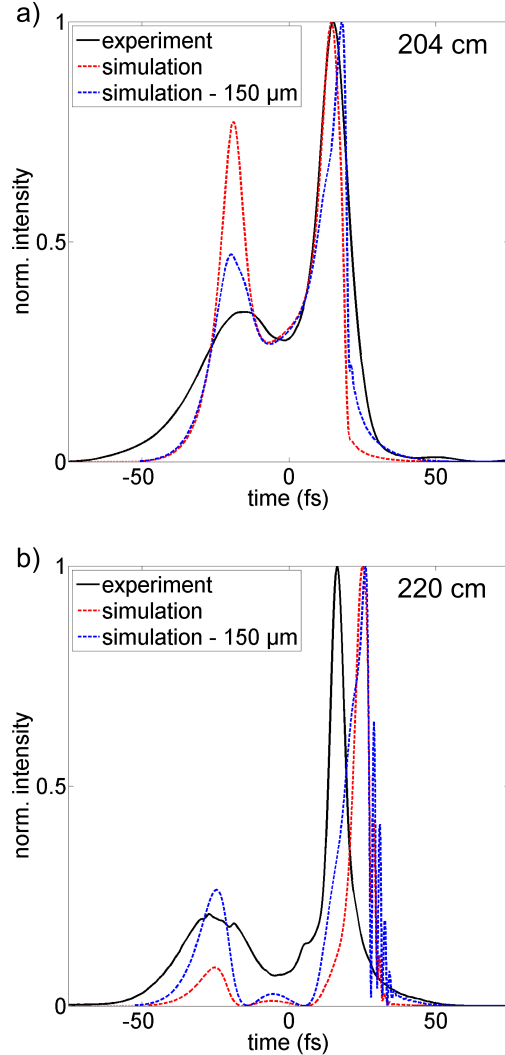


Figure 3.22: Influence of the pinhole setup on the pulse reconstruction. The experimentally measured (black), simulated near-field (red-dotted) and the simulated far-field (150 μm - blue-dotted) pulse shape are displayed for a position of (a) 204 cm and (b) 220 cm.

rates are proven to be valid, but the influence of the ionization model on the theoretical outcome is unexplored up to now. The reason of this investigation is, that many theoretical approaches rely on the application of the computational undemanding MPI- or the ADK-model to investigate filamentary pulse dynamics. The influence of the simplified models needs to be checked by a comparison with the obtained experimental measurements and is subject to the following paragraph.

The evolution of the fundamental pulse along the filamentary propagation direction is simulated for the initial parameters of the experiment (1 bar argon, $f=2$ m, $\tau =47.2$ fs, $E_{\text{in}} = 0.9$ mJ) using the PPT-, MPI- and ADK-ionization rates to model the light-matter interaction under exactly the same numerical conditions. Figure 3.23 compares the simulated results for the three different ionization models by evaluating the temporal pulse-shape as a function of the propagation distance (a-c), the spectral evolution (d-f), the peak intensity along the filament (g) and through the FWHM of the propagating pulse profiles (h). As already stated in the previous section, the PPT-rates yield a very good agreement with the experimental observations. Therefore, no additional justification of these findings is needed, instead the results will be used as a benchmark for the outcome of the other two models.

The results for the MPI-rates show strongly differing pulse dynamics in which the pulse-shape shows no strong influence of the refocusing cycle. As a consequence the propagation dynamics are not evident and no accordance with the numerical PPT-findings can be seen. The spectral evolution in panel (f) completely lacks any significant spectral modulation through SPM. This is connected to the low intensity being present along the complete interaction region, as it can be seen in Fig. 3.23 (g). Accordingly, the pulse-duration is also constantly exceeding 20 fs for all three propagation stages. This can be connected to the overestimation of the ionization rates by this model. The exaggerated generation of free electron leads to a strong defocusing as well as absorption of the incoming pulse, leaving no possibility for the onset of the characteristic refocusing dynamics as the action of the diverging lens generated by the free electrons cannot be counteracted by the Kerr-effect. Consequently, the pulse dynamics show only an influence of the defocusing stage and the spectral evolution shows no features of the propagation-stage. The simulated outcome of the MPI-rates can reliably exclude the applicability of this model for an adequate modeling of filamentary pulse dynamics. The findings connected to the ADK-formalism yield similar returns to the validated PPT-case, as the pulse-splitting connected to the refocusing cycle is present in both cases. However, the models show minor discrepancies for the evolving pulse duration, especially at the later positions along the femtosecond filament. The pulse's envelope shows a very prominent jump to longer pulse durations around 215 cm for the ADK-rates and around 228 cm for the PPT-rates. The experimental measurements range up to 220 cm, which should be able to exhibit the pronounced upward trend in the pulses length in the ADK-model. The fact, that this has not been observed supports the usage of the implemented PPT-rates for modeling the nonlinear pulse dynamics along the femtosecond filament. Unfortunately, the measurements were not able to scan up to a position of 230 cm to actually prove the PPT-predictions. The spectral evolution of the

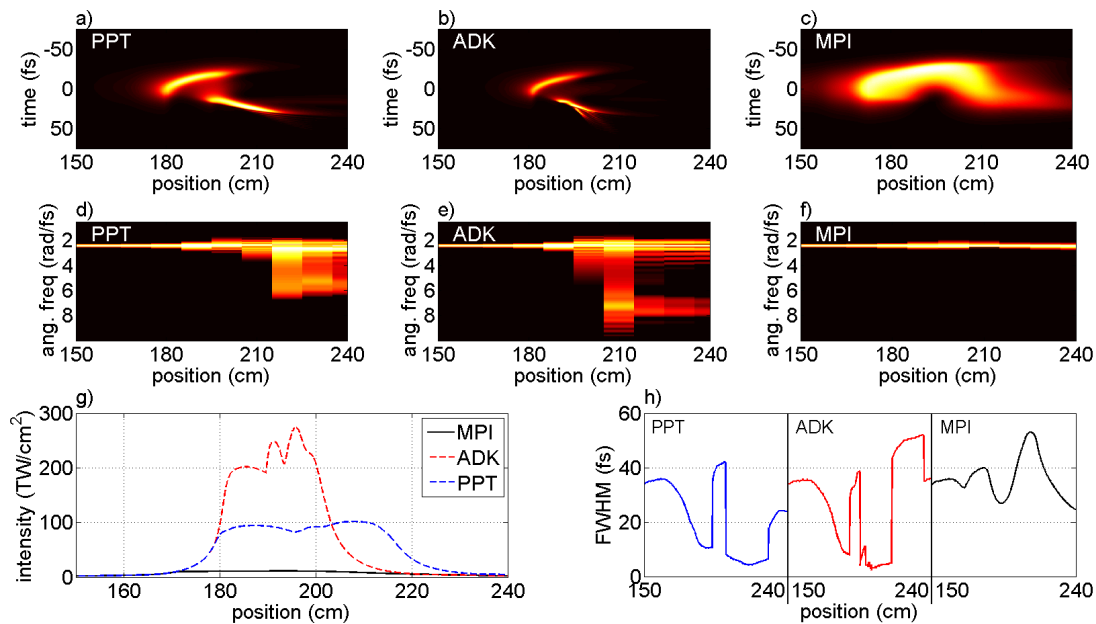


Figure 3.23: Numerical results obtained through the implementation of different ionization-models, namely the PPT- (a,d), MPI- (b,e) and ADK-rates (c,f). The temporal (a-c) and spectral (d-f) evolution is shown for each case. Below, the connected intensity and FWHM pulse-duration is displayed in dependence of the propagation length.

two underlying models delivers a slightly better insight, as the results connected to the ADK-model yield much broader and more structured spectra. This can be understood as the ADK-model yields significantly lesser amounts of free electrons along the pulse, which results in an increase of the achievable intensity. The balance between the Kerr-nonlinearity and the plasma induced effects sets in at higher intensities, increasing the influence of the Kerr-effect on the spectral evolution as well. An experimental access to the fundamental pulses intensity would clearly clarify this remaining ambiguity between the ionization models, since the achievable peak intensity along the filament is differing by a clear factor of ≈ 3 . The evaluation of this missing link is one of the main purposes of the remaining thesis, as high-order harmonic generation will be implemented as a nonlinear tool along the femtosecond filament in the upcoming chapter.

3.3.8 Conclusion

The fundamental pulse's evolution along the experimentally observed femtosecond filament is dominated by the occurring refocusing cycle, which results in very characteristic features of the fundamental pulse shapes along a filament. The generation of free electrons at the beginning of the filament results in the defocusing of the trailing part of the pulse's shape, already leading to a pulse shortening of the initial leading section as it has been numerically predicted in previous works [157]. The re-occurrence of the off-axis components at the optical axis lead to the generation of a short pulse feature and a drastic decline of

the pulse duration. These initial stages show emphasized spatial dynamics that lead to a pulse-shortening. The following propagation of the refocused component is dominated by temporal dynamics, as the pulse undergoes a strong, characteristic self-steepening. The experimentally observed strong spectral modulation into the blue spectral region is connected to these dynamics of the short trailing sub-pulse, being accompanied by a heavy self-shortening down to 5.25 fs. The presented experiments are the first measurements to directly show the self-compression dynamics along a femtosecond filament and the measured amount of self-shortening by a factor of 9 along the filaments propagation direction is the largest factor to date. The direct measurement of the numerically predicted extreme self-steepening dynamics is limited by the beam guiding towards the SHG-FROG device and the phase matching during the SHG process. The comparison of the experimental findings with the simulations reveals, that the applied code can sufficiently predict the pulse's spatio-temporal dynamics and reproduces all of its detected features. Additionally, the measurements can distinguish between self-shortening dynamics connected to the refocusing cycle and dynamics connected to the high-intensity propagation of the fundamental beam.

The use of the double pinhole scheme in the experimental setup is essential for the correct reconstruction of the near-field pulse shapes. The small aperture proves to be beneficial for the suppression of ensuing propagation effects that can strongly disturb the on-axis pulse shape even when the pulse is surrounded by vacuum. It has been shown, that only the leading pulse feature is slightly modified when a 150 μm pinhole is applied. The disagreement between the near-field simulated and experimentally reconstructed pulse-shapes can be traced back to the influence of the vacuum propagation. An application of the self-compressed pulses has to consider that the subsequent propagation, even without the presence of a dispersing medium, can strongly influence the duration and shape of the pulses emerging from the filament. Therefore, a suitable truncation of the beam close to its source point with a double pinhole setup or a suitable imaging setup need to be applied.

The implementation of the PPT-ionization rates proves to be the most suitable for the modeling of femtosecond filamentation. Using the MPI-rates overestimates the ionization and suppresses the refocusing dynamics in the numerical model. Applying the ADK-model shows features of pulse-splitting and self-shortening but results in a much higher on-axis intensity.

In the context of the analysis conclusions for the application of the three filamentary life cycle stages can be drawn. Experiments that strongly depend on the use of ultrashort pulse-characteristics should utilize the propagation stage III along the filament. Here, the self-compression is strong enough to deliver pulses that are short enough for their utilization in Raman-spectroscopy or four-wave-mixing processes [13, 58, 188]. Contrarily, the defocusing stage I favors experiments calling for high intensities or electron densities such as breakdown spectroscopy or discharge-guiding [88, 182, 186, 189].

Chapter 4

Application of an Extreme Nonlinear Probe - Filamentation and High-Order Harmonic Generation

The increasing complexity of the filamentation dynamics has been observed experimentally by investigating the evolution of the fundamental spectrum and the temporal pulse shape emitted along the filament's propagation direction (c.f. Sec. 3.3). As the experimental findings from the previous Sec. 3.3.3 have shown, there are various additional parameters and effects to be measured along the filamentary propagation direction that are only measurable with very high experimental efforts by the lone observation of the fundamental beam properties. These parameters include the intensity dynamics of the pulse or its steep pulse-slopes (c.f. Fig. 3.13). Their evaluation is ideally performed with a highly nonlinear process. Fortunately, it has been shown that the filament can be used as a direct source for high-order harmonic generation [139]. The introduced method of a steep pressure gradient to truncate the filament allows to detect directly emitted harmonic radiation [80–82], providing the necessary tool for the desired assessment.

Along the upcoming section, it will be shown that HHG proves to be sensitive to the fundamental pulse's intensity and is able to serve as a probe for the complex pulse dynamics along a femtosecond filament [2]. At first, the fundamental theory of HHG will be introduced, approaching the microscopic and macroscopic response of the medium. Second, the experimental observation of HHG connected to the pulse dynamics in Sec. 3.3 will be examined to draw conclusions on the pulse's steepness. Hereby, the modeling of the macroscopic response will be adapted to the special case of filamentation. Third, the connected evolving intensity will be extracted by the use of HHG. Additionally, the influence of the external focusing setup is investigated and an analytical model is introduced which is able to describe the clamping intensity under consideration of the external focusing setup.

4.1 Theoretical Description and Modeling of High-Order Harmonic Generation

Frequency up-conversion of the fundamental radiation is commonly done by using the second up to the fifth harmonic order [148]. The conversion process can be described by applying the expansion of the nonlinear polarization term (c.f. Eq. (2.5)). The generation of high-order harmonics fails to be described by perturbation theory [35]. The upcoming section describes the suiting theoretical background of HHG and introduces the spectral features of the harmonic radiation and their respective connection to fundamental pulse properties such as the carrier-envelope-offset (CEO) phase or the intensity.

4.1.1 The Three-Step Model

The most simple approach to the understanding of HHG is given by the semi-classical three-step model, which is sketched in Fig. 4.1 together with a typical spectrum emitted during this process [35]. Here, HHG is divided in three steps: (1) the ionization of the atom, (2) the acceleration of a free electron in the external laser field and (3) the recombination of the electron with its parent ion under emission of high-order harmonic radiation [35]. Efficient HHG calls for the tunneling effect to occur and therefore for driving intensities which are related to a Keldysh-factor smaller than one (c.f. Sec. 2.2.2). The atomic Coulomb potential is bend by the dressing laser field, allowing for the electron to tunnel into the continuum [190, and references therein]. The free electron is assumed to have no initial velocity and its propagation is described by the classical acceleration of the electron by the laser field. The motion of the electron is described by the equation:

$$0 = -\frac{eE_0}{m_e\omega_0^2}(\sin(\omega t_r) - \sin(\omega t_0)) + \frac{eE_0}{m_e\omega_0} \cos(\omega t_0)(t_r - t_0). \quad (4.1)$$

Here, E_0 is the amplitude of the electric field $E = E_0 \cos(\omega t)$, t_0 denotes the time of ionization and t_r the time of recombination. The influence of the long-range potential of the residing ionic core is neglected during the propagation step. The continuum wave-packet of the propagating electron disperses along the propagation pathway, corresponding to the accumulation of a phase [35]. The actual emission of the harmonic radiation within the three-step model is calculated by determining the time-dependent dipole moment $\hat{d}(t) = e\hat{r}$, where \hat{r} is the position-operator [35]. The wavefunction Ψ of the electron is modeled as a superposition of its ground state Ψ_g and the laser-accelerated continuum state Ψ_c [35]:

$$\langle \Psi | \hat{d} | \Psi \rangle = \langle \Psi_c | e\hat{r} | \Psi_g \rangle + c.c. \quad (4.2)$$

A typical spectrum is shown at the bottom of Fig. 4.1 and consists of odd harmonic orders, being separated by twice the fundamental frequency. The spectral features are directly connected to the temporal characteristics of the emission process, which is occurring every

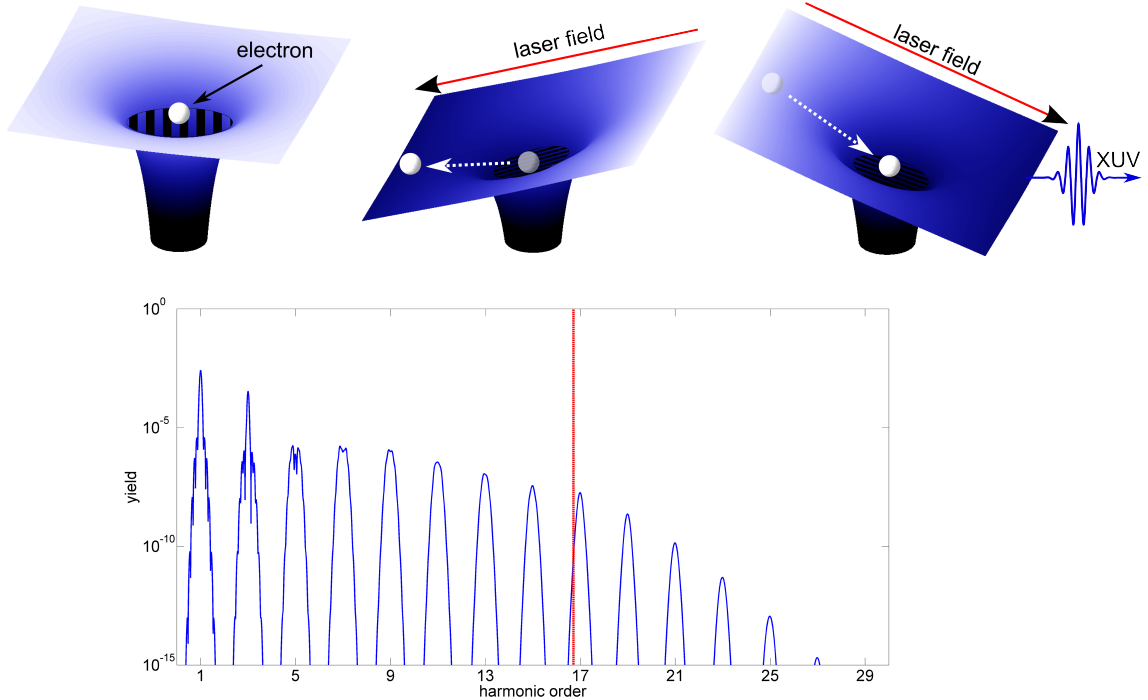


Figure 4.1: (top) Visualization of the basic assumptions of the three-step model, where the electric field of the laser bends the atoms Coulomb potential, enabling tunnel-ionization. The free electron is accelerated by the external laser field and eventually recombines with its parent ion under the emission of high-order harmonic radiation. (bottom) Exemplary high-order harmonic spectrum, showing the common spectral features connected to the generation process.

half cycle along the fundamental electric field (assuming a centro-symmetric medium). Therefore, the spectral separation of the observed harmonic orders is equal to $2\omega_0$ [2]. The exemplary frequency emission is calculated for a 30 fs pulse, centered at 780 nm with an intensity of 60 TW/cm^2 interacting with a single argon atom. Note, that the chosen intensity corresponds to the expected clamping intensity for filamentation in argon (c.f. Tab. 3). The signal amplitude can be intersected into three parts. A perturbative region at the beginning, an intermediate plateau range and a steeply declining section, dubbed the Cut-Off [1]. The highest achievable frequency is defined by the Cut-Off law, connecting the ponderomotive energy U_p (c.f. Eq. (2.11)) and the ionization potential I_p to obtain the Cut-Off energy $E_{\text{CutOff}} = I_p + 3.17U_p$ [2, 191]. The red-dotted line in Fig. 4.1 (bottom) shows the location of the Cut-Off in the harmonic spectrum.

The classical calculation of the electron's motion within the electric field of the driving laser (c.f. Eq. (4.1)) yields two solutions for each frequency emitted, meaning that there are two possible pathways for the electron leading to the same final momentum [37]. These are labeled long and short trajectory, depending on the time τ_{exc} spend during the excursion in the continuum [43]. The two different pathways of the electrons lead to different phase

contributions, the *atomic phase* and is expressed by [192, 193]:

$$\phi_{\text{atom}} = -\tau_{\text{exc}} U_p = -\tau_{\text{exc}} \frac{e^2 \vec{E}^2}{4 m_e \omega^2} \approx \alpha I. \quad (4.3)$$

This term is the reason, that the two distinct electron pathways have distinguishable phase-properties as the traveling time τ_{exc} of the electron differs for the two trajectories. Therefore their spatial as well as spectral emission characteristics can be distinguished in the experiment [42, 43, 194, 195].

4.1.2 The Lewenstein Model

The three step model allows to qualitatively understand the harmonic emission process, but quantitative results call for a more precise description of the propagation and recombination step. The Lewenstein model treats the whole process of HHG in a quantum-mechanical approach with some well grounded approximations [36]. The time dependent Schrödinger-equation (TDSE) is the foundation of the Lewenstein model, in which the evolution of the wavefunction of a shell electron is described by [36, 196]:

$$i \frac{\partial}{\partial t} |\Psi(t)\rangle = \left[-\frac{1}{2} \vec{\nabla}^2 + V(r) + x \vec{E}(t) \right] |\Psi(t)\rangle. \quad (4.4)$$

The atomic core potential is denoted as $V(r)$ and the influence of the external laser field, which is linearly polarized in x direction, is taken into account by $x \vec{E}(t)$. The possible state of the electron under observation is either a ground state $|\Psi_g\rangle$ or one of the vacuum continuum states $|\Psi_c\rangle$. The spectral emission $d(\omega)$ is derived from the time-dependent dipole-moment $d(t)$ by following the train of thought:

$$TDSE \xrightarrow{|\Psi(t)\rangle} d(t) = \langle \Psi(t) | e \hat{r} | \Psi(t) \rangle \xrightarrow{\mathcal{FT}[d(t)]} d(\omega). \quad (4.5)$$

The main approximations to handle the computation of the dipole response reduce the amount of states which have to be considered in the calculations. The ground state of the electron is assumed to be the only contributor, allowing for no field-free coupling between the ground and continuum states. The influence of the long-range Coulomb potential is neglected, since the common field strengths for HHG are sufficiently high to dominate the effect of the long-range core potential. Taking these limitations into account, the dipole-moment $d(t)$ is calculated by: [36, 197]

$$d(t) = i \int_{-\infty}^t dt' \int d^3 p \mathbf{M}^*(\vec{p} + \vec{A}(t)) \exp(-i S_{\text{sc}}(\vec{p}, t, t')) \vec{E}(t') \mathbf{M}(\vec{p} + \vec{A}(t)) + c.c.. \quad (4.6)$$

Here, the dipole-transition matrix element, describing the probability of a transition between $|\Psi_g\rangle$ and $|\Psi_c\rangle$, is denoted as \mathbf{M} . The canonical momentum is labeled as \vec{p} and

$\vec{A}(t)$ is the vector potential of the fundamental electric field. The introduced transition probabilities are calculated by [197]:

$$\mathbf{M}(\vec{p}) = i \frac{2^{7/2} (2I_p)^{5/4}}{\pi} \frac{\vec{p}}{(\vec{p}^2 + 2I_p)^3}. \quad (4.7)$$

The quasi-classical action S_{sc} divides the ionization process $\mathbf{M}(\vec{p} + \vec{A}(t))$ from the recollision $\mathbf{M}^*(\vec{p} + \vec{A}(t))$ and is calculated via [190]:

$$S_{sc}(\vec{p}, t, t') = \int_{t'}^t dt'' \left(\frac{(\vec{p} + \vec{A}(t''))^2}{2} + I_p \right). \quad (4.8)$$

Equation (4.6) has all features of the three-step model imprinted in the dipole-moment. First, the electron is set free at time t' due to the transition from the ground state $|\Psi_g\rangle$ to a continuum state $|\Psi_c\rangle$, governed by the factor $\vec{E}(t') \mathbf{M}(\vec{p} + \vec{A}(t))$. The propagation of the electron between times t' and t is represented by the quasi-classical action and manifests itself as a phase contribution to the dipole-moment [190]. The final recombination at time t is described by the term $\mathbf{M}^*(\vec{p} + \vec{A}(t))$. The resulting spectral representation $d(q\omega_0)$ of the dipole-moment, where q is an integer, for a given harmonic order $q\omega_0$ reads as [190]:

$$d(q\omega_0) = i \int_{-\infty}^{-\infty} dt e^{iq\omega_0 t} d(t). \quad (4.9)$$

The determination of the harmonic spectrum requires the solution of a four-dimensional integral for arbitrary times of ionization and recombination. In order to simplify the expression, a saddle-point analysis of the introduced phase term selects the participating contributions of Eq. (4.9). The phase is usually a rapidly oscillating term, with only a few points of a slowly changing phase contribution. These points are the most dominant contributions to the real signal and can be extracted by analyzing the derivative of the complex phase term $e^{iq\omega_0 t - iS(\vec{p}, t, t')}$ in Eq. 4.9 with respect to the ionization time t' , the recombination time t and the canonical momentum \vec{p} . The analysis yields three boundary conditions, which define constrictions for the process of HHG and are also the principles of the three step model [190]:

$$\begin{aligned} \frac{\partial}{\partial t'} (iq\omega_0 t - iS(\vec{p}, t, t')) = 0 &\implies \frac{[\vec{p} + \vec{A}(t')]^2}{2} + I_p = 0, \\ \frac{\partial}{\partial t} (iq\omega_0 t - iS(\vec{p}, t, t')) = 0 &\implies \frac{[\vec{p} + \vec{A}(t)]^2}{2} + I_p = q\omega_0, \\ \frac{\partial}{\partial \vec{p}} (iq\omega_0 t - iS(\vec{p}, t, t')) = 0 &\implies \int_{t'}^t dt'' [\vec{p} + \vec{A}(t'')] = 0. \end{aligned} \quad (4.10)$$

Since $[\vec{p} + \vec{A}(t')]^2$ needs to be negative in order to fulfill the first equation, the ionization time t' needs to have an imaginary term. The interpretation of imaginary tunneling times is a point of an ongoing debate in the field of high-harmonic generation [198–200]. The second term in Eq. (4.10) sets the requirement of energy conservation during the process of high harmonic generation, stating that the kinetic energy of the electron associated

with $\frac{[\vec{p} + \vec{A}(t')]^2}{2}$ together with the ionization energy I_p yields the harmonic radiation at $q\omega_0$. The third restriction limits the emission process spatially, requiring that the displacement due to the acceleration in the field between the ionization time t' and the recombination time t must be zero. In other words, the electron needs to return to its parent ion in order to emit high-order harmonic radiation. The additional degree of detail, compared to the three step model, slightly modifies the Cut-Off law to $E_{\text{CutOff}} = 1.3I_p + 3.17U_p$, where the difference stems from the fact, that the ionized electron is set free at a slight offset towards the atomic center [36, 201].

4.1.3 Phase Matching - The Macroscopic Response

Phase matching is the investigation of coherence properties of a large scale of single emitters. If all point sources along the generating medium interfere constructively, total phase matching is achieved [191, 192]. Therefore, not only the microscopic response of the medium needs to be optimized and considered during HHG but also the macroscopic build-up. In order to evaluate the phase mismatch, the contributions of different phase terms need to be evaluated. The quality of the phase matching can be estimated in a vectorized representation, where each phase has a corresponding wave-vector $\vec{k} = \vec{\nabla}\phi$ [196]. The contributions can be set apart into [37, 191, 192, 202, 203]:

- **The Geometric Phase:** The phase $\phi_{\text{geo}}(r, z)$ is connected to the focusing properties of the fundamental beam and calculated as [192, 204]:

$$\phi_{\text{geo}}(r, z) = -q \left(\arctan \left(\frac{z}{z_r} \right) + \frac{\pi r^2}{\lambda R(z)} \right). \quad (4.11)$$

The first term is referred to the Gouy-phase, which solely describes the phase-evolution on-axis. The second term includes the influence of the radial phase along the curved wavefront $R(z) = z [1 + (z_r/z)^2]$.

- **Dispersion of Neutrals:** The dispersion properties of the medium influence the quality of phase matching for all kinds of frequency conversion effects, as the pump and signal waves experience different group-velocities along a dispersive medium. The refractive index n_q at the q^{th} harmonic order is directly connected to the susceptibility χ via $n_q = \sqrt{1 + \chi_q} \approx 1 + \chi_q/2$. The neutral medium leads to a phase mismatch $\Delta k_{\text{nt}} \approx \frac{q\omega_0}{2c} (\chi(q\omega_0) - \chi(\omega_0))$, which is related to the differing dispersion properties of the medium at frequencies ω_0 and $q\omega_0$ [196, 205, 206].
- **Dispersion of Electrons:** The ionization of the medium induces a dispersion-related phase-term connected to the generation of free electrons (c.f. Eq. (2.13)) [196, 206, 207]:

$$\Delta k_{\text{el}} = (q^2 - 1) \frac{\omega_{\text{plasma}}^2}{2cq\omega_0}. \quad (4.12)$$

Its dependency on ω_{plasma}^2 results in a direct connection between the wave-vector discrepancy and the amount of free electrons $\Delta k_{\text{el}} \propto \rho_e$ (c.f. Eq. (2.15)).

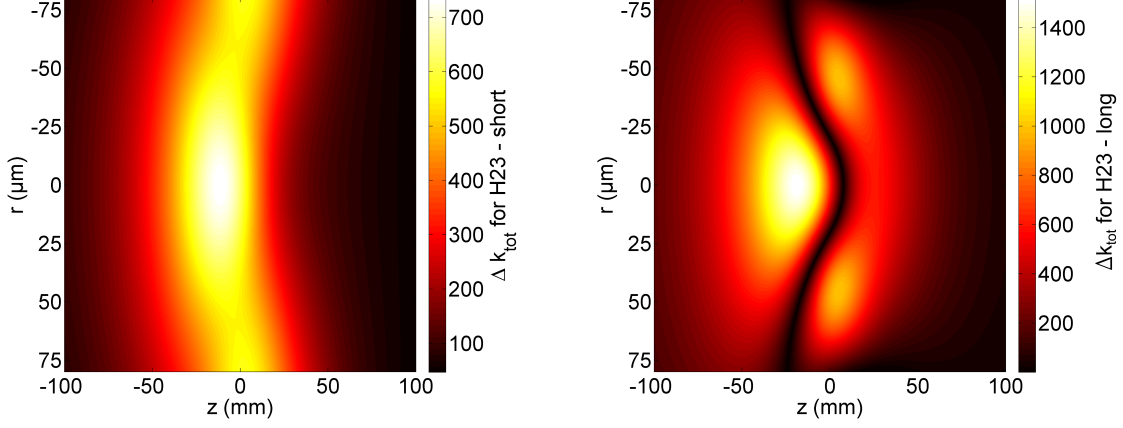


Figure 4.2: Exemplary map of the wave-vector mismatch along the spatial coordinates r and z of a focused Gaussian beam.

- **The Atomic Phase:** ϕ_{atom} is directly linked to the microscopic generation process of HHG [194]. Contrary to the perturbation regime, where the bound electron immediately follows the external electric field, the HHG-process carries an internal phase originating from the fact, that the electron is propagating in an external field during the process of HHG. The atomic phase is expressed as [197]:

$$\phi_{\text{atom}}(r, z, t) = -\tau_{\text{exc}} U_p = -\tau_{\text{exc}} \frac{e^2 \vec{E}^2(r, z, t)}{4 m_e \omega^2(t)} \underset{\substack{\approx \\ \frac{d\omega}{dt} \text{ small}}}{\approx} -\alpha_{1,s} I(r, z, t). \quad (4.13)$$

The influence of the long and short electron trajectories is implemented by a trajectory dependent phase-slope $\alpha_{1,s}$. The corresponding wave-vector $\vec{k}_{\text{atom}} = \vec{\nabla} \phi_{\text{atom}} \approx -\alpha_{1,s} \vec{\nabla} I$ is directly coupled to the spatio-temporal structure of the fundamental pulse's intensity $I(r, z, t)$.

Phase matching of a harmonic order q is achieved when the sum over all wave-vectors corresponds to the q -scaled wave-vector of the fundamental frequency: $q\vec{k}_1 = \vec{k}_q$. The phase mismatch is affiliated to a wave-vector mismatch $\Delta\phi_{\text{total}} = \Delta\vec{k}_{\text{total}}z = (\vec{k}_q - q\vec{k}_1)z$ [196]. The implementation of the single contributions results in:

$$\Delta k_{\text{total}} = |\vec{k}_q - |\vec{k}_{\text{geo}}(r, z) + \vec{k}_{\text{atom}}| + \Delta k_{\text{nt}} + \Delta k_{\text{el}}|. \quad (4.14)$$

If no phase matching is achieved, the mismatch is associated to a coherence length by $L_{\text{coh}} = \pi/\Delta k_{\text{total}}$.

The intensity distribution of the fundamental beam is correlated to the value of Δk_{total} resulting in a spatial dependency that is visualized by phase matching maps. Figure 4.2 displays the total wave-vector mismatch Δk_{total} between the fundamental field and the harmonic field of the 23rd harmonic order for a pulse with a peak intensity of 1×10^{14} W/cm², a central wavelength of $\lambda=800$ nm, a pulse duration of 10 fs and a confocal parameter

b=75 mm interacting with 50 mbar of argon gas. The mismatch is displayed for contributions of the short (a) as well as long (b) trajectories, whose atomic-phase slope differs by a factor of $\alpha_1 = 5\alpha_s$ in this exemplary case [45]. Low values of Δk_{total} correspond to dark colors in the given color-scaling and indicate good phase matching. Positive (negative) values of z denote a position of the medium after (before) the focal point. The short trajectory contribution in panel (a) is phase-matched at positive propagation distances close to the optical axis ($r=0 \mu\text{m}$, $z \geq 30 \text{ mm}$). Contrarily, the contributions from the long trajectories are favorably phase-matched at negative propagation distances along off-axis positions [208]. The phase matching characteristics of the long and short electron trajectories result in a differing spatial profile in the far field, where the radiation connected to the short trajectories is emitted at an on-axis position as opposed to the radiation originating from long trajectories, which is emitted at an off-axis position [42, 43].

The amplitude of a certain harmonic order is not only dependent on the phase matching conditions, but also on the absorption properties and the length L_{med} of the medium. The absorption length is defined as $L_{\text{abs}} = 1/(\rho_{\text{nt}}\sigma_{\text{abs}})$ with the frequency dependent ionization cross-section σ_{abs} and estimates the length over which no significant re-absorption effects occur and the radiation propagates undisturbed. The detected harmonic signal N_{out}^q hereby scales as [209]:

$$N_{\text{out}}^q = \rho^2 d_q^2 \frac{4L_{\text{abs}}^2}{1 + 4\pi^2(L_{\text{abs}}^2/L_{\text{coh}}^2)} \left[1 + e^{-\frac{L_{\text{med}}}{L_{\text{abs}}}} - 2 \cos\left(\frac{\pi L_{\text{med}}}{L_{\text{coh}}}\right) e^{-\frac{L_{\text{med}}}{2L_{\text{abs}}}} \right]. \quad (4.15)$$

The length of the medium is denoted as L_{med} and the dipole strength of the q th harmonic order is labeled as d_q .

4.1.4 Transient Phase Matching

So far, only the spatial influence of the phase mismatch has been observed. These phase matching conditions not only differ along the spatial coordinate of the interaction region, but also change drastically along the temporal envelope of the fundamental pulse [210]. The emission of harmonic radiation therefore can favor certain positions along the temporal shape of the pulse, which do not have to coincide with the peak of the pulse envelope [211–214]. This effect is called transient phase matching (TPM) and is investigated for different positions along z where the radial influence is reduced to the on-axis ($r=0$) contribution along this thesis. Therefore, the wave-vector connected to the geometrical phase $\vec{k}_{geo} = \frac{\partial}{\partial z} \phi_{geo}$ reduces to the Gouy-phase and shows no temporal dependency.

Two of the introduced contributions show a strong variation along the temporal pulses envelope. First, the wave-vector of the atomic phase \vec{k}_{atom} is constantly changing with a linear dependence on the intensity and is expressed by:

$$\vec{k}_{\text{atom}}(z, t) = \frac{\partial}{\partial z} \phi_{\text{atom}}(z, t) = \alpha \left[I(z, t) \frac{2z}{z_r^2 + z^2} \right] \quad (4.16)$$

Again, the two contributions of the long and short trajectory in the plateau region can be distinguished by their varying atomic phase contributions.

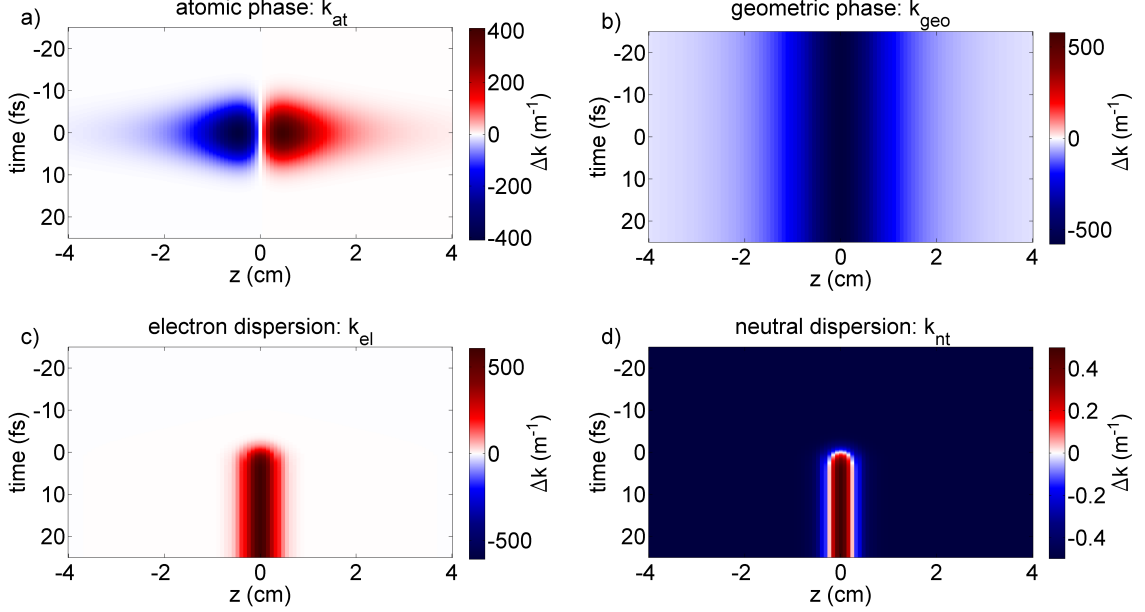


Figure 4.3: Wave-vector mismatch induced by the (a) the atomic phase, (b) the Gouy-phase term, (c) the dispersion of free electrons and (d) the dispersion of neutral atoms. The k -values correspond to a focused ($f=2$ m) Gaussian beam with $I_0 = 100$ TW/cm², $\tau = 10$ fs and $\lambda_0 = 780$ nm.

Second, the phase matching contribution of the free electrons Δk_{el} is directly connected to the density of free electrons $\rho_e(r, t)$, which is rapidly changing along the pulse. This feature has been used to gate the XUV-emission process by using the rapidly changing phase matching properties Δk_{el} from the free electrons [215–217]

Fig. 4.3 displays the evolution of the time-dependent wave-vector mismatch for each contribution in dependence of the propagation distance for a focused beam with a 2 m focal length, a peak intensity of 1×10^{14} W/cm², a wavelength of $\lambda_0 = 780$ nm and a pulse duration of $\tau = 10$ fs. Since the sign of the wave-vector mismatches are important, a color-coding is chosen in which positive mismatches are displayed in a red color-gradient and negative contributions are depicted in a blue color-gradient. The considered harmonic order is the 21st with a constant averaged slope of the atomic phase of $\alpha = 25 \times 10^{-14}$ cm²/W [194], corresponding to the short electron trajectory.

The wave-vector of the atomic phase evolution in panel (a) shows a changing sign as the focal point is passed. It is connected to Eq. 4.16 and negative for $z < 0$ and positive for $z > 0$ [218]. The contribution of $\vec{k}_{\text{geo}} = \frac{\partial}{\partial z} \phi_{\text{geo}}$ (b) is always negative since the Gouy-phase is constantly decreasing along z and has its strongest power at $z = 0$ [196]. The influence of the dispersion of the free electrons is shown in panel (c) and is asymmetric with respect to the temporal axis as the atoms are ionized along the temporal pulse shape (c.f. Figs. 2.4 and 3.14). The same is true for the dispersion of the neutral atoms in (d), which shows only a minor effect on the phase matching. Consequently, only the influence of $\Delta \vec{k}_{\text{geo}}$, $\Delta \vec{k}_{\text{atom}}$ and $\Delta \vec{k}_{\text{el}}$ need to be considered in the following.

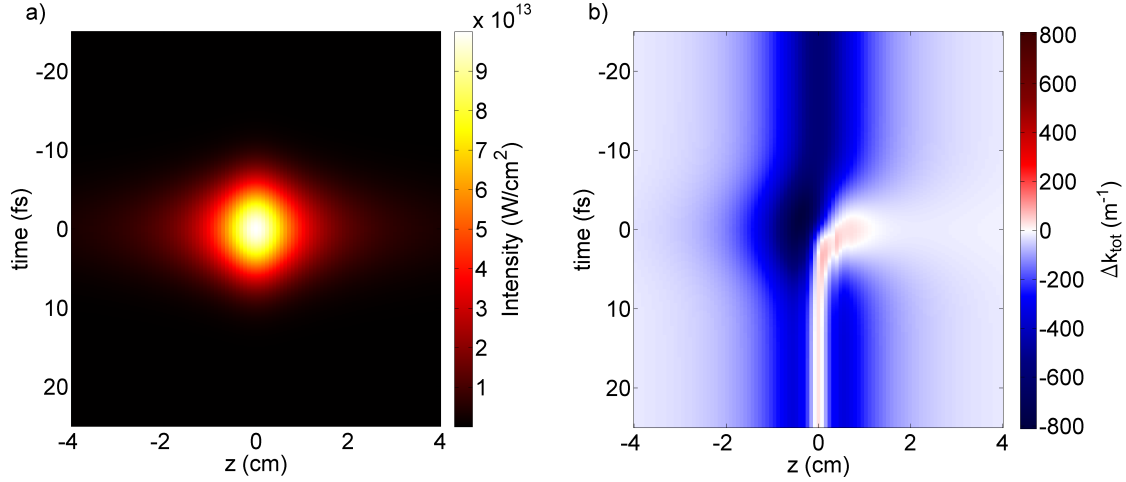


Figure 4.4: Spatio-temporal distribution of a focused Gaussian beam with the same parameters as in Fig. 4.3. (b) Phase-evolution originating from the summed single contributions in Fig. 4.3. The emission of harmonic radiation is favored at $z = 0$ along the trailing part of the pulse and at $z > 0$ at the temporal peak.

Figure 4.4 depicts the total phase mismatch Δk_{total} for the conditions of Fig. 4.3 as well as the intensity distribution along the focus. The three contributions from Fig. 4.3 balance each other out for specific points along the spatio-temporal evolution of the fundamental pulse and therefore phase-match distinct emission points along the temporal shape of the fundamental pulse. For $z < 0$ cm, the phase matching is dominated by the adding contributions from the atomic- and geometric phase. Both have a negative sign (c.f. Fig. 4.3) and add up to a widespread negative displacement of the wave-vector depicted in blue in Fig. 4.4 (b). The trailing edge of the pulse ($t > 0$ fs) shows good phase matching exactly at the focal position at $z = 0$ cm. Here, $\Delta \vec{k}_{\text{atom}} = 0$ and the positive electron dispersion is able to compensate the negative Gouy-mismatch. For $z > 0$ cm, the positive contribution of $\Delta \vec{k}_{\text{atom}}$ compensates $\Delta \vec{k}_{\text{geo}}$. The phase matching for positive z -values in Fig. 4.4 (b) reveals that the temporal peak of the pulse is phase-matched for $z > 0$ cm. The changing Δk_{total} along the pulse shape can leave clear fingerprints in the emitted high-order harmonic spectrum.

Increasing the peak intensity of the pulse non-linearly increases the influence of free electrons to the spatio-temporal phase matching in Fig. 4.4. The point of positive phase-matching therefore shifts towards the front of the pulse leading to an adiabatically changing Δk_{total} along the temporal pulse shape. Adiabatic spectral splitting has been observed in highly ionized gases utilizing the strongly varying electron density and its interplay with the atomic phase contribution as an explanation for multiple phase-matched emission points along the Gaussian pulse shape. [213]. This has been reported to result in a pressure-dependent spectral splitting in the high-order harmonic spectrum [213, 219]. The transient phase matching can also favor certain trajectories along the pulses shape which then can be traced in the emitted high-order harmonic spectrum [214, 220].

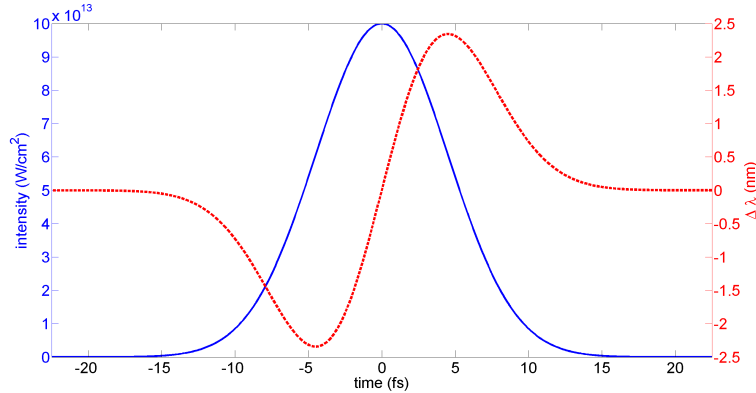


Figure 4.5: Induced shift of the wavelength of the 15th harmonic order generated in argon originating from the atomic phase contribution. The pulse duration is 7.5 fs at a central wavelength of 800 nm with a peak intensity of 100 TW/cm². The harmonic radiation experiences a blueshift (redshift) along the leading (trailing) part of the pulse envelope.

4.1.5 Spectral Properties of HHG

The spatial gradient of the introduced phase contributions determines the degree of phase matching along the interaction volume. The temporal gradient of the phase however defines the instantaneous frequency and influences the spectral properties of the emitted high-order harmonic radiation [220]. Recalling the findings of Sec 4.1.3, ϕ_{atom} shows a strong dependence on the temporal evolution of the fundamental field. Therefore, the atomic phase contributes to a frequency modulation in HHG, as the phase is dependent on the intensity $\phi_{atom} \propto -\alpha I(t)$ [197].

The induced frequency modulation $\omega_{atom} = -\alpha \frac{\partial}{\partial t} I(t)$ is illustrated in Fig. 4.5. In the leading part of the pulse, blue spectral components are generated whereas red spectral components are originating from the falling edge of the pulse [220]. The induced spectral shift is able to result in a spectral separation of the electron trajectory pathways, as the contribution belonging to the long trajectory shows a stronger frequency shift $\Delta\omega \propto \alpha$ than the short ones [42, 220, 221].

The experimental observation of the red-shifted components originating from the falling edge of the pulse is strongly limited since the atomic phase contribution requires high intensities. This leads to ionization of the medium along the rising edge of the pulse, reducing the amount of emitters present along the falling edge of the pulse envelope. If the depletion is avoided, usually the intensity is not sufficient to induce a significant red-shift. Therefore the observation of the atomic phase contribution from the falling edge of the pulse is limited to ultrashort pulses of few optical cycles [1].

Aside from the atomic-phase, the strongly varying electron density $\phi_{el}(t)$, can lead to good phase matching conditions along certain points of the pulse envelope (c.f. Fig. 4.4). The temporal emission properties are imprinted into the spectrum and can result in an adiabatic splitting in the harmonic spectrum [213]. The radiation close to the Cut-Off is

usually not influenced by these effects, since the strongest variation of the free electron density occurs on the rising edge of the fundamental pulse, where the harmonic orders belonging to the plateau are generated.

Moreover, the propagation of the fundamental field is able to influence HHG, as the fundamental spectrum changes due to the influence of SPM and free electrons (c.f. Sec. 2.2). Hence, any change of the fundamental spectrum during propagation also influences the appearance of the harmonic spectrum. The shift of the fundamental wavelength by $\Delta\lambda_0$ imprints on the q^{th} harmonic order as $\Delta\lambda_q = \Delta\lambda_0/q$ [196]. A variation of the fundamental wavelength not only shifts the spectral properties but also strongly influences the efficiency of the HHG process, scaling rapidly with $\lambda^{-5.5}$ [222, 223]. This is connected to the increased spreading of the propagating electron wave-packet in the continuum due to an elongated trajectory along the increased length of the laser cycle, effectively reducing the efficiency of the recombination process [222].

A decreasing pulse duration results in an increasingly unstructured spectrum, as the number of emission events along the driving pulse decreases [2]. A pulse duration in the vicinity of a few optical cycles results in a dependence of the spectral properties of the high-order harmonic radiation upon the carrier-envelope phase (CEP), making harmonics a sensitive tool for not only the envelope evolution but also the electric field distribution below the envelope [2, 224].

Finally, the Cut-Off frequency is directly connected to the fundamental pulses intensity $I(r, z, t)$, the ionization potential I_p and quadratically dependent on the driving wavelength λ_0 . In order to convert to the highest possible frequencies, a strong pulse with a long driving wavelength (usually in the range of $\lambda_0 = 1800\text{-}4500$ nm) has to interact with light noble gases such as He or Ne [225].

During filamentation all the introduced connections influence the harmonic radiation emitted from the filament itself at some position of the filament. The experimentally observed self-compression results in the generation of an ultrashort pulse resulting in an increasingly unmodulated spectrum. The self-steepening dynamics can strongly alter the instantaneous frequency of the harmonic emission (c.f. Fig. 4.5). The intensity evolution along the filament can influence the Cut-Off position as well as the transient phase matching via the generation of free electrons. HHG indeed appears to be an intriguing tool for the evaluation of the complex spatio-temporal dynamics inside the filament, if analyzed properly. The extraction and separation of these dynamics from directly emitted high-order harmonic radiation will be subject of the upcoming section.

4.2 The Experimental Setup

The experimental setup has been modified to enable the detection of XUV-radiation (c.f. Sec. 3.3). Commonly in the field of HHG, this setup is labeled as a semi-infinite gas-cell (SIGC) and operated at low pressures in the vicinity of 1-100 mbar [41, 42]. Here, the

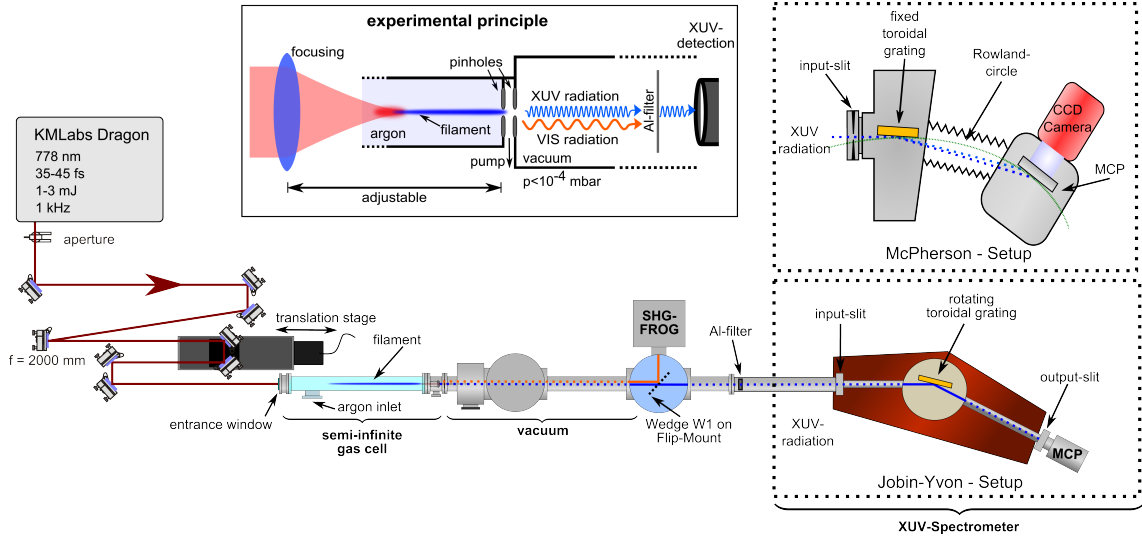


Figure 4.6: Experimental setup, adding the observation of directly emitted high-order harmonic radiation from the filament by using a XUV-spectrometer. In comparison to the pulse detection setup, the pressure after the truncating stage is kept below 1×10^{-4} mbar. The bottom sketch summarizes the detection procedure, as the visible pulse properties, such as the spectrum and the pulse shape are detected together with the XUV-radiation.

filamentation cell served as the generation chamber and has been operated at a pressure of 1 bar [80, 81]. The experimental setup consisting of either the fundamental pulse or the XUV detection is sketched in Fig. 4.6. The truncation setup has been operated in the same manner as in Sec. 3.3.2 and the SHG-FROG scheme could optionally be used through the insertion of a wedged fused-silica plate (W1) into the beam path, enabling the observation of the fundamental pulse. The evacuated area after the second pinhole has been operated at pressures below 1×10^{-4} mbar in order to avoid re-absorption of the generated high-order harmonic emission. For the HHG detection setup, the XUV-radiation has been separated from the fundamental beam by a 100 nm thick aluminum filter. Depending on the desired application, the harmonic radiation has been detected by either one of the two depicted spectrometers. The McPherson setup (Type: 248/310) images the diffracted spectral signal via a reflection from a toroidal grating (300 groves/mm) on a MCP-phosphor screen and detects the signal via a water cooled CCD-camera (Andor-iDus). The camera is positioned tangentially to the Rowland-circle on which the input signal is imaged [226]. This allows to simultaneously detect multiple harmonics on the CCD-camera ($\Delta\lambda \approx 20$ nm at $\lambda_0 = 42$ nm) with an average acquisition time below one second per shot. This way, a quick scan of the evolution of the harmonic radiation along the femtosecond filament is accessible. In order to change the spectral range of detection, the camera needs to be translated along the Rowland-circle.

The Jobin-Yvon setup (Type:LHT-30) enables the observation of a wide range of harmonic orders, but relies on the scan of the signal by rotating a toroidal grating (550 groves/mm). The signal is analyzed by a multi-channel-plate (MCP) detector, which converts the XUV-

radiation into a detectable current through an electron avalanche in the highly charged detector material. The use of an entrance- and exit-slit (height: 2 mm, width: 1 mm) enables a good spectral resolution of the harmonic radiation.

4.3 Direct High-Order-Harmonic Generation Connected to Pulse Dynamics

The experimentally measured pulse dynamics from Sec. 3.3 can be used together with the observations of directly emitted high-order harmonic radiation. The presented results of HHG have been recorded alongside with the observations of the fundamental pulse evolution in Fig. 3.11 and can therefore be directly linked to these findings. Note, that the measurements of the fundamental pulse properties and the directly emitted harmonic radiation result from the same acquisition date and have been performed under the identical experimental conditions, but were not recorded simultaneously.

First, the experimental results will be discussed, concentrating on the spectral properties of the high-order harmonics with a focus on associations to the microscopic response. The macroscopic response will be discussed in an additional part, where the adaption of the common phase matching formalism towards the special case of filamentation will play a crucial role.

4.3.1 Experimental Results

The dependency of the generated harmonic radiation upon the position along the femtosecond filament is shown in Fig. 4.7. For the given parameters of an initial pulse duration of 47.2 fs, a pulse energy of 0.9 mJ focused by a $f=2000$ mm curved mirror, the high-order harmonic radiation starts to emerge at a position of 195 cm which is connected to the end of the defocusing stage I and vanishes at a position of 215 cm, located deep in the propagation stage III along the filament. The lower-order harmonics (17th and 19th in this case) appear at slightly earlier positions than the highest orders. After a few centimeters of propagation, the harmonic signal splits into a red- as well as blue-shifted component. The splitting starts at a position of $z \approx 200$ cm and is observable until a point of 210 cm. The blue dotted line, shown in Fig. 4.7, takes the variation of the fundamental spectrum through the evaluation of its spectral center-of-gravity (CoG) into account (c.f. Fig. 3.8). It sketches the dependency of the 19th harmonic order on the CoG of the fundamental spectrum via the simplified relation $\Delta\lambda_{CoG}/q$. The resulting evolution verifies a simple relation of the blue-shifted harmonic branch to the evolving fundamental spectrum.

A comparison with the findings from the observation of the pulse propagation allows to draw preliminary conclusions on the connection between the observed harmonic spectrum and the dynamic pulse-evolution. The experimentally observed pulse splitting sets in at a position close to $z = 200$ cm, which coincides with the beginning of the spectral splitting in the harmonic spectrum (c.f. Fig. 3.11). The spectral component of each harmonic order, which is shifting into the blue spectral direction mimics the spectral modulation of the fundamental pulse, as it is evident in Fig. 4.7. At position 210 cm, the harmonic spectrum becomes unstructured, indicating that the driving pulse consists of only a few optical cycles, which is in good agreement with the results found in Fig. 3.11, where the pulse duration drops to $\tau < 7$ fs. According to Sec. 4.1.5, the red-shift observed in the harmonic spectrum can be connected to either a changing fundamental frequency or a strong falling slope of the pulse envelope. Both assumptions will be evaluated in the following.

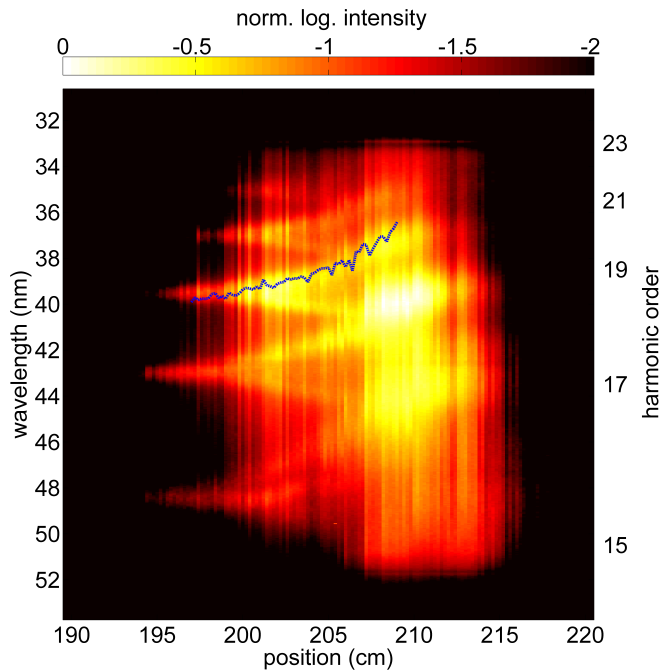


Figure 4.7: Emitted HHG-spectrum as a function of the position along a femtosecond filament. The harmonic radiation shows a spectral splitting of the initial frequency of each generated harmonic order into blue- and red-shifted spectral branches. The blue-dotted line connects the CoG of the fundamental spectrum to the harmonic spectrum of the 19th harmonic order via $\lambda_{19} = \lambda_{CoG}/19$.

4.3.2 Discussion - The Frequency Red-Shift

In this section, the spatio-temporal dynamics of the fundamental pulse are used to narrow down the underlying mechanism leading to the splitting in the high-order harmonic spectrum. Additionally, the Lewenstein-model is applied to connect the calculated single-atom response to features of the fundamental pulse. The code for the efficient numerical determination of the harmonic spectrum according to the Lewenstein-model is an open-source code and reliably handles the microscopic response of the medium [227–229].

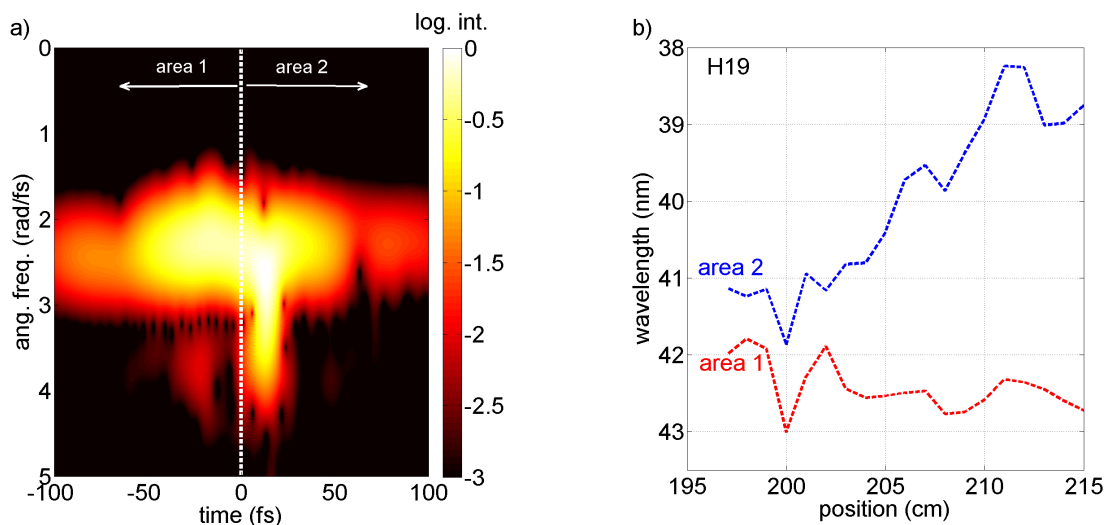


Figure 4.8: (a) Calculated X-FROG trace of the experimentally reconstructed pulse shape at $z = 208$ cm. The white line displays the border for the two areas of spectral integration which determines the CoG for the two sub-pulses. (b) Scaled evolution of the CoG from the two areas. A spectral separation between the leading and trailing pulse is observed.

Influence of the Fundamental Spectrum

Figure 4.7 allows to conclude, that the evolution of the fundamental spectrum has a direct connection towards spectral features in the HHG-spectrum. It has also been concluded in the previous section that the splitting in the high-order harmonic spectrum coincides with the fundamental pulses splitting appearing between 200 cm and 220 cm. This suggests that the changing CoG of each sub-pulse structure of the fundamental beam can influence the harmonic emission individually and result in the observed phenomena. The findings of Sec. 3.3.5 allow to conclude that the leading and trailing pulse features show significantly differing frequencies located beneath the envelope of each sub-pulse. Fig. 4.8 (a) recalls one exemplary X-FROG trace (c.f. Fig 3.19), which results from the experimentally reconstructed spectral intensity and phase at $z = 212$ cm. The two sub-pulses are distinguished by the time $t=0$ fs. Here, the reconstructed pulse-shape is centered and the sub-pulses are shifted to respective positive and negative times in the experimental pulse reconstruction (c.f. Fig. 3.10). Summing up the spectrum for $t > 0$ fs and $t < 0$ fs therefore yields the respective CoG of each sub-pulse structure. The areas of integration are visualized in Fig. 4.8 (a) and denoted as area one ($t < 0$ fs) and area two ($t > 0$ fs). This approach is used to qualitatively describe the connection between the changing fundamental and the generated spectrum at the q^{th} harmonic order by applying the relation $\lambda_q = \lambda_0/q$.

The resulting evolution of the connected high-order harmonic wavelength is shown in Fig. 4.8 (b) for the case of $q=19$. The frequency up-conversion yields a shift of the blue-dotted part of the spectrum, which is connected to an integration along area two. The red-dotted components belong to area one and vary less drastically than the blue ones. A comparison with the measured HHG-spectrum in Fig. 4.7 concludes that the evolution of both spectrally shifted parts follows the measured high-order harmonic spectrum qualitatively. The spectral modulation of the split pulses can indeed be a source of the high-order harmonic splitting, which will be put to test by using the analyzed SHG-FROG data as an input

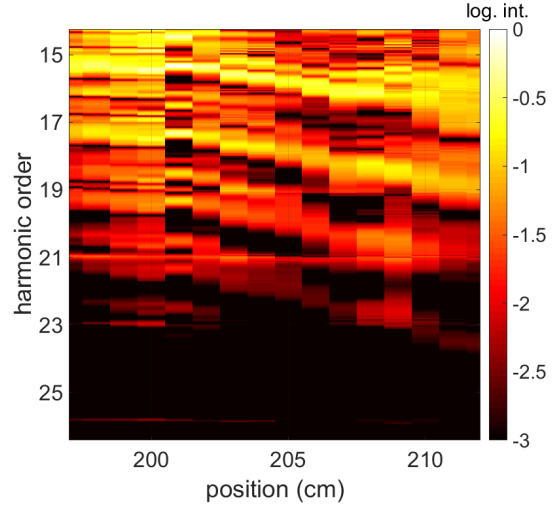


Figure 4.9: Harmonic spectrum calculated by the Lewenstein-model using the experimentally retrieved pulse shapes as an input.

for simulations of the HHG-process. The code which is used along this thesis applies the Lewenstein-model to calculate the dipole response and correspondingly the harmonic spectrum (c.f. Sec. 4.1.2). The influence of the fundamental pulses evolution on the microscopic response can be evaluated precisely with this method. Figure 4.9 shows the theoretically obtained harmonic spectrum for the experimentally retrieved pulse shapes from Sec. 3.3.3. The shift of the harmonic spectrum to higher frequencies can be reproduced very well with the given input shapes, but the evolution of the red-shifted frequency components remains completely undisclosed. Consequently, the different carrier frequencies of the two sub-pulse structures do not result in the observation of the harmonic splitting. By up-converting the changing CoG of the sub-pulses in Fig. 4.8 (b), the whole process of HHG and its inherent conversion efficiency is neglected [222]. The scaling of the HHG conversion efficiency with respect to the fundamental wavelength reads as $\lambda^{-5.5}$ and leads to a further reduction of the conversion efficiency of the red-shifted spectral content. This is the reason for the missing red-shifted components in the theoretical results. The spectral gap $\Delta\lambda$ between the two sub-pulses in addition to the difference in their respective intensities ΔI effectively suppresses HHG from the leading pulse-feature compared to the trailing one. The respective differences are $\Delta\lambda_{max} = 74.8 \text{ nm}$ and $\Delta I = 0.75 \times 10^{14} \text{ W/cm}^2$, resulting in an estimated harmonic signal ratio of ≈ 1000 between the two pulses. The findings of Fig. 4.9 reveal, that the reconstructed pulse shapes of the experimental observation of the spatio-temporal dynamics do not carry the necessary features to explain the splitting in the high-order harmonic spectrum, as the simulated HHG spectra using the reconstructed pulse-shapes could not reveal a spectral red-shift in the harmonic spectrum. The harmonic radiation is either sensitive to a feature of the pulse's spatio-temporal evolution, which can not be captured by the used SHG-FROG setup or the reconstruction of the pulses shape is lacking access to information which the HHG-process experiences, e.g. a modification

of the guiding medium's properties [132], which cannot be tracked with the present code.

Influence of Self-Steepening

Comparing the simulated pulse evolution with the experimental findings, one major discrepancy is the representation of the pulse's falling edge by the SHG-FROG device (c.f. Figs. 3.13 (b) and 3.19). The self-steepening dynamics connected to the rapidly decreasing envelope are an essential contribution to the numerically observed self-shortening dynamics along the propagation stage III of the filament. This section aims at the determination of the propagating pulse's falling slope steepness through an analysis of the detected red-shift in the high-order harmonic spectra. The last section concluded that the red-shifted branch of the harmonic spectrum shows no imminent connection to the CoG of the fundamental spectrum and that the reconstructed pulse-shape do not carry the necessary information to explain the red-shift in the harmonic spectrum which strongly suggests that the missing information of the falling slope in the reconstructed pulse-shapes (c.f. Fig 3.13 (b)) is the missing link to the unobserved red-shift in Fig. 4.9.

To evaluate the frequency-shift more precisely and to decouple the red-shifted signal from the blue-shifted spectral components, the harmonic spectrum at each position along the propagation direction is re-shifted by the respective CoG-value of the fundamental spectrum to obtain the evolution of the corrected harmonic spectrum along the filament. The transformed data-set is given in Fig. 4.10 (left), where the y-axis now refers to the harmonic order of the fundamental spectrum's CoG at each position. This means that for each position along the filament,

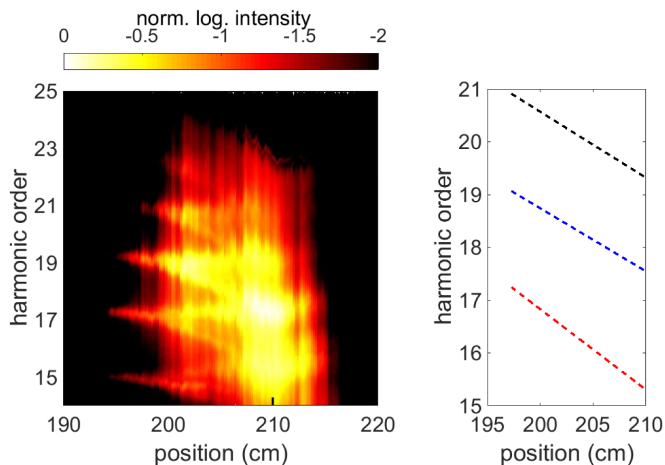


Figure 4.10: Re-shifted HHG-spectrum, where the evolution of the fundamental frequency, as discussed in Fig. 4.7, is corrected. The splitting now concentrates into the red spectral region. The extracted spectral red-shift is displayed in the left hand side for the harmonic orders 17-21.

the spectrum is now referring to a harmonic order determined by the respective CoG of the fundamental spectrum. As a result of the re-centering, the observed splitting in the high-order harmonic spectrum exposes to be a spectrally one sided phenomena focusing solely on the red-shift. The amount of the observed red-shift is extracted and depicted in Fig. 4.10 (right). With reference to the frequency axis, the splitting appears with a linear dependency on the propagation distance along the filament. A comparison with the key values from the fundamental pulse propagation allows to draw preliminary conclusion on the linking between the observed harmonic spectrum and the pulse's dynamic evolution along the filament. The experimentally observed pulse splitting sets in along stage II of

the refocusing cycle (c.f. Fig. 3.11) at a position close to 200 cm, which coincides with the beginning of the spectral splitting in the harmonic spectrum. At position 210 cm, the harmonic spectrum becomes unstructured, indicating that the driving pulse consists of only a few optical cycles. This is in good agreement with the previous experimental results monitoring the pulse envelope in Fig. 3.10 which show that the pulse duration minimizes at 212 cm.

The harmonic spectrum is not only sensitive to the pulse duration, but also to the shape of the envelope as the instantaneous frequency of the atomic phase is related to $\partial/\partial t(I(t))$. Therefore spectral features connected to the increasing self-steepening of the pulse along the femtosecond filament can be detected. In order to simulate the isolated influence of a steepened pulse profile on the HHG process during filamentary propagation, certain assumptions have been applied:

- As the pulse splits into two separated sub-structures, only the trailing intense peak is assumed to contribute significantly to the HHG process. This approximation is validated by the simulations in Fig. 4.9, where no influence of the leading pulse structure can be seen in the emitted harmonic radiation.
- The central frequency is assumed to be directly connected to the CoG of the experimentally measured fundamental spectrum. The calculated X-FROG traces in Fig. 3.19 show, that the trailing part of the experimental pulse carries frequency components ranging from 2.2 to 4 rad/fs, corresponding to a wavelength span between 850 nm and 470 nm. The use of the measured spectrum instead of the results from the X-FROG traces is to be preferred, since the detection of the fundamental spectrum is not limited by the shortcomings of the pulse reconstruction setup (c.f. Sec. 3.3.5) and does not suffer as drastically from the underestimation of the blue spectral components.
- The self-steepening is assumed to act asymmetrically along the pulse shape, meaning that the modification of the refractive index along the temporal structure during propagation results in the trailing part catching up with the peak of the pulse and also leads to the leading part moving away from the peak of the pulse. This will be implemented by an artificial asymmetry-factor.
- A critical value for the simulations is the fundamental pulse's intensity. From the experimental data, the highest observed harmonic order is taken as an input for the relation $E_{\text{CutOff}} = 1.3I_p + 3.17U_p$. Since U_p is directly proportional to the intensity, a value can be extracted for each position along the filament, where harmonic radiation is emitted. Note, that the extraction of the correct intensity is a challenging task itself and will be covered in detail in an upcoming section.

The artificial steepening of the isolated temporal shape is done by the implementation of an asymmetry-factor ζ_a , which modifies the initial pulse's envelope by:

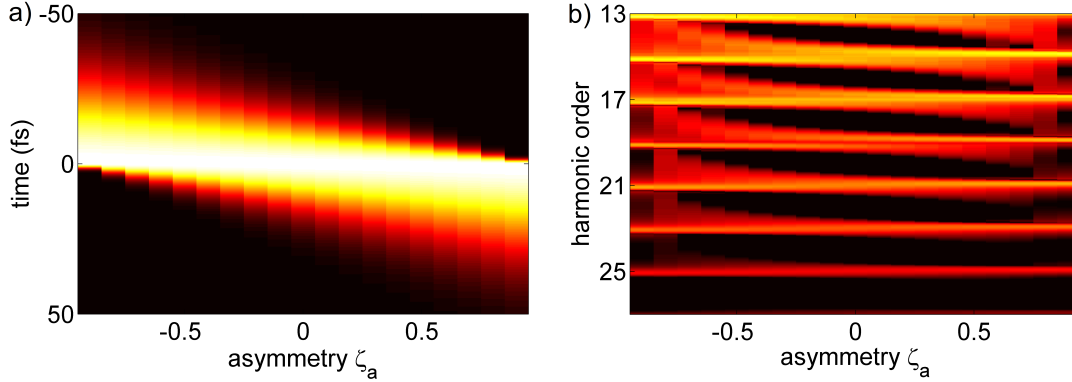


Figure 4.11: Simulations showing the connection between (a) the fundamental pulse's shape and (b) the emitted high-order harmonic spectrum for a pulse with a changing asymmetry (25 fs, 800 nm, 100 TW/cm²). Negative (positive) values of ζ_a steepen the falling (rising) edge and induce a red-(blue-)shift in the harmonic spectrum

$$A = \exp \left[- \left(\frac{t}{\tau + \tau \zeta_a \text{sign}(t)} \right)^2 \right]. \quad (4.17)$$

The pulse is centered around $t=0$, which leads to a stretching of the leading part of the pulse and a compression of the trailing part of the pulse for negative values of ζ_a . The variable can take any number in the range of ± 1 . The effect of a varying asymmetry-factor ζ_a on the harmonic spectrum, which is generated by a 25 fs long pulse, centered at 800 nm with a peak intensity of 1×10^{14} W/cm² is displayed in Fig. 4.11. Panel (a) shows the changing shape of the fundamental pulse in dependence of ζ_a . A negative value of ζ_a corresponds to a steepening of the falling edge of the temporal shape, whereas a positive value steepens the rising edge. In Fig. 4.11 (b), the simulated high-order harmonic spectrum is shown with respect to the changing ζ_a . A steep falling edge shifts the generated frequency components of each harmonic order in the harmonic spectrum towards lower frequencies, whereas a drastically changing rising edge translates the spectrum towards higher frequencies. The fundamental pulse's carrier frequency remains fixed in the simulations, meaning that in this illustrative case, the changing shape of the envelope does not affect the fundamental pulse's frequency distribution. This enables to decouple the microscopic generation process from the spectral dynamics of the fundamental pulse for the exemplary simulations in Fig. 4.11. The observed shift of the wavelength in the harmonic spectrum is therefore a result of the single-atom response to the changing driving field's envelope. The origin of this effect is the intrinsic atomic phase (c.f. Eq.(4.13)), given by $\phi_{\text{atom}} \propto -\alpha I$ (c.f. Sec. 4.1.3). The associated instantaneous frequencies are therefore shifted by a factor proportional to $\partial/\partial t(I)$, as discussed in Fig. 4.5. This connection is used in the reverse direction to link the harmonic red-shift to the temporal slope of the fundamental pulse-shape.

The simulations of the high-order harmonic spectrum are adapted to the experimental data by taking the experimentally reconstructed pulse shape at each position along the

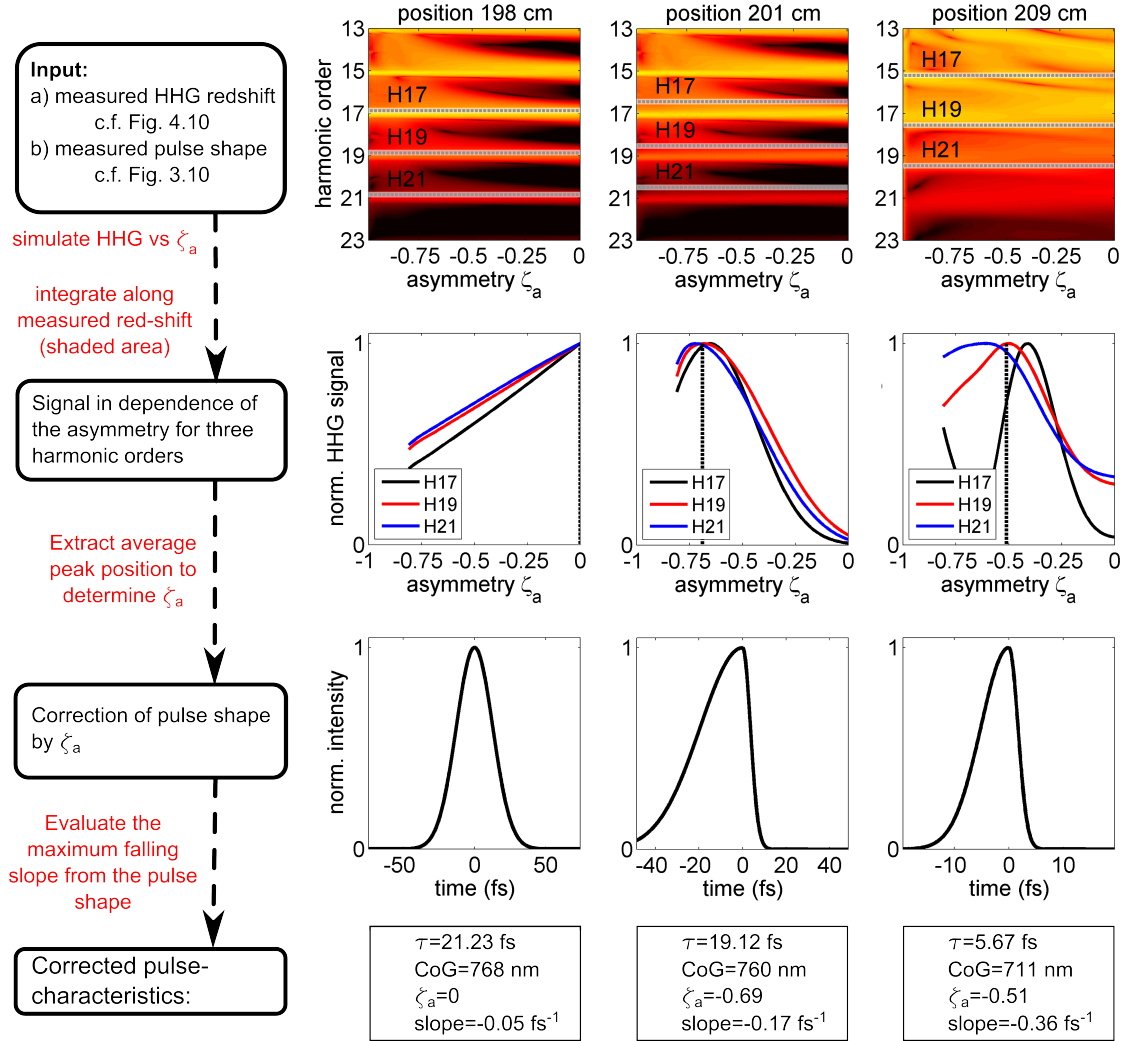


Figure 4.12: Linking the harmonic red-shift to the pulse’s asymmetry. (top) The experimentally retrieved pulses are used as an input for HHG-simulations as a function of the pulses asymmetry (c.f. Fig. 4.11). (middle) The experimentally extracted harmonic red-shift (comp. Fig. 4.9) serves as a reference to determine the asymmetry value. (bottom) The obtained value is used to correct the initial pulse shape.

filament. A single pulse shape centered at the CoG of the fundamental spectrum is used to simulate the HHG spectra using the Lewenstein-model as a function of the asymmetry-factor ζ_a . The usage of the CoG of the fundamental spectrum at each position ensures, that the changing spectral properties of the pulse are taken into account in the HHG-simulations. The correct value of ζ_a is extracted by evaluating the asymmetry-value at which the theoretically obtained red-shifted signal corresponds to the experimentally measured value. The experimental values used for this comparison are the ones obtained by the CoG-corrected high-order harmonic spectra, which are depicted on the right-hand side of Fig. 4.10, delivering three reference points for the determination of the correct ζ_a .

The procedure of the determination of ζ_a is presented and explained in Fig. 4.12 for three exemplary positions along the filamentary propagation direction, being 198 cm, 201 cm and 209 cm. For each position, three figures are shown. The first plot (top) shows the calculated evolution of the harmonic spectrum using the reconstructed pulse duration of the SHG-FROG measurements, the CoG of the fundamental spectrum and the extracted intensity from the HHG-spectrum as an input for the ζ_a -dependent calculation of HHG. The black-dotted lines represent the experimentally measured red-shift in the harmonic spectrum according to Fig. 4.10 for harmonic orders 17-21. The second row from the top in Fig. 4.12 present the integrated simulated HHG signal around those values (within a limit of ± 0.05 harmonic orders). A gray overlay is used to sketch the area of integration. The dependency of this signal on ζ_a serves as a gauge for the correct asymmetry value. The value of ζ_a at which the integrated harmonic signal maximizes is used to correct the fundamental pulse shape. The lower plots in Fig. 4.12 display the final, corrected and normalized pulse shape which is used to determine the slope (1/fs) of the falling edge by evaluating its maximum derivative. The input parameters for the HHG-simulations, the resulting asymmetry and slope values are given below the plots.

At the very beginning of the filament at a position of 198 cm, no harmonic splitting is observed. Therefore, the simulated harmonic signal coincides with the measured shift (being equal to zero) at $\zeta_a = 0$. At 201 cm a red-shift is detected in the harmonic spectrum which shifts the reference points for the harmonic orders 17-21. As a result, the simulated harmonic signal is not representing the red-shift for a value of $\zeta_a = 0$. The correct value of ζ_a can be extracted by looking at the second plot from the top, where the measured red-shift coincides with the simulated one for a value of $\zeta_a = -0.69$. Further propagation changes the asymmetry value, albeit not monotonically in one direction. Since the harmonic red-shift is not solely influenced by the asymmetry-value itself, but by the falling slope of the pulse as well, the self-shortening of the pulse along the filamentary propagation direction can strongly influence the harmonic red-shift without making the pulse more asymmetric during its propagation. This effect can be observed in the data-sets of Fig. 4.12 belonging to a position of $z=209$ cm. The strong amount of the red-shift is already reached for lower values of ζ_a , since the self-shortened pulse itself contributes significantly to the slope of the pulse and therefore to the frequency shift in the high-order harmonic spectrum. The panel at the bottom stresses the necessity to compare the frequency shift for multiple harmonic orders, since the simulated results become very unstructured as the fundamental pulse approaches shorter durations.

The presented simulations of the harmonic spectrum have been performed for two distinct cases, where either contributions only involving the short electron trajectories are considered during the generation process or long and short trajectories are taken into account. (Note, that only the results covering the short trajectory contribution are presented in Fig. 4.12.)

The findings of the evaluation of the fundamental pulses asymmetry in dependence of the propagation distance are summarized in Fig. 4.13. The upper row shows the experi-

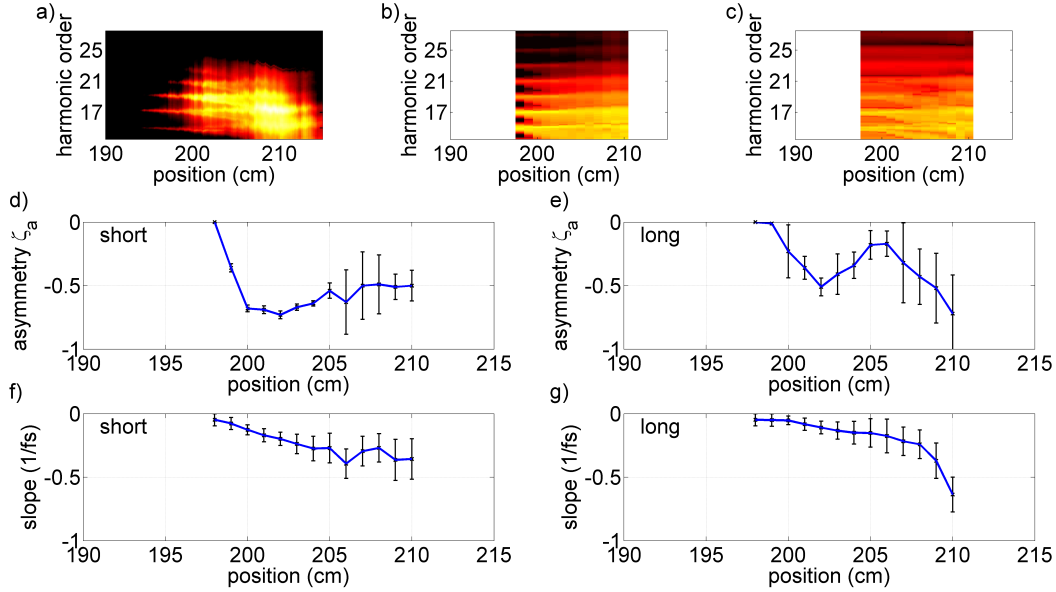


Figure 4.13: Outcome of the analysis according to Fig. 4.12. (a) Measured harmonic spectrum. (b) Reconstructed harmonic spectrum from short trajectory contributions. (c) Same for short and long pathways. (d),(e) Respective asymmetry values ζ_a leading to the harmonic spectra and (f),(g) the corresponding falling slopes of the fundamental pulses.

mentally measured high-order harmonic spectrum in (a) for the sake of comparison. The calculated HHG-spectra in (b) and (c) stem from the asymmetry-corrected pulse shape obtained by the method from Fig. 4.12. Panel (b) shows the results from the isolated short-trajectory components and panel (c) shows the findings obtained with both trajectory contributions. Both spectra show a good agreement to the experimental measurements, as the spectral splitting in the harmonic spectrum along the propagation axis is reproduced. Note, that the agreement of the harmonic spectra is an actual necessity since the asymmetry-modulated simulations of HHG are adjusted to fit to the HHG-measurements. The extracted asymmetry-values are shown for the respective calculations including only short (d) and both trajectories (e). Here, the respective error-bars are plotted in black and originate from the standard-deviation from the determination of the maximum's position in Fig. 4.12. The change of ζ_a with respect to the position along the filament is not a monotonically decreasing value for both cases. At first, a strong drop-off can be observed, which is interpreted as the onset of self-steepening. For increasing positions $z > 200$ cm, the asymmetry shows a stabilizing behavior and its value does not exceed a threshold of $\zeta_a = -0.6$. Figure 4.13 (f) and (g) display the falling slope of the modified pulse-shape. The slope is determined by applying the extracted value of ζ_a to the respective pulse-shapes. The modified shapes can now be analyzed to yield the strongest falling slope, being an indicator for self-steepening along the filament.

In Figure 4.14, the values of the slopes originating from the high-order harmonic spectra (blue line=short, dotted-red=long and short) are compared to the ones obtained from the SHG-FROG measurements (black-dotted) and the simulated pulse-propagation (black-

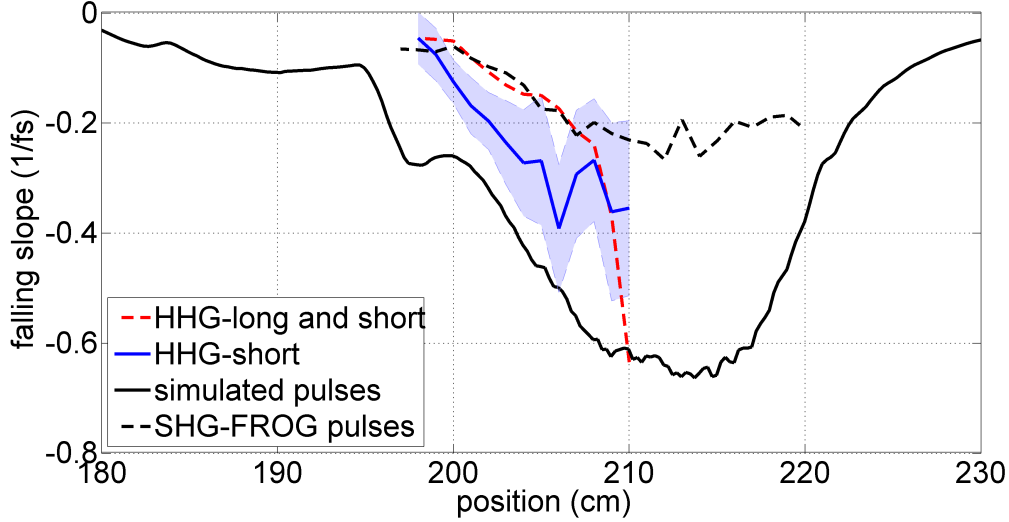


Figure 4.14: Comparison between the falling slopes obtained by differing methods. The results of the pulse-propagation simulations (black) serve as a reference for the comparison to the findings from the SHG-FROG traces (black-dotted), the ζ_a -values for long trajectories (red-dotted) and the ζ_a -values for short trajectories including an estimation for its error (blue). The latter shows the best agreement.

solid) (c.f. Fig. 3.13 (c)). The resulting slope of the short electron trajectory findings shows a better agreement with the simulations than the SHG-FROG measurements and is able to more precisely track the self-steepening dynamics predicted by the simulation of the pulse propagation. Expanding the possible trajectories to long and short electron trajectories results in the underestimation of the falling slope. The long trajectory contributions have a greater pre-factor α to the atomic phase as their excursion time in the continuum τ_{exc} is higher compared to the ones from the short electron trajectories (c.f. Eq. (4.13)). Therefore, the long trajectory contributions can generate a significant red-shift for much weaker falling slopes (c.f. Eq. (4.13)) [42, 43, 197]. The lacking accordance of the long trajectory results is to be expected, since the spatial filtering of the pinhole setup strongly favors signal originating from short electron trajectories. The slight offset between the falling slopes from the numerical findings and the measurements in Fig. 4.14 could be connected to TPM. The determination of the correct, steepest falling slope requires a favorable PM at exactly this point along the pulse shape. The actual position of TPM along the pulse will be the focus of the upcoming section.

Conclusion The influence of the changing CoG of the two sub-pulses occurring during the filamentary propagation can be excluded as a source of the frequency down-shift in the harmonic spectrum. The red-shift in the harmonic spectrum (c.f. Fig. 4.7) could be directly attributed to the self-steepening along the filamentary propagation. The accumulating self-steepening of a high-intensity beam could be directly observed and traced along the pulse’s propagation axis. The findings also show that the harmonic emission is

dominated by contributions from short electron trajectories, as the results from the modeling including long and short trajectory contributions disagree with the simulations of the pulse propagation. The emission of harmonic radiation connected to the short trajectory can be understood by the spatial filtering that is induced by the double-pinhole setup. As shown in Fig. 4.2, the components associated with the long quantum path are preferably emitted at an off-axis position. The splitting still does not appear as clear in the simulated high-order harmonic spectra as it does in the experiments, since the phase matching along the generation volume might effectively filter the spectral emission of HHG. Therefore, the observations need to be expanded from the microscopic towards the macroscopic response of the medium.

4.3.3 Phase Matching of High-Order Harmonic Generation along a Femtosecond Filament

In order to determine the emission points of HHG along the temporal pulse profile, the transient phase matching for the case of filamentation is evaluated in the following. The spatio-temporal dynamics of the fundamental pulse can strongly affect the macroscopic response during HHG. Phase matching is reduced to an on-axis observation, because the double-pinhole setup radially confines the emission volume contributing to the detected harmonic emission.

The adaption of phase matching calculations to filamentation needs a special evaluation of the geometric phase as well as the spatial intensity gradient along the propagation axis, as the refocusing cycle results in the occurrence of a modulated intensity evolution along the filament, strongly differing from a linear Gaussian beam waist. The transient phase matching is calculated by using the results obtained from the simulations considering the spatio-temporal pulse evolution as an input, since the spatial, spectral and temporal properties of the filamenting beam are accessible by the numerical evaluation. To estimate the Gouy-phase evolution along an extended focus, the origin of this phase shift needs to be evaluated further. The Gouy-phase in dependence of the divergence properties of the beam is described as [204]:

$$\phi_{\text{Gouy}} = -\frac{2c}{\omega} \int^z \frac{1}{w^2(z)} dz. \quad (4.18)$$

The implementation of the Gaussian beam evolution $w(z)^2 = w_0^2(1 + (\frac{z}{z_r})^2)$ yields the usual representation of $\phi_{\text{Gouy}} = -\arctan(z/z_r)$ which has already been introduced in Eq. (4.11).

To adapt the phase matching to the case of filamentation, the numerical results from the pulse propagation need to be analyzed:

- The beam waist along the propagation direction is estimated by integrating the spatio-temporal profiles (c.f. Fig 3.12) along the temporal axis for a window of ± 5 fs around the pulse's peak value. The gating enables to monitor the focusing dynamics of the respective strongest part of the pulse and avoids a masking of the determined width of the waist by the temporally separated defocused off-axis components in the

defocusing stage of the filaments life cycle. The resulting dependency of the waist on the propagation distance is displayed in Fig. 4.15 (a). The corresponding phase mismatch is assessed by $\Delta k_{\text{Gouy}} = \frac{\partial}{\partial z} \phi_{\text{Gouy}}$ and displayed in Fig. 4.15 (b).

- The contribution of the atomic phase is evaluated by Eq. (4.16), where the gradient of the on-axis intensity along z is taken from the simulations (c.f. Fig. 3.13 (c)). The phase-slope α is estimated by a preceding calculation of intensity-dependent high-order harmonic spectra using the SFA-theory (c.f. Sec. 4.1.2). The imaginary part of the spectrum allows to determine the intensity-dependent phase and therefore the slope of the atomic dipole phase with respect to the intensity. This corresponds to the value of α and calculates as $1.2 \times 10^{-13} \text{cm}^2/\text{W}$ for the 19th harmonic order in the plateau.
- The evolution of free electrons ρ_e along the pulse shape is calculated according to PPT-theory. To account for the strong chirp of the pulse, the instantaneous frequency is evaluated through the X-FROG traces (c.f. Fig 3.19) and used as a time dependent input together with the corresponding local intensity along the pulse shape. The determination of ρ_e results in the corresponding wave-vector mismatch using Eq. (4.12).

Figure 4.15 displays the extracted parameters from the pulse-propagation simulations in panel (a)-(c), where the z -dependent beam waist (a), the resulting Gouy-phase (b) and the gradient of the intensity evolution (c) are shown. Each evolution has been extracted from the propagation code of filamentary propagation (c.f. Sec. 3.3) and is displayed in a blue line, labeled as "Filament". In comparison, the classical corresponding evolution of a focused Gaussian beam ($f=2.05 \text{m}$) is presented in red-dashed lines. The minimum of the beam waist is strongly extended for the filament case (panel (a)), resulting in a much bigger Gouy-phase shift in panel (b) as compared to a commonly focused Gaussian beam. Also, the evolution of the intensity with respect to z is strongly modified by the filamentary dynamics, resulting in a structured distribution of the intensity gradient in panel (c).

The resulting individual contributions of Δk_{atom} (d), Δk_{Gouy} (e), Δk_{el} (f) and the total phase mismatch Δk_{tot} (g) are shown below for an ambient pressure of 100 mbar of argon. The atomic phase contribution shows strongly varying contributions along z , as it is directly connected to the strongly modulated spatial derivative of the intensity. The geometric phase contribution only depends on the propagation distance z and shows no time dependency, taking strictly negative values, as the Gouy-phase is constantly decreasing along z . The wave-vector mismatch Δk_{el} shows a strong time-dependence, as the free electron density accumulates along the temporal pulse shape.

The overall wave-vector mismatch Δk_{tot} can be interpreted as a transient phase matching map and allows for conclusions on the macroscopic response. As a guide to the eye, the outline of the fundamental pulse evolution from the simulations is marked for a threshold value of $5 \times 10^{13} \text{W}/\text{cm}^2$ in a black-dotted line in Fig. 4.15 (g), estimating the area

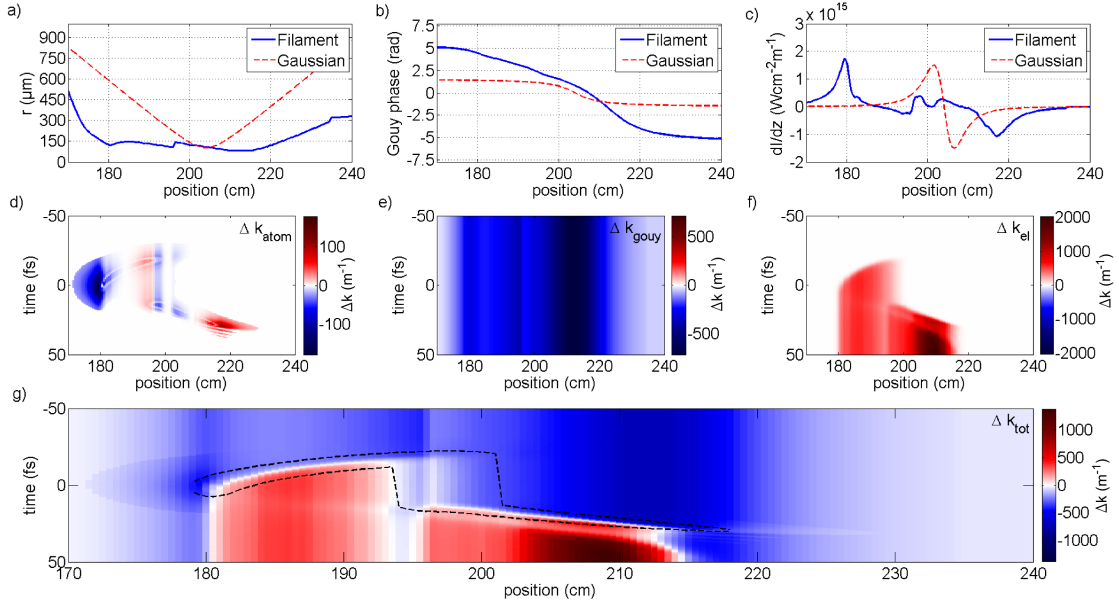


Figure 4.15: Analysis of the on-axis transient phase matching along the filament. Panels (a)-(c) show the foundation for the evaluation of Δk , being (a) the beam-waist along the focus, (b) the corresponding Gouy-phase shift and (c) the derivative of the on-axis intensity with respect to z . The filamentary data are obtained from the numerical output and are depicted in blue. The example of a normal Gaussian focus is shown in red-dotted lines for comparison. The resulting individual wave-vector mismatches are depicted below for (d) the atomic phase, (e) the Gouy-phase and (f) the dispersion of free electrons for the case of an ambient pressure of 100 mbar. The summed mismatch Δk_{total} is displayed in (g) and reveals a preferred PM at the falling edge of the pulse for $z > 200$ cm.

contributing to HHG. Good phase matching is achieved at positions where the interplay between all three contributions compensates each other and is depicted by a white coloring in Fig. 4.15. The free electrons are essential to compensate for the wave-vector mismatch induced by the Gouy-phase term.

During stage I, the defocusing section, the electrons generated along the pulse shape lead to a small area over which good phase matching is achieved as the rising electron density compensates the wave-vector mismatch for a small temporal fraction. This area is located close to the peak of the pulse. The ongoing ionization results in a rapid increase of the phase mismatch after the pulse's peak. The scenario changes during the refocusing as well as defocusing stage II and III. The driving pulses self-shorten and the positive phase mismatch due to free electrons along the pulse shape is drastically reduced. This effect is further amplified by the pulses self-steepening along the propagation stage of the filament, since the position of perfect phase matching moves further into the trailing part of the pulse. This effect can be seen in Fig. 4.15 (g), where the position of good phase matching (white color-coded) is approaching the trailing part of the black-dotted outline of the pulse shape. The observation of the red-shifted components in the harmonic spectrum, which are connected to the steep falling slope of the pulse's envelope, is therefore favored.

The findings from Fig. 4.14 are able to track self-steepening but show a discrepancy between the experimentally traced self-steepening and the numerically predicted one. A possible explanation is a favorable TPM at a point along the falling edge which is not coinciding with the steepest falling slope. This estimation is evaluated in Fig. 4.16, where the color-encoded phase mismatch Δk_{tot} is projected onto the simulated pulse shape for a position of 211 cm. The color encoding is referring to the calculated ones from Fig. 4.15 (g). It can indeed be seen, that the point of optimal TPM is situated closer to the peak of the pulse, explaining the offset in Fig. 4.14. Since a position closer to the peak is favored by TPM, the harmonic signal will predominantly carry the information about the steepness at this temporal position.

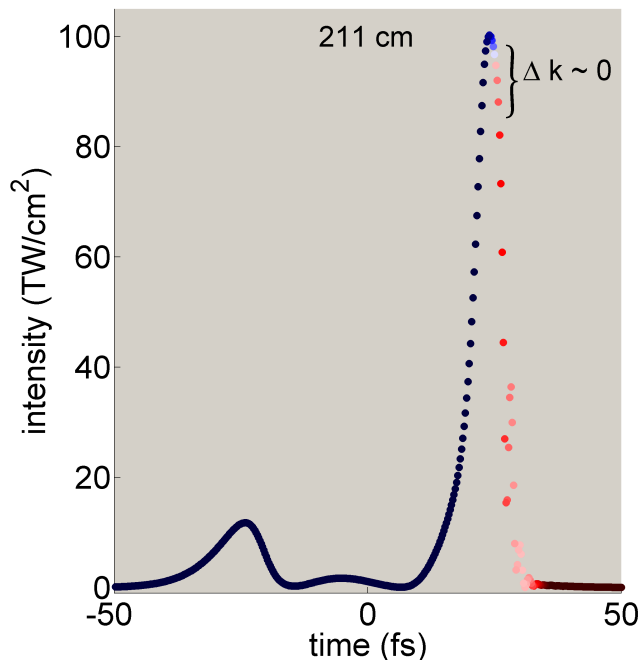


Figure 4.16: Projection of the phase mismatch Δk_{tot} (c.f. Fig. 4.15 (g)) on the temporal pulse shape at a position of 211 cm. The position of optimal phase matching is not coinciding with the position of the maximum falling slope, but shows a slight offset.

One open question in the presented experiments is the actual gas density at which HHG takes place and the influence of the pressure gradient on the phase matching. The known pressures in the experiment are between 1 bar in the filaments cell and 5-10 mbar in the truncation-stage. The harmonic radiation originates from any position along this gradient. The TPM maps are able to give an insight into this issue and can narrow down the possible pressure at which HHG is effectively generated along the gas-density gradient in the truncation stage.

The overall phase mismatch Δk_{tot} , displayed in Fig. 4.15 (g), is evaluated for various ambient pressures. Next, Δk_{tot} is integrated along the area sketched by the black line in panel (g), restricting the region of integration to a section, where the pulse is intense enough to generate the observed harmonic order $q=19$. For the calculations, the intensity which defines the border of the integration is adjusted to $5 \times 10^{13} \text{ W/cm}^2$ and can also be seen in Fig. 4.15 (g). The temporal width of the highlighted area is used to rescale the integrated signal to obtain $|\Delta k_{\text{tot}}|$ per fs.

The findings are shown in Fig. 4.17 for pressures ranging between 1 bar and 5 mbar. Here,

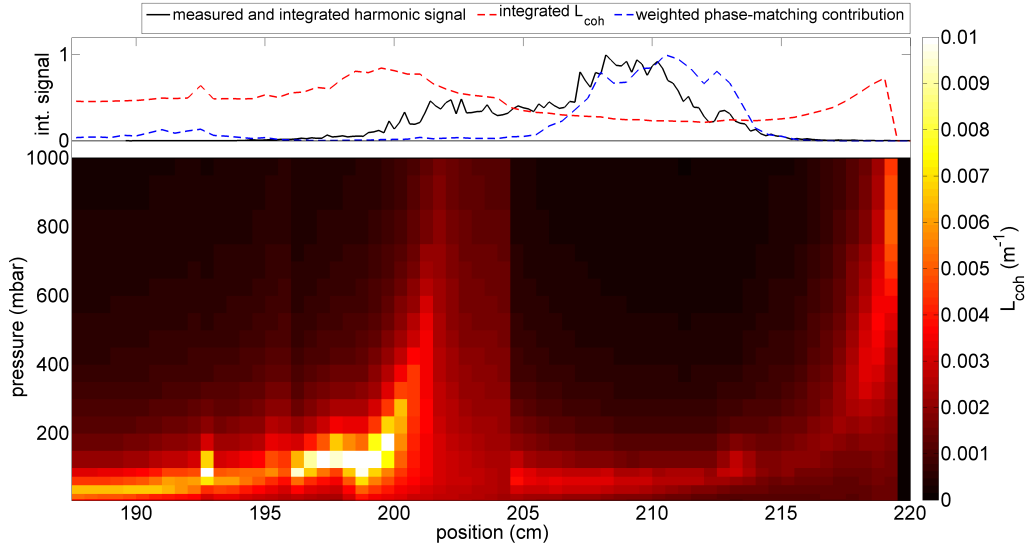


Figure 4.17: Calculation of the pressure-dependent coherence length $L_{\text{coh}} = \pi/|\Delta k_{\text{tot}}|$. For each pressure, Δk_{tot} has been integrated along an temporal area at which the intensity of the pulse shape exceeds $5 \times 10^{13} \text{ W/cm}^2$. The resulting value is used to determine $L_{\text{coh}}(z, p)$. The top plots display the experimentally measured and integrated harmonic signal (black) and the integrated coherence length (red-dotted). The estimated high-order harmonic signal (blue-dotted) has been obtained by evaluating Eq. (4.15).

the coherence length $L_{\text{coh}} = \pi/|\Delta k_{\text{tot}}|$ is presented in dependence of the propagation distance and pressure in the color-encoded representation. The coherence length is chosen because it can be easily integrated along the linearly scaled pressure axis to estimate the harmonic signal in dependence of the propagation distance. Good phase-matching conditions, corresponding to larger L_{coh} , can be found for pressures $p < 200$ mbar, strongly favoring low gas densities in the generating medium. Higher pressures result in a dominant contribution of Δk_{el} , leading to phase matching conditions that suppress an efficient accumulation of the HHG signal.

The reference value for the calculations is given by the integrated harmonic signal from Fig. 4.7, which is displayed in black on top of the color-encoded map for L_{coh} . The measured HHG signal is detected between 194 cm and 216 cm, which covers the defocusing stage II and the propagation stage III of the fundamental pulse.

The integrated (with respect to p) coherence length is displayed in the red-dotted line on top and first of all shows no clear agreement with the experimental measurements. The observation of the coherence length can indicate good and bad conditions for the build-up of the harmonic radiation but neglects the conversion efficiency of the single emission process. In order to estimate the PM further, Eq. 4.15 is evaluated. To approximate the HHG process, common scaling laws are applied. Here, the harmonic source term d_q in Eq. (4.15) is assumed to scale with the intensity as I^{12} and the driving wavelength as $\lambda^{-5.5}$ [223, 230, 231]. The obtained estimation of the harmonic emission is displayed in

a blue dotted line in Fig. 4.17 and shows a much better agreement with the experimental measurements. This implies that the generation-efficiency of the single-atom emission process is responsible for the suppression of the harmonic emission along the defocusing stage I. According to the numerical simulations of the pulse-propagation, the intensity along stage I of the filament is approximately 10% lower than in stages II and III (c.f. Fig. 3.13), favoring the later stages due to the I^{12} scaling. Additionally, the strong blue-shift of the fundamental spectrum (c.f. Fig. 3.11) supports HHG along the propagation stage due to the $\lambda^{-5.5}$ scaling. This leads to a much stronger emission along the later stage III of the filament.

In order to further estimate the influence of the phase matching on the measured harmonic signal in the future, the existing code can be expanded to calculate the dipole strength for each harmonic order along the spatio-temporal evolution of the pulse. This would enable a more precise determination of the strength of the radiating single emitter and avoid the estimation of the harmonic emission through scaling laws.

4.3.4 Influence of Pre-Chirped Pulses

The observation of self-steepening induced features in the high-order harmonic spectrum and their relation to phase matching of HHG were discussed previously. The investigation of the spectral XUV-emission can be used as a tool to directly draw conclusions on pulse- and electron-dynamics inside the medium. The spatio-temporal phase matching along the pulse envelope connects the spectral structures appearing in the harmonic spectrum to rapidly changing values of Δk_{el} and Δk_{atom} . In this section, the influence of the initial pulse chirp on the pulse dynamics along the filament is investigated by the sole analysis of the experimentally measured HHG-spectrum. The conclusions will be validated by the calculation of the TPM.

A change of the initial group-delay-dispersion (GDD) has a multiple effects on the filamentary dynamics. The changing intensity can shift the position of the nonlinear focus as the Kerr self-focusing is affected by the peak intensity of the pulse. The modulated pulse duration also determines the fraction of the initial pulse that is influenced by the plasma-induced lens in the defocusing stage I.

Figure 4.18 displays the measured directly emitted high-order harmonic radiation in dependence of the chirp of the input pulse. The chirp is controlled by adjusting the separation of the gratings in the laser system via a manual micrometer-translation stage (c.f. Sec. 3.3.2). The measurement corresponding to a GDD of $+415 \text{ fs}^2$ is the one used in the previous chapter to analyze the spectral splitting in the high-order harmonic spectrum and serves as the reference value of the initial chirp. The other nominal chirp values are calculated from the respective change of the grating separation.

First the influence on the spectral appearance will be discussed. The largest applied GDD of $+826 \text{ fs}^2$ in panel (a) results in a well-structured and weak emission of high-order harmonic radiation showing no signs of spectral splitting or broadening. A compression of the

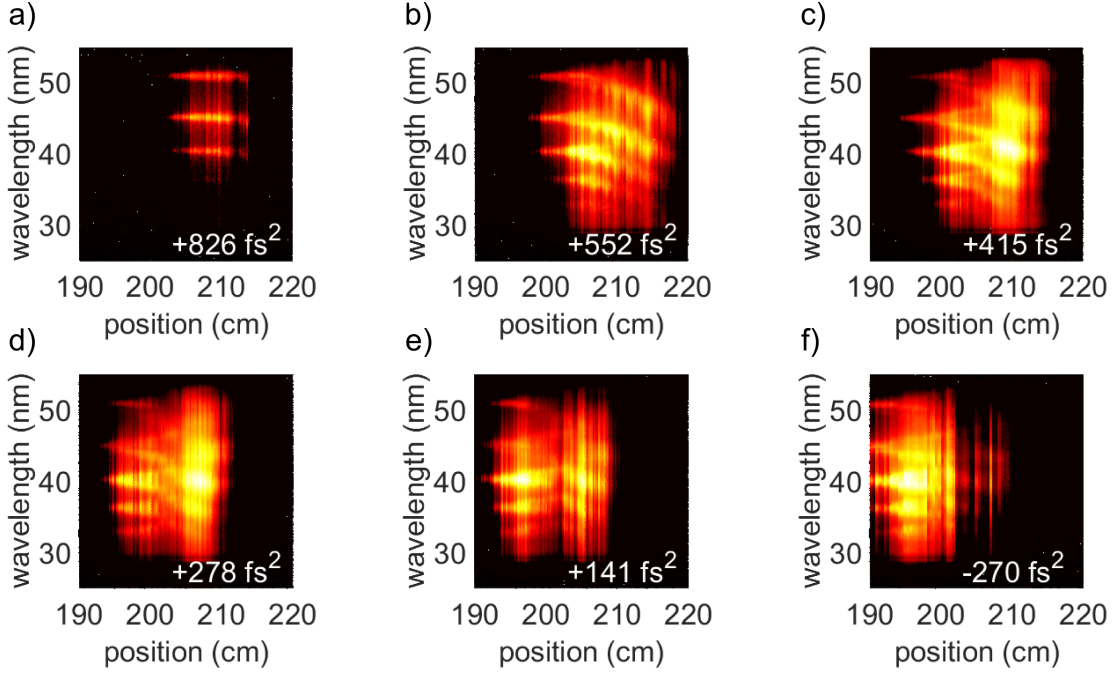


Figure 4.18: Directly emitted high-order harmonic radiation as a function of the fundamental pulse's chirp and the position along the filament. The value of the GDD is denoted in each corresponding figure. The harmonic splitting into two branches is most pronounced in panels (c) and (d).

fundamental pulse to $+512 \text{ fs}^2$ allows for more efficient HHG shown in panel (b), where a dominating blue- but no red-shift of the harmonic orders is observed. The spectral-splitting behavior into blue- and red-shifted components is most pronounced for GDD-values of $+415 \text{ fs}^2$ and $+278 \text{ fs}^2$ in Fig. 4.18 (c) and (d). The positions, at which the splitting is detected, spans between $z=198 \text{ cm}-210 \text{ cm}$ for the first case of $+415 \text{ fs}^2$ and $195 \text{ cm}-207 \text{ cm}$ for the second, less-chirped configuration of $+278 \text{ fs}^2$. Applying a negative chirp of -270 fs^2 in panel (f) shifts the area of high-order harmonic emission towards $z=190-205 \text{ cm}$. Here, the emitted spectrum is modulated and strongly broadened but shows no clear signatures of a blue- or a red-shift.

Figure 4.19 (a) and (b) shows the integrated harmonic signal along the spectral axis in dependence of the position along the filament. The position, as well as the maximum of the integrated signal are shown in (c) and (d). The moderately up-chirped pulses at $+415 \text{ fs}^2$ and $+278 \text{ fs}^2$ lead to the strongest integrated high-order harmonic signal. An increasing chirp of the pulse will shift the onset of the high-intensity region (where harmonic radiation can be detected) to later positions along the filament. Fig. 4.19 (d) shows that the maximum emission of high-order harmonic radiation shifts from a position of $z=195 \text{ cm}$ for a chirp of -270 fs^2 to 208 cm for a chirp of $+415 \text{ fs}^2$.

The findings from Figs. 4.18 and 4.19 allow to conclude that the moderate positive chirp of $+415 \text{ fs}^2$ and $+278 \text{ fs}^2$ aids the onset of self-steepening dynamics along the femtosecond

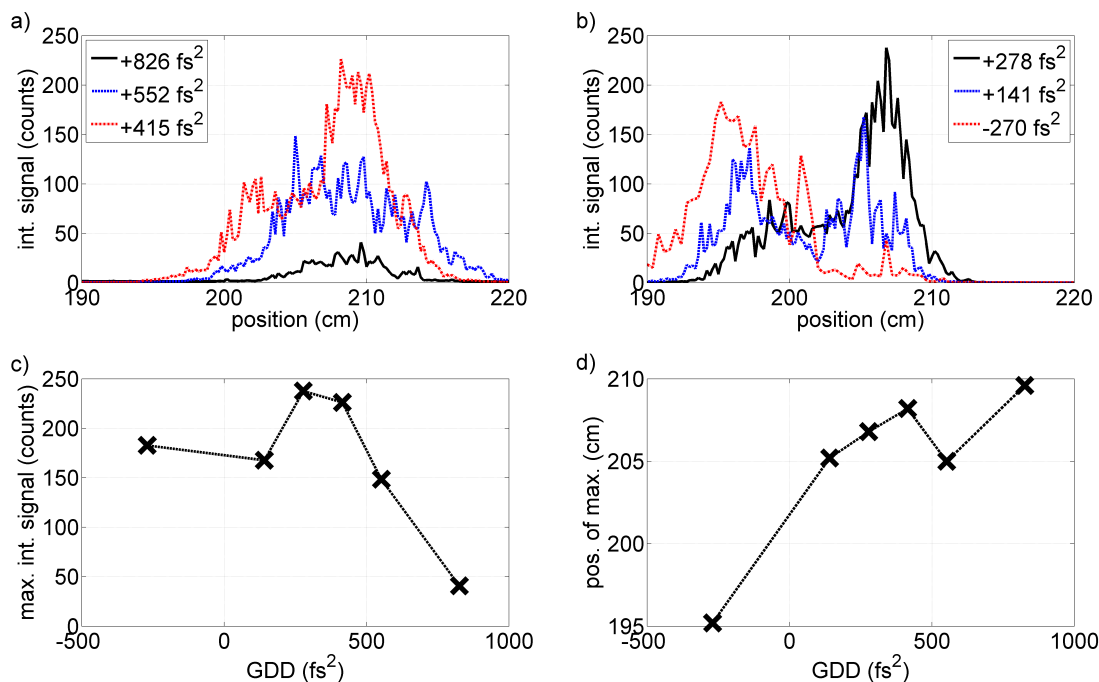


Figure 4.19: (a),(b) HHG-signal from Fig. 4.18 integrated along the complete wavelength axis covering the range between 25 nm and 50 nm. (c) Maximum of the integrated signal and (d) position of said maximum.

filament, as the observed red-shifted components in the HHG-spectrum are connected to those dynamics (c.f. Sec. 4.3.2). The previous section concluded, that not only the existence of the steepened pulses is important, but also the TPM along those pulses. The appearance of the red-shifted branch therefore exposes that the falling edge of the pulse is phase matched. This is possible when the phase induced by the dispersion along the electron density along in the propagation stage III is balancing out the atomic phase and Gouy-phase contributions properly and not overshooting (c.f. Sec. 4.1.4). Since the self-steepening is responsible for the shaping of self-shortened pulses (c.f. Sec 3.3.4), it is favorable for ultrashort pulse generation along the propagation stage to positively chirp the initial pulse.

In this context, the findings for $+512 \text{ fs}^2$ appear counter-intuitive at first sight. The blue-shift in the harmonic spectrum is connected to the changing fundamental frequency. This is shifted towards lower wavelength because of the accumulating effect of self-steepening. Nevertheless, the red-shifted branch is missing for large parts of the harmonic spectrum falsely indicating an absence of self-steepening. For further analysis, the pulse evolution is first calculated by the propagation code and then used to analyze the transient phase matching at hand of the simulated pulse-shapes. The measured contradiction in the HHG spectrum originates from the TPM conditions along the evolving pulse shapes, displayed in Fig. 4.20 (a). The assumed pressure is 100 mbar and the harmonic order under investigation is the 19th, matching the calculations of Fig. 4.15. An drastic increase of the electron

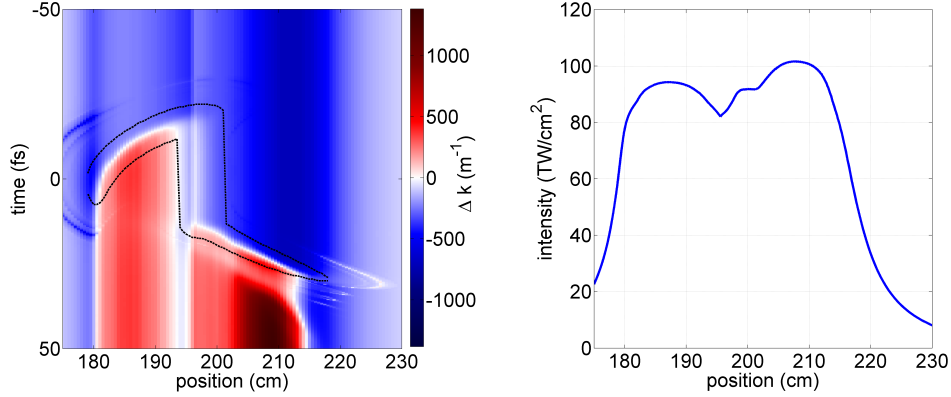


Figure 4.20: (a) Transient phase mismatch for an input pulse with a pre-chirp of $+512 \text{ fs}^2$. (b) Connected intensity-evolution. The black dotted line shows an outline of the pulse evolution at a level of $5 \times 10^{13} \text{ W/cm}^2$. The temporal points of optimal phase-matching for $z > 195 \text{ cm}$ are shifted to the peak of the pulse compared to the findings from Fig. 4.15.

density along the pulse results in a phase mismatch along the falling envelope and therefore suppresses HHG of the red-shifted components. The electron density shows an extremely nonlinear dependency on the intensity and HHG is sensitive to these changes due to the changing TPM properties. This allows to infer that the sole observation of HHG spectral features can discover time-dependent electron density dynamics.

An important finding from the scan of the initial chirp is that the harmonic emission is limited to the propagation stage along the filament, as these stages show a good interplay of Δk_{el} , Δk_{atom} and Δk_{Gouy} . Interestingly, no harmonic emission can be seen along the defocusing stage I which also exhibits a comparable intensity to the propagation stage for the observed chirp values (415 fs^2 and 512 fs^2). This is connected to the frequency evolution of a decreasing CoG along the propagation stage and the $\lambda^{-5.5}$ scaling of the harmonic emission in combination with TPM that supports the propagation stage III. Changing the initial chirp can control the position and strength of high-order harmonic emission and strongly affects the TPM conditions.

4.3.5 Conclusion

The application of directly emitted high-order harmonic radiation proves to be a useful additional tool for the determination of the temporal evolution of the envelope along a filament. It has been shown that the strong blue-shift of the fundamental spectrum during filamentary propagation can lead to a blue-shift in the detected harmonic spectrum. Additionally, the changing slope of the fundamental pulse can manifest itself in a red-shifted

spectral component in the HHG-spectrum. The atomic phase contributing to the HHG process induces an instantaneous frequency connected to the slope of the fundamental pulse's intensity. Using this relation and simulations modeling the microscopic HHG-process, the steepening of the driving pulse along the propagation stage of the filament is directly observed. The findings agree well with the theoretical modeling of the pulse propagation, corroborating the direct measurement of the self-steepening effect along the filamentary life cycle. Furthermore, the macroscopic response of the medium has been investigated for the specific case of filamentation, calling for a specialized modeling of the on-axis Gouy-phase evolution. The phase matching proves that the pulse features which contribute to the self-steepening effect are indeed well phase-matched along the femtosecond filament. Changing the pre-chirp of the fundamental pulse can influence the TPM conditions along the propagation stage and particularly modify the visibility of the red-shifted branch. The spectrum of the detected high-order harmonic radiation will be used in the upcoming section to shift the attention from the fundamental pulse's slope towards its peak intensity along the filament.

4.4 Reevaluation of the Clamping Intensity

As already mentioned in Sec. 3, the clamping intensity I_c is a direct result of the balance of the induced refractive index change Δn_{NL} of self-focusing and plasma defocusing [62, 63, 118, 181].

In this section, Δn_{NL} is adapted to account for the influence of the external focusing. The established methods to evaluate the peak intensity along a filament are introduced and compared to the analytical model developed in this thesis. Finally, I_c is determined by high-order harmonic radiation being used to monitor the intensity-evolution along a femtosecond filament. The experimental observations first focus on the evaluation of the peak intensity for the case of the pulse-shapes of Sec. 3.3. According to Sec. 3.3.7, the experimental determination of the peak intensity allows to distinguish between the validity of the PPT- and ADK-ionization models (c.f. Fig. 3.23). The influence of the external focusing setup on the intensity-dynamics along a filament is investigated at the end of this section.

4.4.1 An Improved Analytical Determination of the Clamping Intensity

In order to find an analytical expression for the clamping intensity I_c which includes the external focusing setup, the balance between the Kerr-effect and the changing plasma-density and its minimization via the refractive index difference $\Delta n_{NL} = \left| n_2 I - \left| \frac{\rho_e(I)}{2\rho_{\text{crit}}} \right| \right|$ is expanded.

Since the phase-variation for the Kerr-nonlinearity and the plasma-density is connected to the wavefront sag via $S_{\text{NL}} = -\int_0^z \Delta n(z') dz'$, the reversed assumption can be applied as well. Therefore, S_g connected to the focusing setup defines a phase change Δn_{Foc} through:

$$S_g = \frac{w_0^2}{2z_r^2}(-z) = -\int_0^z \Delta n_{\text{Foc}}(z') dz' \implies \Delta n_{\text{Foc}} = \frac{w_0^2}{2z_r^2} \quad (4.19)$$

Note, that z_0 has been set to the position of the focus f for the derivation of the induced refractive index change. The concluding expression of $\Delta n_{\text{Foc}} = \frac{w_0^2}{2z_r^2}$ can be related to the divergence of a Gaussian beam $\theta_{\text{div}} = \frac{\lambda}{\pi w_0} = \frac{w_0}{z_r}$ to yield the simple connection $\Delta n_{\text{Foc}} = \theta_{\text{div}}^2/2$. This connection is commonly used to describe diffracting beams and can be found in a modified form in Eq. (3.1) [58, 97]. In this case, the term is contributing as an additional focusing influence for the evaluation of the clamping intensity. The refractive index modulation is extended to:

$$\Delta n_{NL} = \underbrace{n_2 I}_{\Delta n_{\text{Kerr}}} + \underbrace{\frac{w_0^2}{2z_r^2}}_{\Delta n_{\text{Foc}}} - \underbrace{\frac{\rho_e(I)}{2\rho_{\text{crit}}}}_{\Delta n_{\text{El}}}. \quad (4.20)$$

The point at which Δn_{NL} approaches zero is determined in a similar manner as the original method presented in Fig. 3.1.

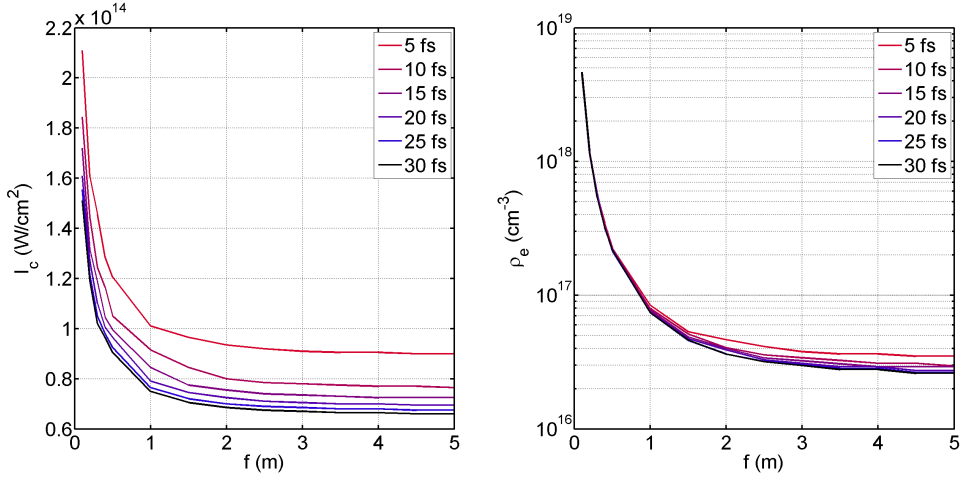


Figure 4.21: (a) Evaluation of the clamping intensity I_c as well as (b) the free electron density ρ_e in dependence of the external focusing and the pulse duration obtained by Eq. (4.20).

- The external focusing length allows to calculate the focusing contribution Δn_{Foc} .
- The free electron density is calculated according to the Yudin-Ivanov-ionization rates until the peak of the temporal pulse shape is reached and delivers Δn_{el} .
- The balance of $\Delta n_{\text{NL}}(f, \tau)$ at the pulses temporal apex is calculated by the implementation of $\Delta n_{\text{Kerr}}(I_0)$.
- The process is repeated for various peak intensities I_0 , giving $\Delta n_{\text{NL}}(f, \tau, I_0)$
- The position at which the balance approaches zero is extracted, yielding the clamping intensity $I_c(f, \tau)$.

The parameters of the external focusing and the pulse duration are scanned to investigate the influence of the external focusing f and the fundamental pulse duration τ . Figure 4.21 (a) shows the clamping intensity I_c . In (b) the connected electron density ρ_e evaluated by Eq. (4.21) is displayed. The decreasing focal length results in an increasing value of I_c exhibiting a weak influence for $f \geq 1$ m and a strong influence for short focal distances. The pulse duration τ of the fundamental pulse also influences I_c , as it is shown for $\tau=5$ -35 fs by the different colored lines in Fig. 4.21. A shorter pulse decreases the temporal window over which the electron density can accumulate along the pulse. In order to obtain a balance of Δn_{NL} , the term $\partial/\partial t(\rho_e)$ needs to increase which is achieved with a higher intensity. The need for a higher intensity leads to a cross-coupling to the focusing term $\Delta n_{\text{Kerr}} = n_2 I$. This change however is moderate, as ρ_e approximately scales with I^K , and the focusing contribution $n_2 I$ scales linearly with the intensity. Focusing on the Kerr-dominated propagation regime (c.f. Sec. 3.2) with $f \geq 1$ m it can be seen, that the clamping intensity can only exceed 100 TW/cm^2 for pulse durations $\tau \leq 5 \text{ fs}$. The resulting free electron density shows a good agreement with previously published numerical findings [232, 233]. Here, the calculated electron density at $f=1$ m in air equals

$\rho_e=4.2\times 10^{16}\text{ cm}^{-3}$ [232] and $\rho_e=6.5\times 10^{16}\text{ cm}^{-3}$ [233]. The introduced analytical model yields $\rho_e=7.35\times 10^{16}\text{ cm}^{-3}$ for a 30 fs pulse, being in qualitative agreement.

Previous Experimental Methods

The analytical calculation of the clamping intensity is straightforward (c.f. Eq. (3.1)), but its experimental determination remains highly challenging. The most common way to gain the information of the intensity inside a filament uses the fluorescing nature of the generated plasma channel and detects the ratio of two well known nitrogen plasma lines in air [140]. This allows to draw conclusions on the free electron density in the filament and a connection to an intensity through modeling of ionization rates. The method is well-established and widely used, but is prone to errors due to the two-step deduction of the intensity which needs a correct connection between ρ_e and I through an appropriate ionization model (c.f. Sec. 2.2.2). The values obtained for propagation in air from the measurements are dependent upon the external focusing and range between 53 TW/cm^2 for a focal length of 3.8 m and approximately 160 TW/cm^2 for a focal length of 10 cm [232]. A change of the guiding medium calls for a proper choice of emission lines to be linked to the electron density or the intensity being present in the filament. Instead of investigating the relative strength of emission lines, the change of the plasma line width in dependence of the encompassing electron density due to Stark-broadening have also been applied for an extraction of the intensity in the medium in O_2 and Ar [140]. This method also first deducts on the electron density in the medium and draws conclusions on the intensity via ionization rates.

The spectral output of propagating filamentary pulses has also been used to prove the appearance of intensity clamping along a filament, showing that at high intensities, the spectral content generated in the blue spectral region can be connected to the fundamental pulses intensity through the spectral modulation initiated by the changing electron density, scaling proportional to the MPI-rate as $\approx I^K$. A saturation of the fundamental blue-shift with respect to an increasing pulse energy is assumed to prove the saturation of the fundamental pulses intensity [63]. In the context of the findings of Fig. 3.11, this can be difficult since the spectral width of the fundamental beam varies along the filament and is not constantly increasing but also decreases along the propagation axis (c.f. Fig. 3.11).

Another method deduces the intensity by detecting the fluence (J/cm^2) of the filamentary pulses, where the filament is used to drill micro-pinholes into thin metal films [65]. The evaluated diameter of the focused beam, combined with the knowledge of the transmitted power and pulse duration enables the determination of the peak intensity inside the filament. The experimental conditions have been similar to the works in this thesis, using a focusing of $f=1\text{ m}$ into air at atmospheric pressures. The measured intensity has been analyzed to be 146 TW/cm^2 , challenging the results from the plasma emission line-methods and inducing a vivid discussion about the applicability of the clamping-intensity model.

The phenomenon of a clamped intensity has been discussed in all the presented measure-

Paper	Method	Gas	f (cm)	I_c	I_{an}
Xu [140]	Side-Imaging:	Ar	20	170	168.5 (5 fs)
			60	130	128 (3 fs)
	line-broadening	Air	100	120	118 (3 fs)
			20	64	
Xu [234]	Side-Imaging:	Air	11	105	104 (750 fs)
			20	98	95 (250 fs)
	comparison of plasma-line amplitudes		30	98	97.5 (100 fs)
			50	68	62 (500 fs)
			100	39	41 (3 ps)
Sun [235]	Side-Imaging comparison	Air	\approx 100	280	283 (0.1 fs)
Mysyrowicz [65]	Fluence	Air	100	146	142 (1 fs)
Lange [83]	HHG	Xe	100	46	
Steingrube [80]	HHG	Ar	200	120	113.5 (2 fs)

Table 4.1: Findings from previous efforts to measure the self-compression in a femtosecond filament. Various methods are compared, as the analysis of super-continuum generation (SCG), fluorescent emission (side-imaging), Fluence detection and high-harmonic generation (HHG). The respective value of the clamping intensity is labeled as I_c . Column I_{an} shows the values obtained by the analytical formula in Eq. (4.20) and the pulse duration τ needed to achieve this intensity.

ments, which are summarized in Tab. 4.1. The exact values of the intensity are differing strongly. The highest values reported to date have been obtained by using strong focusing optics and correspond to 250 and 280 TW/cm². The analysis of setups with a focal length corresponding to the Kerr-regime ($f \geq 100$ cm) allow to deduce values between 39 and 280 TW/cm² (c.f. Tab. 4.1 (bold)).

The strong variation in the findings can be explained by the challenging experimental task of measuring the intensity. The measurement of line emissions is dependent on the evaluation of the plasma density, which is usually only possible up to an accuracy of $\pm 40\%$ and the correct deduction from the measured ρ_e to the present intensity [140]. The determination of the fluence through the diameter of filament-generated micro-pinholes has to exclude effects of the spatio-temporally evolving plasma. The correct determination of the beam diameter is not impossible, but requires extreme experimental care [65]. All previous measurements allow to conclude that the clamping intensity is strongly connected to the applied focusing setup.

In order to check the formula in Eq. (4.20), the values of I_c are calculated for the conditions of the published experiments. Hereby, the changing pulse duration along the filament is used as a control parameter in Eq. (4.20), as the temporal evolution of the pulse along the filament in the published experiments is unknown. The value of the clamping intensity is extracted and displayed in column I_{an} in Tab. 4.1 together with the value of τ which is necessary to obtain the measured intensity. The model is able to reproduce the respective

peak intensity of the experimental results and allows to elaborate on the shortest pulse duration τ along the filament. The resulting τ allows to estimate if the measured value of I_c is over- or underestimated. For the method of line broadening [140], I_c can be reproduced for $\tau = 3\text{-}5$ fs which is feasible for filamentary propagation. The results connected to the method employing the comparison of plasma lines from [234] can only be reproduced by the analytical model when very long pulse durations are assumed, revealing that this method rather underestimates the clamping intensity I_c . The methods from [65, 80, 235] require extremely short pulses as an input to the analytical model. Those are too small, even when accounting for the strong self-compression along the filament.

However, the evolution of the intensity along the filament is undisclosed from the presented experimental methods and the evaluation by the analytical formula. The estimation is crucial for the comparison with the theoretical modeling of the pulse dynamics (c.f. Fig. 3.23) and will be determined in the following by the use of HHG.

4.4.2 Determination of the Clamping Intensity through HHG

Instead of indirectly deriving the fundamental pulse's intensity, the information from the high-order harmonic spectrum can be used to draw conclusions on $I_c(z)$ through the determination of the Cut-Off frequency. Its simple connection to the ponderomotive energy $E_{\text{CutOff}} = 1.3I_p + 3.17U_p$ reveals a direct correlation to the intensity, reading:

$$I = \frac{(E_{max} - 1.3I_p)}{(3.17 \cdot 9.337 \times 10^{-14} \cdot \lambda^2)}, \quad \text{with } [I_p] = eV, [E_{max}] = eV, \\ [\lambda] = \mu m, [I] = W/cm^2. \quad (4.21)$$

Besides the ionization potential I_p , the only experimentally measured values needed for the determination of the intensity are the Cut-Off energy E_{max} and the driving wavelength λ . The resulting value is rather underestimated, since the Cut-Off of the harmonic spectrum can be reduced due to phase matching effects [218]. However, finding the correct spectral position of the Cut-Off is challenging as soon as the fundamental pulse approaches the few-cycle regime or exhibits a non-trivial phase.

Observing the Intensity-Evolution - Connection to Self-Compression

The experimental analysis of the temporal pulse-behavior enabled to prove the pulse-splitting as well as the self-compression of the pulse (c.f. Fig. 3.11). Through investigating the high-order harmonic emission, the self-steepening along the fs-filament has been successfully estimated and is now used to determine the intensity-evolution.

Figure 4.22 (a) displays the experimental data from Sec. 4.3 after the conversion of the wavelength-axis into a corresponding intensity axis. Each spectral component of the harmonic emission is connected to a certain intensity value via Eq. (4.21), where the CoG of

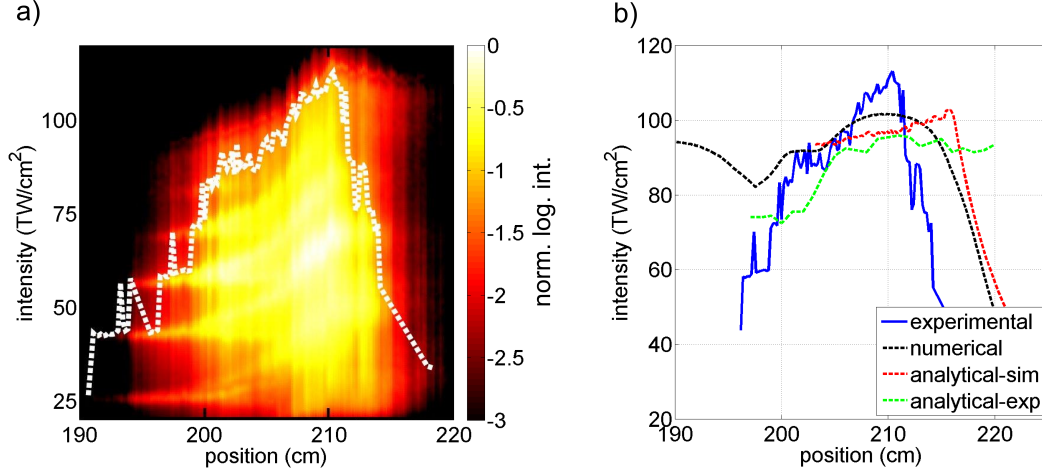


Figure 4.22: (a) Converted HHG data-set from Fig. 4.7, where the y-axis represents an intensity scale, evaluated using the relation of Eq. (4.21). The white dotted line displays the extracted values of the highest intensity being present at each position along the femtosecond filament. (b) Comparison of these intensities (blue) with the findings from the numerical simulations (black) and the analytical formula (red and green) (Eq. (4.20)).

the fundamental spectrum serves as an input for the corresponding λ values. In order to draw a conclusion on the intensity evolution, the Cut-Off needs to be determined. In this case, the highest observable harmonic signal ($>5\%$ of the maximum spectral intensity) is chosen and displayed as a white-dotted line in Fig. 4.22. The error induced by picking a neighboring harmonic order corresponds to ± 15 TW/cm² for a carrier-wavelength of 800 nm. The presented intensity-values are also the ones used as an input for the simulations of HHG-splitting in Fig. 4.13.

The measured on-axis intensity can be extracted from ≈ 195 cm on, as harmonic radiation is emitted due to the increasing quality of PM (c.f. Sec. 4.3.3 and Fig. 4.17). It is steadily rising until a peak value of 109.2 TW/cm² is reached at position 210.2 cm, followed by a strong decrease thereafter. The self-compression detected by the SHG-FROG measurements in Fig 3.11 manifests itself in the intensity-evolution as the shorter pulse supports a higher clamping intensity I_c according to Fig. 4.21.

The experimental results (blue) are compared to the computed intensity evolution in Fig. 4.22 (b), where the black-dotted line corresponds to the values extracted from the numerical simulation of the pulse-evolution and the red-dotted and green-dotted lines show findings obtained by the analytical formula from Eq. (4.20).

The measured intensity evolution from the HHG spectrum and the numerically obtained one follow the same trend and show an excellent agreement between positions 197 cm and 205 cm. For increasing positions, the experimental findings slightly exceed the numerical predictions with a maximum deviation of 8% between $I_c=109.2$ TW/cm² (experiment) and $I_c=101.6$ TW/cm² (simulations). The measurements prove that high-order harmonic radiation can indeed serve as a tool to monitor the intensity dynamics along the refocus-

ing and propagation stages II and III of the filament. Only the defocusing stage I remains undisclosed by the HHG process as no harmonic radiation is detected in this region.

For the evaluation of the analytical results, the pulse duration $\tau(z)$ from the numerical simulations (red-dotted) or the SHG-FROG measurements (green-dotted) is used as an input. The adaption of the clamping intensity by the external focusing factor in Eq. (4.20) is sufficient to yield a good agreement with the numerically and experimentally retrieved intensity values in Fig. 4.22.

The usage of the simulated pulse durations (red-dotted line) results in a marginally better agreement compared to the input of the experimentally measured pulse lengths, as the pulses from the simulations are slightly shorter than the measured ones. The external focusing length is a constant value for the analytical model, meaning that the self-focusing or refocusing dynamics do not change the influence of the focusing term in the balance in Eq. (4.20). Therefore, the analytical evaluation is able to isolate the influence of the changing pulse duration on the intensity evolution along the filament.

The findings allow to conclude that the changing pulse duration, which has been observed in Sec. 3.3, influences the achievable intensity I_c along the femtosecond filament. The deviation of the analytical results from the numerical ones could be attributed to the spatial dynamics along the filament. The next section will evaluate the influence of the other parameter which regulates the clamping intensity in Eq. 4.20, the external focusing setup.

Influence of the External Focusing

The influence of the other parameter affecting the clamping intensity in Fig. 4.21 will be examined by changing the external focusing conditions and detecting the directly emitted high-order harmonic radiation from the filament itself. The goal is to experimentally examine the influence of the external focusing on the intensity along the filament to estimate the quality of the derived analytical formula.

The recorded parameters used for the evaluation of the clamping intensity are the fundamental as well as the HHG-spectrum. The focal length of the curved mirror (c.f. Fig. 4.6) is changed to either $f=1$ m, 1.5 m, 2 m or 3 m, ensuring that the filamentary propagation regime is within the Kerr-dominated regime. The respective input pulse energy for each focal length was 1 mJ with an estimated initial pulse duration close to 45-50 fs.

The process of data acquisition is illustrated in Figure 4.23 for the exemplary case of $f=1$ m. First, the evolution of the pulse shape is displayed in (a). This measurement has been performed in order to test if the previously determined propagation stages I-III are also present for the case of the strongest focusing used in the measurements. It can be seen that all stages are occurring for $f=1$ m and that the pulse envelope is modified through pulse splitting and self-compression, which will be important for the application of the analytical formula. The measured pulse duration minimizes to $\tau = 11.5$ fs along the propagation direction being approximately a factor of two bigger than for the case of $f=2$ m

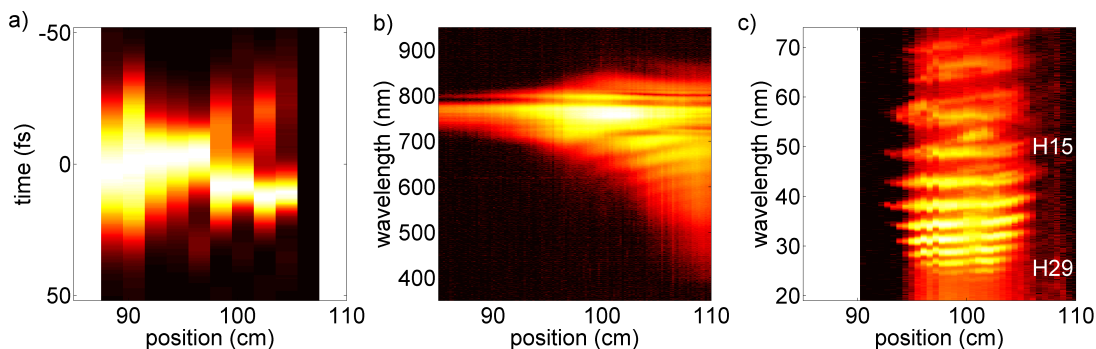


Figure 4.23: Recordings for the evaluation of the clamping intensity. (a) Fundamental pulse evolution along the filament. (b) Evolving fundamental spectrum and (c) HHG spectrum. Datasets (b) and (c) are necessary for the determination of I_c . Panel (a) is used to prove the occurrence of a refocusing cycle at $f=1$ m.

in Sec. 3.3.3. The fundamental spectrum is displayed in panel (b) and its CoG is used as an input in Eq. 4.21. The high-order harmonic spectrum is shown in (c) and used to extract the Cut-Off frequency E_{\max} . The appearance of the high-order harmonic spectrum is not limited to the refocusing and propagation stages II and III along the filament. Contrary to the case of $f=2$ m (c.f. Figs. 4.7 and 4.22), harmonic radiation has been detected along the defocusing stage I as well. The onset of pulse splitting can be traced in the harmonic spectrum through the appearance of red-shifted spectral components for positions >97 cm.

In order to determine the intensity along the filament, the Cut-Off of the high-order harmonic spectrum needs to be evaluated from the experimental spectra. Three different methods are chosen to yield the desired wavelength corresponding to the Cut-Off. The first two methods are undemanding, as the highest observable harmonic order on either a linear- or a logarithmic intensity-scale are read out. This is also the method used in the previous section. The third applied method tries to attain a more precise definition of the Cut-Off. It takes advantage of the strongly differing atomic phase contribution in the plateau than in the Cut-Off region of the harmonic spectrum and the drastically reduced recombination cross-section for the electrons generating the Cut-Off radiation (c.f. Sec. 4.1.2). Consequently, the signal will drop off much more drastically from one harmonic order to the neighboring, when the XUV-radiation is located in the Cut-Off. The third method requires a well calibrated detector with respect to the relative intensity evolution along the spectral axis and also benefits from the detection of a large spectral range. This is the reason, why the approach could not be applied in the previous measurements of the clamping intensity in Fig. 4.20, as the used McPherson setup has a strongly changing sensitivity along the relatively small spectral window.

The procedure for the evaluation of the intensity via the third method is illustrated in Fig. 4.24 for exemplary simulated HHG-spectra. Here, the evolution of the 15th up to the 51th harmonic order is shown on a linear ((a) and (c)) as well as a logarithmic scale ((b) and (d)). The upper set of spectra corresponds to an interaction of a 10 fs pulse, centered at

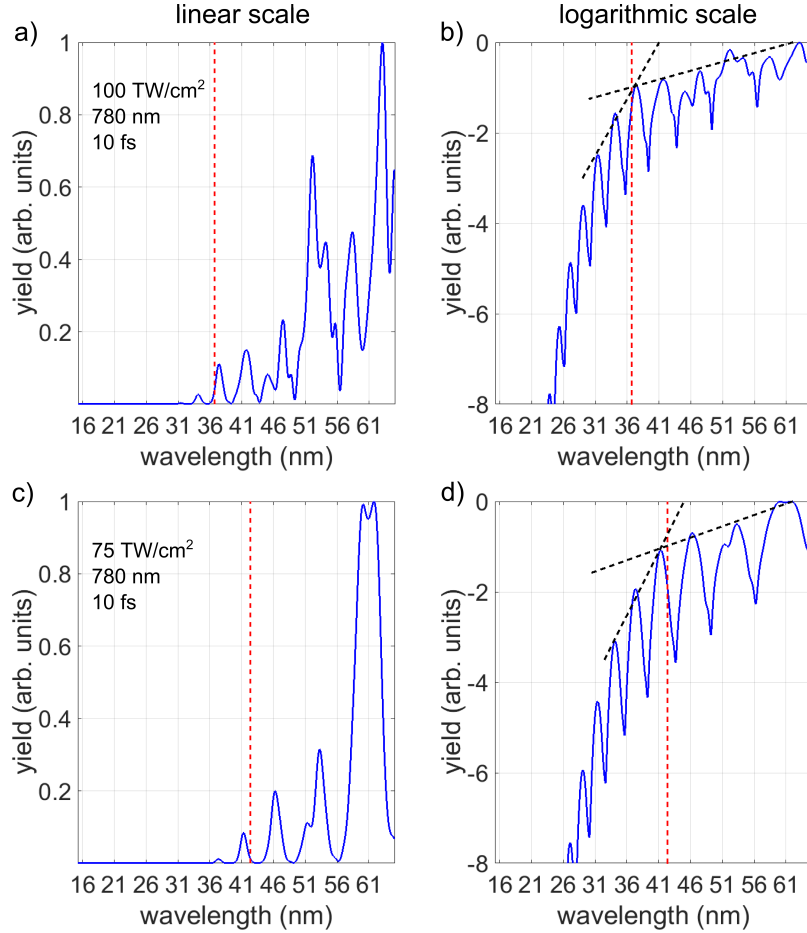


Figure 4.24: Calculated harmonic spectra obtained by using the Lewenstein-model, stressing the troublesome definition of the Cut-Off. The upper plots show the emitted harmonic radiation for a 10 fs pulse with a peak intensity of 100 TW/cm^2 interacting with argon. The spectra are shown on a linear (left) and logarithmic (right) scale. The red-dotted line displays the spectral position of the Cut-Off from the calculations. The black dotted lines in the right panel visualize the different slopes of the signal with respect to the wavelength for harmonics belonging to the plateau and to the Cut-Off. Their crossing-point can be closely connected to the actual position of the Cut-Off frequency. The panels on the bottom display the same features, only for an intensity of 75 TW/cm^2 .

780 nm with a peak intensity of 100 TW/cm^2 with argon. The lower set corresponds to the same parameters, only with a reduced peak intensity of 75 TW/cm^2 . The position of the Cut-Off according to the Lewenstein model is displayed by the red-dotted lines respectively. The black dotted lines in the logarithmic representations (b) and (d) sketch the decreasing slope of the harmonic signal in dependence of its location in either the plateau or Cut-Off region by a linear approximation. The crossing-point of these fits is able to approximate the calculated position of the Cut-Off (red-dotted line). The first important finding of the presented calculations is, that the simple choice of the highest observed harmonic order, even on a linear scale, can introduce a deviation to the real position of the Cut-Off. The

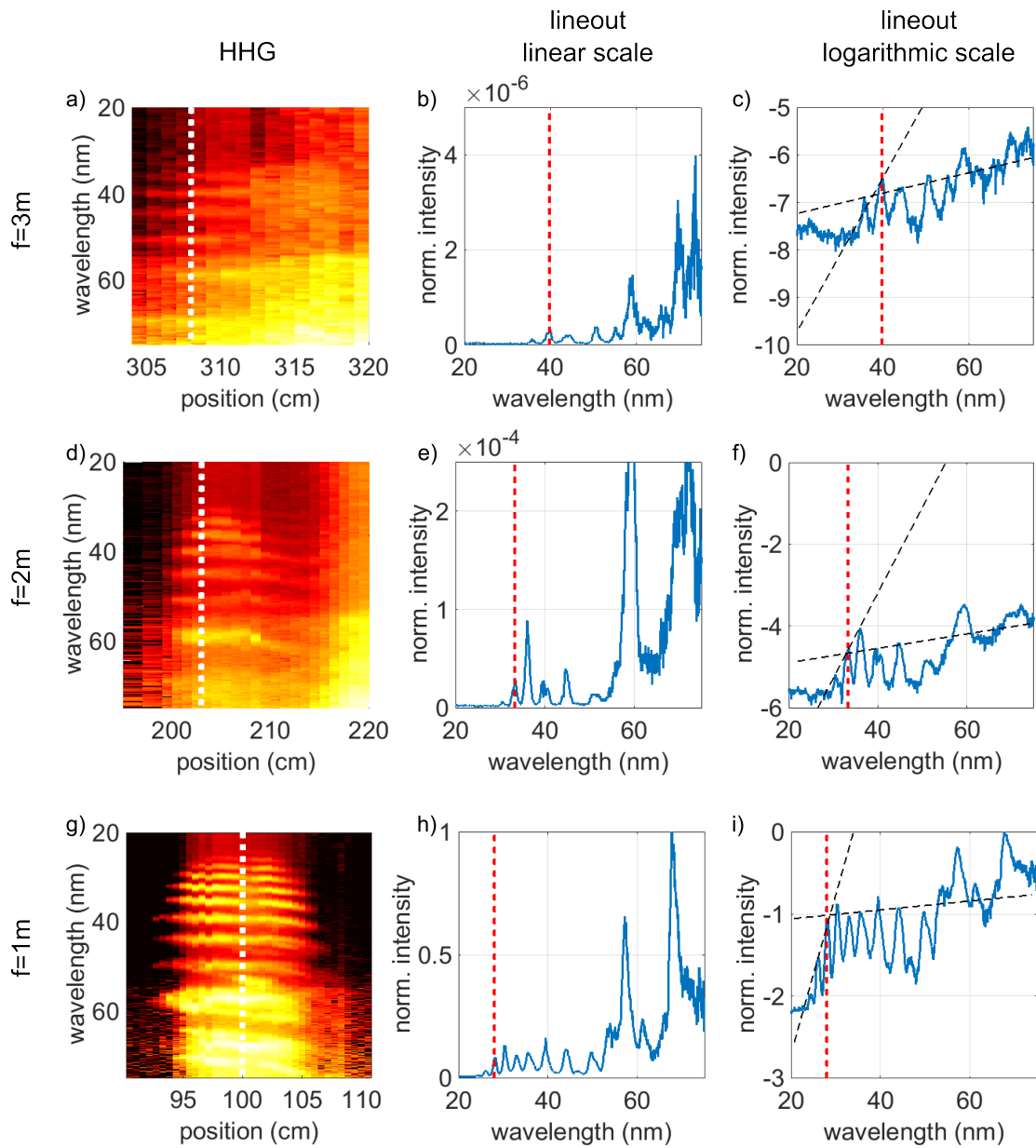


Figure 4.25: Exemplary analysis of experimentally obtained harmonic spectra to determine the Cut-Off frequency. Panels (a),(d) and (g) display the HHG-signal with respect to the position along the filament for three different external focusing setups. The middle and right plots show the high-order harmonic spectra for one position along the filament (highlighted by the white dotted line) on a linear and logarithmic scale together with the extracted position of the Cut-Off (red-dotted line). The linear fits along the harmonic signal evolution (black-dotted lines) are used to evaluate the Cut-Off.

introduced method is more accurate than just picking the highest observed harmonic order out of a XUV-spectrum, but also calls for a more elaborated experimental detection. The

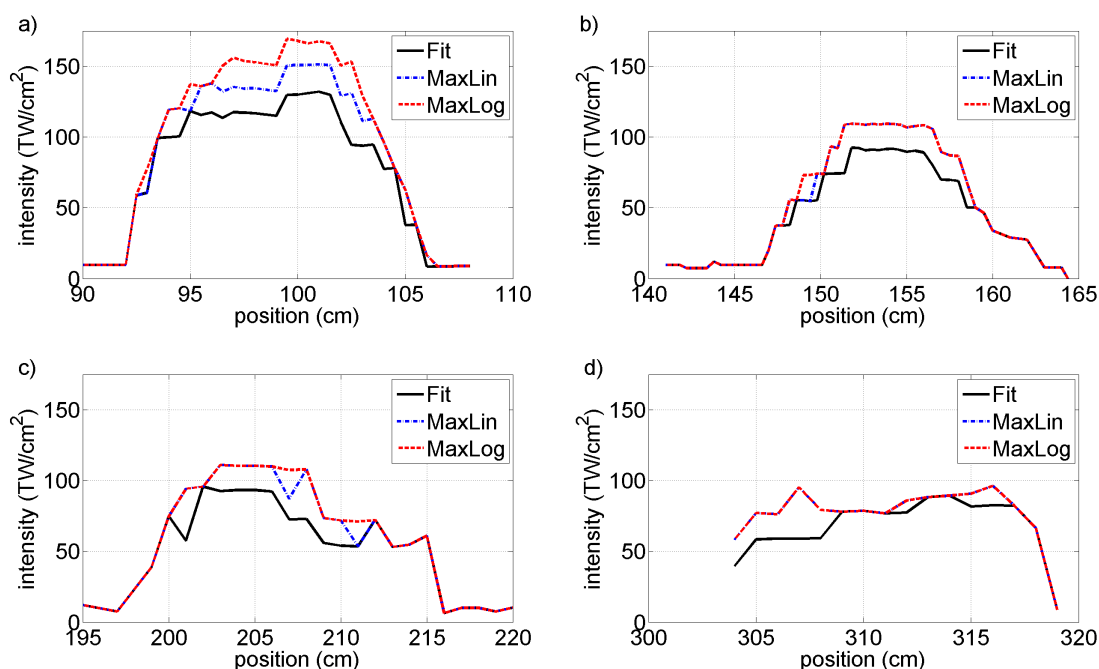


Figure 4.26: Experimentally extracted intensities resulting from the three possible approaches for the determination of the Cut-Off frequency. For each panel either the first visible harmonic order on the linear (blue) or logarithmic (red) scale are extracted. The third method (black) relies on the determination of the signal-slopes, introduced in Fig. 4.25. Panels (a)-(d) show the resulting evolution of the intensity in dependence of the position along the femtosecond filament for four different external focusing geometries (a) $f=1$ m, (b) 1.5 m (c) 2 m and (d) 3 m.

introduced method will be applied to experimental data of HHG in the following.

Figure 4.25 shows three examples of the analysis through the fitting procedure. Sub-figures (a),(d) and (g) show the evolution of the high-order harmonic spectrum with respect to the propagation direction along the filament for an external focusing of 3 m, 2 m as well as 1 m. The HHG spectra are re-calibrated to account for the sensitivity of the diffraction grating. The spectrum used for the exemplary investigation is highlighted by the white-dotted line on top of the color-encoded plot. The middle section in Fig. 4.25 shows the investigated harmonic spectrum on a linear intensity scale, whereas the right hand side shows the same data-set on a logarithmic scale. The linear fits are shown in black-dotted lines in panels (c),(f) and (i). The spectral ranges for the fitting algorithm are adjusted for each HHG spectrum. First, the plateau region is fitted along a spectral range $\lambda < 50$ nm. For higher wavelengths, the sensitivity curve of the diffraction-grating, used for the correction of the data, is enhancing the signal too drastically to faithfully predict the intensity evolution for $\lambda > 50$ nm. The linear fit along the plateau region is performed for an increasing window size from $\lambda = 50$ nm to lower wavelength values. The lower border is defined by the point, where the quality of the linear fit starts to decline drastically. This point defines the upper

border for the fit along the Cut-Off region, applying the same mechanism. The crossing of the linear approximations gives the position of the Cut-Off, which is highlighted by the red-dotted line in Fig. 4.25 (c),(f) and (i).

The procedure is applied to all the measured harmonic spectra shown in the color-encoded plots in Fig. 4.25. In addition to the displayed scans, a measurement with a focal length of $f=1.5$ m has been performed. The fundamental spectrum has been recorded simultaneously for all scans and is used to evaluate the CoG, enabling the calculation of the clamping intensity I_c from the recorded harmonic spectra.

Figure 4.26 shows the final experimental findings for the evolving intensity along a femtosecond filament. Panels (a)-(d) show the local intensity along the propagating filament for external focusing length's of (a) 1 m, (b) 1.5 m, (c) 2 m and (d) 3 m. For each scan, the results of all three methods are shown for reason of comparison, where the fitting procedure is shown in black and the maximum procedures in dotted lines. A stronger external focusing setup leads to a greater discrepancy between the applied methods. However, the agreement is tolerable for $f \geq 2$ m, indicating, that the method used in the previous section is sufficiently accurate to determine the correct intensity along the femtosecond filament (c.f. Fig. 4.22). The maximum deviation between the three methods for $f=2$ m is 18 %. Figure 4.27 shows the maximal intensity along the measured filament in Fig. 4.26 as a function of the external focusing length. The experimental findings are again shown for all three methods where their assignment in the figure corresponds to the previously used ones and can be found in the key. The values connected to the fitting procedure also display the error, which can be induced by selecting a neighboring harmonic order from the high-order harmonic spectrum. The analytically obtained clamping intensities from Eq. (4.20) is calculated for a pulse duration of 6 fs (dark-green). It can be concluded that the external focusing has a strong influence on the achievable clamping intensity I_c along the filament. Selecting a stronger external focusing setup in the Kerr-dominated regime can indeed increase the intensity along a femtosecond filament.

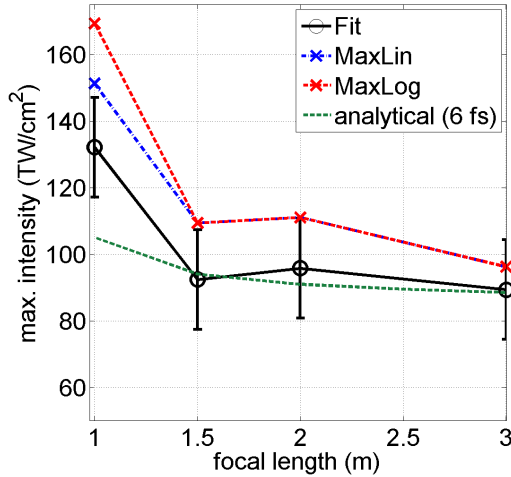


Figure 4.27: Processed results from Fig. 4.26 showing the maximum intensity along the filament in dependence of the external focusing setup. The black solid line shows the findings from the slope evaluation, whereas the blue and red-dotted lines correspond to the maximum value analysis. The green-dotted line displays the evolution of the intensity derived from the analytical Eq. (4.20) with the assumption of a 6 fs pulse being present at each maximum.

A strong variation between the results from the different experimental methods can be seen for shorter focal lengths of $f=1$ m. The analytical model is able to qualitatively reproduce this influence but shows a disagreement for the shortest focal length. The accordance to the experimental results is still much better than the value obtained by the original clamping formula $I_c \approx 60 \text{ TW/cm}^2$, which proves the benefit of the inclusion of a focusing term in Eq. (4.20).

The three-step model and the Lewenstein-model deliver slightly differing definitions of the clamping intensity. The intensity-evaluation according to the Cut-Off frequency via $E_{\text{CutOff}} = 3.17U_p + I_p$ is presented in Fig. 4.28 and yields significantly higher intensities compared to the findings from the Lewenstein-model. Consequently, care has to be taken when the three-step model formula is used to determine the intensity. The correction factor connected to the Lewenstein-model $E_{\text{CutOff}} \propto 1.3I_p$ has to be taken into account to truthfully estimate the intensity I_c . The fitting procedure is the most accurate method to determine the Cut-Off frequency. However, the variation between the applied methods for the Cut-Off readout decreases with an increasing external focusing length.

4.4.3 Conclusion

High-order harmonic radiation is able to monitor the intensity evolution along a femtocond filament with a comparable precision to the established methods. The findings agree well to the results obtained by simulations, further proving the good applicability of the numerical pulse-propagation model. Referring to Sec. 3.3.7, the results exclude the possibility to apply the ADK-model for the determination of the free electron model in the propagation code. The experimentally measured peak intensity in Fig. 4.22 shows an excellent agreement with the results from the PPT-model and differ by a factor of three with respect to the findings connected to the ADK-model. Despite their good applicability to monitor the intensity in a very precise manner along the filament, the analysis of high-order harmonic radiation has the drawback to be dependent on well tuned phase matching. This narrows the possible window along which the intensity can be analyzed by the given method. The developed analytical model can sufficiently include the effects of an external focusing setup as well as a changing pulse-duration and can be used to more precisely estimate the clamping intensity, compared to the initial estimation in Eq. 4.21.

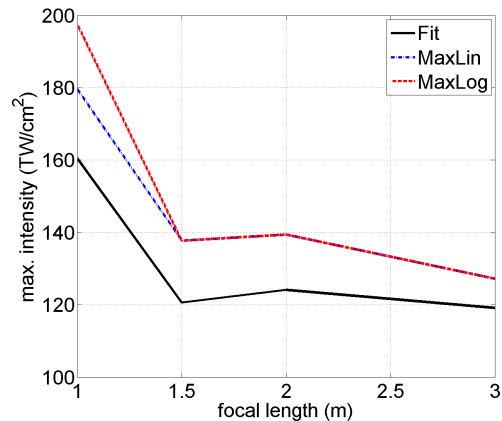


Figure 4.28: The same final dependency of the maximum intensity in the filament upon the external focusing setup using the semi-classical formula (c.f. Sec. 4.1) to obtain the intensity value inside the filament. The findings show a strong sensitivity, since the ponderomotive potential U_p is of similar strength as the ionization potential I_p .

Chapter 5

Conclusion and Outlook

In this thesis, nonlinear pulse dynamics along a femtosecond filament have been systematically investigated experimentally and numerically. The dominant spatial influence of the nonlinear effects has been determined by a spectral measurement in dependence of the external focusing. The experiments have been compared to an analytical determination of the wavefront sag, a measure for the radial curvature induced by each linear and nonlinear contribution. Hereby, spectral features have been identified which allow to distinguish between Kerr-dominated and a plasma-dominated focusing regimes of filamentation. The evaluation of the spectral width and the spectral weight allows to experimentally distinguish these two regimes.

Additionally, the temporal evolution of a pulse propagating under Kerr-dominated conditions has been studied by an analysis of the changing on-axis pulse shape. Therefore, a combination of a differential pumping stage truncating the filament and an all-vacuum SHG-FROG detection scheme have been used, allowing to analyze the pulse-evolution in-situ. The implementation of a double-pinhole setup proves to be essential for the detection system to observe the near-field dynamics of the filament. The experiments reveal a temporal splitting of the pulse-envelope along the filamentary propagation axis, accompanied with a significant self-compression from 47.2 fs to 5.25 fs. This corresponds to a self-shortening factor of 9, being the highest amount of filament-induced self-compression to date.

The comparative analysis of the detected dynamics with the outcome from numerical simulations is in good agreement. The filament's life cycle shows to decompose into three distinct stages, differentiating between a defocusing-, refocusing- and a propagation-stage. It has been demonstrated that the initial de- and refocusing effects strongly contribute to the mechanism of self-compression as they initiate the experimentally observed pulse-splitting event, showing an accordance to numerical predictions [157]. The subsequent propagation stage has been proven to decrease the pulse-duration of the propagating pulse through self-steepening dynamics. The predictions of the applied theoretical modeling have been validated by the good agreement to the experimental results. Furthermore, the

implementation of the ionization-rates according to Peremolov-Popov-Ternetev are found to be fully able to model the complex pulse dynamics correctly.

High-order harmonic generation has been applied as a tool to probe the characteristics of the pulse inside the filament using its highly nonlinear nature. A spectral splitting in the XUV-spectrum, showing a blue- and red-shifted component, has been detected and connected to two contributions: The blue-shifted XUV-radiation is directly related to a frequency-shift of the center-of-gravity of the fundamental spectrum, whereas the accumulated redshift is attributed to the self-steepening of the fundamental pulse along the filament. The shift to lower frequencies is connected to the intrinsic atomic phase of the HHG process and simulations applying the Lewenstein model were used to retrieve the exact falling slope of the pulse. Consequently, the effect of self-steepening could be tracked as it accumulates along the filament, reconstructing descending pulse-slopes that drop within one optical cycle from peak to minimum.

The phase matching between the fundamental and the harmonic frequencies has been calculated to account for the complex spatio-temporal characteristics of the filament through an adaption of the contributing phase terms. The findings refine the understanding of the harmonic emission points along the life cycle of the filament. The initial defocusing stage, albeit of carrying the highest intensity along the filament, emits no harmonic radiation due to poor phase matching conditions. Contrary, the harmonic emission along the subsequent propagation stage of the filament is in phase with the generating field. Therefore this accounts for the part of the filament that could be analyzed by high-order harmonic spectroscopy. Additionally, the influence of the fundamental pulse's chirp on the phase matching along the femtosecond filament shows, that the spectral-splitting features in the high-order harmonic spectrum can be controlled by stretching the input pulse.

The link between the HHG Cut-Off and the fundamental pulse's intensity has been used to track the peak-values of the previously reconstructed pulse-shapes. A method for a precise evaluation of the Cut-Off wavelength in the harmonic spectrum through a linear approximation of the spectral amplitude in the plateau and the Cut-Off has been introduced and its deviation from the simple detection of the highest observed wavelength has been discussed. The fundamental pulse's duration has been demonstrated to be directly linked to the evolving peak-intensity distribution along the filament. The maximum intensity along the propagation stage of the observed pulse dynamics is estimated to be 109 TW/cm^2 for focusing conditions of $f=2 \text{ m}$. Additionally, the influence of the external focusing setup on the peak intensity has been investigated, where the intensity along the filament exhibits a direct connection to the focal strength, as a longer focusing length is connected to a peak intensity of 92 TW/cm^2 ($f=3 \text{ m}$) and the shorter one increases this value to 132 TW/cm^2 ($f=1 \text{ m}$). The common analytical formula for the determination of the clamping intensity has been modified to account for the effect of an external focusing setup and yields a reasonable agreement with the experimental findings.

The presented experimental setup proves to be an ideal tool for the analysis of the complex filamentary pulse dynamics as the fundamental beam properties can be tracked directly,

revealing the mechanisms of a plasma-induced pulse break-up and self-compression. The detection of high-order harmonic radiation serves as a variable nonlinear tool to not only monitor the peak-intensity of the fundamental pulse, but also its falling slope.

Outlook

The process of self-compression along a filament allows for the generation of ultrashort pulses without the need for an external pulse-compression scheme. Along the time spend in research, various ideas for future experiments emerged to further understand and employ the complex self-shortening dynamics.

Detection of Self-CEP stabilization along a filament Previous experiments aimed at the detection of a CEP self-stabilizing effect which has been predicted in the literature and indirectly observed by utilizing HHG along a filament [73, 80]. A Stereo-ATI-phasemeter, capable of a simultaneous detection of the pulse's duration and CEP phase, has been applied. A single pinhole setup for truncation and an external - out of vacuum - pulse detection was used to characterize the pulse-shapes [60]. The findings from Sec. 3.3.6 reveal that a single pinhole scheme is not suitable for the undisturbed detection of the near-field pulse features due to the strong interaction of the differently diverging frequency components. Albeit challenging, the detection setup should be changed to utilize an all-vacuum Stereo-ATI-detection scheme applying either a double pinhole setup or a suiting spatial imaging of the near field into the pulse detection setup. This would enable, in combination with the presented methods, to extend the characterization of the filament towards a complete analysis of the fundamental pulse's duration, spectrum, intensity, slope and the CEP and could further challenge the degree of accuracy of the numerical modeling. If the predictions of the theoretical works are true, a source of self-CEP stabilized pulses from an unlocked amplifier system is possible [73].

Time-of-Flight Detection This setup, not necessarily operated with a Stereo-ATI-setup but a conventional time-of-flight spectrometer, could further elaborate on the phenomena of the clamping intensity. The detection of ATI-peaks or even ion-species is strongly dependent on the intensity and enables a qualitative scan of the relative intensity distribution along a femtosecond filament which is decoupled from the observed phase matching restrictions in the process of HHG. Therefore, the de- and refocusing stages could also be monitored for a better understanding of the stages initiating the filamentary life cycle.

External HHG Imaging of the near-field would also allow for a efficient extraction of the emerging pulses since the spatial restrictions of the second pinhole can be circumvented. The extracted and self-compressed pulse can then be applied as a driver for external HHG, leaving a free choice of the generating medium, pushing the Cut-Off to much higher energies due its direct connection to the ionization potential $E_{\max} \propto 1.3I_p$ of the medium. An external XUV-generation stage will also decouple the phase matching of HHG from the complex dynamics along the filament and could also monitor the qualitative evolution of the intensity and to some extend also the CEP along the filament. The dynamic nonlinear

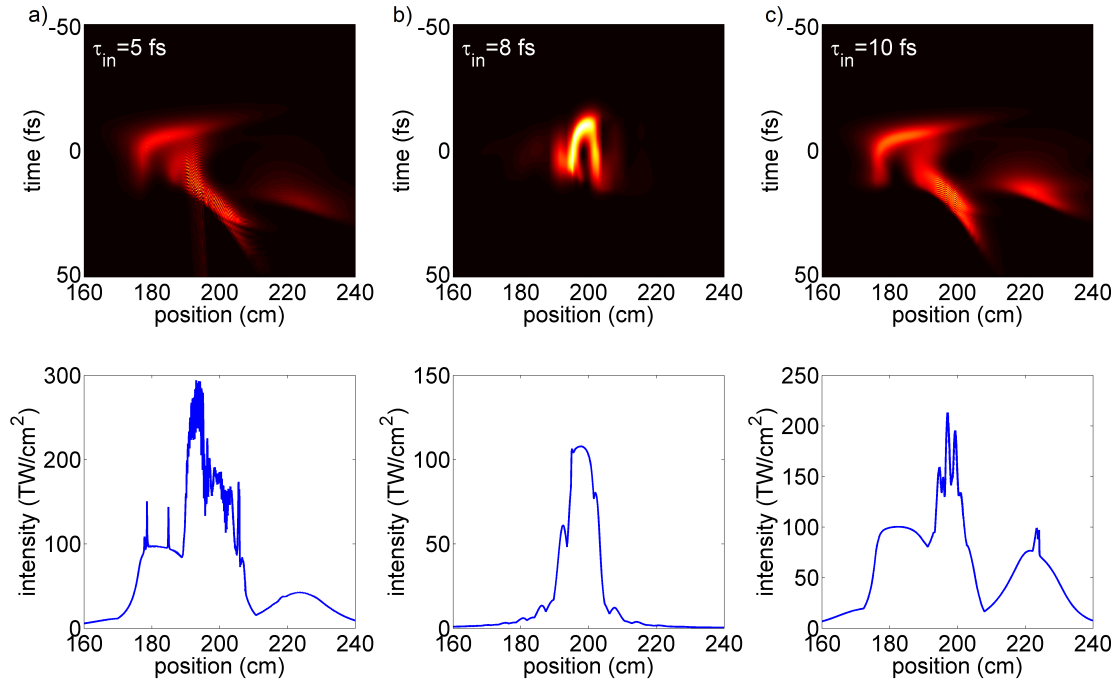


Figure 5.1: Simulated pulse propagation as a function of the input pulse duration together with the respective evolution of the on-axis intensity. The chosen pulse durations are (a) $\tau_{in}=5$ fs, (b) $\tau_{in}=8$ fs and (c) $\tau_{in}=10$ fs.

evolution of the fundamental pulse along the plasma-channel can also be further influenced to optimize the process of filamentation itself. With this approach, the generation and control of isolated attosecond pulses can be obtained without an external pulse compression scheme.

Filamentation of ultrashort pulses One possibility to strongly influence the dynamics along the filament is the manipulation of the initial pulse duration by a foregoing pulse-shortening setup. Applying a hollow-core-fiber in front of the filament would be beneficial in two ways since the spatial mode would be cleaned by the fiber setup and the pulse could be shortened down to the few-cycle regime. The influence of a changing initial pulse duration has been evaluated by numerical simulations in Fig. 5.1. The global parameters for the simulations are $f=2$ m, $p=1$ bar (Ar) and $E_{in}=0.9$ mJ. The evolving temporal shape as well as the on-axis intensity are displayed for initially Fourier-limited pulse durations of $\tau_{in}=5$, 8 or 10 fs. The temporal evolution predicts to be strongly modified for the case of $\tau_{in}=5$ fs and $\tau_{in}=10$ fs, showing prominent spikes whose origin is still unclear so far. The corresponding peak-intensity is also strongly enhanced due to the appearance of the spike-like structures. Interestingly, these structures completely vanish for $\tau_{in}=8$ fs and a less drastic change of scenery is predicted, which can be understood more intuitively. The on-axis intensity slightly increases compared to the case of 47 fs input pulses in the thesis. This is in accordance to the findings from the analytical model in Sec. 4.4.1. The propagation dynamics vanish as a smaller fraction of the pulse is defocused and suppresses

the refocusing cycle. Clearly, the dynamics can be strongly influenced by the changing pulse duration and a further investigation of the strongly varying behavior is necessary to probe the authenticity of the numerically obtained spiking features for $\tau_{\text{in}}=5$ fs and 10 fs.

Dynamics of the Medium The measurements along this thesis so far only concentrated on the dynamics of fundamental pulse and completely neglected that the medium itself can undergo unexpected dynamics during the interaction with the high-intensity pulses. These dynamics are always closely correlated to an unresolved controversy about the existence of higher-order-Kerr-terms (HOKE) in light-matter interaction [129, 130]. The unexpected saturation of the Kerr-effect has been theoretically explained by various approaches like the appearance of Kramers-Henneberger-states [132] or resonant multiphoton-ionization [236] and the significance of the HOKE approach to filamentation is still an open question [129–131, 146].

As it can be seen, there are numerous ways to further push the understanding of filamentation and multiple interesting experiments can be performed in this field.

Appendix A

Determination of Ionization Rates

A.1 Keldysh-Rates

The foundation of the theoretical description of ionization has been laid out by Keldysh on the basis of perturbation theory. As mentioned in the main body of the thesis, the so called Keldysh-parameter is used to determine whether the multiphoton- or the tunneling-ionization is predominant.

The Keldysh parameter reads as:

$$\gamma = \sqrt{I_p/2U_p}, \quad (\text{A.1})$$

connecting the ponderomotive energy $U_p = \frac{e^2 E^2}{4m_e \omega^2}$ with the ionization potential I_p .

The ionization rate $W_{Keldysh}(\gamma, \omega)$, connected to the Keldysh-theory can be calculated by:

$$W_{Keldysh}(\gamma, \omega) = A_\gamma \omega \left(\frac{I_p}{\hbar\omega}\right)^{\frac{3}{2}} \left(\frac{\gamma}{\sqrt{1+\gamma^2}}\right)^{\frac{5}{2}} \exp\left(-\frac{2I_\gamma}{\hbar\omega}(\operatorname{arcsinh} \gamma - \gamma \frac{\sqrt{1+\gamma^2}}{1+2\gamma^2})\right) S\left(\gamma, \frac{I_\gamma}{\hbar\omega}\right). \quad (\text{A.2})$$

Despite its dependency upon γ , the ionization rate is also dependent on the fundamental frequency ω and the effective ionization potential $I_\gamma = I_p(1 + \gamma^{-2}/2)$. The prefactor A_γ serves as a normalization factor (being unit-less) to account for the details of the atomic structure. The function $S(\gamma, \frac{I_\gamma}{\hbar\omega})$ is described as:

$$S(\gamma, x) = \sum_{n=0}^{\infty} \exp\left(-2(\langle x+1 \rangle - x + n)(\operatorname{arcsinh} \gamma - \frac{\gamma}{\sqrt{1+\gamma^2}})\right) \phi(y). \quad (\text{A.3})$$

Here, $\langle x \rangle$ is the integer part of x and $\phi(y) = \int_0^y e^{z^2-y^2} dz$ is the dawson-integral with $y = (\frac{2\gamma}{\sqrt{1+\gamma^2}}(\langle x+1 \rangle - x + n))^{1/2}$.

A.2 Multi-Photon Ionization-Rates

The multiphoton ionization rates are the easiest ones to obtain. They simply assume a nonlinear connection between the laser-intensity and the ionization rate by connecting these two values through a cross-section σ .

$$W_{\text{Multiphoton}} = \sigma_k I^K \quad (\text{A.4})$$

In this formula K denotes the number of photons necessary to overcome the ionization potential I_p .

The connecting factor σ_K can be taken from the literature. Coulomb interaction, atomic level shifting or resonance effects are completely ignored in this basic approach.

A.3 PPT-Theory

The group of Peremolov, Popov and Terentev tried to modify the Keldysh approach by taking care of the influence of the atomic structure and Coulomb interaction in a more elaborated way.

The ionization rate takes the form:

$$W_{PPT}(E, \omega) = \frac{I_p}{\hbar} |C_{n^*l^*}|^2 f(l, m) A_m(\omega, \gamma) \sqrt{\frac{6}{\pi}} \left(\frac{2E_0}{E\sqrt{1+\gamma^2}} \right)^{2n^*-|m|-\frac{3}{2}} \exp\left(-\frac{2E_0}{3E} g(\gamma)\right) \quad (\text{A.5})$$

This expression is again composed of many sub-expression, starting with the easiest one, the inner-atomic field strength $E_0 = I_p^{\frac{3}{2}} \frac{2\sqrt{2m_e}}{e\hbar}$.

The factor $f(l, m)$ takes the form:

$$f(l, m) = \frac{(2l+1)(l+|m|)!}{2^{|m|}|m|!(l-|m|)!} \quad (\text{A.6})$$

The mentioned factor accounts for the inner atomic structure by implementing the quantum numbers l and m into a pre-factor of the ionization rates.

The factor $g(\gamma)$ in the exponential reads as:

$$g(\gamma) = \frac{3}{2\gamma} \left[\left(1 + \frac{1}{2\gamma^2}\right) \operatorname{arcsinh} \gamma - \frac{\sqrt{1+\gamma^2}}{2\gamma} \right] \quad (\text{A.7})$$

The missing part is the factor $A_m(\omega, \gamma)$, which accounts for a similar sum as Eq.A.3 of the Keldysh-rates.

$$A_m(\omega, \gamma) = \frac{4\gamma^2}{(1 + \gamma^2)\sqrt{3\pi}|m|!} \sum_{n > I_\gamma/(\hbar\omega)}^{\infty} \exp(-\alpha(n - I_\gamma/(\hbar\omega))) \phi_{PPT}(\sqrt{\beta(n - I_\gamma/(\hbar\omega))}) \quad (\text{A.8})$$

Again, a few more expressions are needed to finally compute everything:

$$\alpha = 2(\operatorname{arcsinh} \gamma - \frac{\gamma}{\sqrt{1 + \gamma^2}}) \quad (\text{A.9})$$

$$\beta = \frac{2\gamma}{\sqrt{1 + \gamma^2}} \quad (\text{A.10})$$

and

$$\phi_{PPT}(x) = e^{-x^2} \int_0^x e^{y^2} (x^2 - y^2)^{|m|} dy \quad (\text{A.11})$$

The computed values fit well to experimentally obtained ionization rates. The last unknown fitting parameter is the pre-factor $|C_{n^*l^*}|$.

A.4 ADK-Theory

The findings from Ammosov, Delone and Krainov revealed an explicit representation for the pre-factor $|C_{n^*l^*}|$, completing the above formalism.

$$|C_{n^*l^*}|^2 = \frac{2^{2n^*}}{n^*\Gamma(n^* + l^* + 1)\Gamma(n^* - l^*)} \quad (\text{A.12})$$

Here, $\Gamma(x)$ is the Euler-Gamma-function. The placeholders n^* and l^* are the principal and orbital quantum numbers, with $n^* = Z\sqrt{\frac{I_p}{I_p - H}}$. In this simple expression, Z denotes the charge of ionization degree (meaning, that if the resulting ionization state will be +1, then $Z=1$) and I_{p-H} is the ionization potential of the hydrogen atom.

The works by ADK, also resulted in a formula, solely adapted for the tunneling regime of ionization.

$$W_{ADK}(E) = \sqrt{\frac{6}{\pi}} f(l, m) |C_{n^*l^*}|^2 \frac{I_p}{\hbar} \left(\frac{2E_0}{E}\right)^{2n^* - |m| - 3/2} \exp\left(-\frac{2E_0}{3E}\right) \quad (\text{A.13})$$

The ADK-formalism can be used to gauge the fitting parameter A_γ in the Keldysh-theory, by forcing an overlap of the calculated ionization rates at high intensities.

The resulting A_γ take values of 3.5, 15, 30 and 40 for helium, neon, argon and krypton respectively.

The ionization rates (being proportional to t^{-1}) are connected to electron densities through rate equations, following the assumption, that the changing electron density ρ_e can be expressed as $\partial_t \rho_e = W(I)(\rho_{nt} - \rho_e)$. The resulting $\rho_e(t)$, then reads as:

$$\rho_e(t) = \rho_{nt} \left(1 - \exp \left(\int_{-\infty}^t W(t') dt' \right) \right) \quad (\text{A.14})$$

Appendix B

Calculation of the wavefront sag

In this section, the definition of the various wavefront sag contributions are explained in more detail. The geometrical wavefront sag S_g can easily be calculated by putting together the values sketched in Fig. B.1 into the sentence of Pythagoras. As a result, $R(z)^2 = (R(z) - S_g)^2 + w(z)^2$ is obtained. Solving for S_g yields $S_g = R(z) - \sqrt{R(z)^2 - w(z)^2}$. Expanding this expression finally yields:

$$S_g \approx R(z) - R(z) \left(1 - \frac{w(z)}{2R(z)^2} + \dots \right) \approx \frac{w(z)^2}{2R(z)^2}. \quad (\text{B.1})$$

This formula can further be simplified, using the relations $R(z) = z(1 + (\frac{z_r}{z})^2)$ and $w(z) = w_0 \sqrt{1 + (\frac{z}{z_r})^2}$ to yield the formula used throughout the thesis (note, that the zero-position is shifted from $z=0$ to $z=f$):

$$S_g = \frac{w_0^2}{2z_r^2} (z - f). \quad (\text{B.2})$$

The nonlinear contributions are calculated in a more simple manner, as they are not reduced to an analytical formula (as done in [144]), but instead are evaluated directly by solving the integral connected to the wavefront sag $S_{\text{nonlinear}} = \int_0^z \Delta n(z') dz'$. The expressions can be squeezed to result analytical expressions, however, the implementation of the integral in MATLAB is much simpler.

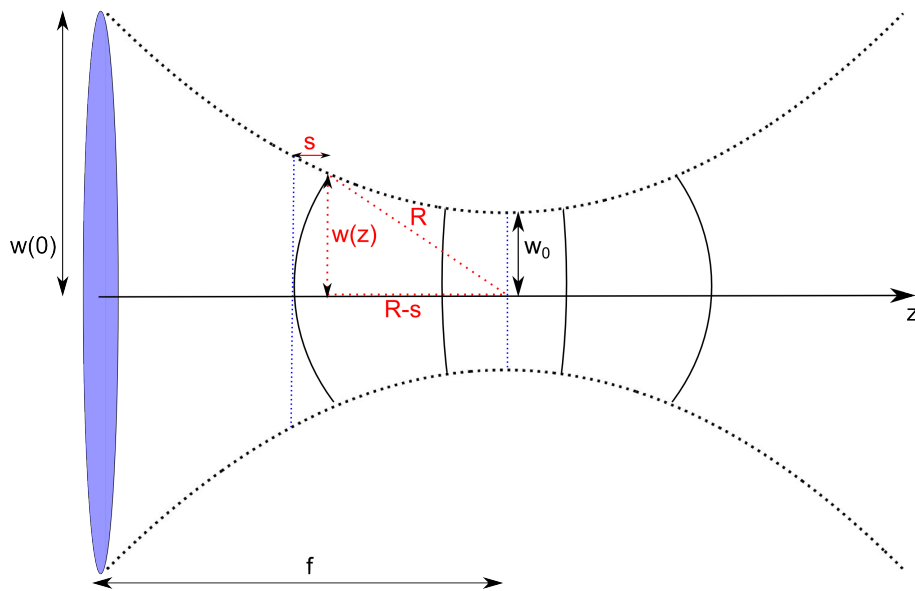


Figure B.1: Sketch describing the basic idea behind the calculation of the wavefront sag at the hand of a focused Gaussian beam. The wavefront sag follows the wavefront curvature which is imprinted by the focusing optic and shows a decreasing behavior as it reaches the focus.

Bibliography

- [1] T. Brabec and F. Krausz, “Intense few-cycle laser fields: Frontiers of nonlinear optics,” *Rev. Mod. Phys.*, vol. 72, no. 2, pp. 545–591, 2000.
- [2] F. Krausz and M. Ivanov, “Attosecond physics,” *Rev. Mod. Phys.*, vol. 81, pp. 163–234, Feb 2009.
- [3] W. Sibbett, A. A. Lagatsky, and C. T. A. Brown, “The development and application of femtosecond laser systems,” *Opt. Express*, vol. 20, pp. 6989–7001, Mar 2012.
- [4] R. Dörner, V. Mergel, O. Jagutzki, L. Spielberger, J. Ullrich, R. Moshhammer, and H. Schmidt-Böcking, “Cold target recoil ion momentum spectroscopy: a momentum microscope to view atomic collision dynamics,” *Physics Reports*, vol. 330, no. 2-3, pp. 95 – 192, 2000.
- [5] M. Hentschel, R. Kienberger, C. Spielmann, G. A. Reider, N. Milosevic, T. Brabec, P. Corkum, U. Heinzmann, M. Drescher, and F. Krausz, “Attosecond metrology,” *Nature*, vol. 414, pp. 509–513, 2001.
- [6] M. R. Leahy-Hoppa, J. Miragliotta, R. Oslander, J. Burnett, Y. Dikmelik, C. McEnnis, and J. B. Spicer, “Ultrafast laser-based spectroscopy and sensing: applications in libs, cars and thz spectroscopy,” *Sensors (Basel, Switzerland)*, vol. 10, no. 5, pp. 4342–4372, 2010.
- [7] A. H. Zewail, “Femtochemistry: Atomic-scale dynamics of the chemical bond,” *The Journal of Physical Chemistry A*, vol. 104, no. 24, pp. 5660–5694, 2000.
- [8] S. Pedersen, J. Herek, and A. Zewail, “The validity of the diradical hypothesis: Direct femtosecond studies of the transition-state structures,” *Science*, vol. 266, pp. 1359–1364, 1994.
- [9] G. Cerullo, G. Lanzani, M. Muccini, C. Taliani, and S. De Silvestri, “Real-time vibronic coupling dynamics in a prototypical conjugated oligomer,” *Phys. Rev. Lett.*, vol. 83, pp. 231–234, Jul 1999.
- [10] A. Sugita, T. Saito, H. Kano, M. Yamashita, and T. Kobayashi, “Wave packet dynamics in a quasi-one-dimensional metal-halogen complex studied by ultrafast time-resolved spectroscopy,” *Phys. Rev. Lett.*, vol. 86, pp. 2158–2161, Mar 2001.

- [11] O. D. Mücke, T. Tritschler, M. Wegener, U. Morgner, and F. X. Kärtner, “Signatures of carrier-wave rabi flopping in gaas,” *Phys. Rev. Lett.*, vol. 87, p. 057401, Jul 2001.
- [12] F. Calegari, C. Vozzi, S. D. Silvestri, and S. Stagira, “Molecular rotovibrational dynamics excited in optical filamentation,” *Opt. Lett.*, vol. 33, pp. 2922–2924, Dec 2008.
- [13] J. Odhner and R. Levis, “Optical spectroscopy using gas-phase femtosecond laser filamentation,” *Annual Review of Physical Chemistry*, vol. 65, no. 1, pp. 605–628, 2014. PMID: 24423375.
- [14] W. Drexler, U. Morgner, F. X. Kärtner, C. Pitris, S. A. Boppart, X. D. Li, E. P. Ippen, and J. G. Fujimoto, “In vivo ultrahigh-resolution optical coherence tomography,” *Opt. Lett.*, vol. 24, pp. 1221–1223, Sep 1999.
- [15] U. Morgner, W. Drexler, F. X. Kärtner, X. D. Li, C. Pitris, E. P. Ippen, and J. G. Fujimoto, “Spectroscopic optical coherence tomography,” *Opt. Lett.*, vol. 25, pp. 111–113, Jan 2000.
- [16] F. Shimizu, “Frequency broadening in liquids by a short light pulse,” *Phys. Rev. Lett.*, vol. 19, pp. 1097–1100, Nov 1967.
- [17] R. R. Alfano and S. L. Shapiro, “Observation of self-phase modulation and small-scale filaments in crystals and glasses,” *Phys. Rev. Lett.*, vol. 24, pp. 592–594, Mar 1970.
- [18] R. H. Stolen and C. Lin, “Self-phase-modulation in silica optical fibers,” *Phys. Rev. A*, vol. 17, pp. 1448–1453, Apr 1978.
- [19] R. L. Fork, C. H. B. Cruz, P. C. Becker, and C. V. Shank, “Compression of optical pulses to six femtoseconds by using cubic phase compensation,” *Opt. Lett.*, vol. 12, pp. 483–485, Jul 1987.
- [20] O. Martinez, “3000 times grating compressor with positive group velocity dispersion: Application to fiber compensation in 1.3-1.6 μm region,” *IEEE J. Quantum. Electron.*, vol. 23, pp. 59 – 64, Jan 1987.
- [21] G. Veith, “Useful and detrimental aspects of self-phase modulation in fiber optical applications,” *Fiber and Integrated Optics*, vol. 7, no. 3, pp. 205–215, 1988.
- [22] U. Morgner, F. Kärtner, S.-H. Cho, Y. Chen, H. A. Haus, J. G. Fujimoto, E. P. Ippen, V. Scheuer, G. Angelow, and T. Tschudi, “Sub-two-cycle pulses from a kerr-lens mode-locked ti: sapphire laser,” *Optics letters*, vol. 24, no. 6, pp. 411–413, 1999.
- [23] R. R. Alfano, *The Supercontinuum Laser Source*. 978-0-387-25097-7, Springer New York, 2006.

-
- [24] S. Rausch, T. Binhammer, A. Harth, J. Kim, R. Ell, F. X. Kärtner, and U. Morgner, “Controlled waveforms on the single-cycle scale from a femtosecond oscillator,” *Opt. Express*, vol. 16, pp. 9739–9745, Jun 2008.
- [25] T. Sudmeyer, S. V. Marchese, S. Hashimoto, C. R. E. Baer, G. Gingras, B. Witzel, and U. Keller, “Femtosecond laser oscillators for high-field science,” *Nat Photon*, vol. 2, pp. 599–604, Oct. 2008.
- [26] D. Strickland and G. Mourou, “Compression of amplified chirped optical pulses,” *Opt. Commun.*, vol. 55, no. 6, pp. 447 – 449, 1985.
- [27] M. Nisoli, S. De Silvestri, and O. Svelto, “Generation of high energy 10 fs pulses by a new pulse compression technique,” *Applied Physics Letters*, vol. 68, no. 20, pp. 2793–2795, 1996.
- [28] T. Nagy and P. Simon, “Generation of 200- μ mandsub-25-fs deep-uv pulses using a noble-gas-filled hollow fiber,” *Opt. Lett.*, vol. 34, pp. 2300–2302, Aug 2009.
- [29] T. Nagy, V. Pervak, and P. Simon, “Optimal pulse compression in long hollow fibers,” *Opt. Lett.*, vol. 36, pp. 4422–4424, Nov 2011.
- [30] R. Szipöcs, C. Spielmann, F. Krausz, and K. Ferencz, “Chirped multilayer coatings for broadband dispersion control in femtosecond lasers,” *Opt. Lett.*, vol. 19, pp. 201–203, Feb 1994.
- [31] A. Stingl, R. Szipöcs, M. Lenzner, C. Spielmann, and F. Krausz, “Sub-10-fs mirror-dispersion-controlled ti:sapphire laser,” *Opt. Lett.*, vol. 20, pp. 602–604, Mar 1995.
- [32] M. Nisoli, S. de Silvestri, O. Svelto, R. Szipecs, K. Ferencz, C. Spielmann, S. Sartania, and F. Krausz, “Compression of high-energy laser pulses below 5 fs,” *Opt. Lett.*, vol. 22, pp. 522–524, 1997.
- [33] F. X. Kärtner, U. Morgner, R. Ell, T. Schibli, J. G. Fujimoto, E. P. Ippen, V. Scheuer, G. Angelow, and T. Tschudi, “Ultrabroadband double-chirped mirror pairs for generation of octave spectra,” *J. Opt. Soc. Am. B*, vol. 18, pp. 882–885, 2001.
- [34] L. Gallmann, T. Pfeifer, M. J. Abel, P. M. Nagel, D. M. Neumark, and S. R. Leone, “Direct comparison of the hollow-core fiber and filamentation techniques for few-cycle pulse generation,” in *15th International Conference on Ultrafast Phenomena*, p. MH18, Optical Society of America, 2006.
- [35] P. B. Corkum, “Plasma perspective on strong-field multiphoton ionization,” *Phys. Rev. Lett.*, vol. 71, no. 13, pp. 1994–1997, 1993.
- [36] M. Lewenstein, P. Balcou, M. Y. Ivanov, A. L’Huillier, and P. B. Corkum, “Theory of high-harmonic generation by low-frequency laser fields,” *Phys. Rev. A*, vol. 49, no. 3, pp. 2117–2132, 1994.

- [37] P. Salières, A. L’Huillier, and M. Lewenstein, “Coherence control of high-order harmonics,” *Phys. Rev. Lett.*, vol. 74, no. 19, p. 3776, 1995.
- [38] A. Rundquist, C. G. Durfee, Z. Chang, C. Herne, S. Backus, M. M. Murnane, and H. C. Kapteyn, “Phase-matched generation of coherent soft x-rays,” *Science*, vol. 280, p. 1412, 1998.
- [39] N. Papadogiannis, C. Kalpouzos, E. Goulielmakis, G. Nersisyan, D. Charalambidis, F. Augé, F. Weihe, and P. Balcou, “Kilohertz extreme-ultraviolet light source based on femtosecond high-order harmonic generation from noble gases,” *Appl. Phys. B*, vol. 73, pp. 687–692, 2001.
- [40] J. Sutherland, E. Christensen, N. Powers, S. Rhynard, J. Painter, and J. Peatross, “High harmonic generation in a semi-infinite gas cell,” *Opt. Exp.*, vol. 12, pp. 4430–4436, Sep 2004.
- [41] D. S. Steingrube, T. Vockerodt, E. Schulz, U. Morgner, and M. Kovačev, “Phase-matching of high-order harmonics in a semi-infinite gas cell,” *Phys. Rev. A*, vol. 80, p. 043819, 2009.
- [42] M. Kretschmar, C. Hernández-García, D. S. Steingrube, L. Plaja, U. Morgner, and M. Kovačev, “Spatial contributions of electron trajectories to high-order-harmonic radiation originating from a semi-infinite gas cell,” *Phys. Rev. A*, vol. 88, p. 013805, Jul 2013.
- [43] M. Bellini, C. Lyngaa, A. Tozzi, M. B. Gaarde, T. W. Hänsch, A. L’Huillier, and C.-G. Wahlström, “Temporal coherence of ultrashort high-order harmonic pulses,” *Phys. Rev. Lett.*, vol. 81, pp. 297–300, Jul 1998.
- [44] M. B. Gaarde, F. Salin, E. Constant, P. Balcou, K. J. Schafer, K. C. Kulander, and A. L’Huillier, “Spatiotemporal separation of high harmonic radiation into two quantum path components,” *Phys. Rev. A*, vol. 59, pp. 1367–1373, Feb 1999.
- [45] M. B. Gaarde and K. J. Schafer, “Quantum path distributions for high-order harmonics in rare gas atoms,” *Phys. Rev. A*, vol. 65, p. 031406, Mar 2002.
- [46] Y. Mairesse, A. de Bohan, L. J. Frasinski, H. Merdji, L. C. Dinu, P. Monchicourt, P. Breger, M. Kovacev, R. T. B. Carre, H. G. Muller, P. Agostini, and P. Salieres, “Attosecond synchronization of high-harmonic soft x-rays,” *Science*, vol. 302, p. 1540, 2003.
- [47] E. Goulielmakis, M. Schultze, M. Hofstetter, V. S. Yakovlev, J. Gagnon, M. Uiberacker, A. L. Aquila, E. M. Gullikson, D. T. Attwood, R. Kienberger, F. Krausz, and U. Kleineberg, “Single-cycle nonlinear optics,” *Science*, vol. 320, p. 1614, 2008.
- [48] K. Zhao, Q. Zhang, M. Chini, Y. Wu, X. Wang, and Z. Chang, “Tailoring a 67 attosecond pulse through advantageous phase-mismatch,” *Opt. Lett.*, vol. 37, pp. 3891–3893, Sep 2012.

- [49] H. J. Wörner, J. B. Bertrand, D. V. Kartashov, P. B. Corkum, and D. M. Villeneuve, “Following a chemical reaction using high-harmonic interferometry,” *Nature*, vol. 466, no. 7306, pp. 604–607, 2010.
- [50] R. Torres, T. Siegel, L. Brugnera, I. Procino, J. G. Underwood, C. Altucci, R. Velotta, E. Springate, C. Froud, I. C. E. Turcu, M. Y. Ivanov, O. Smirnova, and J. P. Marangos, “Extension of high harmonic spectroscopy in molecules by a 1300 nm laser field,” *Opt. Express*, vol. 18, pp. 3174–3180, Feb 2010.
- [51] T. T. Luu, M. Garg, S. Y. Kruchinin, A. Moulet, M. T. Hassan, and E. Goulielmakis, “Extreme ultraviolet high-harmonic spectroscopy of solids,” *Nature*, vol. 521, pp. 498–502, 2015.
- [52] I. J. Sola, E. Mevel, L. Elouga, E. Constant, V. Strelkov, L. Poletto, P. Villoresi, E. Benedetti, J. P. Caumes, S. Stagira, C. Vozzi, G. Sansone, and M. Nisoli, “Controlling attosecond electron dynamics by phase-stabilized polarization gating,” *Nat. Phys.*, vol. 2, no. 5, pp. 319–322, 2006.
- [53] H. J. Wörner, J. B. Bertrand, D. V. Kartashov, P. B. Corkum, and D. M. Villeneuve, “Following a chemical reaction using high-harmonic interferometry,” *Nature*, vol. 466, no. 7306, pp. 604–607, 2010.
- [54] E. Goulielmakis, Z.-H. Loh, A. Wirth, R. Santra, Rohringer, V. S. Yakovlev, S. Zherebtsov, T. Pfeifer, A. M. Azzeer, M. F. Kling, S. R. Leone, and F. Krausz, “Real-time observation of valence electron motion,” *Nature*, vol. 466, pp. 739–743, 2010.
- [55] H. J. Wörner, J. B. Bertrand, B. Fabre, J. Higuët, H. Ruf, A. Dubrouil, S. Patchkovskii, M. Spanner, Y. Mairesse, V. Blanchet, E. Mével, E. Constant, P. B. Corkum, and D. M. Villeneuve, “Conical intersection dynamics in no2 probed by homodyne high-harmonic spectroscopy,” *Science*, vol. 334, no. 6053, pp. 208–212, 2011.
- [56] J. Marburger, “Self-focusing: Theory,” *Prog. Quant. Electr.*, vol. 4, no. Part 1, pp. 35 – 110, 1975.
- [57] A. Braun, G. Korn, X. Liu, D. Du, J. Squier, and G. Mourou, “Self-channeling of high-peak-power femtosecond laser pulses in air,” *Opt. Lett.*, vol. 20, pp. 73–75, Jan 1995.
- [58] A. Couairon and A. Mysyrowicz, “Femtosecond filamentation in transparent media,” *Physics Reports*, vol. 441, no. 2-4, pp. 47 – 189, 2007.
- [59] C. P. Hauri, W. Kornelis, F. W. Helbing, A. Couairon, A. Mysyrowicz, J. Biegert, and U. Keller, “Generation of intense carrier-envelope phase-locked few-cycle laser pulses through filamentation,” *Appl. Phys. B*, vol. 79, pp. 673–677, 2004.

- [60] D. S. Steingrube, M. Kretschmar, D. Hoff, E. Schulz, T. Binhammer, P. Hansinger, G. G. Paulus, U. Morgner, and M. Kovačev, “Sub-1.5-cycle pulses from a single filament,” *Opt. Express*, vol. 20, pp. 24049–24058, Oct 2012.
- [61] J. Kasparian, R. Sauerbrey, and S. Chin, “The critical laser intensity of self-guided light filaments in air,” *Appl. Phys. B*, vol. 71, p. 877, 2000.
- [62] A. Becker, N. Aközbeke, K. Vijayalakshmi, E. Oral, C. Bowden, and S. Chin, “Intensity clamping and re-focusing of intense femtosecond laser pulses in nitrogen molecular gas,” *Appl. Phys. B*, vol. 73, no. 3, pp. 287–290, 2001.
- [63] W. Liu, S. Petit, A. Becker, N. Akzbeke, C. Bowden, and S. Chin, “Intensity clamping of a femtosecond laser pulse in condensed matter,” *Optics Communications*, vol. 202, no. 1-3, pp. 189 – 197, 2002.
- [64] S. L. Chin, Y. Chen, O. Kosareva, V. P. Kandidov, and F. Théberge, “What is a filament?,” *Laser Physics*, vol. 18, no. 8, pp. 962–964, 2008.
- [65] S. I. Mitryukovskiy, Y. Liu, A. Houard, and A. Mysyrowicz, “Re-evaluation of the peak intensity inside a femtosecond laser filament in air,” *Journal of Physics B: Atomic, Molecular and Optical Physics*, vol. 48, no. 9, p. 094003, 2015.
- [66] E. T. J. Nibbering, P. F. Curley, G. Grillon, B. S. Prade, M. A. Franco, F. Salin, and A. Mysyrowicz, “Conical emission from self-guided femtosecond pulses in air,” *Opt. Lett.*, vol. 21, pp. 62–65, 1996.
- [67] A. Brodeur, C. Y. Chien, F. A. Ilkov, S. L. Chin, O. G. Kosareva, and V. P. Kandidov, “Moving focus in the propagation of ultrashort laser pulses in air,” *Optics Letters*, vol. 22, no. 5, pp. 304–306, 1997.
- [68] M. Mlejnek, E. M. Wright, and J. V. Moloney, “Dynamic spatial replenishment of femtosecond pulses propagating in air,” *Opt. Lett.*, vol. 23, pp. 382–384, Mar 1998.
- [69] M. Kolesik, J. V. Moloney, and M. Mlejnek, “Unidirectional optical pulse propagation equation,” *Phys. Rev. Lett.*, vol. 89, p. 283902, Dec 2002.
- [70] M. Kolesik and J. Moloney, “Nonlinear optical pulse propagation simulation: From maxwells to unidirectional equations,” *Phys. Rev. E*, vol. 70, p. 033604, 2004.
- [71] A. Couairon, J. Biegert, C. P. Hauri, W. Kornelis, F. W. Helbing, U. Keller, and A. Mysyrowicz, “Self-compression of ultra-short laser pulses down to one optical cycle by filamentation,” *J. Mod. Opt.*, vol. 53, no. 1, pp. 75–85, 2006.
- [72] C. Brée, A. Demircan, S. Skupin, L. Bergé, and G. Steinmeyer, “Self-pinching of pulsed laser beams during filamentary propagation,” *Opt. Express*, vol. 17, pp. 16429–16435, Sep 2009.

-
- [73] A. Couairon, H. S. Chakraborty, and M. B. Gaarde, “From single-cycle self-compressed filaments to isolated attosecond pulses in noble gases,” *Phys. Rev. A*, vol. 77, p. 053814, 2008.
- [74] G. Stibenz, N. Zhavoronkov, and G. Steinmeyer, “Self-compression of millijoule pulses to 7.8 fs duration in a white-light filament,” *Opt. Lett.*, vol. 31, pp. 274–276, Jan 2006.
- [75] S. Skupin, G. Stibenz, L. Bergé, F. Lederer, T. Sokollik, M. Schnürer, N. Zhavoronkov, and G. Steinmeyer, “Self-compression by femtosecond pulse filamentation: Experiments versus numerical simulations,” *Phys. Rev. E*, vol. 74, p. 056604, Nov 2006.
- [76] J. Bethge, C. Brée, H. Redlin, G. Stibenz, P. Staudt, G. Steinmeyer, A. Demircan, and S. Duesterer, “Self-compression of 120 fs pulses in a white-light filament,” *Journal of Optics*, vol. 13, no. 5, p. 055203, 2011.
- [77] L. Bergé, S. Skupin, R. Nuter, J. Kasparian, and J.-P. Wolf, “Ultrashort filaments of light in weakly ionized and optically transparent media,” *Reports on Progress in Physics*, vol. 70, no. 10, p. 1633, 2007.
- [78] D. Faccio, A. Matijosius, A. Dubietis, R. Piskarskas, A. Varanavičius, E. Gaizauskas, A. Piskarskas, A. Couairon, and P. Di Trapani, “Near- and far-field evolution of laser pulse filaments in kerr media,” *Phys. Rev. E*, vol. 72, p. 037601, Sep 2005.
- [79] O. Kosareva, N. Panov, D. Uryupina, M. Kurilova, A. Mazhorova, A. Savel’ev, R. Volkov, V. Kandidov, and S. Chin, “Optimization of a femtosecond pulse self-compression region along a filament in air,” *Applied Physics B*, vol. 91, no. 1, pp. 35–43, 2008.
- [80] D. S. Steingrube, E. Schulz, T. Binhammer, M. B. Gaarde, A. Couairon, U. Morgner, and M. Kovačev, “High-order harmonic generation directly from a filament,” *New J. Phys.*, vol. 13, no. 4, p. 043022, 2011.
- [81] T. Vockerodt, D. S. Steingrube, E. Schulz, M. Kretschmar, U. Morgner, and M. Kovačev, “Low- and high-order harmonic generation inside an air filament,” *Applied Physics B*, vol. 106, no. 3, pp. 529–532, 2012.
- [82] E. Schulz, D. S. Steingrube, T. Binhammer, M. B. Gaarde, A. Couairon, U. Morgner, and M. Kovačev, “Tracking spectral shapes and temporal dynamics along a femtosecond filament,” *Phys. Rev. A*, 2011. submitted.
- [83] H. R. Lange, A. Chiron, J.-F. Ripoche, A. Mysyrowicz, P. Breger, and P. Agostini, “High-order harmonic generation and quasiphase matching in xenon using self-guided femtosecond pulses,” *Phys. Rev. Lett.*, vol. 81, pp. 1611–1613, Aug 1998.

- [84] U. K. Sapaev, I. Babushkin, and J. Herrmann, “Quasi-phase-matching for third harmonic generation in noble gases employing ultrasound,” *Opt. Express*, vol. 20, pp. 22753–22762, Sep 2012.
- [85] L. Shi, W. Li, H. Zhou, D. Wang, L. Ding, and H. Zeng, “Generation of multicolor vacuum ultraviolet pulses through four-wave sum-frequency mixing in argon,” *Phys. Rev. A*, vol. 88, p. 053825, Nov 2013.
- [86] S. Tzortzakis, D. Anglos, and D. Gray, “Ultraviolet laser filaments for remote laser-induced breakdown spectroscopy (libs) analysis: applications in cultural heritage monitoring,” *Opt. Lett.*, vol. 31, pp. 1139–1141, Apr 2006.
- [87] J.-F. Daigle, Y. Kamali, G. Roy, and S. L. Chin, “Remote filament-induced fluorescence spectroscopy from thin clouds of smoke,” *Applied Physics B*, vol. 93, no. 4, pp. 759–762, 2008.
- [88] S. L. Chin, H. L. Xu, Q. Luo, F. Theberge, W. Liu, J. F. Daigle, Y. Kamali, P. T. Simard, J. Bernhardt, S. A. Hosseini, M. Sharifi, G. Mejean, A. Azarm, C. Marceau, O. Kosareva, V. P. Kandidov, N. Akozbek, A. Becker, G. Roy, P. Mathieu, J. R. Simard, M. Chateaufneuf, and J. Dubois, “Filamentation "remote" sensing of chemical and biological agents or pollutants using only one femtosecond laser source,” *Applied Physics B*, vol. 95, no. 1, pp. 1–12, 2009.
- [89] I. Babushkin, W. Kuehn, C. Köhler, S. Skupin, L. Bergé, K. Reimann, M. Woerner, J. Herrmann, and T. Elsaesser, “Ultrafast spatiotemporal dynamics of terahertz generation by ionizing two-color femtosecond pulses in gases,” *Phys. Rev. Lett.*, vol. 105, p. 053903, Jul 2010.
- [90] L. Bergé, S. Skupin, C. Köhler, I. Babushkin, and J. Herrmann, “3d numerical simulations of thz generation by two-color laser filaments,” *Phys. Rev. Lett.*, vol. 110, p. 073901, Feb 2013.
- [91] A. D. Koulouklidis, V. Y. Fedorov, and S. Tzortzakis, “Spectral bandwidth scaling laws and reconstruction of thz wave packets generated from two-color laser plasma filaments,” *Phys. Rev. A*, vol. 93, p. 033844, Mar 2016.
- [92] J. C. Maxwell, “A dynamical theory of the electromagnetic field,” *Philosophical Transactions of the Royal Society of London*, vol. 155, pp. 459–512, 1865.
- [93] R. L. Byer, “Nonlinear optical phenomena and materials,” *Annual Review of Materials Science*, vol. 4, no. 1, pp. 147–190, 1974.
- [94] R. de L. Kronig, “On the theory of dispersion of x-rays,” *J. Opt. Soc. Am.*, vol. 12, pp. 547–557, Jun 1926.
- [95] J. N. Lalena, “From quartz to quasicrystals: probing nature’s geometric patterns in crystalline substances,” *Crystallography Reviews*, vol. 12, no. 2, pp. 125–180, 2006.

- [96] Y. R. Shen and M. M. T. Loy, “Theoretical interpretation of small-scale filaments of light originating from moving focal spots,” *Phys. Rev. A*, vol. 3, pp. 2099–2105, Jun 1971.
- [97] R. Y. Chiao, E. Garmire, and C. H. Townes, “Self-trapping of optical beams,” *Phys. Rev. Lett.*, vol. 13, pp. 479–482, Oct 1964.
- [98] G. Fibich and A. L. Gaeta, “Critical power for self-focusing in bulk media and in hollow waveguides,” *Opt. Lett.*, vol. 25, pp. 335–337, Mar 2000.
- [99] P. Agostini, G. Barjot, J. Bonnal, G. Mainfray, C. Manus, and J. Morellec, “Multiphoton ionization of hydrogen and rare gases,” *IEEE Journal of Quantum Electronics*, vol. 4, pp. 667–669, Oct 1968.
- [100] L. V. Keldysh, “Ionization in the field of a strong electromagnetic wave,” *Sov. Phys. JETP*, vol. 20, pp. 1307–1314, 1965.
- [101] G. Mainfray and G. Manus, “Multiphoton ionization of atoms,” *Reports on Progress in Physics*, vol. 54, no. 10, p. 1333, 1991.
- [102] M. V. Ammosov, N. B. Delone, and V. P. Krainov, “Tunnel ionization of complex atoms and of atomic ions in an alternating electromagnetic field,” *Sov. Phys. JETP*, vol. 64, p. 1191, 1986.
- [103] A. M. Perelomov, V. S. Popov, and M. V. Terentev, “Ionization of atoms in an alternating electric field,” *Sov. Phys. JETP*, vol. 23, no. 5, pp. 924–934, 1966.
- [104] G. L. Yudin and M. Y. Ivanov, “Nonadiabatic tunnel ionization: Looking inside a laser cycle,” *Phys. Rev. A*, vol. 64, p. 013409, Jun 2001.
- [105] J. L. Krause, K. J. Schafer, and K. C. Kulander, “High-order harmonic generation from atoms and ions in the high intensity regime,” *Phys. Rev. Lett.*, vol. 68, no. 24, pp. 3535–3538, 1992.
- [106] D. Bauer and P. Mulser, “Exact field ionization rates in the barrier-suppression regime from numerical time-dependent schrödinger-equation calculations,” *Phys. Rev. A*, vol. 59, pp. 569–577, Jan 1999.
- [107] F. Yan-Zhuo, Z. Song-Feng, and Z. Xiao-Xin, “Multiphoton and tunneling ionization of atoms in an intense laser field,” *Chinese Physics B*, vol. 21, no. 11, p. 113101, 2012.
- [108] S.-F. Zhao, L. Liu, and X.-X. Zhou, “Multiphoton and tunneling ionization probability of atoms and molecules in an intense laser field,” *Optics Communications*, vol. 313, pp. 74 – 79, 2014.
- [109] R. Wiehle, B. Witzel, H. Helm, and E. Cormier, “Dynamics of strong-field above-threshold ionization of argon: Comparison between experiment and theory,” *Phys. Rev. A*, vol. 67, p. 063405, Jun 2003.

- [110] J. Muth-Böhm, A. Becker, and F. H. M. Faisal, “Suppressed molecular ionization for a class of diatomics in intense femtosecond laser fields,” *Phys. Rev. Lett.*, vol. 85, pp. 2280–2283, Sep 2000.
- [111] I. V. Litvinyuk, K. F. Lee, P. W. Dooley, D. M. Rayner, D. M. Villeneuve, and P. B. Corkum, “Alignment-dependent strong field ionization of molecules,” *Phys. Rev. Lett.*, vol. 90, p. 233003, Jun 2003.
- [112] J. Wu, H. Zeng, and C. Guo, “Comparison study of atomic and molecular single ionization in the multiphoton ionization regime,” *Phys. Rev. Lett.*, vol. 96, p. 243002, Jun 2006.
- [113] H. Kang, W. Quan, Y. Wang, Z. Lin, M. Wu, H. Liu, X. Liu, B. B. Wang, H. J. Liu, Y. Q. Gu, X. Y. Jia, J. Liu, J. Chen, and Y. Cheng, “Structure effects in angle-resolved high-order above-threshold ionization of molecules,” *Phys. Rev. Lett.*, vol. 104, p. 203001, May 2010.
- [114] K. Burnett, P. L. Knight, B. R. M. Piraux, and V. C. Reed, “Suppression of ionization in strong laser fields,” *Phys. Rev. Lett.*, vol. 66, pp. 301–304, Jan 1991.
- [115] A. Scrinzi, M. Geissler, and T. Brabec, “Ionization above the coulomb barrier,” *Phys. Rev. Lett.*, vol. 83, pp. 706–709, Jul 1999.
- [116] X. M. Tong and C. D. Lin, “Empirical formula for static field ionization rates of atoms and molecules by lasers in the barrier-suppression regime,” *Journal of Physics B: Atomic, Molecular and Optical Physics*, vol. 38, no. 15, p. 2593, 2005.
- [117] Q. Zhang, P. Lan, and P. Lu, “Empirical formula for over-barrier strong-field ionization,” *Phys. Rev. A*, vol. 90, p. 043410, Oct 2014.
- [118] S. L. Chin, *Femtosecond Laser Filamentation*. Springer, 2010.
- [119] M. F. Saleh, W. Chang, P. Hölzer, A. Nazarkin, J. C. Travers, N. Y. Joly, P. S. J. Russell, and F. Biancalana, “Theory of photoionization-induced blueshift of ultrashort solitons in gas-filled hollow-core photonic crystal fibers,” *Phys. Rev. Lett.*, vol. 107, p. 203902, Nov 2011.
- [120] P. Hölzer, W. Chang, J. C. Travers, A. Nazarkin, J. Nold, N. Y. Joly, M. F. Saleh, F. Biancalana, and P. S. J. Russell, “Femtosecond nonlinear fiber optics in the ionization regime,” *Phys. Rev. Lett.*, vol. 107, p. 203901, Nov 2011.
- [121] L. S. G. S. Y. R. Boyd, Robert W., *Self-focusing: Past and Present*. ISBN 978-0-387-34727-1, 10.1007/978-0-387-34727-1: Springer New York, 2009.
- [122] T.-T. Xi, X. Lu, and J. Zhang, “Spatiotemporal moving focus of long femtosecond-laser filaments in air,” *Phys. Rev. E*, vol. 78, p. 055401, Nov 2008.

- [123] C. Conti, S. Trillo, P. Di Trapani, G. Valiulis, A. Piskarskas, O. Jedrkiewicz, and J. Trull, “Nonlinear electromagnetic x waves,” *Phys. Rev. Lett.*, vol. 90, p. 170406, May 2003.
- [124] M. A. Porras, A. Parola, D. Faccio, A. Dubietis, and P. D. Trapani, “Nonlinear unbalanced bessel beams: Stationary conical waves supported by nonlinear losses,” *Phys. Rev. Lett.*, vol. 93, p. 153902, Oct 2004.
- [125] M. Kolesik, E. M. Wright, and J. V. Moloney, “Dynamic nonlinear x waves for femtosecond pulse propagation in water,” *Phys. Rev. Lett.*, vol. 92, p. 253901, Jun 2004.
- [126] D. Faccio, A. Averchi, A. Couairon, M. Kolesik, J. Moloney, A. Dubietis, G. Tamosauskas, P. Polesana, A. Piskarskas, and P. D. Trapani, “Spatio-temporal reshaping and x wave dynamics in optical filaments,” *Opt. Express*, vol. 15, pp. 13077–13095, Oct 2007.
- [127] F. Bragheri, D. Faccio, A. Couairon, A. Matijosius, G. Tamosauskas, A. Varanavicius, V. Degiorgio, A. Piskarskas, and . . Di Trapani, P. Phys. Rev. A 76, “Conical-emission and shock-front dynamics in femtosecond laser-pulse filamentation,” *Phys. Rev. A*, vol. 76, p. 025801, 2007.
- [128] D. Faccio, A. Averchi, A. Lotti, P. D. Trapani, A. Couairon, D. Papazoglou, and S. Tzortzakis, “Ultrashort laser pulse filamentation from spontaneous x wave formation in air,” *Opt. Express*, vol. 16, pp. 1565–1570, Feb 2008.
- [129] V. Loriot, E. Hertz, O. Faucher, and B. Lavorel, “Measurement of high order kerr refractive index of major air components,” *Opt. Express*, vol. 17, pp. 13429–13434, Aug 2009.
- [130] P. B ejot, E. Hertz, J. Kasparian, B. Lavorel, J. P. Wolf, and O. Faucher, “Transition from plasma-driven to kerr-driven laser filamentation,” *Phys. Rev. Lett.*, vol. 106, p. 243902, Jun 2011.
- [131] C. Br ee, A. Demircan, and G. Steinmeyer, “Saturation of the all-optical kerr effect,” *Phys. Rev. Lett.*, vol. 106, p. 183902, May 2011.
- [132] M. Richter, S. Patchkovskii, F. Morales, O. Smirnova, and M. Ivanov, “The role of the kramers-henneberger atom in the higher-order kerr effect,” *New Journal of Physics*, vol. 15, no. 8, p. 083012, 2013.
- [133] P. Sprangle, J. Penano, B. Hafizi, D. Gordon, and M. Scully, “Remotely induced atmospheric lasing,” *Applied Physics Letters*, vol. 98, no. 21, 2011.
- [134] P. Ding, S. Mitryukovskiy, A. Houard, E. Oliva, A. Couairon, A. Mysyrowicz, and Y. Liu, “Backward lasing of air plasma pumped by circularly polarized femtosecond pulses for the sake of remote sensing (black),” *Opt. Express*, vol. 22, pp. 29964–29977, Dec 2014.

- [135] M. Ziolk, R. Naskrecki, and J. Karolczak, “Some temporal and spectral properties of femtosecond supercontinuum important in pump-probe spectroscopy,” *Optics Communications*, vol. 241, no. 1-3, pp. 221 – 229, 2004.
- [136] N. Aközbek, S. A. Trushin, A. Baltuska, W. Fuß, E. Goulielmakis, K. Kosma, F. Krausz, S. Panja, M. Uiberacker, W. E. Schmid, A. Becker, M. Scalora, and M. Bloemer, “Extending the supercontinuum spectrum down to 200 nm with few-cycle pulses,” *New J. Phys.*, vol. 8, p. 177, 2006.
- [137] A. Mysyrowicz, A. Couairon, and U. Keller, “Self-compression of optical laser pulses by filamentation,” *New Journal of Physics*, vol. 10, no. 2, p. 025023, 2008.
- [138] L. Zhang, T. Xi, Z. Hao, and J. Lin, “Supercontinuum accumulation along a single femtosecond filament in fused silica,” *Journal of Physics D: Applied Physics*, vol. 49, no. 11, p. 115201, 2016.
- [139] M. Gaarde and A. Couairon, “Intensity spikes in laser filamentation: Diagnostics and application,” *Phys. Rev. Lett.*, vol. 103, p. 043901, 2009.
- [140] S. Xu, J. Bernhardt, M. Sharifi, W. Liu, and S. L. Chin, “Intensity clamping during laser filamentation by tw level femtosecond laser in air and argon,” *Laser Physics*, vol. 22, no. 1, pp. 195–202, 2011.
- [141] P. S. J. Russell, P. Holzer, W. Chang, A. Abdolvand, and J. C. Travers, “Hollow-core photonic crystal fibres for gas-based nonlinear optics,” *Nat Photon*, vol. 8, pp. 278–286, Apr. 2014.
- [142] X.-L. Liu, X. Lu, X. Liu, L.-B. Feng, J.-L. Ma, Y.-T. Li, L.-M. Chen, Q.-L. Dong, W.-M. Wang, Z.-H. Wang, Z.-Y. Wei, Z.-M. Sheng, and J. Zhang, “Broadband supercontinuum generation in air using tightly focused femtosecond laser pulses,” *Opt. Lett.*, vol. 36, pp. 3900–3902, Oct 2011.
- [143] H. Schroeder, S. Hosseini, Q. Luo, and S. Chin, “Self-steepening is an abrupt process,” *Optics Communications*, vol. 266, no. 1, pp. 302 – 306, 2006.
- [144] K. Lim, M. Durand, M. Baudelet, and M. Richardson, “Transition from linear- to nonlinear-focusing regime in filamentation,” *Scientific Reports*, vol. 4, pp. 7217–, Dec. 2014.
- [145] G. P. Agrawal, *Nonlinear Fiber Optics*. Quantum Electronics Principles and Applications Series, 1989.
- [146] P. Polynkin, M. Kolesik, E. M. Wright, and J. V. Moloney, “Experimental tests of the new paradigm for laser filamentation in gases,” *Phys. Rev. Lett.*, vol. 106, p. 153902, Apr 2011.
- [147] C. Brée, J. Bethge, S. Skupin, L. Bergé, A. Demircan, and G. Steinmeyer, “Cascaded self-compression of femtosecond pulses in filaments,” *New Journal of Physics*, vol. 12, no. 9, p. 093046, 2010.

-
- [148] R. W. Boyd, *Nonlinear Optics (Third Edition)*. Burlington: Academic Press, third edition ed., 2008.
- [149] P. Kinsler, “Optical pulse propagation with minimal approximations,” *Phys. Rev. A*, vol. 81, p. 013819, Jan 2010.
- [150] J. K. Ranka and A. L. Gaeta, “Breakdown of the slowly varying envelope approximation in the self-focusing of ultrashort pulses,” *Opt. Lett.*, vol. 23, pp. 534–536, Apr 1998.
- [151] V. Zakharov and A. Shabat, “Exact theory of twodimensional selffocusing and one-dimensional self-modulation of waves in nonlinear media,” *Sov. Phys. JETP* 101, 62 (1972), vol. 101, p. 62, 1972.
- [152] T. Brabec and F. Krausz, “Nonlinear optical pulse propagation in the single-cycle regime,” *Phys. Rev. Lett.*, vol. 78, p. 3282, 1997.
- [153] C. Brée, *Self-compression of intense optical pulses and the filamentary regime of nonlinear optics*. PhD thesis, Humboldt-Universität zu Berlin, 2011.
- [154] C. Brée, S. Amiranashvili, and U. Bandelow, “Spatio-temporal pulse propagation in nonlinear dispersive optical media,” *Optical and Quantum Electronics*, vol. 45, no. 7, pp. 727–733, 2012.
- [155] Dalgarno and Kingston, “The refractive indices and Verdet constants of the inert gases,” *Proc. Roy. Soc. London Ser. A*, vol. 259, pp. 424–429, 1966.
- [156] C. Brée, A. Demircan, and G. Steinmeyer, “Asymptotic pulse shapes in filamentary propagation of intense femtosecond pulses,” *Laser Physics*, vol. 19, no. 2, pp. 330–335, 2009.
- [157] C. Brée, A. Demircan, S. Skupin, L. Bergé, and G. Steinmeyer, “Plasma induced pulse breaking in filamentary self-compression,” *Laser Physics*, vol. 20, no. 5, pp. 1107–1113, 2010.
- [158] A. Couairon, M. Franco, A. Mysyrowicz, J. Biegert, and U. Keller, “Pulse self-compression to the single-cycle limit by filamentation in a gas with a pressure gradient,” *Opt. Lett.*, vol. 30, pp. 2657–2659, Oct 2005.
- [159] D. Faccio, A. Lotti, M. Kolesik, J. Moloney, S. Tzortzakis, A. Couairon, and P. D. Trapani, “Spontaneous emergence of pulses with constant carrier-envelope phase in femtosecond filamentation..,” *Opt. Express*, vol. 16, pp. 11103–11114, Jul 2008.
- [160] L. Bergé, S. Skupin, and G. Steinmeyer, “Self-recompression of laser filaments exiting a gas cell,” *Phys. Rev. A*, vol. 79, p. 033838, Mar. 2009.
- [161] C. Brée, A. Demircan, and G. Steinmeyer, “Modulation instability in filamentary self-compression,” *Laser Physics*, vol. 21, no. 7, pp. 1313–1318, 2011.

- [162] F. Frank, C. Arrell, T. Witting, W. Okell, J. McKenna, J. Robinson, C. Haworth, D. Austin, H. Teng, I. Walmsley, J. Marangos, and J. W. G. Tisch, “Invited review article: technology for attosecond science,” *Rev. Sci. Instrum.*, vol. 83, p. 071101, 2012.
- [163] E. Schulz, T. Binhammer, D. S. Steingrube, S. Rausch, M. Kovačev, and U. Morgner, “Intense few-cycle laser pulses from self-compression in a self-guiding filament,” *Appl. Phys. B*, vol. 95, pp. 269–272, 2009.
- [164] I. Ahmad, L. Bergé, Z. Major, F. Krausz, S. Karsch, and S. A. Trushin, “Redshift of few-cycle infrared pulses in the filamentation regime,” *New Journal of Physics*, vol. 13, no. 9, p. 093005, 2011.
- [165] C. P. Hauri, A. Trisorio, M. Merano, G. Rey, R. B. Lopez-Martens, and G. Mourou, “Generation of high-fidelity and down-chirped sub-10-fs-mJ pulses through filamentation for driving relativistic laser-matter interactions at 1 kHz,” *Applied Physics Letters*, vol. 89, no. 15, 2006.
- [166] D. Uryupina, M. Kurilova, A. Mazhorova, N. Panov, R. Volkov, S. Gorgutsa, O. Kosareva, A. Savelev, and S. L. Chin, “Few-cycle optical pulse production from collimated femtosecond laser beam filamentation,” *JOSA B*, vol. 27, no. 4, pp. 667–674, 2010.
- [167] J. O’Hner and R. J. Levis, “Direct phase and amplitude characterization of femtosecond laser pulses undergoing filamentation in air,” *Optics Letters*, vol. 37(10), p. 1775, 2012.
- [168] J. H. O’Hner, D. A. Romanov, and R. J. Levis, “Self-shortening dynamics measured along a femtosecond laser filament in air,” *Phys. Rev. Lett.*, vol. 105, p. 125001, Sep 2010.
- [169] B. Alonso, Í. J. Sola, Ó. Varela, J. Hernández-Toro, C. Méndez, J. S. Román, A. Zaïr, and L. Roso, “Spatiotemporal amplitude and phase reconstruction by fourier-transform of interference spectra of high-complex-beams,” *J. Opt. Soc. Am. B*, vol. 27, pp. 933–940, May 2010.
- [170] B. Alonso, I. J. Sola, J. S. Roman, O. Varela, and L. Roso, “Spatiotemporal evolution of light during propagation in filamentation regime,” *J. Opt. Soc. Am. B*, vol. 28(8), p. 1807, 2011.
- [171] S. Akturk, C. D’Amico, M. Franco, A. Couairon, and A. Mysyrowicz, “A simple method for determination of nonlinear propagation regimes in gases,” *Opt. Express*, vol. 15, pp. 15260–15267, Nov 2007.
- [172] G. Point, Y. Brelet, A. Houard, V. Jukna, C. Milián, J. Carbonnel, Y. Liu, A. Couairon, and A. Mysyrowicz, “Superfilamentation in air,” *Phys. Rev. Lett.*, vol. 112, p. 223902, Jun 2014.

-
- [173] A. Baltuska, M. S. Pshenichnikov, and D. A. Wiersma, “Second-harmonic generation frequency-resolved optical gating in the single-cycle regime,” *IEEE Journal of Quantum Electronics*, vol. 35, pp. 459–478, Apr 1999.
- [174] G. Steinmeyer, “A review of ultrafast optics and optoelectronics,” *Journal of Optics A: Pure and Applied Optics*, vol. 5, no. 1, p. R1, 2003.
- [175] R. Trebino, K. W. DeLong, D. N. Fittinghoff, J. N. Sweetser, M. A. Krumbugel, B. A. Richman, and D. J. Kane, “Measuring ultrashort laser pulses in the time-frequency domain using frequency-resolved optical gating,” *Review of Scientific Instruments*, vol. 68, no. 9, pp. 3277–3295, 1997.
- [176] M. Kretschmar, C. Brée, T. Nagy, A. Demircan, H. G. Kurz, U. Morgner, and M. Kovačev, “Direct observation of pulse dynamics and self-compression along a femtosecond filament,” *Opt. Express*, vol. 22, pp. 22905–22916, Sep 2014.
- [177] M. A. Porras, A. Dubietis, E. Kučinskas, F. Bragheri, V. Degiorgio, A. Couairon, D. Faccio, and P. Di Trapani, “From x- to o-shaped spatiotemporal spectra of light filaments in water,” *Optics Letters*, vol. 30, pp. 3398–3400, 2005.
- [178] Z.-H. He, J. A. Nees, B. Hou, K. Krushelnick, and A. G. R. Thomas, “Ionization-induced self-compression of tightly focused femtosecond laser pulses,” *Phys. Rev. Lett.*, vol. 113, p. 263904, Dec 2014.
- [179] B. Beaupaire, D. Guénot, A. Vernier, F. Böhle, M. Perrier, A. Jullien, R. Lopez-Martens, A. Lifschitz, and J. Faure, “Limitations in ionization-induced compression of femtosecond laser pulses due to spatio-temporal couplings,” *Opt. Express*, vol. 24, pp. 9693–9705, May 2016.
- [180] L. Bergé, “Self-compression of 2000 nm laser filaments,” *Opt. Express*, vol. 16, pp. 21529–21543, Dec 2008.
- [181] N. Aközbek, M. Scalora, C. Bowden, and S. Chin, “White-light continuum generation and filamentation during the propagation of ultra-short laser pulses in air,” *Optics Communications*, vol. 191, no. 3-6, pp. 353 – 362, 2001.
- [182] S. L. Chin, S. A. Hosseini, W. Liu, Q. Luo, F. Theberge, N. Akzbek, A. Becker, V. P. Kandidov, O. G. Kosareva, and H. Schroeder, “The propagation of powerful femtosecond laser pulses in optical media: physics and applications and new challenges,” *Canadian Journal of Physics*, vol. 83, no. 9, pp. 863–905, 2005.
- [183] A. Couairon, E. Gaizauskas, D. Faccio, A. Dubietis, and P. Di Trapani, “Nonlinear x-wave formation by femtosecond filamentation in kerr media,” *Physical Review E*, vol. 73, no. 016608, 2006.
- [184] C. Brée, A. Demircan, J. Bethge, E. T. J. Nibbering, S. Skupin, L. Bergé, and G. Steinmeyer, “Filamentary pulse self-compression: The impact of the cell windows,” *Phys. Rev. A*, vol. 83, p. 043803, Apr 2011.

- [185] C. Brée, M. Kretschmar, T. Nagy, H. G. Kurz, U. Morgner, and M. Kovacev, “Impact of spatial inhomogeneities on on-axis pulse reconstruction in femtosecond filaments,” *Journal of Physics B: Atomic, Molecular and Optical Physics*, vol. 48, no. 9, p. 094002, 2015.
- [186] S.-L. Chin and H.-L. Xu, “Population inversion in fluorescing fragments of super-excited molecules inside an air filament,” *Chinese Physics B*, vol. 24, no. 1, p. 013301, 2015.
- [187] C. P. Hauri, A. Guandalini, P. Eckle, W. Kornelis, J. Biegert, and U. Keller, “Generation of intense few-cycle laser pulses through filamentation - parameter dependence,” *Opt. Exp.*, vol. 13, no. 19, p. 7541, 2005.
- [188] Y. Kida, J. Liu, T. Teramoto, and T. Kobayashi, “Sub-10 fs deep-ultraviolet pulses generated by chirped-pulse four-wave mixing,” *Opt. Lett.*, vol. 35, no. 11, p. 1807, 2010.
- [189] E. Cabrera-Granado, Y. Chen, I. Babushkin, L. Bergé, and S. Skupin, “Spectral self-action of thz emission from ionizing two-color laser pulses in gases,” *New Journal of Physics*, vol. 17, no. 2, p. 023060, 2015.
- [190] O. Smirnova and M. Ivanov, *Multielectron High Harmonic Generation: Simple Man on a Complex Plane*, pp. 201–256. Wiley-VCH Verlag GmbH & Co. KGaA, 2014.
- [191] C. Winterfeldt, C. Spielmann, and G. Gerber, “*Colloquium* : Optimal control of high-harmonic generation,” *Rev. Mod. Phys.*, vol. 80, pp. 117–140, Jan 2008.
- [192] P. Balcou and A. L’Huillier, “Phase-matching effects in strong-field harmonic generation,” *Phys. Rev. A*, vol. 47, no. 2, p. 1447, 1993.
- [193] P. Salières, P. Antoine, A. de Bohan, and M. Lewenstein, “Temporal and spectral tailoring of high-order harmonics,” *Phys. Rev. Lett.*, vol. 81, pp. 5544–5547, Dec 1998.
- [194] M. Lewenstein, P. Salières, and A. L’Huillier, “Phase of the atomic polarization in high-order harmonic generation,” *Phys. Rev. A*, vol. 52, no. 6, pp. 4747–4754, 1995.
- [195] M. Bellini, C. Corsi, and M. C. Gambino, “Neutral depletion and beam defocusing in harmonic generation from strongly ionized media,” *Phys. Rev. A*, vol. 64, p. 023411, 2001.
- [196] A. L’Huillier, K. H. Schafer, and K. C. Kulander, “Theoretical aspects of intense field harmonic generation,” *J. Phys. B: At. Mol. Opt. Phys.*, vol. 24, pp. 3315–3341, 1991.
- [197] M. B. Gaarde, J. L. Tate, and K. J. Schafer, “Macroscopic aspects of attosecond pulse generation,” *J. Phys. B: At. Mol. Opt. Phys.*, vol. 41, p. 132001, 2008.

-
- [198] P. Eckle, A. N. Pfeiffer, C. Cirelli, A. Staudte, R. Dörner, H. G. Muller, M. Büttiker, and U. Keller, “Attosecond ionization and tunneling delay time measurements in helium,” *Science*, vol. 322, no. 5907, pp. 1525–1529, 2008.
- [199] A. S. Landsman and U. Keller, “Attosecond science and the tunnelling time problem,” *Physics Reports*, vol. 547, pp. 1 – 24, 2015. Attosecond science and the tunneling time problem.
- [200] L. Torlina, F. Morales, J. Kaushal, I. Ivanov, A. Kheifets, A. Zielinski, A. Scrinzi, H. G. Muller, S. Sukiasyan, M. Ivanov, and O. Smirnova, “Interpreting attoclock measurements of tunnelling times,” *Nat Phys*, vol. 11, no. 6, pp. 503–508, 2015.
- [201] A. L’Huillier, M. Lewenstein, P. Salieres, P. Balcou, M. Y. Ivanov, J. Larsson, and C. Wahlström, “High-order harmonic-generation cutoff,” *Phys. Rev. A*, vol. 48, p. R3433, 1993.
- [202] P. Salières, A. L’Huillier, P. Antoine, and M. Lewenstein, “Study of the spatial and temporal coherence of high order harmonics,” *arXiv:quant-ph*, vol. 9710060v1, 1997.
- [203] E. T. F. Rogers, S. L. Stebbings, A. M. de Paula, C. A. Froud, M. Praeger, B. Mills, J. Grant-Jacob, W. S. Brocklesby, and J. G. Frey, “Spatiotemporal phase-matching in capillary high-harmonic generation,” *J. Opt. Soc. Am. B*, vol. 29, pp. 806–812, Apr 2012.
- [204] S. Feng and H. G. Winful, “Physical origin of the gouy phase shift,” *Opt. Lett.*, vol. 26, pp. 485–487, Apr 2001.
- [205] B. Henke, E. Gullikson, and J. Davis, “X-ray interactions: photoabsorption and scattering and transmission and reflection at $e=50-30000$ eV and $z=1-92$,” *Atomic Data and Nuclear Data Tables*, vol. 54, pp. 181 – 342, July 1993.
- [206] C. Delfin, C. Altucci, F. De Filippo, C. de Lisio, M. B. Gaarde, A. L’Huillier, L. Roos, and C.-G. Wahlström, “Influence of the medium length on high-order harmonic generation,” *J. Phys. B: At. Mol. Opt. Phys.*, vol. 32, pp. 5397–5409, 1999.
- [207] L. Roos, E. Constant, E. Mevel, P. Balcou, D. Descamps, M. B. Gaarde, A. Valette, R. Haroutunian, and A. L’Huillier, “Controlling phase matching of high-order harmonic generation by manipulating the fundamental field,” *Phys. Rev. A*, vol. 60, pp. 5010–5018, Dec 1999.
- [208] P. Salières, T. Ditmire, M. D. Perry, A. L’Huillier, and M. Lewenstein, “Angular distributions of high-order harmonics generated by a femtosecond laser,” *J. Phys. B: At. Mol. Opt. Phys.*, vol. 29, no. 20, p. 4771, 1996.
- [209] E. Constant, D. Garzella, P. Breger, E. Mevel, C. Dorrer, C. Le Blanc, F. Salin, and P. Agostini, “Optimizing high harmonic generation in absorbing gases: Model and experiment,” *Phys. Rev. Lett.*, vol. 82, no. 8, p. 1668, 1999.

- [210] F. Wang, L. He, C. Zhai, W. Shi, Q. Zhang, P. Lan, and P. Lu, “Time-dependent phase matching of high-order-harmonic generation,” *Phys. Rev. A*, vol. 92, p. 063839, Dec 2015.
- [211] C. Altucci, R. Bruzzese, C. de Lisio, M. Nisoli, S. Stagira, S. De Silvestri, O. Svelto, A. Boscolo, P. Ceccherini, L. Poletto, G. Tondello, and P. Villoresi, “Tunable soft-x-ray radiation by high-order harmonic generation,” *Phys. Rev. A*, vol. 61, p. 021801(R), 1999.
- [212] Y. Wang, Y. Liu, X. Yang, and Z. Xu, “Spectral splitting in high-order harmonic generation,” *Phys. Rev. A*, vol. 62, p. 063806, 2000.
- [213] F. Zhong, J. Deng, X. Hu, Z. Li, Z. Zhang, and Z. Xu, “The effect of ionization of gases on the high harmonic splitting,” *Phys. Lett. A*, vol. 278, pp. 35–43, 2000.
- [214] C. M. Heyl, J. Gdde, U. H. Hfer, and A. L’Huillier, “Spectrally resolved maker fringes in high-order harmonic generation,” *Phys. Rev. Lett.*, vol. 107, p. 033903, Jul 2011.
- [215] P. Lan, P. Lu, W. Cao, Y. Li, and X. Wang, “Attosecond ionization gating for isolated attosecond electron wave packet and broadband attosecond xuv pulses,” *Phys. Rev. A*, vol. 76, p. 051801, Nov 2007.
- [216] M. J. Abel, T. Pfeifer, P. M. Nagel, W. Boutu, M. J. Bell, C. P. Steiner, D. M. Neumark, and S. R. Leone, “Isolated attosecond pulses from ionization gating of high-harmonic emission,” *Chemical Physics*, vol. 366, no. 1-3, pp. 9 – 14, 2009. Attosecond Molecular Dynamics.
- [217] A. Dubrouil, O. Hort, F. Catoire, D. Descamps, S. Petit, E. Mvel, V. Strelkov, and E. Constant, “Spatio-spectral structures in high-order harmonic beams generated with terawatt 10fs pulses,” *Nature Communications*, 2014.
- [218] P. Balcou, P. Salires, A. L’Huillier, and M. Lewenstein, “Generalized phase-matching conditions for high harmonics: The role of field-gradient forces,” *Phys. Rev. A*, vol. 55, pp. 3204–3210, Apr 1997.
- [219] Z. Fangchuan, L. Zhong, Z. Zhinan, Z. Zhengquan, L. Ruxin, and X. Zhizhan, “Spectral splitting of high-order harmonic emissions from ionizing gases,” *Phys. Rev. A*, vol. 65, p. 033808, 2002.
- [220] E. Brunetti, R. Issac, and D. A. Jaroszynski, “Quantum path contribution to high-order harmonic spectra,” *Phys. Lett. A*, vol. 77, p. 023422, 2008.
- [221] C. Altucci, T. Starczewski, E. Mevel, C.-G. Wahlstrm, B. Carr, and A. L’Huillier, “Influence of atomic density in high-order harmonic generation,” *J. Opt. Soc. Am. B*, vol. 13, p. 148, 1996.

- [222] J. Tate, T. Auguste, H. G. Muller, P. Salières, P. Agostini, and L. F. DiMauro, “Scaling of wave-packet dynamics in an intense midinfrared field,” *Phys. Rev. Lett.*, vol. 98, p. 013901, Jan 2007.
- [223] A. D. Shiner, C. Trallero-Herrero, N. Kajumba, H.-C. Bandulet, D. Comtois, F. Légaré, M. Giguère, J.-C. Kieffer, P. B. Corkum, and D. M. Villeneuve, “Wavelength scaling of high harmonic generation efficiency,” *Phys. Rev. Lett.*, vol. 103, p. 073902, Aug 2009.
- [224] P. Rudawski, A. Harth, C. Guo, E. Lorek, M. Miranda, C. M. Heyl, E. W. Larsen, J. Ahrens, O. Prochnow, T. Binhammer, U. Morgner, J. Mauritsson, A. L’Huillier, and C. L. Arnold, “Carrier-envelope phase dependent high-order harmonic generation with a high-repetition rate opcpa-system,” *The European Physical Journal D*, vol. 69, no. 3, pp. 1–6, 2015.
- [225] T. Popmintchev, M.-C. Chen, D. Popmintchev, P. Arpin, S. Brown, S. Ališauskas, G. Andriukaitis, T. Balčiunas, O. D. Mücke, A. Pugzlys, A. Baltuška, B. Shim, S. E. Schrauth, A. Gaeta, C. Hernández-García, L. Plaja, A. Becker, A. Jaron-Becker, M. M. Murnane, and H. C. Kapteyn, “Bright coherent ultrahigh harmonics in the kev x-ray regime from mid-infrared femtosecond lasers,” *Science*, vol. 336, no. 6086, pp. 1287–1291, 2012.
- [226] H. Noda, T. Namioka, and M. Seya, “Geometric theory of the grating,” *J. Opt. Soc. Am.*, vol. 64, pp. 1031–1036, Aug 1974.
- [227] A.-T. Le, T. Morishita, and C. D. Lin, “Improved lewenstein model for high-order harmonic generation of atoms and molecules with scattering wavefunctions,” *ArXiv e-prints*, vol. arXiv:0707.4192, July 2007.
- [228] M. Högner, “Optical high-order harmonic generation in gas targets with spatially tailored driving fields,” Master’s thesis, Ludwig-Maximilians-Universität München, Fakultät für Physik,, 2013.
- [229] I. Pupeza, M. Högner, J. Weitenberg, S. Holzberger, D. Esser, T. Eidam, J. Limpert, A. Tünnermann, E. Fill, and V. S. Yakovlev, “Cavity-enhanced high-harmonic generation with spatially tailored driving fields,” *Phys. Rev. Lett.*, vol. 112, p. 103902, Mar 2014.
- [230] A. L’Huillier, P. Balcou, S. Candel, K. J. Schafer, and K. C. Kulander, “Calculations of high-order harmonic-generation processes in xenon at 1064 nm,” *Phys. Rev. A*, vol. 46, no. 5, pp. 2778–2790, 1992.
- [231] C. M. Heyl, H. Coudert-Alteirac, M. Miranda, M. Louisy, K. Kovacs, V. Tosa, E. Balogh, K. Varjú, A. L’Huillier, A. Couairon, and C. L. Arnold, “Scale-invariant nonlinear optics in gases,” *Optica*, vol. 3, pp. 75–81, Jan 2016.

- [232] F. Théberge, W. Liu, P. T. Simard, A. Becker, and S. L. Chin, “Plasma density inside a femtosecond laser filament in air: Strong dependence on external focusing,” *Phys. Rev. E*, vol. 74, p. 036406, Sep 2006.
- [233] M. Chen, P. Arpin, T. Popmintchev, M. Gerrity, B. Zhang, M. Seaberg, D. Popmintchev, M. M. Murnane, and H. C. Kapteyn, “Soft x-ray harmonics spanning the water window from a tabletop light source,” *Phys. Rev. Lett.*, vol. 105, p. 173901, 2010.
- [234] S. Xu, X. Sun, B. Zeng, W. Chu, J. Zhao, W. Liu, Y. Cheng, Z. Xu, and S. L. Chin, “Simple method of measuring laser peak intensity inside femtosecond laser filament in air,” *Opt. Express*, vol. 20, pp. 299–307, Jan 2012.
- [235] X. Sun, S. Xu, J. Zhao, W. Liu, Y. Cheng, Z. Xu, S. L. Chin, and G. Mu, “Impressive laser intensity increase at the trailing stage of femtosecond laser filamentation in air,” *Opt. Express*, vol. 20, pp. 4790–4795, Feb 2012.
- [236] C. Brée and M. Hofmann, “Adiabatic floquet model for the optical response in a femtosecond filament,”

List of Figures

1	(top) A filament being truncated by a pressure gradient. (bottom) Angular dispersed spectral emission from a filament.	e
2.1	Calculation of the effect of self-phase modulation on the fundamental spectrum for pulses with a different steepness. For this case a 30 fs pulse with an intensity of 100 TW/cm ² is used to model the generation of new frequency components along the temporal pulse shape. Case (a) shows the initial pulse and its spectrum, (b) shows the SPM-effect for a Gaussian pulse, whereas case (c) displays the results for a 30 fs pulse steepened by a factor of 0.45.	8
2.2	Color-encoded values of the Keldysh-parameter γ in dependence of the laser intensity and wavelength. The Coulomb potential of an atom interacting with the external laser field is drawn in black for the case of multi-photon ionization and tunneling ionization.	10
2.3	(a) Ionization rates in dependence of the driving intensity. (b) Corresponding evolution of the Keldysh-parameter. The gas chosen for the calculations is argon which interacts with a 780 nm driving wavelength.	11
2.4	Evolution of the degree of ionization along a 35 fs pulse at 780 nm with an peak intensity of 250 TW/cm ² . The results from the different ionization models are compared and their assignment is denoted in the key.	12
3.1	Determination of the clamping intensity I_c through the evolution of the nonlinear refractive index change Δn_{NL} in dependence of the intensity. The points, where the absolute value approaches zero determines I_c	17
3.2	Sketch describing the basic idea behind the calculation of the wavefront sag for the case of a focused Gaussian beam. The wavefront sag S follows the wavefront curvature $R(z)$ which is imprinted by the focusing optic and shows a decreasing behavior as it reaches the focus at position f . Here, w_0 is the minimum beam waist, $w(z)$ is the waist in dependence of the propagation distance z	19

3.3 The contribution of the different wavefront sags for $f=2\text{m}$ and an input power of 25 GW. The term connected to the Kerr effect S_k crosses the fundamental Gaussian distribution S_g before the plasma curvature S_p can affect the propagation significantly. 20

3.4 Determination of the dominating nonlinear effect to filamentation at different focusing geometries. Sub-figure (a) sketches the experimental setup, where the fundamental beam (1.35 mJ, 35-40 fs, 780 nm) is focused by different curved mirrors ($f=500, 625, 750, 1000, 1250, 1500\text{ mm}$) into an argon-filled gas cell. The emerging spectrum is detected after the interaction chamber and displayed in panel (b), where the color-code represents the normalized spectral intensity. Three examples of the spectral evolution are presented in (c). The spectral width at a 2% level as well as the central wavelength of the recorded spectra is shown in (d). The evolution of the wavefront sag is shown for three focusing setups in (e). It can be seen that the propagation dynamics change between a Kerr-dominated and plasma-dominated propagation regime. 22

3.5 On-axis temporal intensity profile along the filament and the corresponding on-axis intensity evolution for a reduced numerical model. The pulse shape at a position of 1.55 m is shown in the bottom right panel. (Figure taken from [157]) 27

3.6 Sketch of the experimental setup for the detection of the fundamental pulses dynamics. The filament can be scanned along a truncating differential pumping stage, allowing for a subsequent all-vacuum detection of the fundamental spectrum and pulse shape in dependence of the filament length. 30

3.7 Calculated FROG traces for a 10 fs pulse centered at 800 nm with different imprinted phases. The influence of a linear or a SPM-induced chirp is observed. . . . 32

3.8 Evolution of the fundamental spectrum emerging from the femtosecond filament as a function of the propagation distance along the filament. The blue line displays the center-of-gravity (CoG) of each recorded spectrum [176]. 33

3.9 SHG-FROG traces recorded at positions of 198 cm, 204 cm and 212 cm. Next to the recorded traces, the reconstructed pulse shape with the corresponding FWHM pulse duration and the reconstructed spectrum are shown. The evolution of the intensity signal is displayed in black, whereas the phase evolution is shown in blue. 34

3.10 Reconstructed temporal pulse-shapes as a function of the propagation direction, detected with the SHG-FROG setup. The pulse's FWHM duration is shown below the evolving pulse shapes. A clear splitting into two sub-pulses is observed, coinciding with a pronounced pulse-shortening [176]. 35

3.11	Comparison of the measured pulse-characteristics with the results from the numerical model. In (a) and (b) the experimental results from Sec. 3.3.2 are shown again. Panel (c) displays the simulated on-axis evolution of the pulse envelope as a function of the propagation length. The corresponding spectrum is shown in (d). The labels I-III refer to stages dominated by defocusing (I), refocusing (II) and propagation dynamics (III).	37
3.12	Simulated spatio-temporal profiles which characterize three stages I-III along the life cycle of the filament. I is the defocusing stage, II covers the refocusing event and III the pulse propagation after refocusing.	38
3.13	Derived properties from the evolution of the pulse shape. The (a) full-width-half-maximum, (b) falling slope of the pulse, being a measure for the steepness and (c) the peak intensity are shown for the propagating on-axis ($r=0$) pulses.	39
3.14	Change of the plasma-induced refractive index along a 20 fs pulse with a peak intensity of 100 TW/cm ² . The refractive index jump is defined to a small window along the temporal pulse shape.	40
3.15	Divergence θ of the spectral components at positions 175 cm and 185 cm. The defocusing of blue-shifted spectrum can be seen at 185 cm. The white dotted line depicts the highest experimentally measured frequency.	41
3.16	Comparison of the simulated and measured pulse-shape at a position of 204 cm. The refocusing event results in a double-peak structure, which is clearly visible in the simulations. The measurements show this behavior to a lesser extend.	42
3.17	Angular resolved emission for positions 197 cm and 200 cm. The initially defocused spectral features approach the optical axis and new frequencies are generated through SPM.	43
3.18	Spectral emission at positions 214 cm and 220 cm along the propagation stage III. The modulated spectrum shows strongly frequency-dependent divergence properties. The highest frequencies form a fish-tail like structure and a weak signal between 3 rad/fs and 5 rad/fs. The initial carrier at 2.4 rad/fs is the most dominant spectral component but strongly modulated.	45
3.19	Calculated X-FROG traces, portraying the spectral distribution along the on-axis temporal shapes. The traces are calculated for the pulse shapes originating from the experimental measurements and the simulations.	47
3.20	Influence of the pinhole setup upon the measurable pulse dynamics. Panel (a) shows the already introduced pulse dynamics inside the filament. The sub-figures (b)-(f) show the pulse evolution, which will be measured after passing a pinhole with a diameter of $d=150, 250, 500, 1000 \mu\text{m}$ plus 1 m of vacuum propagation. The detectable pulse dynamics rapidly change with an increasing pinhole diameter. . .	49

3.21	Influence of the pinhole setup on the subsequent propagation. The radial properties of the spectrum is strongly structured. A small-diameter filtering by a 100 μm pinhole (white line) cuts out a uniform profile, limiting the distortions during subsequent propagation. A bigger pinhole diameter of 500 μm allows for a mixing due to the strongly differing divergence properties of the frequencies.	50
3.22	Influence of the pinhole setup on the pulse reconstruction. The experimentally measured (black), simulated near-field (red-dotted) and the simulated far-field (150 μm - blue-dotted) pulse shape are displayed for a position of (a) 204 cm and (b) 220 cm.	51
3.23	Numerical results obtained through the implementation of different ionization-models, namely the PPT- (a,d), MPI- (b,e) and ADK-rates (c,f). The temporal (a-c) and spectral (d-f) evolution is shown for each case. Below, the connected intensity and FWHM pulse-duration is displayed in dependence of the propagation length.	53
4.1	(top) Visualization of the basic assumptions of the three-step model, where the electric field of the laser bends the atoms Coulomb potential, enabling tunnel-ionization. The free electron is accelerated by the external laser field and eventually recombines with its parent ion under the emission of high-order harmonic radiation. (bottom) Exemplary high-order harmonic spectrum, showing the common spectral features connected to the generation process.	57
4.2	Exemplary map of the wave-vector mismatch along the spatial coordinates r and z of a focused Gaussian beam.	61
4.3	Wave-vector mismatch induced by the (a) the atomic phase, (b) the Gouy-phase term, (c) the dispersion of free electrons and (d) the dispersion of neutral atoms. The k -values correspond to a focused ($f=2\text{m}$) Gaussian beam with $I_0 = 100 \text{ TW/cm}^2$, $\tau = 10 \text{ fs}$ and $\lambda_0 = 780 \text{ nm}$	63
4.4	Spatio-temporal distribution of a focused Gaussian beam with the same parameters as in Fig. 4.3. (b) Phase-evolution originating from the summed single contributions in Fig. 4.3. The emission of harmonic radiation is favored at $z = 0$ along the trailing part of the pulse and at $z > 0$ at the temporal peak.	64
4.5	Induced shift of the wavelength of the 15th harmonic order generated in argon originating from the atomic phase contribution. The pulse duration is 7.5 fs at a central wavelength of 800 nm with a peak intensity of 100 TW/cm^2 . The harmonic radiation experiences a blueshift (redshift) along the leading (trailing) part of the pulse envelope.	65

4.6	Experimental setup, adding the observation of directly emitted high-order harmonic radiation from the filament by using a XUV-spectrometer. In comparison to the pulse detection setup, the pressure after the truncating stage is kept below 1×10^{-4} mbar. The bottom sketch summarizes the detection procedure, as the visible pulse properties, such as the spectrum and the pulse shape are detected together with the XUV-radiation.	67
4.7	Emitted HHG-spectrum as a function of the position along a femtosecond filament. The harmonic radiation shows a spectral splitting of the initial frequency of each generated harmonic order into blue- and red-shifted spectral branches. The blue-dotted line connects the CoG of the fundamental spectrum to the harmonic spectrum of the 19 th harmonic order via $\lambda_{19} = \lambda_{CoG}/19$	69
4.8	(a) Calculated X-FROG trace of the experimentally reconstructed pulse shape at $z = 208$ cm. The white line displays the border for the two areas of spectral integration which determines the CoG for the two sub-pulses. (b) Scaled evolution of the CoG from the two areas. A spectral separation between the leading and trailing pulse is observed.	70
4.9	Harmonic spectrum calculated by the Lewenstein-model using the experimentally retrieved pulse shapes as an input.	71
4.10	Re-shifted HHG-spectrum, where the evolution of the fundamental frequency, as discussed in Fig. 4.7, is corrected. The splitting now concentrates into the red spectral region. The extracted spectral red-shift is displayed in the left hand side for the harmonic orders 17-21.	72
4.11	Simulations showing the connection between (a) the fundamental pulse's shape and (b) the emitted high-order harmonic spectrum for a pulse with a changing asymmetry (25 fs, 800 nm, 100 TW/cm ²). Negative (positive) values of ζ_a steepen the falling (rising) edge and induce a red-(blue-)shift in the harmonic spectrum	74
4.12	Linking the harmonic red-shift to the pulse's asymmetry. (top) The experimentally retrieved pulses are used as an input for HHG-simulations as a function of the pulses asymmetry (c.f. Fig. 4.11). (middle) The experimentally extracted harmonic red-shift (comp. Fig. 4.9) serves as a reference to determine the asymmetry value. (bottom) The obtained value is used to correct the initial pulse shape.	75
4.13	Outcome of the analysis according to Fig. 4.12. (a) Measured harmonic spectrum. (b) Reconstructed harmonic spectrum from short trajectory contributions. (c) Same for short and long pathways. (d),(e) Respective asymmetry values ζ_a leading to the harmonic spectra and (f),(g) the corresponding falling slopes of the fundamental pulses.	77

4.14	Comparison between the falling slopes obtained by differing methods. The results of the pulse-propagation simulations (black) serve as a reference for the comparison to the findings from the SHG-FROG traces (black-dotted), the ζ_a -values for long trajectories (red-dotted) and the ζ_a -values for short trajectories including an estimation for its error (blue). The latter shows the best agreement.	78
4.15	Analysis of the on-axis transient phase matching along the filament. Panels (a)-(c) show the foundation for the evaluation of Δk , being (a) the beam-waist along the focus, (b) the corresponding Gouy-phase shift and (c) the derivative of the on-axis intensity with respect to z . The filamentary data are obtained from the numerical output and are depicted in blue. The example of a normal Gaussian focus is shown in red-dotted lines for comparison. The resulting individual wave-vector mismatches are depicted below for (d) the atomic phase, (e) the Gouy-phase and (f) the dispersion of free electrons for the case of an ambient pressure of 100 mbar. The summed mismatch Δk_{total} is displayed in (g) and reveals a preferred PM at the falling edge of the pulse for $z > 200$ cm.	81
4.16	Projection of the phase mismatch Δk_{tot} (c.f. Fig. 4.15 (g)) on the temporal pulse shape at a position of 211 cm. The position of optimal phase matching is not coinciding with the position of the maximum falling slope, but shows a slight offset.	82
4.17	Calculation of the pressure-dependent coherence length $L_{\text{coh}} = \pi/ \Delta k_{\text{tot}} $. For each pressure, Δk_{tot} has been integrated along an temporal area at which the intensity of the pulse shape exceeds 5×10^{13} W/cm ² . The resulting value is used to determine $L_{\text{coh}}(z, p)$. The top plots display the experimentally measured and integrated harmonic signal (black) and the integrated coherence length (red-dotted). The estimated high-order harmonic signal (blue-dotted) has been obtained by evaluating Eq. (4.15).	83
4.18	Directly emitted high-order harmonic radiation as a function of the fundamental pulse's chirp and the position along the filament. The value of the GDD is denoted in each corresponding figure. The harmonic splitting into two branches is most pronounced in panels (c) and (d).	85
4.19	(a),(b) HHG-signal from Fig. 4.18 integrated along the complete wavelength axis covering the range between 25 nm and 50 nm. (c) Maximum of the integrated signal and (d) position of said maximum.	86
4.20	(a) Transient phase mismatch for an input pulse with a pre-chirp of +512 fs ² . (b) Connected intensity-evolution. The black dotted line shows an outline of the pulse evolution at a level of 5×10^{13} W/cm ² . The temporal points of optimal phase-matching for $z > 195$ cm are shifted to the peak of the pulse compared to the findings from Fig. 4.15.	87
4.21	(a) Evaluation of the clamping intensity I_c as well as (b) the free electron density ρ_e in dependence of the external focusing and the pulse duration obtained by Eq. (4.20).	90

-
- 4.22 (a) Converted HHG data-set from Fig. 4.7, where the y-axis represents an intensity scale, evaluated using the relation of Eq. (4.21). The white dotted line displays the extracted values of the highest intensity being present at each position along the femtosecond filament. (b) Comparison of these intensities (blue) with the findings from the numerical simulations (black) and the analytical formula (red and green) (Eq. (4.20)). 94
- 4.23 Recordings for the evaluation of the clamping intensity. (a) Fundamental pulse evolution along the filament. (b) Evolving fundamental spectrum and (c) HHG spectrum. Datasets (b) and (c) are necessary for the determination of I_c . Panel (a) is used to prove the occurrence of a refocusing cycle at $f=1$ m. 96
- 4.24 Calculated harmonic spectra obtained by using the Lewenstein-model, stressing the troublesome definition of the Cut-Off. The upper plots show the emitted harmonic radiation for a 10 fs pulse with a peak intensity of 100 TW/cm^2 interacting with argon. The spectra are shown on a linear (left) and logarithmic (right) scale. The red-dotted line displays the spectral position of the Cut-Off from the calculations. The black dotted lines in the right panel visualize the different slopes of the signal with respect to the wavelength for harmonics belonging to the plateau and to the Cut-Off. Their crossing-point can be closely connected to the actual position of the Cut-Off frequency. The panels on the bottom display the same features, only for an intensity of 75 TW/cm^2 97
- 4.25 Exemplary analysis of experimentally obtained harmonic spectra to determine the Cut-Off frequency. Panels (a),(d) and (g) display the HHG-signal with respect to the position along the filament for three different external focusing setups. The middle and right plots show the high-order harmonic spectra for one position along the filament (highlighted by the white dotted line) on a linear and logarithmic scale together with the extracted position of the Cut-Off (red-dotted line). The linear fits along the harmonic signal evolution (black-dotted lines) are used to evaluate the Cut-Off. 98
- 4.26 Experimentally extracted intensities resulting from the three possible approaches for the determination of the Cut-Off frequency. For each panel either the first visible harmonic order on the linear (blue) or logarithmic (red) scale are extracted. The third method (black) relies on the determination of the signal-slopes, introduced in Fig. 4.25. Panels (a)-(d) show the resulting evolution of the intensity in dependence of the position along the femtosecond filament for four different external focusing geometries (a) $f=1$ m, (b) 1.5 m (c) 2 m and (d) 3 m. 99

4.27 Processed results from Fig. 4.26 showing the maximum intensity along the filament in dependence of the external focusing setup. The black solid line shows the findings from the slope evaluation, whereas the blue- and red-dotted lines correspond to the maximum value analysis. The green-dotted line displays the evolution of the intensity derived from the analytical Eq. (4.20) with the assumption of a 6 fs pulse being present at each maximum. 100

4.28 The same final dependency of the maximum intensity in the filament upon the external focusing setup using the semi-classical formula (c.f. Sec. 4.1) to obtain the intensity value inside the filament. The findings show a strong sensitivity, since the ponderomotive potential U_p is of similar strength as the ionization potential I_p . 101

5.1 Simulated pulse propagation as a function of the input pulse duration together with the respective evolution of the on-axis intensity. The chosen pulse durations are (a) $\tau_{in}=5$ fs, (b) $\tau_{in}=8$ fs and (c) $\tau_{in}=10$ fs. 106

B.1 Sketch describing the basic idea behind the calculation of the wavefront sag at the hand of a focused Gaussian beam. The wavefront sag follows the wavefront curvature which is imprinted by the focusing optic and shows a decreasing behavior as it reaches the focus. 114

List of Tables

1	Abbreviations.	V
2	Mathematical symbols.	VII
3.1	Values used for the calculation of the wavefront sag for 1 bar of argon interacting with a pulse centered at 800 nm [144].	20
3.2	Findings from previous efforts to measure the self-compression in a femtosecond filament.	29
4.1	Findings from previous efforts to measure the self-compression in a femtosecond filament. Various methods are compared, as the analysis of super-continuum generation (SCG), fluorescent emission (side-imaging), Fluence detection and high-harmonic generation (HHG). The respective value of the clamping intensity is labeled as I_c . Column I_{an} shows the values obtained by the analytical formula in Eq. (4.20) and the pulse duration τ needed to achieve this intensity.	92

LIST OF TABLES

Acknowledgments

Last but not least, i would like to thank everyone who has been a part of this scientific journey. First of all i would like to thank Uwe Morgner and Milutin Kovačev for the possibility to do research in this complex and interesting field of science. I highly appreciate your optimism and support during the last couple of years. Thank you for the constant input, may it be for the preparation of papers or to answer questions occurring in the daily scientific life.

Second, i would like to thank Carsten Brée for supplying the pulse-propagation code and Ayhan Demircan for many fruitful discussions. The scientific input coming from both of you has been supportive and valuable and encouraged me a lot of times to think outside of the experimentalist's box.

I would also like to acknowledge some people who have been a great support regarding the laboratory works. Daniel Steingrube deserves credit for introducing me to the laser-system during my diploma thesis and the early days of the PhD works. The employees from Venteon have always been able to give hints concerning the improvement of our laser system. Heiko Kurz and Tamas Nagy should have an extra page of appreciation. You are great, knowledgeable colleagues as well as friends and have made the time inside and outside of the laboratory enjoyable.

Not only the direct working partners enriched the years in the research group. I thank Bruno, Jose and Welm for being livid colleagues and for their (sometimes quite off-topic) discussions. Additionally, colleagues like Moritz, Tino, Thomas, Stefan, Guido, Berhard, Liping and Hauke have always been contributing to the positive mindset at the workplace. I also would like to thank the external groups at FORTH and LOA, which allowed me to participate in research projects with them. The time spend at your institutes has been a great enrichment to my scientific and personal knowledge.

Besides the scientific staff, i would like to thank the secretariat for managing the business-matters, the workshop for their special constructions and Kai-Martin Knaak for electronic aid.

Aside from the working environment, i would like to thank all the members of my basketball team - you always have been a great influence and the sport was a good balance for the everyday work.

Saving the best until last, i would like to thank my family and especially Antje. You have been a caring and loving support during my whole PhD-studies.

ACKNOWLEDGMENTS

Publications

Scientific Publications

1. Vockerodt, T.; Steingrube, D.S.; Schulz, E.; Kretschmar, M.; Morgner, U. and Kovačev, M.
Low- and high-order harmonic generation inside an air filament
Applied Physics B: Lasers and Optics **106**, 529-532 (2012)
2. Steingrube, D.S.; Kretschmar, M.; Hoff, D.; Schulz, E.; Binhammer, T.; Hansinger, P.; Paulus, G.G.; Morgner, U. and Kovačev, M.
Sub-1.5-cycle pulses from a single filament
Optics Express **20** (21), 24049-24058 (2012)
3. Kretschmar, M.; Hernández-García, C.; Steingrube, D.S.; Plaja, L.; Morgner, U. and Kovačev, M.
Spatial contributions of electron trajectories to high-order-harmonic radiation originating from a semi-infinite gas cell
Physical Review A **88**, 013805 (2013)
4. Böhle, F.; Kretschmar, M.; Jullien, A.; Kovacs, M.; Miranda, M.; Romero, R.; Crespo, H.; Morgner, U.; Simon, P.; Lopez-Martens, R. and Nagy, T.
Compression of CEP-stable multi-mJ laser pulses down to 4 fs in long hollow fibers
Laser Physics Letters **11**, 095401 (2014)
5. Kretschmar, M.; Brée, C.; Nagy, T.; Demircan, A.; Kurz, H.G.; Morgner, U. and Kovačev, M.
Direct observation of pulse dynamics and self-compression along a femtosecond filament
Optics Express **22** (19), 22905-22916 (2014)
6. Brée, C.; Kretschmar, M.; Nagy, T.; Kurz, H.G.; Morgner, U. and Kovačev, M.
Impact of spatial inhomogeneities on on-axis pulse reconstruction in femtosecond filaments
J. Phys. B: At. Mol. Opt. Phys. **48**, 094002 (2015)

Contributions at international conferences

1. International Conference on Ultrafast Structural Dynamics (ICUSD), 2012, Berlin, Germany
Poster: *Probing Femtosecond Filamentation via High-order Harmonics*
Steingrube, D.S.; Schulz, E.; Kretschmar, M.; Binhammer, T.; Gaarde, M.; Couairon, A.; Morgner, U. and Kovačev, M.
2. International Symposium on Filamentation (COFIL), 2012, Tucson, USA
Poster: *Sub-1.5-cycle pulses emerging from a single femtosecond filament*
Kretschmar, M.; Steingrube, D.S.; Hoff, D.; Schulz, E.; Binhammer, T.; Hansinger, P.; Paulus, G.G.; Morgner, U. and Kovačev, M.

3. International Symposium on Filamentation (COFIL), 2012, Tucson, USA
Oral: *Probing femtosecond filamentation via high-order harmonics*
Kretschmar, M.; Nagy, T.; Kurz, H.G.; Morgner, U. and Kovačev, M.
4. Extreme Nonlinear Optics and Solitons, 2013, Berlin, Germany
Poster: *Direct observation of pulse dynamics and self-compression along a femtosecond filament*
Kretschmar, M.; Nagy, T.; Demircan, A.; Brée, C.; Kurz, H.G.; Morgner, U. and Kovačev, M.
5. High-Intensity Lasers and High-Field Phenomena (HILAS), 2014, Berlin, Germany
Oral: *Direct observation of pulse splitting dynamics and self-compression along a femtosecond filament*
Kretschmar, M.; Brée, C.; Demircan, A.; Nagy, T.; Kurz, H.G.; Morgner, U. and Kovačev, M.
6. Conference on Lasers and Electro-Optics (CLEO), 2014, San Jose, USA
Oral: *Direct observation of pulse dynamics, influencing high-order harmonic emission along a filament*
Kretschmar, M.; Nagy, T.; Demircan, A.; Brée, C.; Hofmann, M. Kurz, H.G.; Morgner, U. and Kovačev, M.
7. International Symposium on Filamentation (COFIL), 2014, Shanghai, China
Oral: *Tracking pulse dynamics along a femtosecond filament, influencing direct high-order harmonic emission*
Kretschmar, M.; Nagy, T.; Demircan, A.; Brée, C.; Hofmann, M. Kurz, H.G.; Morgner, U. and Kovačev, M.
8. Conference on Lasers and Electro-Optics (CLEO), 2015, Munich, Germany
Poster: *Direct High-Order Harmonic Radiation as a Tool for the Characterization of Femtosecond Filaments*
Kretschmar, M.; Brée, C.; Nagy, T.; Kurz, H.G.; Morgner, U. and Kovačev, M.